UNIVERSIDAD COMPLUTENSE DE MADRID
FACULTAD DE CIENCIAS FÍSICAS

TESIS DOCTORAL

Optimización de la producción de radioisótopos en el nuevo ciclotrón superconductor AMIT

Optimizing the radioisotope production of the novel AMIT superconducting weak focusing cyclotron

MEMORIA PARA OPTAR AL GRADO DE DOCTOR

PRESENTADA POR

Pedro Calvo Portela

DIRECTORA

Concepción Celia Oliver Amorós

Madrid

Universidad Complutense de Madrid

Facultad de Ciencias Físicas

TESIS DOCTORAL

Optimización de la producción de radioisótopos en el nuevo ciclotrón superconductor AMIT

Optimizing the radioisotope production of the novel AMIT superconducting weak focusing cyclotron

Memoria para optar al grado de Doctor
presentada por

Pedro Calvo Portela

Director
Concepción Celia Oliver Amorós

Madrid
Septiembre 2020

Author Pedro Calvo Portela
Particle Accelerator Unit
Department of Technology
CIEMAT
Madrid, Spain

Supervisor Dra. Concepción Celia Oliver Amorós
Particle Accelerator Unit
Department of Technology
CIEMAT
Madrid, Spain

Coordinator Dr. Luis Mario Fraile Prieto
Department of Structure of Matter, Thermal Physics and Electronics
Faculty of Physical Sciences
Universidad Complutense de Madrid
Madrid, Spain

Reviewers Dra. María de los Ángeles Faus-Golfe
Laboratoire de Physique des 2 Infinis Irène Joliot-Curie - IJCLab
Université Paris-Saclay
Orsay, France

Dr. Sergey A. Antipov
Deutsches Electronen-Synchrotron - DESY
Hamburg, Germany

No se olvide que es siempre la lectura una colaboración

— Ortega y Gasset

Acknowledgments

I think the first page of this thesis should be devoted to say thanks to all people who made this work possible.

First of all, I would like to thank Conchi for giving me the opportunity to do something I like. Thanks for all the support, the fruitful discussions, the wise advice and all the dedicated review of my work, overcoming all the difficulties and limitations we have had in these years. It is because of your trust that I have been able to find my way into a new field to me, increasing my knowledge in Physics and attending conferences and courses to continue my beginnings in research.

I would like to acknowledge the help received from all my colleagues at CIEMAT during these years with my work, from scientist to technicians and administrative staff. Especially, I have to thank Diego Obradors for all his advice, help and support given during my work. Without him a great part of the achievements of this thesis would not have been possible. Thanks also to Dani, Ivan, Manuel, Antonio, Rodrigo, Javi and Fernando for having contributed to the development of my work. I have to thank greatly the help and all the technical support given by CETA-CIEMAT group that has allowed the execution of this thesis.

I am also indebted to Andreas Adelmann for allowing me to join the OPAL development group, supporting me during my research stay at PSI and giving me valuable advice. All my thanks to the people who have helped me to become part of this research group in computational particle physics. Thanks to Achim Gsell, Matthias Frey, Jochem Snuverink and Daniel Winklehner, for giving me all the help and passing me their experience.

I would also like to thank all the people who have trusted me throughout my academic and research career. Thanks to Felipe J. Llanes-Estrada, José Manuel Udias, Luis Mario Fraile and Sergio Ibarmia, who encouraged and helped me from my period at the university to the beginning of my PhD.

Finally, thanks to my friends and family, which I am really proud of. To my father for always encouraging me to learn more, and to my brothers and sisters for their attention and always stay close. And now, even most important is to say thanks to Celia, for accompanying me in this last period, the most difficult and hardest, for persevering and suffering with me all this time.

Summary

Nuclear imaging techniques are becoming one of the most widely used medical diagnostics tools for certain illness such as cancer and Alzheimer disease. The increase in these medical procedures, particularly positron emission tomography, is leading to a saturation of the actual radioisotope production system. Therefore, particle accelerators, specially the cyclotron, emerged as an alternative to the traditional supply system based on centralized production in nuclear reactors. Its characteristics from the physical and technological point of view allow a controlled and localized production, especially relevant in the case of short-lived radionuclides, through a well-known technology developed for decades without the use of a large and expensive facilities.

With that in mind, the AMIT project (Advanced Molecular Imaging Technologies) aims to extend the use of these medical procedures with the development of a new compact cyclotron focused on the on-site short-life radioisotopes production, specifically ^{11}C and ^{18}F, in hospitals and research centers. In order to achieve this main objective, the AMIT cyclotron is based on a classical weak focus configuration with high magnetic field provided by a superconducting magnet with an autonomous cryogenic system. In addition, with the aim of reducing the total size of the accelerator, the cyclotron employs an internal H^- ion source with an electron stripping system that provides a final proton beam that is transported to the production target.

This thesis evaluates the challenging combination of all the technical characteristics of the AMIT cyclotron, which results in a balance of the beam dynamics with all the subsystems to achieve an optimal radioisotope production. For this goal, all the physical processes associated with the beam acceleration from the ions production and the injection into the accelerator, to the extraction of the resulting beam and its transport to the target are studied by means of theoretical analysis, computational calculations and experimental measurements.

Firstly, the experimental results obtained in the characterization campaigns of the cyclotron ion source are presented. The output beam current, and therefore, the fulfillment of the main requirements of the accelerator, depends largely on the current injected into the accelerator. For this reason, the knowledge related to the operation of the ion source and the resultant beam has been analyzed in a dedicated facility at CIEMAT (Centro de Investigaciones Energéticas, Medioambientales y Tecnológicas).

The beam dynamics have been assessed by means of simulations carried out with the OPAL code (Object Oriented Parallel Accelerator Library). The study includes all the relevant effects from the point of view of particle accelerator physics, with special attention to those characteristics that allow the precise adjustment of the cyclotron operation and the optimization of the

radioisotope production under different conditions. For this purpose, the adjustment of the different subsystems within the design tolerances and the possible modification of some of them in their final assembly are analyzed, as well as the impact of some significant parameters variations in the magnetic field, the radiofrequency system, the acceleration gap or the beam extraction system.

In addition, a relevant feature in a compact H^- cyclotron with internal ion source is the beam interactions with the residual gas and the electromagnetic field. Therefore, the computational implementation of these physical processes within the opal code is presented, as well as their application in the AMIT cyclotron in order to minimize the beam losses and optimize the final beam current with the control of the vacuum conditions in the accelerator.

All these studies allow to combine the different elements of the cyclotron with the beam dynamics for an optimal and efficient radioisotope production, essential for the commissioning and the optimization of the cyclotron operation.

Resumen en castellano

Las técnicas de imagen nuclear se están convirtiendo en uno de los diagnósticos médicos más empleados para ciertas enfermedades como el cáncer y el Alzheimer. El incremento de estos procedimientos médicos, en particular de la tomografía por emisión de positrones, está dando lugar a una saturación del sistema actual de producción de radioisótopos. Por ello, los aceleradores de partículas, en especial el ciclotrón, surgieron como una alternativa al sistema tradicional de suministro basado en la producción centralizada en reactores nucleares. Sus características desde el punto de vista físico y tecnológico permiten una producción controlada y localizada, especialmente relevante en el caso de radionucleidos de vida corta, a través de una tecnología bien conocida y desarrollada desde hace décadas sin necesidad de una gran y costosa instalación.

De esta forma, el proyecto AMIT (Advanced Molecular Imaging Technologies) pretende ampliar el empleo de estos procedimientos médicos con el desarrollo de un nuevo ciclotrón compacto diseñado para la producción in-situ de radioisótopos de vida corta, concretamente ^{11}C y ^{18}F, en hospitales y centros de investigación. Con el fin de lograr este principal objetivo, el ciclotrón está basado en una configuración clásica de enfoque débil con alto campo magnético proporcionado por un imán superconductor con un sistema criogénico autónomo. Además, con el fin de contribuir a la reducción del tamaño total del acelerador, el ciclotrón emplea una fuente interna de iones H^- con un sistema de extracción por desprendimiento de electrones que proporciona un haz final de protones que es transportado hasta el blanco de producción.

Esta tesis evalúa la exigente conjunción de todas las características técnicas del ciclotrón AMIT, que da lugar a un balance de la dinámica del haz con todos los subsistemas para lograr una óptima producción de radioisótopos. Con este fin, todos los procesos físicos asociados con la aceleración del haz desde la producción de los iones y su inyección en el acelerador, hasta la extracción del haz resultante y su transporte hasta el blanco, son estudiados mediante análisis teóricos, mediciones experimentales y cálculos computacionales.

Primeramente, se presentan los resultados experimentales obtenidos en las campañas de caracterización de la fuente de iones del ciclotrón AMIT. La corriente final del haz, y por tanto, el cumplimiento de los requisitos principales del acelerador, dependen en gran medida de la corriente inyectada en el acelerador. Por este motivo, el conocimiento relativo al funcionamiento de la fuente de iones y al haz resultante se han analizado en una instalación dedicada en el CIEMAT (Centro de Investigaciones Energéticas, Medioambientales y Tecnológicas).

La dinámica del haz ha sido analizada mediante simulaciones realizadas con el código OPAL (Object Oriented Parallel Accelerator Library). El estudio incluye todos los efectos relevantes

desde el punto de vista de la física de aceleradores de partículas, con especial atención a aquellas características que permiten el ajuste preciso de la operación del ciclotrón y la optimización de la producción de radioisótopos bajo distintas condiciones. Para ello, se evalúan la regulación de los distintos subsistemas dentro de las tolerancias de diseño y la posible modificación de alguno de ellos en su ensamblaje final, así como el impacto que podría tener ciertas variaciones significativas en los parámetros de operación, tales como el campo magnético, el sistema de radiofrecuencia, la brecha de aceleración o el sistema de extracción del haz.

Además, un factor de gran relevancia en un ciclotrón compacto de H^- con fuente de iones interna como AMIT es la interacción del haz con el gas residual y el campo electromagnético. Por ello, se presenta la implementación computacional de dichos procesos físicos dentro del código OPAL así como su aplicación en el ciclotrón AMIT con el fin de minimizar las pérdidas de haz y optimizar la corriente final del haz con el control de las condiciones de vacío en el acelerador.

Todos estos estudios permiten aunar los distintos elementos del ciclotrón con la dinámica del haz para una óptima y eficiente producción de radioisótopos, esencial para el commissioning y la optimización de operación del ciclotrón.

Contents

List of Figures

List of Tables

All I wanted to do was try to live the life that was inside me, trying to get out
— Hermann Hesse

Preface

The development of nuclear medicine, especially medical imaging techniques, has been highly relevant to enhance the accurate diagnosis and effective treatment of many illnesses like cancer and Alzheimer's disease. In this framework, Positron Emission Tomography (PET) has experienced a significant growth over the last years with the corresponding positive impact on society. These medical procedures require the use of radioisotopes, unstable elements most of them artificially produced. One of the increasingly widespread techniques for the radioisotope production is based on the bombardment of a target with a high-energy particle beam to produce the desired radionuclide through a nuclear reaction. This requires a particle accelerator, being the cyclotron the most widely used for this purpose. Nevertheless, the high cost associated with the development, maintenance and operation of an accelerator as well as the typically short half-life of the radioisotopes limit the number of centers employing these leading-edge techniques.

With the ultimate aim of facilitating the expansion of such advanced nuclear imaging techniques, a compact cyclotron, AMIT, has been developed. It relies on superconducting technology that makes it possible to significantly improve the compactness of the accelerator, contributing to its deployment in hospitals and non-conventional centers for an on-site production that will reduce the corresponding delivery costs. It allows access to diagnostic techniques that require very short half-life radioisotopes. The reduction of the overall size imposes severe limitations on the beam dynamics, connected mainly with the use of an internal ion source, the high acceleration voltage combined with a high magnetic field and the limited acceleration region. For this reason, a complete evaluation of the beam dynamics of the AMIT cyclotron emerges as a primary need to fulfill the objectives of this ambitious project. Furthermore, the acquisition of a comprehensive knowledge of all associated physical effects and the technological challenges to be overcome, allows the accelerator optimization for an efficient radioisotope production, reducing maintenance and operating costs, and limiting the environmental and radiological impact.

In order to carry out an in-depth study of the beam dynamics of a cyclotron, it is necessary to use a versatile tool allowing the reliable reproduction of all the characteristics involved in particle accelerator physics. Within the great variety of existing simulation codes, OPAL has emerged as a versatile, powerful and well-supported option for performing the simulations of the AMIT cyclotron. In addition, the implementation of new computational features within OPAL allows to extend the code to new relevant features in particle accelerators. In particular, the analysis of the physical interaction of particles with matter have been extended to analyze relevant residual beam interactions, applying it to AMIT cyclotron.

The work presented in this thesis is focused on the analysis and comprehension of the beam dynamics for AMIT cyclotron[1], being the objectives summarized in the following points:

- The evaluation of the beam dynamics of the AMIT compact superconducting cyclotron.
- A detailed analysis of the influences of the final tolerances of the subsystems on the fulfillment of the beam requirements, as well as potential alignment issues in the final assembly.
- The experimental characterization of the AMIT H^- ion source in a devoted test facility previous the cyclotron operation.
- The optimization of radioisotope production efficiency and the minimization of the cyclotron activation through a specific study of the beam residual interactions.

With that in mind, this dissertation is divided in six main chapters, where the different results obtained during the PhD research period are presented and developed.

- Chapter 1 is organized in two introductory sections. On the one hand, the fundamentals of nuclear medicine imaging are presented, in particular the physics behind PET. Then, a wide discussion concerning the status of the different methods used for medical radioisotopes production is showed, reviewing both the traditional reactor-based methods and the accelerator-produced radioisotope procedures, with special focus on the cyclotron. On the other hand, the second section gives a brief description of the fundamental concepts related with the cyclotron from the particle accelerator physics point of view.
- In Chapter 2 a detailed description of the AMIT cyclotron with a dedicated outline of each subsystem is presented.
- Chapter 3 illustrates OPAL code features and the AMIT beam dynamics model, emphasizing all the performances used for the simulations.
- In Chapter 4, the experimental measurements of the ion source characterization performed in a devoted facility are presented, determining the optimal operational conditions and the beam quality through the extracted current and beam profile measurements.
- Chapter 5 brings forward the main beam dynamics results from AMIT simulations performed with OPAL, with an overview of the fundamentals effects and a detailed analysis of the ultimate tolerances of the subsystems.
- Chapter 6 provides a comprehensive study of the residual interactions affecting the beam stripping during the acceleration for the cyclotron optimization and the losses characterization. The computational implementation in OPAL of these particle-matter interactions is described.

At the end, the general conclusions of this thesis and the publications and conference proceedings derived from this work are presented.

[1]This work was partially supported by the Spanish Ministry of Economy and Competitiveness - State Research Agency under project FPA2016-78987-P.

Of what a strange nature is knowledge! It clings to the mind, when it has once seized on it, like a lichen on the rock

— Mary Shelley

Chapter 1

Introduction

Particle accelerators have been one of the pillars to understand the behavior of matter at subatomic scales. Research on fundamental physics has been the driving force for particle accelerator development, where the validation of the Standard Model and the search for the new physics beyond it has demanded increasing accelerators capabilities through remarkable technology improvements to reach high-quality beams. From the cathode-ray tubes [1], going through the first linear accelerator built by Cockcroft and Walton in 1930 [2] and the first cyclotron by Lawrence and Livingston in 1932 [3], until the 27-km-circumference Large Hadron Collider at CERN [4], an increasingly precise technology has been developed and optimized.

Beyond the research in physics, the enhancements around particle accelerator technologies have led to a broad range of applications in diverse fields of knowledge, which is continuously extended. They are also a relevant tool in many interdisciplinary research environment as chemistry, biology, earth sciences, materials science and cosmology. As a consequence, their use is widespread to all areas of society. In industry, particle accelerators are extensively used in several techniques as the analysis and characterization of material damage, ionic implantation, neutrography, beam aided chemical reactors, modification of crystals, etc. Other fields of application for particle accelerators include archaeology, art and national security. Nevertheless, it is in medicine where particle accelerators have a meaningful impact on society, using them for particle therapy as well for diagnostic procedures based on radioisotopes.

Nuclear medicine has became one of the most significant advances in the science of the twentieth century. Since the discovery of X-rays phenomenon by Roentgen in 1895 [5] and the natural radioactivity in 1896 by Becquerel [6], diverse uses of radioisotopes have emerged as diagnostic or treatment tools. First medical applications of the radioactivity [7–9] were followed by extensive animal and human studies employing radioactive substances under the 'tracer principle'. Pioneered by Hevesy [10, 11], this principle supports the base of modern nuclear imaging techniques.

1.1 Radioisotopes in Medicine

The comprehension of the most significant diseases in the 21st century, like cancer, cardiovascular and Alzheimer's diseases entails the scientific progress of knowledge about their causes. In addition, the development and application of advanced techniques is essential to lead to an efficient and accessible early diagnosis and treatment. Medicine benefits from achievements in the field of nuclear sciences to apply radioactive substances in controlled and advanced procedures, becoming an independent and relevant medical specialty. The use of radioactive tracers in Nuclear Medicine enables the assessment of bodily physiological functionality to diagnose and treat diseases. Its potential lies in the capability to provide sensitive measures of an extensive range of biologic processes in the body as well as an alternative and complementary procedure to treat diverse illnesses, mainly carcinogen tumors.

The therapeutic application of radioisotopes is based on the introduction into the body, either mechanically (brachytherapy) or via a biochemical pathway (endoradiotherapy), of certain radionuclides emitting high energy radiation that will be absorbed in the affected tissue to destroy the malignant cells. Different isotopes are employed for such therapeutic purposes, according to the radiobiological effectiveness and range of action. The choice of the nuclide lies in the best suited physical and nuclear characteristics to a particular type of tumor. The most effective isotopes for therapeutic purposes are β^-, γ and e-Auger emitters.

On the other hand, medical imaging processes provide an effective tool for diagnosis, treatment planning, evaluation, and follow-up of numerous diseases as well for research applications (Figure 1.1). Nuclear imaging is developed as an interdisciplinary medical area based on the detection of radiation emitted behind the decay of a radionuclide. A pharmacology process chemically binds the radionuclides to molecules with well-known biological properties, synthesizing a radiotracer which is administered to the patient. At that point, the molecules are concentrated on specific organs or cellular receptors with a certain biological function. The radioisotopes will be decaying in the tissue, and the radiation emitted is accurately measured by a specific detector. Lastly, the collected data are processed to reconstruct an image of the body through visualization of spatial and temporal distribution accumulated. This technique allows nuclear medicine to determine the location and extent of the disease in the body by functional imaging of the internal anatomy with a millimeter or sub-millimeter resolution.

In nuclear medicine, two main modalities of physiological functional imaging are considered: Single-Photon Emission Computed Tomography (SPECT) and Positron Emission Tomography (PET), relying on different radioactive decay modes resulting in the emission of energetic single photons in the range of hundred keV or annihilation gamma rays. Additionally, morphological knowledge provided by Computed Tomography (CT), Magnetic Resonance Imaging (MRI), or ultrasounds can be combined implementing advanced image reconstruction techniques to provide complementary data. Meaningful medical information is obtained, like the segmentation of a tumor and organs at risk, as well as the identification of radioresistant subareas which might require a locally enhanced radiation dose for more successful tumors eradication [12]. A treatment

plan is then generated using computational tools that optimizes the intended dose according to the structures identified in the multimodal images used. Thus, nuclear medicine imaging provides unique information on physiological function and metabolic activity.

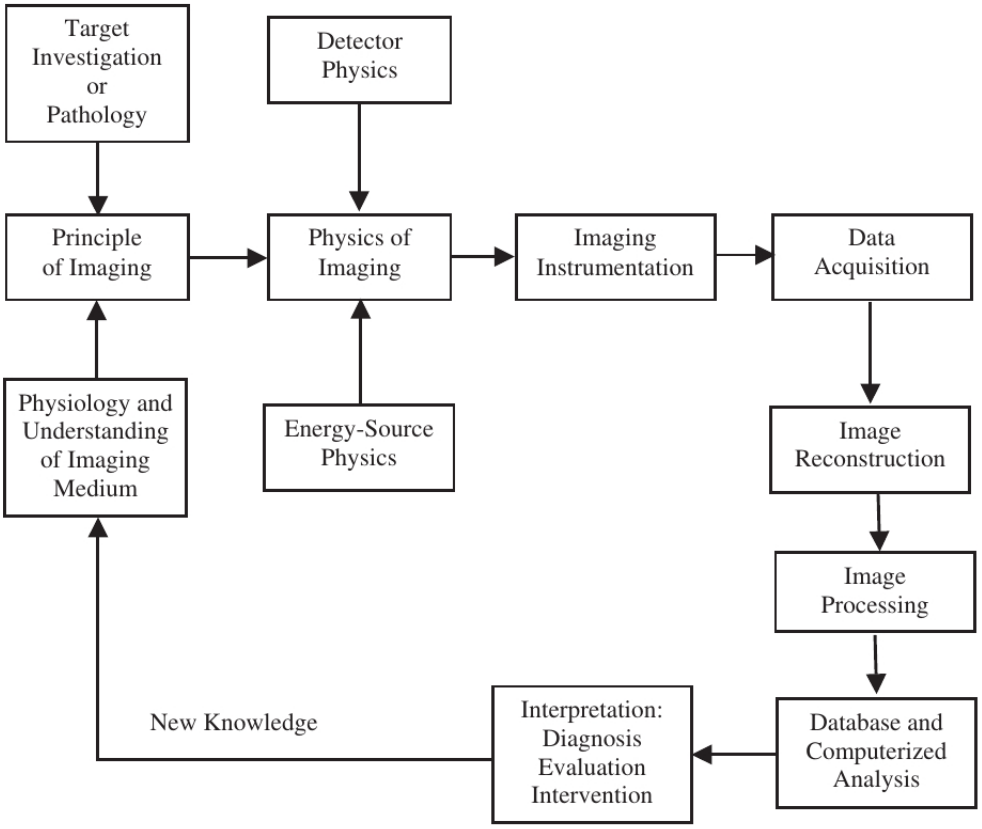

Figure 1.1: *Conceptual diagram of medical imaging process [13].*

1.1.1 Nuclear imaging techniques

The medical uses of radionuclides in nuclear imaging can be organized into two standardized diagnostic procedures, according to the physical processes on which they are based: SPECT and PET. On the whole, the radionuclides are introduced into the patient by the administration of radiation emitting radiopharmaceuticals in remarkably small quantities without causing any significant physiologic or pharmacologic effects. The radiation is penetrating enough to escape the body and it can be subsequently counted outside by the detectors.

Single-Photon Emission Computed Tomography

SPECT diagnostic technique is based on the radiation detection of a single-photon-emitting radionuclide by isomeric transition or electron capture in a dedicated gamma-camera. This tomography method arose from the use of a rectilinear scanner from different angles around the body [14]. The detector assembly consists of a large area scintillator crystal, a light guide, and

an array of photosensors, usually photomultiplier tubes. The camera is able to rotate around the patient and captures a series of images. SPECT detector accurately determines the energy of the measured photon and localizes the gamma photon event in the detector assembly. The resulting distribution is digitized and reconstructed into 3D tomographic images.

The extensive use of SPECT techniques covers different medical fields [15,16], since cardiology in studies of myocardial perfusion for assessing coronary artery disease and heart muscle damage following infarction, going through neurology, evaluating brain functions or pathological brain disorders, until oncology with radionuclide accumulation in cancerous cells for tumor detection.

For SPECT imaging, ^{99m}Tc is the most widely radio-tracer used in all nuclear medicine procedures performed worldwide [17]. It is extensively employed because it can be easily incorporated into a multitude of radioligands allowing the visualization and quantification of a broad range of physiological processes. Therefore, ^{99m}Tc is typically used to diagnose diseases in a large amount of tissue and organ systems. The half-life is sufficient to be employed in nuclear medicine procedures but not excessive to entail severe doses to the patient. Detectors are high efficient on the energy range of its decay photons, increasing the quality of the resulting images. An effective mechanism production based on radioisotope generators can supply to hospitals regular amount of the radionuclides for a significant number of scans. In addition, other gamma emitters are used in SPECT procedures for other specific medical issues (Table 1.1).

Table 1.1: *Main characteristics of SPECT radioisotopes [18]*

Isotope	Half-life (h)	γ energies (keV)
^{67}Ga	78.281 (12)	91, 93, 184, 209, 300, 393
^{99m}Tc	6.0072 (9)	140
^{111}In	67.3128 (96)	171, 245
^{123}I	13.2234 (19)	159
^{131}I	192.605 (14)	284, 364, 637, 722
^{201}Tl	73.010 (41)	135, 167, 71*(from ^{201}Hg)

Positron Emission Tomography

PET is a tomography imaging modality based on the detection in coincidence of annihilation photons resulting from the interactions of an ordinary electron and a positron, the positively charged antiparticle of the electron. The positrons come from a β^+ decay process of a radionuclide by the conversion of a proton into a neutron with the emission of a positron and a neutrino, a non-interacting particle.

The total energy released in the decay process is distributed between the positron and the neutrino, giving rise to a continuous spectrum of emission energies [19]. The emitted positron travels through human tissue in a tortuous path (called Line Of Response, LOR), giving up its kinetic energy mainly by Coulomb interactions, until it achieves thermal energies ($\sim k_B T$). At that point, the positron is annihilated with a nearby electron in a matter-antimatter event. In

this process, a pair of two photons (γ-rays) is produced simultaneously, each one with an energy of 511 keV, traveling in (nearly) opposite directions (Figure 1.2).

$$ {}^{A}_{Z}X \xrightarrow{\beta^+} {}^{A}_{Z-1}Y + e^+ + \nu_e $$

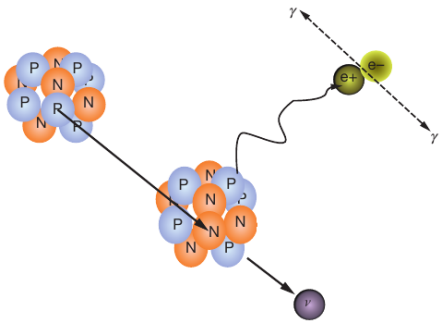

Figure 1.2: *Schematic representation of β^+ decay process of a radionuclide and the subsequent positron annihilation event with an electron [20].*

The imaging process is accomplished when these two photons are detected in coincidence by an array of detectors. The PET camera consists of a full ring of several thousand of scintillation detectors to generate the image, resulting in a higher sensitivity to radioactivity and a better spatial resolution than the conventional gamma camera. Consequently, the subsequently reconstructed image provides a very precise three-dimensional representation of the tissue through the distribution of radioactivity within the body of a patient.

The advances in PET technology have developed hybrid procedures based on the merging of physiologic images and detailed morphological or anatomical images [15, 20–23]. Thus, PET single modality is combined with computed tomography (PET/CT), magnetic resonance imaging (PET/MRI) or recently the Time-of-flight PET (TOF/PET), improving the image diagnostic accuracy and expanding the clinical diagnostic horizons of PEcET.

Relevant factors have to be taken into account in the imaging reconstruction process. First, the positron range, that is to say, the distance between the positron emission point and the final annihilation location. It depends on the initial energy distribution of the positron emitted as well on the electronic density of the material where the decay process takes place. The positron range is one of the primary restraining factors to the final image resolution. Furthermore, the two γ-rays are not emitted necessarily in collinearity [24–26]. This non-collinearity effect is due to the linear momentum conservation law when the positron has not lost all its energy just before the annihilation or if the event occurs with an electron from the atomic shell [27]. Consequently, collinearity represents another critical factor to be considered, limiting the image resolution. In addition, the radionuclides can decay through different decay modes. The fraction of each individual decay process is called branching ratio. A significant branching of decay modes implies a lower image resolution as well as a potential higher dose for the patient.

PET technique is practiced in nuclear medicine for quantitative measurements of physiologic parameters in vivo with a wide range of clinical and research applications [21, 28] in cardiology;

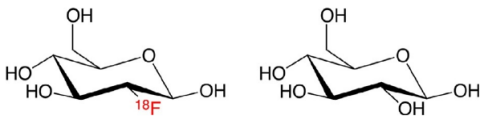

Figure 1.3: *Chemical structure of a ^{18}F-FDG molecule (left) in comparison with glucose (right) [21].*

neurology, in the evaluation of the pathophysiology of many brain disorders as well as in the study of neurophysiology of the non-affected brains; to quantify radiation dose in internal radiotherapy or to follow others metabolic process. However, the principal use is predominantly oncology for tumor detection.

The most commonly administered PET radionuclide is ^{18}F, used for the production of 2-deoxy-2-^{18}F fluoro-D-glucose (^{18}F-FDG) [29,30], the glucose analogous in which an oxygen atom is replaced by a positron-emitting fluorine-18 atom (Figure 1.3). Its chemical similarity to glucose enables the uptake of ^{18}F-FDG into cells but, in contrast to glucose, is not further metabolized, thus is accumulated in cells ('metabolic trapping'). As the glucose is overexpressed in many tumor cell types as compared to normal cells, ^{18}F-FDG is concentrated in these tumors. This enables PET to visualize tumors as regions of increased radioactivity accumulation. Clinical applications of brain PET are focused on the use of ^{18}F-FDG (glucose metabolism) and ^{18}F-amyvid (β-amyloid imaging).

Moreover, other positron-emitting nuclides used in PET imaging [31] are non-metals isotopes with a significantly short half-life and low energy positron emitters like ^{11}C, ^{13}N and ^{15}O. These radioisotopes can be substituted for stable atoms of the corresponding elements in compounds of biologic importance, resulting in radiolabeled molecules with identical biochemical properties as the original. In addition, other advantages using short-lived radionuclides arise from the reduced dose associated with each administration, the capacity of performing serial studies from the point of view of radiation protection and minimization of radioactive waste disposal problems. Despite some drawbacks as the requirement of a nerby radioisotope production facility, rapid chemical procedures especially for the formation of more complex compounds or the geographical dispensation available according to the half-life, the use of short-lived radioisotopes in PET diagnostics highly relevant.

Among these short-lived radioisotopes, ^{11}C is especially engaging from the biochemical point of view due to almost all biological molecules are based on carbon. Besides that, the very short half-life of ^{11}C offers several significant advantages like the possibility of multiple scans in a brief period of time and the reduction of radiation burden for the patient. In this way, ^{11}C has become a relevant tracer in PET technique applied to diverse medical areas, especially in neuroimaging.

In the same way, new emerging PET radionuclides are expanding to supply tracers for many physiological and biological mechanisms in humans slower in comparison with standard PET isotopes half-life, like ^{64}Cu and ^{124}I [32]. Table 1.2 includes some pertinent nuclear properties of the main radionuclides used in PET scans, like half-life, the mean and maximum β^+ energies, the maximum and the Root-Mean-Square (RMS) positron range and the branching ratio (the percentage of total decays resulting in positron emission instead of electron capture).

Table 1.2: *Main characteristics of PET radioisotopes [18, 33]*

Isotope	Half-life (min)	Mean energy (keV)	Max energy (keV)	Max range (mm)	RMS range (mm)	Branching ratio (%)
^{11}C	20.363 (13)	385.7 (4)	960.4 (10)	3.9	0.4	99.7669 (25)
^{13}N	9.965 (4)	491.82 (12)	1198.5 (3)	5.1	0.6	99.8036 (20)
^{15}O	2.037 (3)	735.28 (23)	1732.0 (5)	8.0	0.9	99.9003 (10)
^{18}F	109.77 (5)	249.8 (3)	633.5 (6)	2.3	0.2	96.7 (4)
^{62}Cu	9.67 (3)	1319.0 (7)	2936.9 (5)	15	1.6	97.8 (3)
^{64}Cu	762.06 (12)	278.21 (9)	653.03 (20)	2.0	0.2	17.60 (22)
^{66}Ga	569.4 (18)	1750 (18)	4153 (3)	20	3.3	57 (4)
^{68}Ga	67.71 (8)	829.5 (13)	1899.1 (12)	9.0	1.2	88.91 (9)
^{76}Br	972 (12)	1180 (90)	3941 (9)	19	3.2	55 (3)
^{82}Rb	1.2575 (2)	1481 (12)	3382 (3)	18	2.6	95.4 (6)
^{124}I	6013.44 (43)	820 (70)	2137.6 (19)	7.0	0.8	22.7 (13)

1.1.2 Radioisotope criteria for nuclear medicine

Despite the numerous radionuclides that can be physically produced, only a few of them are appropriate to be used in nuclear medicine. The choice of the adequate radionuclide is critical to achieve successful diagnostic imaging and cancer treatment outcomes. Radiotracers have to satisfy high quality criteria to be employed in medical procedures, including nuclear, physical and biological characteristics [15, 34].

As regards decay properties of the radionuclide, the half-life should be short enough to reduce the dose to the patient, but some longer half-life radioisotopes could be required for the tracing of longer metabolism processes. In addition, the half-life must be sufficiently long for the radiopharmaceutical preparation and injection into the patient. If radionuclide half-life is excessively long, the radiation is emitted outside the examination time, which can result in a high radiation dose to the patient in relation to the number of decays detected during the study. Long-lived radionuclides can also cause problems in terms of storage and disposal.

For imaging purpose, the radiation energy determines the availability of useful gamma rays during the detection process. Photons should be in the 50-600 keV energy range for a suitable measurement by the detectors. Lower energy photons would have a high interaction probability inside the patient body, increasing the radiation dose and reducing the rate of detected gamma rays.

The specific activity of the radionuclide largely determines the mass of a compound introduced for a given radiation dose. Because nuclear medicine relies on the use of subpharmacologic tracer doses that do not perturb the biologic system under study, the amount of the radionuclide should be low and the specific activity high.

The radionuclides purity, defined as the fraction of the total radioactivity in a sample in the form of the desired radionuclide, has to be increased to prevent radionuclides contaminants, that

may enlarge the radiation dose to the patient, raise the detector dead time, and may result in incorrect counting rate deteriorating the image reconstruction.

In the case of therapeutic applications, the ratio of non-penetrating (corpuscular radiation) to penetrating (photon) radiation should be high, in contrast to nuclear imaging use. Moreover, the emitted corpuscular radiation should have a suitable linear energy transfer and range in the tissue. In both cases, the daughter nuclide should be a short-lived or stable isotope.

Attending to the biochemical properties of the radionuclides, it is assumed that the radioactive isotopes are chemically identical to stable isotopes of the corresponding element. Therefore, the tracer does not alter the chemical or physical properties of the molecule it is attached to. Nevertheless, some considerations have to be taken into account. Radionuclides of elements that can be easily incorporated into biomolecules, producing useful precursors, that is to say, chemical forms that react readily to prepare a broad range of labeled products, and that can undergo a wide range of chemical syntheses are preferred. Although other elements, like metals, that involve a greater challenge of incorporation in biological molecules are widely used as labels in nuclear medicine. In the case of radionuclides for endotherapeutic use, the situation is more stringent since the stability of the therapeutic entity is demanded over a more extended time period than in the case of a diagnostic pharmaceutical. Thus, the basis for successful endoradiotherapy incorporates selective concentration and prolonged retention of the therapeutic radionuclide in the tumor as well as minimum uptake in normal tissue.

Beyond all these requirements the use of a particular radioisotope is conditioned to the production techniques that allow its obtaining in a simple way at reduced cost.

1.1.3 Radioisotopes production

The extended use of radioisotopes in nuclear medicine has been parallel to the development of the associated production technologies. The unstable nature of the radioisotopes results in the nuclear decay in a mean lifetime with the emission of gamma rays or subatomic particles according to radioactive decay law. Therefore, most of them do not exist in nature and they must be artificially produced through nuclear reactions with high-energy particles interacting with stable isotopes. Two main technologies for radioisotopes production have been settled down: Nuclear reactors and particle accelerators. The radioisotopes generators can be constituted like a third method, conditioned to the use of the previous techniques for the production of the parent radioisotope.

The continuing requiring to produce and supply radioisotopes for nuclear medicine procedures has been increasing in the last decades, specially radioisotopes for PET techniques. The fulfillment of this demand entails improvements in radioisotope production techniques as well as a permanent interdisciplinary enhancement of the technology. In addition, the current radioisotope production system and the corresponding supply network have to overcome some issues in the short to the medium-term future.

- The progress of nuclear medicine procedures is directly associated with the availability of new radionuclides and the discovery of new radiopharmaceuticals. The medicine draws upon increasingly to radioisotopes for the better understanding of disease mechanisms, diagnosis and therapy with innovative progress in cutting-edge procedures as radioimmunotherapy or nanotechnology. However, the radioisotope employment for the diagnosis and treatment is hampered by issues in the supply as well as the production constraints of non-standard isotopes, especially those that have theragnostic properties. The research and the improvements in radiopharmaceuticals availability and the quality enhancement of the radionuclides will benefit to the nuclear medicine procedures for diagnostics, therapy, and palliation.

- Most medical radionuclides have been historically produced in nuclear reactors, especially the most employed radioisotope, ^{99m}Tc. The current extensive production was in charge of a few research reactors. However, unexpected incidents in some radioisotope produced reactors have resulted in shortcomings, unreliability, and threatened supply constraints [35]. Furthermore, the radioisotope supply system has to deal with the aging of many research reactors worldwide, the uncertainties about the replacement facilities, the opposition of part of the society against the nuclear reactors, and the required control related to nuclear non-proliferation. Particle accelerator technology research is leading up to new methods of radioisotope production dispense with reactors.

- The increasing demand of isotopes for imaging procedures as well as the emerging deployment of non-standard radioisotopes, especially PET radionuclides, require a reliable supply network. For that purpose, it is necessary moving away from centralized production systems based on reactor production, to a distributed supply. Under those circumstances, a single facility provides the isotope necessities of hospitals in the surrounding region. The radionuclides self-provisioning is extremely relevant in the case of shorter-lived isotopes, whose production requests a nearby distribution system incompatible with the current model. Otherwise, the application of these radioisotopes and the medical advantages derived from their use will be constrained in a restricted area around the facility. The production from compact accelerators is focused to resolve this issue, expanding the use of radioisotopes and expanding the benefit of radiopharmaceuticals to society.

During the last years an increased effort has been realized to promote new and enhanced radioisotope production technologies. To ensure the nuclear medicine development making use of the acquired experience and the technology improvements, the research activity is focused on remarkable key goals [36]:

- Reduce costs of traditional infrastructures, optimize workflow and minimizing staff needs requirement for radiopharmaceuticals production

- Increase access to radioisotopes implementation investing in novel technology advancements, standardizing validated methods and maintaining quality and regulatory standards to produce clinical doses

- Improve the quality of the final products enabling personalized diagnosis through the access to molecular imaging tracers and enhancing production capabilities to expand the ability to produce a wider tracer spectrum.

Reactor-produced radionuclides

Nuclear reactors have historically provided substantial quantities of radionuclides for nuclear medicine. It constitutes a centralized production method which provides the supply to an extensive region. Nuclear reactors are a significant source of neutrons, therefore, radioisotope production in reactors is based on neutron capture in a target material, either by activation or generation of radioisotopes from the fission of the target material. The neutron flux irradiates samples situated around the reactor core, allowing simultaneous several targets irradiation to produce a broad variety of radioisotopes [37, 38].

Neutron-rich radioisotopes can be produced making use of the resultant fission fragments. Radioisotopes with the sufficiently long half-life can be subsequently extracted from fission fragments by chemical separation and used as medical radionuclides. Fission products may be carrier-free, that is to say, no stable isotope of the element of interest is produced, even though other radioisotopes of the element of interest can also be produced in the fission fragments. The lack of specificity of the fission process resulting in a relatively low yield of the radionuclide of interest among a large amount of other radionuclides. The most important isotope produced by separation from fission products is ^{99}Mo. It carries out a meaningful role in nuclear medicine as it is the parent radionuclide of ^{99m}Tc [17,39], the most worldwide imaging radioisotope employed.

On the other hand, the large neutron flux available in nuclear reactors can produce radionuclides by neutron activation. The neutron flux irradiates samples situated around the reactor core. A target nucleus may be converted into a radioactive product as a result of neutron capture reactions as (n, γ) or (n, p). The method of choice principally depends on the yield of the desired radionuclide, whether suitable sample materials are available for neutron activation, cost considerations and the desired specific activity, a measure of the relative number of radioactive isotopes in a sample. The products of the neutron reaction are not carrier-free because they are the same chemical element as the bombarded target material. Even in intense neutron fluxes, only an insignificant fraction of the target nuclei is actually activated. Thus, reactor-produced radioisotopes have mostly high production yield but reduced specific activity.

Accelerator-produced radioisotopes

Particle accelerators are bringing forward an increasing interest as a radioisotope production technology. The development of compact, reliable and low-cost machines can perform a crucial role in addressing current sourcing issues, ensuring a reliable supply of medical isotopes in the future. Charged-particle accelerators employ different well-known nuclear reactions for isotope production [34, 40, 41] mainly based on proton beams, although deuterons and helium nuclei are also employed. Even for some traditionally reactor-produced radioisotopes, such as $^{99}Mo/^{99m}Tc$,

particle accelerators are becoming a potential suitable solution to cope with the supply chain challenges [42].

Accelerators can provide isotopes with more suitable decay properties (particle emission, half-life, gamma rays, ...) than reactor-produced radionuclides. The principal advantages for the production of medical radionuclides lies in the high specific activity products, an important feature for many of the radioisotopes of interest, particularly in PET procedures. Moreover, the separation of the product from the target material can be easily performed through a suitable chemical or physical techniques because they are different elements. Fewer radioisotopic impurities are achieved by selecting the energy window for irradiation and the target material. It should be underlined the strong reduction of generated radioactive waste. Furthermore, the cost-effectiveness, the rapid delivery of short-lived radioisotopes to hospitals, the localized production and scalability to daily demand are determining factors to emphasize. In addition, the drawbacks of reactor-based isotope production of nuclear weapon proliferation risk, decommissioning costs and limited access to reactors are overtaken with accelerators. However, as the main disadvantage, are sometimes requiered enriched (and expensive) targets for the production of a sufficient amount of radionuclide, given the lower production yield compared to reactors.

The production of radionuclides with particle accelerators requires beams with some specific characteristics, like energy window to optimize the production yield according to the nuclear reaction. Additionally, the beam energy must be controlled to minimize the level of impurities produced by side-channel reactions resulting in unwanted radionuclides. Concerning the intensity, a sufficient beam current is entailed with the purpose of producing viable quantities of the desired nuclide. High current intensity would increase the production yields at the cost of carefully target development, shielding and maintenance level. Hence, the choice of beam parameters (energy and current) represents a key role in the most demanding features of advanced accelerators: downsize of the machine and low costs while enhancing intensity, stability and efficiency. Therefore, a trade-off should be made between energy and current, resulting in a more versatile facility. Additionally, improvements in targetry development, processing, and recycling have to result in a cost-effective radiopharmaceutical production facility fulfilling standard requirements.

Different types of particle accelerators are available to produce radioisotopes by means of diverse nuclear reactions [43–49]. Hadron accelerators, like cyclotrons, linacs or electrostatic machines, make use of direct production, whereas photo-induced reactions are employed in electron machines. Moreover, neutron-induced reactions for radioisotope production are employed on Compact Accelerated Neutron Sources (CANS) or on high-energy spallation based reaction sources. Last, but not the least, accelerator-driven reactors rely on particle-induced fission reactions. The main characteristics, strong points and vulnerabilities of the most significant of particle accelerators focused on radionuclides production with medical purposes are presented hereafter.

Cyclotrons

The cyclotron is the most widely used type of particle accelerator for the production of important medical radionuclides, because of its adaptability for on-site production of the shorter-lived proton-rich radioisotopes, among other reasons. It is based on a very mature technology developed since the 30s and improved through the decades, especially with the application of superconducting technology to the magnetic system. In addition, the circular concept allows to employ the accelerating resonators many times, that is to say, the beam is always accelerated by the same RF cavities. Those enhancements have endowed the cyclotrons with compactness, versatility and commercially availability. Furthermore, they have enabled to accommodate cyclotrons facilities in hospitals, academic-research institutes and commercial installations specialized in producing and selling radioactive isotopes for an on-site preparation of short-lived positron emitters. Hence, an increasing number of cyclotron facilities for medical purposes are ensuing throughout the world [50], in spite of the list of radioactive nuclides produced and the applications have not changed significantly over the last decades [51–53].

Cyclotrons for biomedical radionuclide production are typically based on the acceleration of light ions. After acceleration, the beam is extracted at fixed energy by different techniques, as the stripping mechanism or electromagnetic deflectors. The use of negative ions combined with stripping mechanism is supported by the very high extraction efficiency and excellent beam qualities, and it is favorable in order to reduce the losses and activation around the beam extraction region, although very good high vacuum conditions have to be reached. The use of internal ion sources provides the most cost-effective solution, although with limitation on the maximum achievable current and the deterioration of vacuum levels. Cyclotrons using external ion sources enhance the demanded beam current at the expense of increasing the accelerator complexity and declining the compactness of the facility. Some cyclotron concept includes two beam extraction ports to prepare two different radionuclides simultaneously. The targets are able to be nestled either within the cyclotron (internal targets) or in external beam-lines (external targets). In addition, some advanced cyclotrons applied to medical purposes make use of superconducting magnets to provide intense magnetic fields with advantages in power consumption, size and weight, wherefore in compactness. However, the magnet requires a cryogenic system to maintain the magnet coils at liquid helium temperatures, entailing a more expensive machine.

Current cyclotrons have been classified according to the main features required for PET radioisotope production (<15 MeV, low current), SPECT and longer PET isotopes (15–30 MeV, high current) and therapeutic applications (>30 MeV, high current). In accordance with this beam energy criterion, a list of a wide range of cyclotrons for isotope production developed by commercial companies and research centers is reported in Table 1.3.

Table 1.3: *A list of the current cyclotrons used in radioisotope production for medical applications and some selected specifications [45, 49, 54–68]*

Cyclotron model	Company	Beam particles	Energy (MeV)	Current (μA)	Magn. field (T)	Cycl. weight (t)	Power (kW)
TR14	ACSI	H^-	14	>100	2.1	22	60
TR19/9	ACSI	H^-/D^-	19/9	>300/100	2.1	22	65
TR24	ACSI	H^-	24	>300	2.1	84	80
TR30/15	ACSI	H^-/D^-	30/15	>1600/400	2.1	56	150
BG-75	ABT	H^-	7.5	5	1.16	–	–
Best 15p	Best	H^-	15	400	–	14	–
Best 25p	Best	H^-	≤ 25	400	–	30	–
Best 30p	Best	H^-	30	400	–	50	–
Best 35p	Best	H^-	≤ 35	800	–	50	–
Best 70p	Best	H^-	≤ 70	≤ 100	1.6	150	–
LOTUS	CEA	H^-	12	50	2.3	–	–
CYCIAE-14	CIAE	H^-	14	400	–	–	–
CYCIAE-70	CIAE	H^-	70	750	–	–	–
CYCIAE-100	CIAE	H^-	100	≤ 500	–	–	–
AMIT	CIEMAT	H^-	8.5	10	4.0	1.2	–
Isotrace	EUROMEV	H^-	12	100	2.36	3.8	40
ION-12SC	Ionetix	H^-	12	10	4.5	–	–
IsoDAR	-	H_2^+	60	10000	2.11	450	2700
GENtrace	GE	H^-	7.8	–	2.2	6.7	30
MINItrace	GE	H^-	9.6	>50	2.2	9	35
PETtrace	GE	H^-/D^-	16.5/8.6	>100/65	1.9	22	70
Cyclone 3	IBA	D^-	3.8	60	1.8	5	14
Cyclone 10/	IBA	H^-/D^-	10/5	>100/35	1.9	12	35
Cyclone 11	IBA	H^+	11	120	1.9	13	35
Cyclone 18/9	IBA	H^-/D^-	18/9	150/40	1.9	25	50
Cyclone 30	IBA	H^-/D^-	$\leq 30/\leq 15$	$\leq 1200/50$	1.7	50	≤ 180
Cyclone 70	IBA	H^-/D^-	$\leq 70/35$	750/50	1.6	140	40
Cyclone KIUBE	IBA	H^-	18	≤ 300	1.6	18	≤ 65
KIRAMS-30	KIRAMS	H^-	≤ 30	500	1.9	–	–
C-18/9	NIEFA	H^-/D^-	18/9	100/50	–	20	60
Eclipse RD	Siemens	H^-	11	40	1.9	10	35
Eclipse HP	Siemens	H^-	11	60	1.9	–	35
HM-7	SHI	H^-/D^-	7.5/3.8	–	–	–	–
HM-10	SHI	H^-/D^-	9.6/4.8	–	–	–	–
HM-12	SHI	H^-/D^-	12/6	>60/30	2	11	45
HM-18	SHI	H^-/D^-	18/10	>90/50	2	24	55
HM-20	SHI	H^-/D^-	20/10	–	–	–	–

Linear accelerators

Electron linacs are extensively used in nuclear medicine for radiotherapy with photons emitted by a high-Z converted as a consequence of bremsstrahlung radiation of the accelerated electrons. The identical physical principle can be employed to produce radioisotopes through photo-nuclear reactions (photo-neutron or photo-proton mainly) or photo-fission reactions. Electron accelerators represent a well-known technology, therefore, reliable for high current machines. Consequently, electron linacs have been demonstrated as a feasible tool for radionuclide production with medical interest, specially short-life PET isotopes likewise other medical radionuclides [69, 70].

The main advantage for radioisotope production in comparison to proton-induced reactions is that the irradiation target is simpler in preparation as it is not subjected to direct beam heating, as well as cheaper since target nuclides are composed of naturally abundant isotopes. Therefore, isotopic enrichment is unrequired. The design of the target can also take into account the high penetrability of photons. Additionally, fewer gamma-reaction channels are available resulting in a reduction of the undesired isotopes and the consequent radioactive waste. Moreover, the recent advances in superconducting radiofrequency (SRF) accelerating structures are promoting the potential of electron linacs for this purpose. Despite this, the photo-induced yield production is lower than nuclear reactions obtained with protons. This demands a high power electron linac, which in combination with a thicker target, could produce a sufficiently high total isotope yield. On the other hand, a careful design of the electron-photon converter is required, where only a fraction of electrons is converted to photons, with the consequent energy inefficiency and activation.

With regard to ion linear accelerators, they have been proven to represent a feasible alternative for radioisotope production by hadron nuclear reactions [71, 72]. The advantage of linacs is the possibility of using multiple simultaneous target stations at several beam energies, the limited radiation levels and the associated reduced shielding. However, high operation cost for continuous wave (CW) operation at a fixed energy are needed. Linacs usually operate in a pulsed mode and the instantaneous power deposited on the target forces complicated engineering targetry solutions. Moreover, the requirement of large facility increases the civil construction cost.

New developments in hadron linear accelerators technologies aimed at minimizing the construction costs by reducing the linac length. Thus, modern ion linacsdevoted to radionuclide production make use of high frequency structures to reduce the length of the accelerator. Some of them consist of a high frequency radiofrequency quadrupole (RFQ) accelerator usually injecting a relatively low energy proton or deuteron beam into a drift tube linac. This type of technology applied to radionuclide production is nowadays in development and new and innovative projects progress with potential interest [73–75].

Electrostatic accelerators

Electrostatic accelerators also arise as an alternative to radioisotope production. The tandem cascade accelerator, based on the Van de Graaff principle, has been proven for PET isotope production. Some prototype accelerators have been installed and tested to produce usable quantities of shorted-lived PET isotopes through nuclear reactions driven by intense protons or deuterons beams [76–79]. Electrostatic accelerators could become a less expensive alternative for the production of radiopharmaceuticals on a localized production system. Irradiating at low energies has the potential to produce very pure radionuclides, with a minimum number of isotopic impurities and fewer elemental impurities. Furthermore, it is a solution with low machine activation, low-cost, power-efficient and simple-operating system. However, electrostatic accelerators do not provide adequate current at the energies of interest and therefore have limited applicability to be used in a broad radionuclide spectrum production.

Other accelerators-based alternatives

Other promising proposals may constitute an effective source for medical radionuclides, focused on providing a feasible method to supply the increasing demand for isotopes preventing the reactor-based production techniques. The strong focusing present in a Fixed-Field Alternating Gradient (FFAG) accelerator represent an alternative for higher beam currents that can be used for isotope production [80]. In addition, the high peak power lasers developed in many laboratories worldwide could provide the production of isotopes of medical interest through photon-induced nuclear reactions [81–84]. On the other hand, studies are ongoing to analyze the potential of plasma facilities for the production of short-lived radioisotopes [85–87].

Nevertheless, those innovative methods are based on still immature accelerating technologies demanding further progress to become a valid sustainable solution. They have to demonstrate a superior performance or lower cost in comparison against the traditional methods, as well as they require extensive and sophisticated research studies to prove it.

Particle accelerators have demonstrated their relevance for radioisotope production in comparison with nuclear reactors. They are becoming a suitable solution for the actual radionuclide supply system. The most remarkable feature is the capability of on-site production, extending the application of isotope medical procedures as well as the implicit benefit for the society.

The choice of a specific accelerator for radionuclide production must be intimately connected to its purpose, that is to say, which radionuclides are to be produced and the required quantities. The commercial or research aim of the accelerator has to be equally considered. Afterward, the election relates to the available reaction production channels, the associated energy and current requirements as well as radioisotopes yield considerations. Other not less significant concerns are the operating and maintenance costs, the actual commercial solutions and the required engineering development. In consequence, the advantages of each accelerator technology applied to the particular radionuclide production have to be meticulously evaluated.

Radionuclides generators

The third category of radioisotope production system is the radioisotope generator, which must be mentioned by its high relevance and application in nuclear medicine [15]. It is a production method that requires the use of a reactor or an accelerator system to produce the parent radionuclide.

The technique consists of a parent-daughter radionuclide pair contained in a system that holds the parent and afford to separate easily the daughter for clinical use. The generators are based on the transient equilibrium of nuclear decay. The situation occurs when the parent half-life is longer than the daughter half-life but is not huge in comparison. The daughter-product activity increases and attains a maximum value. At that point, it decreases and follows the decay of the parent. When the production and decay rates are equal, that is to say, parent and daughter activities are decreasing but the ratio of parent-to-daughter activities is constant, the parent and daughter are said to be in transient equilibrium. Henceforth, the daughter nuclide of interest is extracted from the device through the elution for single-dose preparation, resuming the production from new initial parent-daughter conditions. In consequence, the daughter product activity is replenished continuously by the decay of the parent and might be extracted repeatedly.

The parent radionuclides are used to be reactor-produced, although the increase in demand for this type of system for mature and emerging markets, respectively, urges the need to consolidate the isotope production with different accelerator-based approaches [88]. Some of the most radionuclides of interest in nuclear medicine imaging are produced by the use of generators [89], such as $^{99}Mo/^{99m}Tc$ system [17, 39] as well some radioisotopes for therapeutic use [90].

Radioisotope generators make available short-lived radioisotopes far away from the parent nuclide production facility. Moreover, they provide a continuous source of short-lived radionuclides for clinical or research studies. Additionally, the generators that yield radionuclides with half-lives of minutes allow special applications of imaging for the quantification of ventilation or perfusion, as well as the opportunity to repeat studies.

1.2 Cyclotrons

Cyclotrons are the most extensively used type of particle accelerator used for radioisotope production due to its powerful concept, simplicity and versatility. A cyclotron is a resonance accelerator of hadrons (protons or ions) with high average intensity in which the beam moves along a spiral path outward from the center. The ions are accelerated by a high frequency oscillating electric field through two or more hollow electrodes. Three different accelerating configurations are historically developed. They are classified according to the focusing and the acceleration synchronism scheme in: classical cyclotrons, isochronous cyclotrons and synchrocyclotron accelerators.

1.2.1 Classical cyclotron

The classical cyclotron, one of the first particle accelerators developed, consists in an alternating radiofrequency (RF) high voltage applied to some D-shaped hollow electrodes, usually called dees. Particles, usually light ions, are accelerated as they pass from one dee to the next one by the electric field present in the gap between them. A uniform magnetic field generated by a magnet with flat parallel pole tips bends the particle trajectories. The acceleration process takes place continuously, which means that the production is in a continuous-wave (CW) beam mode. Once the beam is accelerated up to the nominal energy, it is extracted out of the cyclotron in a continuous way by different techniques (electrostatic deflectors, stripping mechanism...). The original cyclotron concept is schematically illustrated in Figure 1.4.

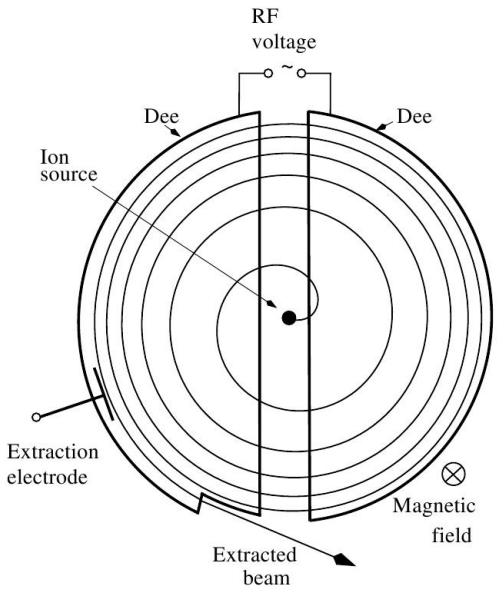

Figure 1.4: *Conceptual representation of a classical cyclotron in the median plane view [91].*

To describe the acceleration mechanism, let's consider a particle with charge q and mass m moving with constant velocity in a uniform and orthogonal magnetic field B. According to classical electrodynamics theory, the centripetal force is provided by the Lorentz force acting on the particle:

$$\left.\begin{array}{l} \mathbf{F}_{cent.} = \dfrac{m\mathbf{v}^2}{r}\hat{r} \\ \\ \mathbf{F}_{mag.} = q\,(\mathbf{v}\times\mathbf{B}) \end{array}\right\} \longrightarrow \frac{m\mathbf{v}^2}{r}\hat{r} = q\,(\mathbf{v}\times\mathbf{B}) \longrightarrow \frac{mv^2}{r} = qvB \tag{1.1}$$

The particular motion follows a circular trajectory whose radius depends on the magnetic field and the momentum of the particle:

$$\rho = \frac{mv}{qB} = \frac{p}{qB} \tag{1.2}$$

The angular velocity of a particle, also called revolution frequency or gyrofrequency, is given by:

$$\omega_{rev} = \frac{v}{\rho} = \frac{qB}{m} \tag{1.3}$$

In the non-relativistic limit the revolution frequency of a charge particle moving in a uniform magnetic field is constant, being independent of the orbit radius and therefore, of the energy of the particles. The particle takes the same time to make each turn which defines the isochronism condition.

On the other hand, a time oscillating RF voltage is applied between the dee electrodes

$$V = V_0 \cos\left(\omega_{RF}\, t\right) \tag{1.4}$$

increasing the particle energy as they cross the gap. In the non-relativistic limit with a uniform magnetic field and constant in time, the synchronism condition is achieved meanwhile the accelerating voltage oscillates with the same frequency as the particles.

$$\omega_{RF} = h\,\omega_{rev} \tag{1.5}$$

where h, taking values of natural numbers, is so-called RF harmonic number or mode. Consequently, under this accelerating condition, particles arriving at the gap will perceive the same acceleration by the electric field, increasing their energy and the radius of the trajectory according to the equation (1.2). Therefore, the beam is bunched with the same time structure than the RF field, each bunch laying on an accelerating wave (Figure 1.5). The AC generator alternates the polarity of the dees in order to give to the ion the same acceleration in each gap. Thus, the diameter of the orbit increases until the particle can be extracted from the outer edge of the machine.

However, the relativistic increase of velocity with energy has to be taking into account; effect also misleadingly called relativistic mass increase, though this concept is subject to misunderstanding and it has been rejected by Einstein himself [93] and by particle physicists community [94, 95]. Thus, taking into account relativistic effects, the revolution frequency of the particles is no longer constant during the acceleration in a uniform magnetic field:

$$\omega_{rev} = \frac{qB}{\gamma m_0} \tag{1.6}$$

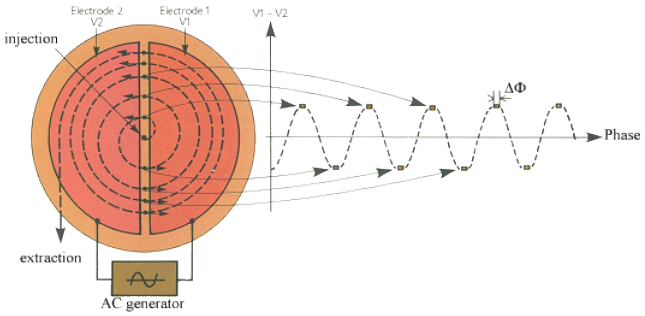

Figure 1.5: *Accelerating field configuration with dees on harmonic $h = 1$ [92].*

where m_0 is the particle 'rest mass' and γ the relativistic factor. Hence, the ideal situation for the particle acceleration is disrupted when the relativistic effects are taken into account due to the revolution frequency decreases as the beam gains energy. Thus, the synchronism condition is broken in a classical cyclotron.

Transverse beam dynamics

Magnetic weak focusing

Heretofore, the motion of a particle located at an ideal orbit in the median plane has been described. However, due to the thermal motion of the particles inside the ion source plasma, as well as possible optical aberration in the injection, the particles follow a distribution of transversal velocities resulting in small deviations respect of the ideal orbit. Additionally, some effects produced by misalignment on the accelerating field or beam residual interactions would modify particles from their ideal orbit. Therefore, restoring forces are needed to confine the beam, leading to a stable motion, enhancing the beam transmission and reducing the power losses during acceleration.

Considering the paraxial approximation, all trajectories are assumed to be close to the optical axis, which means that radial and axial deviations from the ideal orbit ($r = \rho$) are small ($x << \rho$):

$$r = \rho + x = \rho \left(1 + \frac{x}{\rho}\right) \tag{1.7}$$

Thus, it is defined a coordinate system (Figure 1.6) that moves with the particle along the orbit with x pointing in the radial and z in the axial direction (Frenet-Serret coordinates).

For any other orbit radius r, a restoring force in radial direction appears. Considering the movement in a region with an axial magnetic field and without accelerating electric fields, the equation of motion of a particle slightly deviated from the ideal orbit is given by:

$$F_x = \frac{d}{dt}(m\dot{x}) = \frac{mv^2}{r} - qvB_z \tag{1.8}$$

The magnetic field in the medium plane for particles out of the ideal trajectory is expanded in Taylor series along radial dimension:

$$B_z = B_{0z} + \frac{\partial B_z}{\partial x}\, x + \mathcal{O}(^2) \simeq B_{0z} \left(1 + \frac{\rho}{B_{0z}} \frac{\partial B_z}{\partial x} \frac{x}{\rho}\right) = B_{0z} \left(1 - n \frac{x}{\rho}\right) \tag{1.9}$$

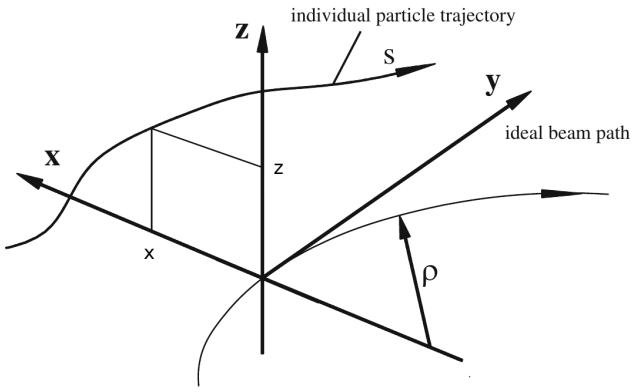

Figure 1.6: *Schematic representation of particle trajectories according to the Frenet-Serret coordinates system [96] for an ideal particle and for an individual particle with small deviations from the ideal one.*

where the field index n is defined as the fractional change of the axial component of the field associated with a fractional change of radius

$$n = -\frac{\rho}{B_{0z}}\frac{\partial B_z}{\partial x} \tag{1.10}$$

Replacing (1.7) and (1.9) into (1.8) and considering the equilibrium orbit (1.1) with $r = \rho$, the restoring force in the horizontal plane is:

$$m\ddot{x} \simeq m\frac{v^2}{\rho}\left(1 - \frac{x}{\rho}\right) - qvB_{0z}\left(1 - n\,\frac{x}{\rho}\right) = -\frac{mv^2}{\rho}\frac{x}{\rho}(1-n) \tag{1.11}$$

$$\ddot{x} + \omega_r^2\, x = 0 \tag{1.12}$$

which is the equation of an harmonic oscillator with the frequency $\omega_r = \omega_0 v_r$, where $\omega_0 = v/\rho$ is the orbital revolution frequency of the particle on a closed orbit and $v_r = \sqrt{1-n}$ the horizontal Betatron number. The first term represents the force which restores the particle to the equilibrium orbit. To prevent the exponentially grown of the Betatron oscillation amplitude, a stability criterion arises from the frequency of the oscillations:

$$n < 1 \tag{1.13}$$

The particle will continually be forced back to the equilibrium orbit whenever it becomes displaced from that orbit. This condition imposes the compensation between the centrifugal, mv^2/r, and the magnetic forces, $qB_z v$, defining the equilibrium orbit. Outside this radius, the inward magnetic force will be greater, inside this radius, the outward centrifugal force will be greater. Therefore, there will be a net force restoring the particle to the equilibrium orbit.

Similarly, for the motion in the vertical plane:

$$F_z = m\ddot{z} = qvB_x \tag{1.14}$$

$$\vec{\nabla} \times \vec{B} = 0 \longrightarrow \frac{\partial B_x}{\partial z} + \frac{\partial B_z}{\partial x} = 0 \longrightarrow B_x = -n\frac{B_{0z}}{\rho}z \tag{1.15}$$

$$\ddot{z} + \omega_z^2 z = 0 \tag{1.16}$$

where the vertical Betatron oscillation frequency is $\omega_z = \omega_0 v_z$ and $v_z = \sqrt{n}$ the vertical Betatron number. Particles perform stable oscillations about the horizontal median plane as long as the field index is positive:

$$n > 0 \tag{1.17}$$

In this case, the stability condition establishes that the field would decrease with increasing radius to keep the particle in the equilibrium orbit.

Restoring forces are needed to obtain a stable and controlled movement of the particles along the path of the cyclotron. Otherwise, the effect of a small deviation is amplified after some turns, resulting in beam particle losses and current reduction. The transverse focusing motion in a classical cyclotron, with simultaneous horizontal and vertical stability, is obtained by combining both the equations (1.13) and (1.17) criterion leading to the Steenbeck's criterion [97]:

$$0 < n < 1 \tag{1.18}$$

Therefore, in a classical cyclotron, a slightly decreasing magnetic field with increasing radius will provide the desired focusing forces to prevent the particles deviations in the vertical or axial direction. Particles out of equilibrium orbit will experiment restoring force proportional to the displacement from the equilibrium orbit, tending to return them to the median plane. A schematic representation of the magnetic restoring force between the poles of a magnet is shown in Figure 1.7.

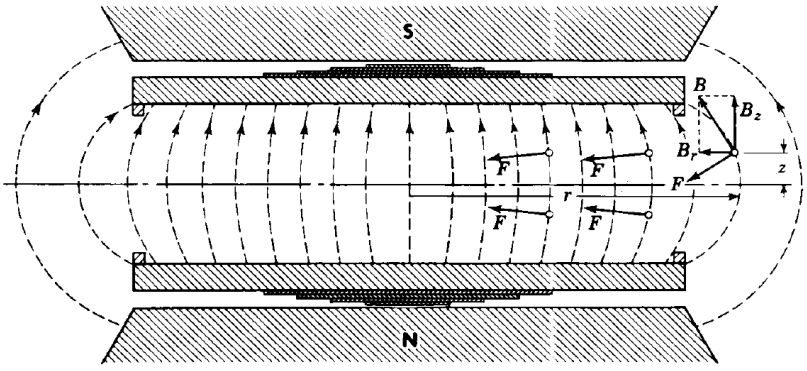

Figure 1.7: *Magnetic field between poles of a cyclotron magnet [98]. A magnetic field decreasing radially provides focusing to axial and radial deviations.*

The focusing restoring force imposes a decreasing magnetic field, and therefore, a classical cyclotron entails a weak focusing concept. The field index is not constant with the radius. Symmetry requires that the field index be zero at the center of the magnet. It increases rapidly with the radius at the edge of the pole. However, cyclotron magnets are designed for a small index over most of the acceleration area to minimize non-synchronism of particle orbits, since the frequency of the Betatron oscillation is lower than the revolution frequency. Consequently, the revolution frequency of the particles decreases, according to the equation (1.6).

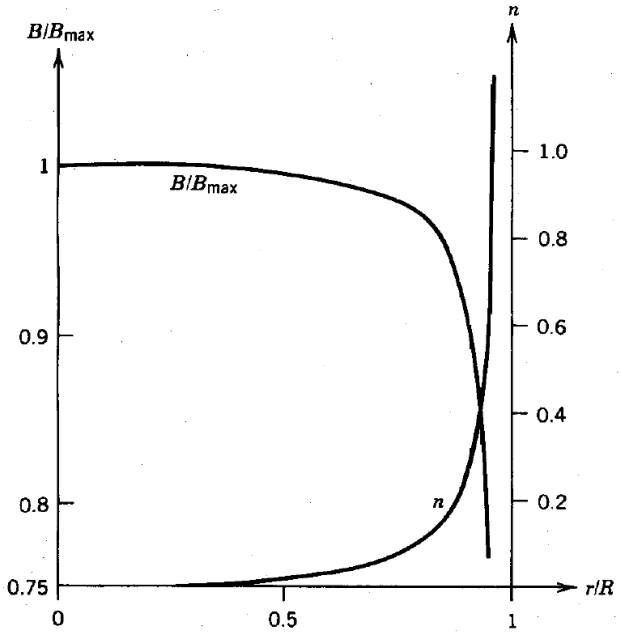

Figure 1.8: *Magnetic field of a weak focusing cyclotron [98]. Radial variation of vertical field component and field index in front of the radial component.*

Electric focusing

In addition to the focusing obtained from the magnetic field there is a residual effect associated with the electric field which plays a significant role under certain conditions. The electric field arrangement between the dees is worked out as the one-dimensional equivalent of the electrostatic lens, excepting some differences related to the oscillating RF behavior. There is an axial transverse focusing component of the electric field at the entrance of the acceleration gap and a defocusing component when particles return to the dee (Figure 1.9). The electric focusing in case of cyclotrons can be analyzed under the consideration of the transit time of the acceleration is small in comparison with electric field variation. Thus, two contributions to the electric field focusing can be distinguished: the effects of energy gain neglecting the time variation and the effect of the time variation of the transverse electric field component assuming no energy change during the gap traversal.

Firstly, since the ion is being accelerated to higher velocity during its passage across the gap, focusing is enhanced by the fact that the beam traverses the second half of the gap in less time than the first half, so it spends less time under the influence of the divergent field. This energy change effect is most pronounced in early accelerating stages when ion energy is low and the change in velocity is most significant.

Secondly, particles crossing the gap will experience an electric field that changes during the transit time. If the ion crosses the gap when the RF field is decreasing in magnitude, the convergent force on entering the gap will be larger in magnitude than the divergent force on leaving so the net result in a focusing effect. Conversely, during the other portion of the RF cycle, the effect will be reversed and the result will be a net defocusing force. The contribution

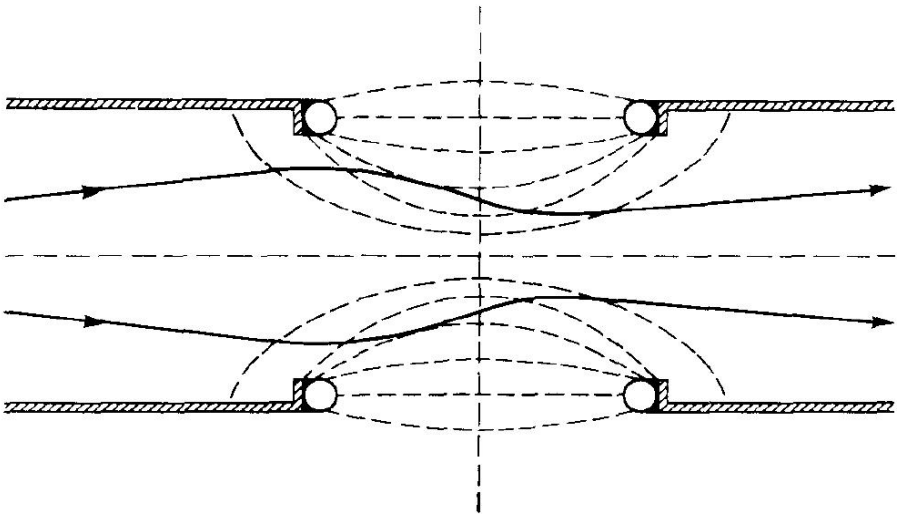

Figure 1.9: *Schematic representation of electric focusing effect [98]. Cross section of dees around acceleration gap showing schematically the transversal focusing of the beam produce by the electric forces. Solid lines represent the ions path and the dashes are the electric field lines between the dees.*

of this field variation effect also decreases with the energy and orbit radius due to the time spent in crossing the gap. Therefore, the focusing effects become smaller.

The contribution of both effects to the variation of the axial position, z, respect to the longitudinal coordinate, y, can be expressed as [99–102]:

$$\left[\Delta \frac{dz}{dy}\right]_{energy\ change} = -\frac{b}{2}\left(\frac{qV_0}{E}\right)^{3/2}\frac{z}{r}\cos^2\phi \tag{1.19}$$

$$\left[\Delta \frac{dz}{dy}\right]_{field\ variation} = -\frac{qV_0}{E}\frac{z}{r}\sin\phi\left[1-\left(\frac{qV_0}{E}\right)^{1/2}\left(\frac{qV_0}{2\omega^2 d^2}\right)^{1/2}\sin\phi\right] \tag{1.20}$$

being V_0 the peak voltage, E the energy of the particles at the center of the acceleration region, ω the RF frequency, ϕ the phase of the electric field, r the orbit radius, d the dee gap separation, and b other geometry parameter.

The net result of these two main processes is an effective focusing only during the early stages of acceleration and for particles within a rather limited RF phase band. Hence, the accelerating electric field has a beam focusing function in the central region of the cyclotron with remarkable relevance for beam stability because there is no vertical magnetic focusing at the center of the magnet.

Longitudinal beam dynamics

As it has been mentioned, the synchronism condition between particles and the accelerating field is disregarded in a classical cyclotron due to the relativistic effects. Additionally, the stability criteria for focusing conditions introduce an additional desynchronization between the RF field

and particle motion. Since the magnetic field decreases with the radius, the revolution frequency of the particles decreases, according to the equation (1.6).

A phase difference between the RF field phase and the particle motion will arise during the acceleration, that is to say, the RF electric field will be in another phase of the cycle when the particles will be at the same azimuthal position, θ. The phase of the RF cycle seen by the particle and its variation in time are defined as:

$$\varphi = \omega_{RF}\, t - \theta \tag{1.21}$$

$$\dot{\varphi} = \omega_{RF} - \dot{\theta} = \omega_{RF} - \omega_{rev} \tag{1.22}$$

Assuming that the effects of the gap width are neglected, that energy increases continually and that phase is a continuous function of energy; the change of phase for a particle during transit through a 180° dee is:

$$\Delta\varphi = \dot{\varphi}\,\frac{\pi}{\omega_{rev}} = \pi \cdot \left(\frac{\omega_{RF}}{\omega_{rev}} - 1\right) \tag{1.23}$$

The acceleration is produced by the voltage applied between the dees (eq. (1.4)). However, the phase variation introduces a limitation to the acceleration. The energy gain per gap for particles with phase φ is:

$$\Delta E = q\, V_0 \sin\varphi \tag{1.24}$$

Considering the equations (1.23) and (1.24), an approximation for the energy dependence of φ is obtained [103]:

$$\frac{d\varphi}{dE} \simeq \frac{\Delta\varphi}{\Delta E} = \frac{\pi}{q\, V_0 \sin\varphi}\left(\frac{\omega_{RF}}{\omega_{rev}} - 1\right) \tag{1.25}$$

$$\begin{aligned} \sin\varphi\, d\varphi &= \frac{\pi}{q\, V_0}\left(\frac{\omega_{RF}}{\omega_{rev}} - 1\right) dE \\ &= \frac{\pi}{q\, V_0}\left(\frac{\omega_{RF} E}{q c^2 B_0} - 1\right) dE \end{aligned} \tag{1.26}$$

where the revolution frequency of the particles (equation (1.6)) has been replaced as a function of the total relativistic energy of the particles:

$$E = K + m_0 c^2 = \gamma m_0 c^2 \tag{1.27}$$

Integrating the equation (1.26), a solution for the phase as a function of energy is obtained, usually expressed in terms of the kinetic energy of the particles, K:

$$\cos\varphi = \cos\varphi_0 - \frac{\pi}{q\, V_0}\left(1 - \frac{\omega_{RF}}{\omega_0}\right) K - \frac{\pi}{2q\, V_0 m_0 c^2}\left(\frac{\omega_{RF}}{\omega_0}\right) K^2 \tag{1.28}$$

where φ_0 is the initial phase of the field and ω_0 the non-relativistic revolution frequency.

Thus, the acceleration of the particles is determined by the peak voltage, the mass of the particles and mainly by the relationship between RF frequency and revolution frequency. The greater the phase excursion of the particles throughout the cycle, the greater the final energy reached. In each gap, greater energy gain will be obtained when $\omega_{RF} < \omega_0$. The maximum kinetic

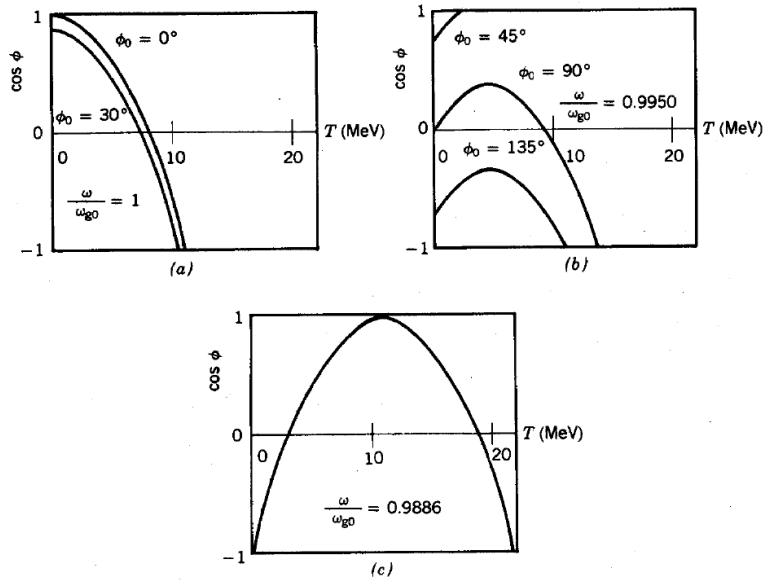

Figure 1.10: *Example of phase excursion in a cyclotron [103]. $\cos\varphi$ is plotted as a function of the kinetic energy for different injection phase. Three cases are presented according to the relation between the RF frequency, ω_{RF}, and the non-relativistic revolution frequency, ω_0. The maximum achievable energy corresponds to the curve in subfigure (c) representing the maximum possible phase excursion of ions during acceleration and therefore the longest possible time of acceleration.*

energy will be achieved when $\cos\varphi = -1$. During acceleration, the ion phase may traverse the interval $\varphi = (0°, 180°)$. Figure 1.10 illustrates the phase excursion with energy in different cases.

Considering a maximum phase excursion cycle, a relationship for both frequencies and the maximum kinetic energy reached is obtained as a first approximation:

$$\frac{\omega_{RF}}{\omega_0} = \frac{1}{1 + \dfrac{K_{max}}{2m_0c^2}} \tag{1.29}$$

$$K_{max} \simeq \sqrt{\frac{16}{\pi} q\, V_0 m_0 c^2} \tag{1.30}$$

These results expose the relevance of non-synchronism in a classical cyclotron and the consequent effects as the limitation in the maximum energy achievable, the demand for a high voltage and the careful choice of the radiofrequency to optimize the final energy.

However, previously the magnetic field has been considered radially uniform. When a decreasing magnetic field providing weak focusing is included, an additional source of phase shift is introduced. The RF frequency has to be tuned to keep the synchronism point before that the beam deceleration takes place. Figure 1.11 shows the beam excursion considering the weak focusing. In the central region of the cyclotron, the revolution frequency of the particles is higher than the RF frequency. By this reason, the phase of the electric field perceive by a particle at each gap is lower, until it reaches the isochronous point. This condition is exclusively fulfilled in an intermediate radius of the path. At this point, the revolution frequency and RF frequency

are exactly the same. Beyond that point, the RF phase perceived by the particles will be larger in each gap, because the RF frequency is now higher than the revolution frequency. The beam extraction should be done before reaching the decelerating phase region. There are also additional factors that limit the phase excursion and therefore, they reduce the maximum energy. The phase excursion is also limited by the RF phase perceive at the injection, which must be around the peak to extract the ions from the source. Furthermore, the synchronous point must not be near 0^{o} to limit the defocusing phases.

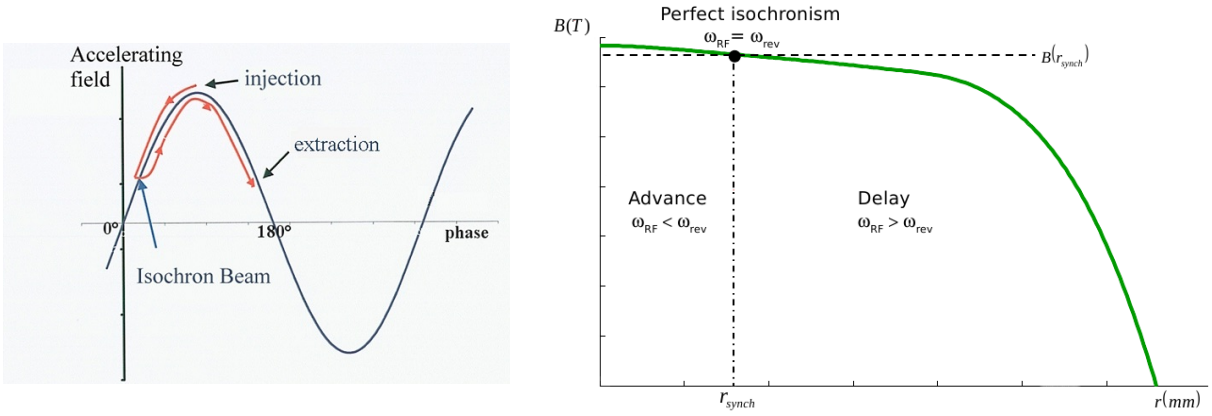

(a) (b)

Figure 1.11: *(a) Beam phase evolution in a weak focusing classical cyclotron [92]. Particle runs steadily out of phase with respect to the RF except at one radius when synchronism condition is reached according to the magnetic field decrease (b), constraining the acceleration time.*

1.2.2 Isochronous cyclotron

The restrictions in the final energy in a classical cyclotrons arising from the non-synchronism imposed by the weak focusing forces, promoted the emergence of new alternative cyclotron arrangements. These designs have been developed to overcome this limit. One of these alternatives is the isochronous cyclotron, which it is based on an increasing magnetic field along the path to the rise in the total energy keeps the particle revolution frequency constant. Thus, the mean field has to increase according to the relativistic factor:

$$B(r) = \gamma(r)B(0) \tag{1.31}$$

However, this is in opposition to the weak focusing condition. According to the Steenbeck's criterion (equation 1.18), the particle motion is no longer stable and some axial and radial defocusing forces will arise. To compensate them, the magnetic field profile is modified along the azimuth direction. A succession of high-field sectors (hills), separated by low-field regions (valleys) introduces a modulation in the field (Figure 1.12). This is the base of the Azimuthal Varying Field cyclotron (AVF) [104]. The variation of the vertical field along the path leads to

transverse focusing forces on the particles introducing by a field component, B_θ, in the Lorentz equation. The trajectory of the beam is no longer a circle, and a radial component of the beam velocity, v_r, is created.

$$F_z = q\left(\mathbf{v}\times\mathbf{B}\right)_z = q\left(v_r B_\theta - v_\theta B_r\right) \tag{1.32}$$

Furthermore, the vertical focusing created in an AVF cyclotron is enhanced if the shape of the sectors is changed from straight to an spiral [105, 106], due to the fact that the valley-hill transition is more focusing while the hill-valley transition is less focusing.

The strength of the azimuth field variation by the sectors in a cyclotron is expressed by the flutter function:

$$F = \frac{\overline{B^2} - \overline{B}^2}{\overline{B}^2} \tag{1.33}$$

where $\overline{B}$ denotes the average over the azimuthal range in one turn. The focusing is described by the Betatron oscillations number, that, in case of a N sector magnet can be expressed with approximations in terms of the flutter:

$$v_z^2 \simeq n + \frac{N^2}{N^2-1} F\left(1 + 2\tan^2\xi\right) \tag{1.34}$$

$$v_r^2 \simeq (1-n) + \frac{3N^2}{(N^2-1)(N^2-4)} F\left(1 + 2\tan^2\xi\right) \tag{1.35}$$

where ξ is the spiral angle of the pole.

To aim at high energy cyclotrons where the Lorentz factor becomes large, the flutter must be increased to maintain an effective vertical focusing. The ultimate limit is reached lowering the field in the valley to zero, which leads to the separate sector cyclotron [107].

The isochronous cyclotron was developed to improve the limitations of the classical cyclotrons. Therefore, high energies are achievable solving the synchronism issues. The azimuthally varying field and the adequate focusing elements result in the overcoming of the relativistic effects. An additional advantage of AVF cyclotrons is that the stronger vertical focusing allows higher beam intensity. However, there are limitations to apply high magnetic fields due to the magnet configuration saturates reducing the flutter. Furthermore, the enhanced technologies of isochronous

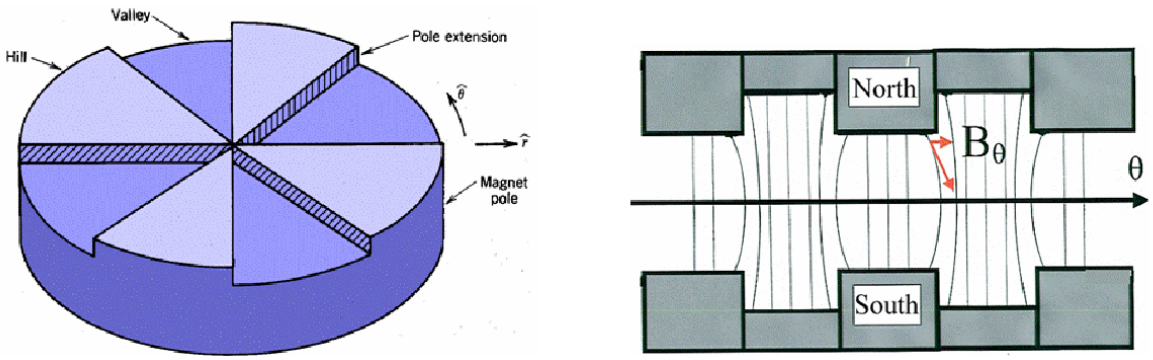

Figure 1.12: *Magnet scheme of an azimuthally varying field cyclotron.*

cyclotron as the spiral cyclotron and the separated-sector cyclotron extend some accelerating advantages. However, the complexity of the assembly and the facilities are increased. The isochronous cyclotron has been broadly spread since it can be used for the same purpose as the classical cyclotron providing some substantial advantages.

1.2.3 Synchrocyclotron

An alternative solution to overcome the beam limitations in a classical cyclotron is the frequency modulated cyclotron or synchrocyclotron [108–110], where the RF frequency is gradually decreased as the particles gain energy to compensate for the relativistic effects. Kinetic energies for protons to $\sim$ GeV have been achieved. The final beam energy is enlarged in comparison with cyclotrons, but at the expense of a decreasing the beam intensity. This is due to the fact that the beam can only be captured into phase stable orbits during a small fraction of the RF modulation cycle, resulting in a pulsed operation mode. Thus, the timing between the RF frequency, voltage, and ion source needs to be optimized and controlled. Moreover, the extraction system is complicated because the low dee voltage implies that orbits have small turn separation ($<$ 1 mm), even though all turns can be extracted at the same time by a pulsed electrostatic field because they are closely radial spaced. On the other hand, a magnetic field decreasing gradually with the radius provides a weak beam focusing as in classical cyclotron in order to achieve a negative field index (eq. (1.10)).

Woe to the studious man who belongs to no coterie

— Stendhal

Chapter 2

AMIT project

The Advanced Molecular Imaging Technologies (AMIT) project is a research collaboration between 10 companies and 14 research laboratories, supported by the Spanish government. Its ultimate purpose is the development of the core technology for molecular imaging in medicine and biomedicine with a significant focus on the human brain and specially mental diseases. One of the primary goals of this ambitious project represents the development of a groundbreaking compact cyclotron to study the viability of providing single doses of short half-life radioisotopes for sintering radio-tracers employed in Positron Emission Tomography (PET) diagnostics. In addition, other work-packages are focused on leading-edge miniaturized radiopharmacy, novel PET instrumentation or advanced molecular software imaging. The ultimate scientific motivation of the cyclotron lies in the claim of the medical sector for modern features to radiopharmaceuticals supply system [36] overcoming the main current drawbacks, as it is summarized in the following key points:

- Capability for providing single doses on demand of emerging radioisotopes which would contribute to improve diagnosis or treatments of specific diseases for patients.

- Extend the local production of radioisotopes to hospitals and institutes which are not traditionally well-prepared for hosting conventional facilities, reducing the delivery time and the radioactive decay of the active molecule, and, consequently, enhancing the ratio of useful to produced amount of the compound.

- Establish an efficient system to produce selected radio-tracers at an affordable cost enhancing the market competitiveness and sustainability, and improving the custom-made radiopharmaceuticals availability to a more significant number of potential patients.

- A cost-effective method for on-site production in non-dedicated facilities will make advanced medical procedures accessible to small cities or remote sparsely populated areas. Additionally, it avoids logistic problems and the associated costs of a large facility.

2.1 Accelerator specifications

The AMIT project will address scientific challenges in the cyclotron development geared to provide a requested alternative to the current centralized radioisotope production supply system. The miniaturization of the accelerator would allow its installation in hospitals and laboratories, leading the way to on-demand production. Besides the facility compactness, the project approach additional challenges related to on-site production, sustainability and effective user access. Consequently, the AMIT cyclotron has to accomplish the following particular requirements:

- Compact and short-sized design to minimize the weight of the accelerator and the size of the whole facility requires.
- Cost-effective and autonomous design to reduce the economical costs of manufacturing, assembling and maintenance, as well as the electrical power consumption and the personnel provision for the operation of the installation. Moreover, the accelerator must to reduce the radiation levels and the subsequent associated shielding. The final design should be adjustable to on-site needs for radioisotope production.

Such specific requirements ensure a versatile and competitive facility as well as respectful of the environment. This project will enable a ground-breaking step change in technological developments to address the increasing demand of radioisotopes for medical application.

The challenge of a compact facility is achieved by designing a superconducting cyclotron with a high magnetic field. Given the relation between the bending radius and the magnetic field (see equation (1.2)), this solution minimizes the extraction radius and consequently the whole machine size. A superconducting magnet is a well-known technology that produces a high magnetic field, reducing drastically the size of the cyclotron compared to the resistive magnet alternative. Furthermore, a superconducting cyclotron will provide additional advantages as the shielding reduction and the beneficial impact on running costs given the lower power consumption. However, the cryogenic system for the superconducting coils adds complexity and specific maintenance.

A preliminary trade-off study analyzed the different accelerator configurations to fulfill the requirements of the project, concluding that a classical cyclotron with a high magnetic field ($B =$ 4 T) represents an adequate solution. The compactness requirement, demanding a high magnetic field, has discarded the isochronous cyclotron option. In such high magnetic field conditions, the iron circuit is strongly saturated, resulting in a very small reluctance difference between hills and valleys. As a consequence, a very low flutter function (equation (1.33)), responsible for the beam focusing, could be obtained, disabling this type of cyclotron as a preference. Thus, a classical weak focusing cyclotron arises as a preferred option for a simple compact machine. Other solutions, as those based on magnetic elements with higher saturation level or by using additional superconducting coils, would result in much more expensive and complex machines, being therefore discarded.

In the interest of compactness, an internal ion source has been chosen for AMIT cyclotron,

despite the drawbacks related to the central region design and the vacuum level. On the other hand, in order to achieve an efficient beam extraction, optimizing the extracted current and minimizing the losses and the potential radioactive activation, a stripping-based extraction system has been set, a generalized method in cyclotrons [111–114]. With that in mind, the cyclotron accelerates negative hydrogen ions (H^-) to simplify the problems associated with the extraction of protons without significant losses. When the negative ion beam achieve the nominal energy, it passes through the stripping foil, positioned near the perimeter of the machine, which converts the negative ions to positives. The magnetic field of the cyclotron deflects the positive ions in the opposite direction, and the beam is cleanly extracted and transported to the target.

To summarize, AMIT accelerator entails a cutting-edge design based on a compact superconducting weak focused classical cyclotron configuration gear toward to achieve the challenges of a reliable on-site radioisotope production for medical purpose.

2.1.1 Beam requirements

The main cyclotron specifications have to be balanced with the beam requirements to achieve an acceptable radioisotope production, that is to say, the beam has to optimize the radioisotope production with the fulfillment of the compactness objective. AMIT cyclotron design is appointed to produce ^{11}C and ^{18}F radioisotopes through protons nuclear reactions (Table 2.1). Therefore, the final beam extracted from the cyclotron must satisfy some minimal energy and current requirements to generate optimally single-dose of the considered radioisotopes.

The nuclear interaction of the beam with the material of the target is described in terms of the cross section, related with the quantum interaction probability of the particles [115]. The cross section data for the reactions have been experimentally measured during decades as well as compiled and fitted regarding nuclear model calculations [40, 116]. The total cross sections for the AMIT radionuclides production reactions are shown in Figure 2.1. This cross section is referred as the sum of cross sections of all reaction channels on a well-defined target nucleus leading to direct production of the final nuclide.

The cross section determines the instantaneous production rate, which is a measure of the production of secondary nuclei by the incident flux on a well-characterized target. Hence, the physical reaction yield is defined as the ratio of the number of produced nuclei in the nuclear

Table 2.1: *AMIT radioisotopes*

Isotope	Dose	Target	Reaction	$T_{1/2}$
^{18}F	40 mCi	Water enriched in ^{18}O	$^{18}_{8}O + ^{1}_{1}H \longrightarrow n + ^{18}_{8}F$	110 min
^{11}C	100 mCi	Nitrogen gas	$^{14}_{7}N + ^{1}_{1}H \longrightarrow ^{4}_{2}He + ^{11}_{6}C$	20 min

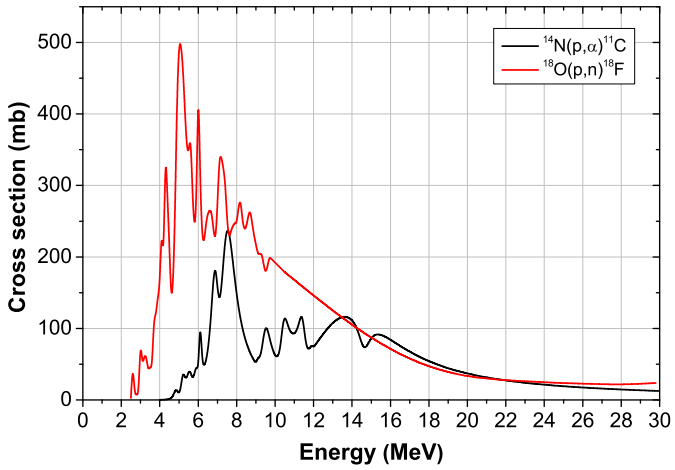

Figure 2.1: *Cross section of the reactions* $^{14}N(p,\alpha)^{11}C$ *and* $^{18}O(p,n)^{18}F$*, fitted from recommended data [40, 116].*

reaction per incoming charged particle on the target:

$$Y(E) = \frac{n \int_0^E \sigma(E) dE}{\frac{dE}{dx}} \tag{2.1}$$

where n is the target atom density, $\sigma(E)$ is the cross section as a function of the energy of incident particle and dE/dx is the energy loss of penetrating particles. The yield definition is frequently modified to include information about the ratio of irradiation time to the half-life of the radioisotope. Thus, for a finite irradiation time it is defined the activity produced for 1 h irradiation with 1 μA beam current, A_1. When the irradiation time is comparable or longer than the half-life of the produced isotope, saturation of the number of secondary radioactive nuclei occurs and for very long bombardments the induced activity, called saturation activity, A_2, becomes independent of time for a given beam current. The above-mentioned physical yield is related through the law of radioactive decay as a function of irradiation time, t:

$$Y = \frac{A_1 \lambda}{1 - e^{-\lambda t}} = A_2 \lambda \tag{2.2}$$

where λ is the decay constant of the produced isotope. The yield data and the saturation yield of the reactions for ^{11}C and ^{18}F production are represented in Figure 2.2 and 2.3 respectively.

Finally, from cross section and yield reaction data, the energy and current requirements for a single-dose production of radioisotopes have been obtained for different irradiation times (Figure 2.4). These results have considerable relevance in the cyclotron design because they determine the final beam specifications influencing in all accelerator subsystems. The evaluation of the individual single-dose production in accordance with the more restrictive reaction, in this case the production of ^{11}C, has set the minimal beam energy and current objectives for the cyclotron to optimize and reduce irradiation time. Therefore, the final beam requirements for AMIT cyclotron have been determined as a proton beam of energy over 8.5 MeV and a beam current greater than 10 μA.

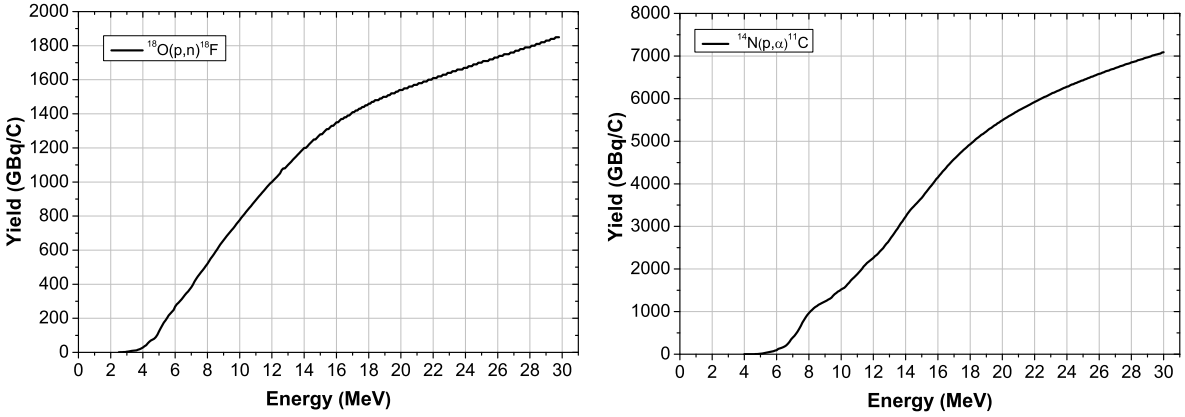

(a) (b)

Figure 2.2: *Physical yield of (a) $^{18}O(p,n)^{18}F$ and (b) $^{14}N(p,\alpha)^{11}C$ reactions*

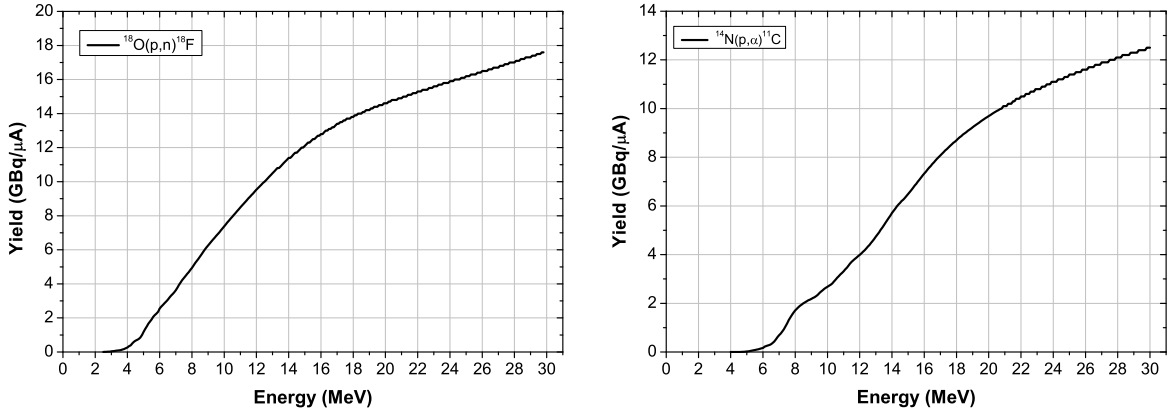

(a) (b)

Figure 2.3: *Saturation yield of (a) $^{18}O(p,n)^{18}F$ and (b) $^{14}N(p,\alpha)^{11}C$ reactions calculated from the evaluated cross sections.*

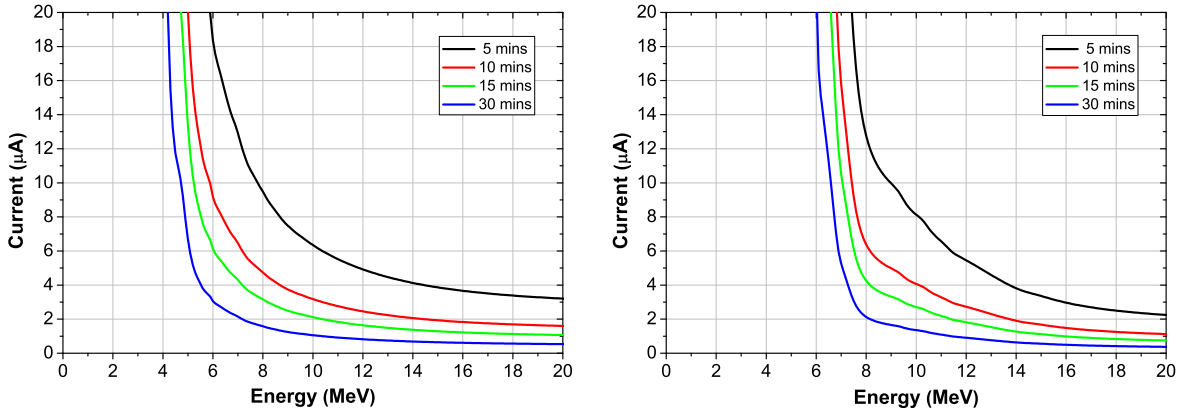

(a) ^{18}F (b) ^{11}C

Figure 2.4: *Proton beam conditions (energy and current) for single-dose production of ^{18}F and ^{11}C for different irradiation time.*

2.2 AMIT cyclotron subsystems

The primary goal a of cost-effective on-site radioisotopes production for medical applications can then only be achieved through a comprehensive design of the whole accelerator. In this regard, the beam dynamics determine the main specifications of the different subsystems integrating the cyclotron. Additionally, the weak focusing and classical nature of the cyclotron lead the technical specifications to the limit. Consequently, cutting-edge technology has been implemented in the different AMIT components. A 3D picture of the cyclotron including all the components is displayed in Figure 2.5. The description of the elements is presented in this section to bring together all the features of the cyclotron. Furthermore, an exhaustive introduction of the associated subsystems must clarify the issues involving the beam dynamics studies related to the objectives of this thesis.

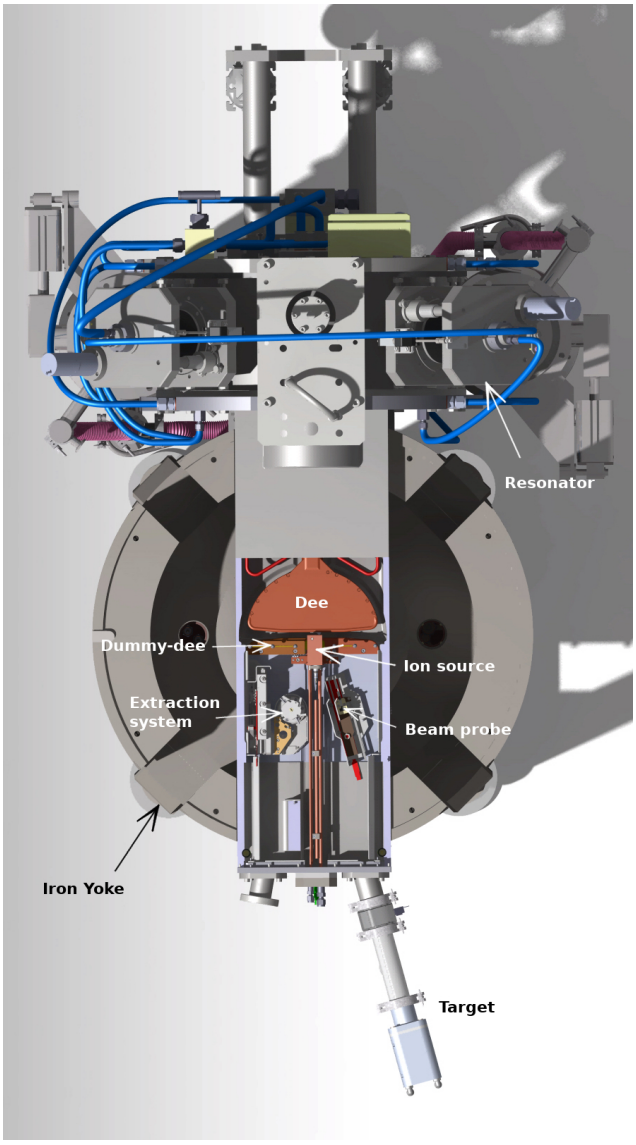

Figure 2.5: *Top view of the* AMIT *cyclotron 3D model.*

2.2.1 Magnet and cryogenic system

The AMIT cyclotron magnet (Figure 2.6) is based on NbTi superconducting technology producing a nominal field of 4 T [117, 118]. The magnetic circuit includes two coils in Helmholtz arrangement and the iron yoke, in a warm iron configuration where only the coils are kept cold inside a common cryostat. The coils are cooled down with two-phase helium, circulating in a closed circuit and re-condensed externally. A casing structure hosts the magnet, including a channel fully tight to circulate helium. To reduce the effects of radial forces, coils include an outer aluminum shrink-fitted cylinder that induces azimuthal compressive stresses in the coil, compensating vertical forces that can lead to mechanical damage or deformations affecting the field quality. Moreover, a stainless steel structure blocks axial movements of the coils. Coils and casing are inserted in the cryostat to maintain it at cryogenic temperature, including a thermal shield to decrease the losses by radiation.

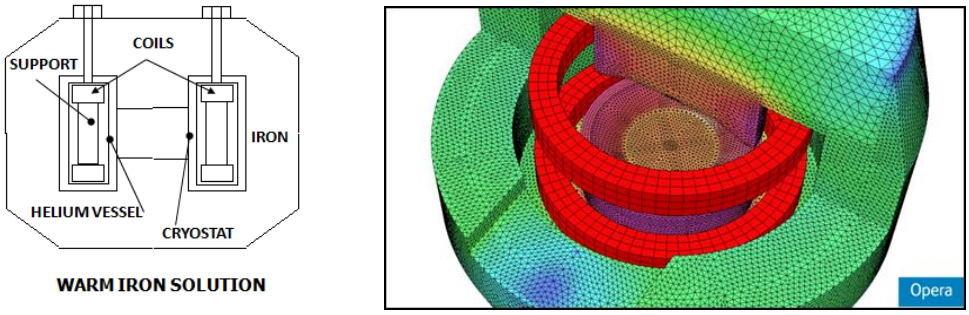

Figure 2.6: *Left: Schematic view of the different parts related to the magnet system. Right: 3D electromagnetic simulations with OPERA code.*

Liquid and gas helium circulate through helical channels along the inner wall of the coil casing. Both flows are supplied by a Cryogenic Supply System (CSS), a breakthrough closed pumped helium circuit developed in a collaboration with CERN. The CSS is a novel and versatile cooling system that provides for an autonomous, cheap and compact radioisotope production facility, minimizing the maintenance and the running costs as it eliminates the need of periodic

Table 2.2: *AMIT superconducting magnet and cryogenic system parameters*

Magnetic central field	4 T
Radial field gradient @ $r = 105$ mm	1.49 %
Nominal current	108.9 A
Self-inductance (Both coils) @ Nom. current	38.35 H
Insulated wire diameter	0.896 mm
Cu/Sc ratio	4.5 : 1
Operational temperature	4.2 K
Thermal losses at cryocooler first stage	34 W
Thermal losses at cryocooler second stage	0.7 W

refrigerant refills. The overall configuration of the CSS consists of a number of heat exchangers and thermal anchoring to the two stages of the cryocooler. Helium is transferred from the CSS through a low-loss Transfer Line that is connected to the Cyclotron Connection Box, a built-in device that provides space, electrical insulation and thermal refrigeration for the current leads, instrumentation and all the safety valves, sensor wires and the piping needed for the whole cryogenic circuit. A brief of the most critical parameters of the magnetic and the thermal design can be found in Table 2.2, and the overall picture of the system is presented in figure 2.7.

The magnet and the cryogenic system have been tested [119, 120] to analyze the thermal performance of the magnet and verify the cooling concept capacity of the casing cooling channel and the heat exchanger. This test was performed employing an external injector cooling system. In addition, the magnetic field in superconducting state has been measured. In order to validate mechanical and thermal concepts, steady-state conditions were achieved under cryogenic conditions. The magnetic measurements have been realized in the median plane along the magnet pole diameter with a new magnetic test bench developed in collaboration with CELLS-ALBA [121]. The measurements were carried out below the nominal operational status. The maximum testing current value was 65 A due to some unexpected problems related to the alignment and supporting system of the coils. The magnetic results werer in good agreement with simulations, although slight discrepancies on the field shape have been identified under the measurement conditions. These divergences with the design values have to be checked with more isolated measurements at nominal current and with the autonomous cooling operation provided by the CSS after new mechanical adjustments and the final assembly of the transfer line.

Figure 2.7: *AMIT magnet and cryogenic system supply in the final assembly for autonomous operation.*

2.2.2 Radiofrequency

A radiofrequency system in a one 180° dee configuration provides the electric field for the beam acceleration as well as contributes to the transverse focusing, specially important in the low energy regime [122]. The non-isochronous condition of AMIT cyclotron carries away the RF system close to the technical limits, demanding a minimum voltage of 60 kV. The RF cavity (Figure 2.8) is a quarter-wave resonator in horizontal position with the dee at the end of a copper stem. The cavity is composed of the vacuum chamber and a cylindrical resonator which supplies the RF power directly via a coaxial loop, which couples inductively with the magnetic field. The beam acceleration process places in the vacuum chamber, which is independent from the magnet and adapted to the aperture space.

On the cylindrical resonator, two plungers or tuners with steppers motors are placed to control fine frequency shifts caused by various effects as heating detuning. The dee has been designed considering the available space for the beam circulation as well as the required gaps for the beam dynamics remarks. The thickness of the materials has been properly chosen for a reasonable heat evacuation. Open holes on the dee back wall will optimize the vacuum extraction. The mechanical and geometric design has been optimized to minimize as much as possible the risk of sparking from surfaces which are exposed to intense electric fields in puller and dee. The half of the chamber where no RF fields accommodate the extraction system, beam diagnostics and the vacuum ports for the ion source and the target. Table 2.3 shows some significant parameters of the RF system.

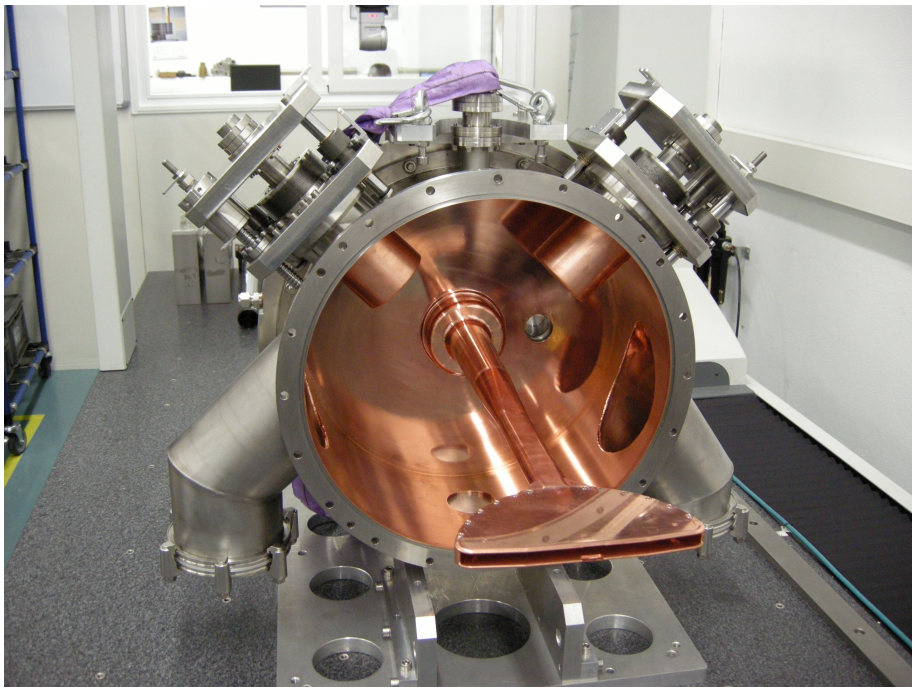

Figure 2.8: *Picture from the opened RF structure with the cylindrical resonator, two legs for vacuum pumps, the stem fixed at the end plate and the dee.*

Table 2.3: *Radiofrequency system parameters*

Voltage	60 kV
Design frequency	60.134 MHz
Tuning range	± 250 kHz
Frequency resolution	1 kHz
Accelerating gap	10 mm
Operation RF harmonic	1
Inner dee radius	115 mm
Internal dee height	12 mm

The acceleration gap between dee and dummy-dee can be classified in three different regions (Figure 2.9). Firstly, the central region where the gap is optimized to increase the energy gain in the first turns. The intermediate region has a constant 10 mm wide gap, where the beam is accelerated until a medium-high energy. Lastly, the external region, at higher radius ($\sim$ 56 mm from the cyclotron center), where a 5° opening angle is introduced due to reduce the capacity and the field concentration at the corner of the dee end. The result is an increasing aperture gap (up to 18 mm at 103.5 mm). However, the high velocity of the particles in this region makes the effect of this gap variation almost negligible in the transit time; although it introduces radial electric field components, resulting in radial oscillations during the beam transport.

The RF system for the AMIT cyclotron has been successfully tested [123]. The detailed analysis of such measurements is out of the scope of this dissertation, but it is relevant to be presented. Low power measurements under vacuum conditions have provided results of the resonant frequency, coupling factor, and tuners regulation range in accordance with design parameters and simulations. High power tests and conditioning have been performed, exceeding accurately the design target, emphasizing the capability to extend the high voltage of the cavity.

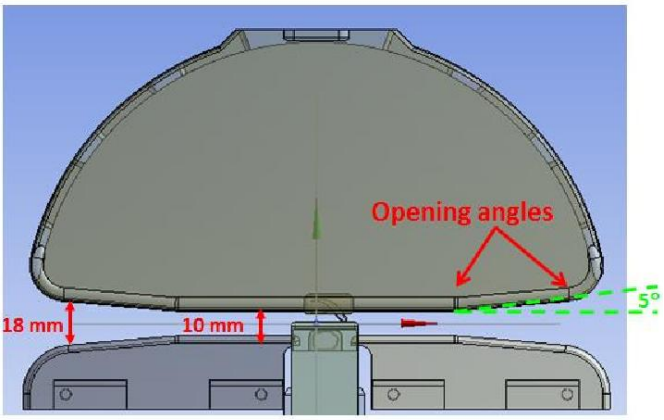

Figure 2.9: *Top view of the dee arrangement with the ion source and the puller illustrating the different acceleration gap regions as well as the practiced opening angles in the dee.*

2.2.3 Ion source

A cold-cathode Penning Ionization Gauge (PIG) ion source has been developed to produce a H^- beam for the AMIT cyclotron. The ion source consists of two cathodes made of tantalum, and a hollow anode cylinder, usually called chimney, with an aperture for beam extraction (Figure 2.10). The slit size is 6x0.2 mm^2 with 0.1 mm thickness to improve the penetration of the electrical field of extraction. A plasma expansion gap of 0.3 mm, a distance between the plasma boundary and the anode slit wall, is added in the chimney to facilitate the production and survival of the H^- in the plasma.

The ion production begins to be relevant with the thermionic electron emission by the cathodes. Then the gas injected into the chimney is ionized, generating a plasma which is confined by the magnetic field orthogonal to the cathode surface. In the anode volume, the production of negative hydrogen ions is primarily determined by the equilibrium between the creation and destruction processes through different reactions [124–126] (see Table 2.4) between gas molecules and electrons, depending on the energy of the electrons (Figure 2.11).

The low binding energy of H^- (0.754195(19) eV [127]) allows the secondary electron to be easily stripped by collisions with high energy electrons. Thus, H^- ions survive mainly on the outer shell of the plasma column, where the energy of electrons is lower and the simultaneous production of H^+ and H^- is limited. To compensate for the destruction channel, the design of the ion source enhances the H^- ion production by the implementation of an expansion gap between the arc column and extraction slit.

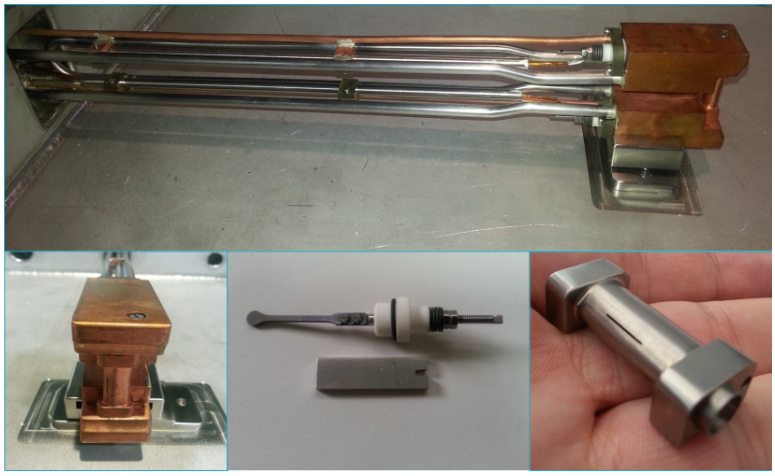

Figure 2.10: *Pictures of the ion source showing a lateral view (top), a frontal view (bottom left), a cathode with electrical insulator (bottom center) and the chimney (bottom right).*

The ion source has been characterized in a devoted facility at CIEMAT [128]. This test bench facility has been designed to reproduce the operational conditions of the source and to optimize the beam extraction from the plasma through different beam diagnostics. The analysis of this experimental work, that it has required the collaboration of people from Particle Accelerator Unit, constitutes one of the objectives of this thesis. Hence, the results of the ion source

characterization are specifically presented in Chapter 4 of this dissertation.

The use of an internal ion source introduces a significant limitation in the cyclotron, because the continuous gas injection deteriorates the vacuum level specially in the central region of the cyclotron. This condition coupled with the low binding energy of the ions contributes to increase the interaction probability with the remaining molecules of the gas. These processes result in the electron detachment of the negative hydrogen ions, reducing the survival rate of the beam and consequently the total beam transmission. Additionally, this residual interaction represents a relevant source of sustained losses that will cause damage in the material and increase the radiation background level.

Table 2.4: *Atomic reactions of production and destruction of H^- ions in a Penning ion source*

Production processes	
Dissociative attachment	$H_2 + e \rightarrow H^- + H$
	$H_2 + e \rightarrow H^- + H^*$
Polar dissociation	$H_2 + e \rightarrow H^- + H^+ + e$
Dissociative recombination	$H_2^+ + e \rightarrow H^- + H^+$
	$H_2^+ + e \rightarrow H + H^*$
Charge exchange	$H^- + H \rightarrow H + H^-$
Radiative capture	$H + e \rightarrow H^- + \gamma$
Destruction processes	
Collisional detachment	$H^- + e \rightarrow H + 2e$
	$H^- + H \rightarrow 2\,H + e$
	$H^- + H_2 \rightarrow H + H_2 + e$
Associative detachment	$H^- + H \rightarrow H_2 + e$
	$H^- + H^+ \rightarrow H_2^+ + e$
	$H^- + H_2^+ \rightarrow H_3^+ + e$
	$H^- + H_3^+ \rightarrow 2\,H + H_2$
Non-Associative detachment	$H^- + H^+ \rightarrow H + H^+ + e$
Charge transfer	$H^- + H^+ \rightarrow 2\,H$
	$H^- + H_2^+ \rightarrow H + H_2$

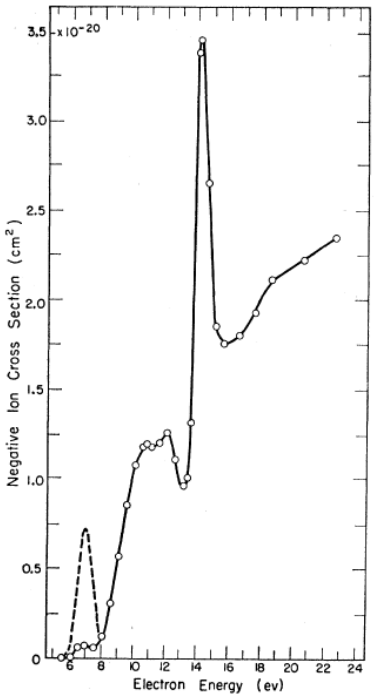

Figure 2.11: *Negative ion cross section production from hydrogen gas as a function of electron energy [124]. The different peaks of the curve are associated with different reactions.*

2.2.4 Central region

The central region of a cyclotron encompasses the initial acceleration stages, from the ion source beam injection to the first beam turns. Its design is crucial for the suitable performance of the cyclotron acceleration because significant features of the beam as the phase acceptance and the transverse emittance are primarily determined by the first few turns within the machine. Therefore, the achievement of an optimum radioisotope production is directly related to a proper design of the central region of the cyclotron.

From the beam dynamics point of view, the study of the central region has a great relevance. The output beam current relies directly on the transmission efficiency through the cyclotron center. The acceleration during the first turns is set by the electric and magnetic field configuration produced by the central region structures, that is to say, the ion source and the puller electrodes. Furthermore, the effect on the beam transport and acceleration is not limited to the first few turns, but modifies the whole beam trajectory, being necessary to perform a comprehensive beam dynamics assessment to determine the optimum configuration of the central region. Thus, the study aims to determine the appropriate puller and ion source arrangement producing the optimum electromagnetic configuration to achieve a high quality focused beam and consequently to enhance the final beam transmission. For an enhanced understanding of the central region influence as well as given its high relevance in the beam dynamics studies, the main features related to the central region design [101, 129–131] are exposed follow-up.

Beam injection

The beam injection into the cyclotron from the ion source is determined by the puller. The gap between the chimney and the puller establishes the energy gain in the first accelerating gap, which is extremely important due to the low energy of particles extracted from the ion source. The puller has been designed with a specific geometry to be close to the ion source to compress the electric fields and to increase the energy gain. Besides, both the puller and the ion source faces must be parallel to obtain a uniform electric field. The smaller the ion source-puller gap the stronger is the bunching in energy and orbit centers for the beam. In addition, it is also critical to gain enough energy in the first turn to increase the first orbit radius, enhancing the available area for the ion source location. On the other hand, the beam current extracted from the chimney of the ion source depends on the applied extraction voltage, V, and the gap distance, d, according to the Child–Langmuir law [132, 133]:

$$J = \frac{4\sqrt{2}}{9}\,\varepsilon_0 \sqrt{\frac{q}{m}}\,\frac{V^{3/2}}{d^2} \tag{2.3}$$

where ε_0 is the vacuum permittivity, and q/m the charge-mass relation of the extracted particles. Therefore, the more intense the electric field, the higher probability of extracting the ions from the ion source, increasing the beam current injected into the cyclotron. However, the ion source-puller gap distance is limited by sparking limit, the maximum electric field withstood with the high voltage applied. During the RF design stage detailed studies of electrical fields were carried out. A peak electric field of 14.2 MV/m (1.5 times Kilpatrick criterion) was assumed in all parts except the puller [122]. Then a combined iterative process of beam dynamics and RF system analysis was performed to assess the implications on the central region to delimit the optimal configuration. The smallest possible gap permitted by the highest peaks of the expected electric fields on the dee front and the shooter (up to 24 MV/m, 2.6 times Kilpatrick) was determined.

Geometric arrangement

On the other hand, the location of the ion source in the central region must be meticulously adopted such that the beam will be appropriately centered during the acceleration and the orbit centers of the beam overlap with the machine center at extraction point after many turns. Central region geometric configuration depends on many parameters, like the initial phase of the particles, the transit time and the energy gain in the first accelerating gap, among other things. In addition, the evolution of these parameters in the following gap crossings has to be considered. Theoretical studies have discussed the source location (radial and angular displacements from the cyclotron center) [134]. From these considerations, the optimum source emplacement and puller-to-dee angle is seen to depend essentially on the details of ion motion in the central region and more rigorously on the first gap. These theoretical approaches are the starting point of the central region arrangement to be contrasted and evaluated through beam dynamics verification.

Phase acceptance

The central region configuration has to consider the starting phase of the favorable ions to provide an adequate acceleration. The range of the electric field RF cycle that allows the efficient particle injection from the ion source, going through the central region without colliding with some components structures, and providing a good beam focusing until reach the extraction point, is called RF phase acceptance. The interval of useful starting phases is centered at the phase where particles achieve the maximum energy gain at the first gap. The central region should be adjusted to increase the interval of useful starting phases of the RF cycle considering diverse factors, such as the phase of the electric field that supplies the maximum energy gain at the first gap, the RF frequency of the field and the final beam energy.

Axial motion

Beam focusing in a classical cyclotron is based on a weak focusing scheme. It is produced by the radial slightly decreasing magnetic field complemented by the electric field forces generated during the acceleration gap. Regardless of electric or magnetic nature, the axial forces vanish at the median plane and increases in magnitude as the particle moves further away from it. The magnetic field gradient is very small in the central region, resulting in negligible magnetic focusing forces near the center of the accelerator. By the other hand, the electric field produces axial forces particularly relevant at low energies. These electric forces have a focusing effect at the entrance of the gap but the effect is defocusing after crossing the median plane of the gap space. The total effect is totally dependent of the RF phase and therefore the central region must be optimized to improve the focusing effect. Apart from that, the space charge effects tend to expand the beam, being more important at low energy and high current. Therefore, it is essentially a comprehensive study of axial movement. A balanced combination of the focusing effects at low energies of the particles requires a very careful design of the electrical forces, which is directly related to the geometry of the puller.

Beam losses

The puller has to be designed to optimize beam transmission and to keep under control the possible beam losses, specially avoiding high-energy losses. Particles with inadequate starting conditions, having no chance of survival and unwanted molecular ions can be removed from the beam near the source making use of specific puller aperture slits, thus avoiding unnecessary electric power dissipation, cooling and radiation problems. However, particles within a proper electric field phase range have to be preserved from possible collisions with elements in the central region. Hence, the puller must be arranged so that ions with the desired range of phases can be accelerated without hitting the electrodes.

These critical aspects of the central region have been taking into account for the AMIT cyclotron central region design. Preliminary beam dynamics studies were carried out at the

beginning of the project to determine the adequate characteristics of the central region and to achieve an optimum beam transport of the beam. The final injection configuration (ion source-puller) is illustrated in Figure 2.12.

Regarding the ion source, the shape and dimensions of the outer profile, an essential part of the central region geometry, have been designed with the purpose of optimizing the first few orbits, incorporating a flat surface of the chimney facing the puller and a special shape of the rear side of the source to enable the beam transmission. Furthermore, the chimney extraction wall has to be very thin to facilitate the penetration of the electric field into the plasma column inside of the chimney and achieve an optimum beam injection into the cyclotron. The ion source is located backward from the cyclotron center and displaced horizontally to enlarger the trajectories during the first gap, increasing the energy gain and the phase excursion. For the same purpose, the flat surface of the chimney is rotated 40° respect to the horizontal plane.

Concerning the puller, it has been designed to be composed of two posts: the outer one, called 'puller 1', located at a higher radius and the smaller one, 'puller 2', located at tan inner radius. 'Puller 1' has been lengthened to be closer to the ion source slit with the objectives of minimizing the first acceleration gap (from 10 to 6 mm) and concentrating the electric field lines. With that in mind, the energy gain is increased as well as the extracted current from the ion source. Moreover, the 'puller 1' face in front of the ion source is parallel and flat to prevent any electric field distortion, avoiding radial oscillations and guiding the beam into a centered orbit. 'Puller 2' has been included to make the voltage constant during the first turn avoiding any deceleration resulting from the RF phases during the motion through that region. The geometry of the puller has been built to clear inappropriate particles of the first turn, particles far from the optimal phase that could contribute to high energetic losses in somewhere in an intermediate part of the cyclotron. The thickness of both pullers has been chosen from a balance between

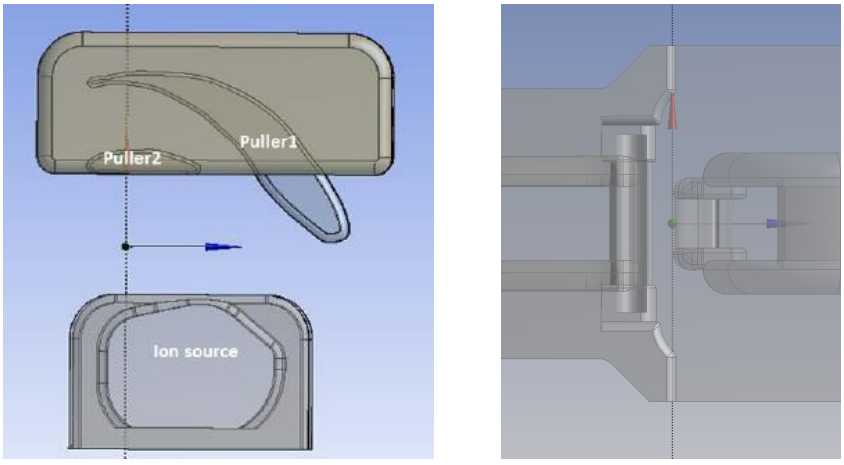

(a) (b)

Figure 2.12: *Schematic design of the central region of* AMIT *cyclotron showing in detail the ion source-puller system from top (a) and lateral point of view (b). It is clearly visible the parallelism between the faces of the ion source-puller and the off-center position of the ensemble respect to the cyclotron center.*

the minimum that can be considered from the manufacturing point of view and the maximum imposed by particle trajectories, emphasizing the challenge of a final good arrangement given the small dimensions of the central region.

2.2.5 Extraction system

The design of the extraction system in a cyclotron is considerably significant in the final beam conditions as it determines the final energy and current available for the radioisotope production. Furthermore, it influences to a large extent in the activation of the machine. The beam extraction system of AMIT cyclotron is based on the stripping mechanism, a method that allows the removal of electrons from H^- ions by the interaction with Carbon atoms of a thin foil of pyrolytic graphite. As a result, the negative ions are transformed into protons (H^+) and the curvature of accelerated particle trajectories in the magnetic field reverses enabling the proton transport to the target. Extraction of particles from cyclotrons using charge exchange of H^- has considerable advantages, as high extraction efficiency, high quality of extracted beams and the capacity of tuning the output beam conditions smoothly by a movable stripper mechanism.

The thickness of the foil plays an important role in the stripping process, the resulting beam transmission and the availability of the accelerator. Thicker stripping foils will enhance the fraction of beam being stripped. Nevertheless, the scattering of the beam also increases with the thickness as well as the power deposition on the foil, which can overheat and damage it. These processes deteriorate the quality of the extracted beam. The optimum thickness has to be established through a balance between three factors: the stripping efficiency, the beam transmission and the scattering.

Stripping efficiency

Charge-exchange reactions can be used for a good understanding of the stripping process efficiency. When a high energy beam goes through a material, numerous interactions could take place. Neglecting nuclear reactions, only charge-exchange processes can be considered. The variation of the charge fraction, F, in a high energy beam during the passage through the matter is described by the following differential equations [135]:

$$\frac{dF_i}{dx} = \sum_{j \neq i} \sigma_{ji} F_j - \sum_{j \neq i} \sigma_{ij} F_i \tag{2.4}$$

where σ_{ij} is the sum over all cross sections of processes in which the ion with charge i is transformed to j charge state. The first term on the right-hand side represents the increase in the fraction of ions at charge state i through the transformation from all other possible charge states j, while the second term represents the decrease of the ions in charge state i through the transformation into all other possible charge states j.

For energies above 100 keV the cross sections for electron capture reactions are negligible ($\sigma_{ji} << \sigma_{ij}$, $j < i$). Thus, the charge fraction for H^- ions through a foil thickness x can be

described by three differential equations:

$$\frac{dF_{-1}}{dx} = -\left(\sigma_{-10} + \sigma_{-11}\right) F_{-1} \tag{2.5}$$

$$\frac{dF_0}{dx} = \sigma_{-10}\, F_{-1} - \sigma_{01}\, F_0 \tag{2.6}$$

$$\frac{dF_1}{dx} = \sigma_{-11}\, F_{-1} + \sigma_{01}\, F_0 \tag{2.7}$$

where F_{-1}, F_0 and F_1 are, respectively, the fractions of negative hydrogen ions, neutral hydrogen and protons. Additionally, considering the beam charge conservation:

$$F_{-1} + F_0 + F_1 = 1 \tag{2.8}$$

the solutions for the three charge fractions can be obtained as:

$$F_{-1} = e^{-(\sigma_{-10}+\sigma_{-11})\,x} \tag{2.9}$$

$$F_0 = \frac{\sigma_{-10}}{\sigma_{-10}+\sigma_{-11}-\sigma_{01}}\left[e^{-\sigma_{01}\,x} - e^{-(\sigma_{-10}+\sigma_{-11})\,x}\right] \tag{2.10}$$

$$F_1 = 1 - F_{-1} - F_0 \tag{2.11}$$

Hence, the yield of each charge state depends on the thickness of the foil, the material and the energy of the incident particles. A proper choice of the thickness would provide a single jet of protons. The cross section of the involved reactions in the stripping process (Figure 2.13) can be obtained from experimental and theoretical studies [136–138].

The efficiency of the stripping process for AMIT beam requirements ($E = 8.5$ MeV) has been evaluated, obtaining the fraction of different charge states of the beam in front of the foil thickness (Figure 2.14). The cross section data at the nominal energy employed in the calculation has been exported from the theoretical results [137]. This analysis provides a minimum carbon

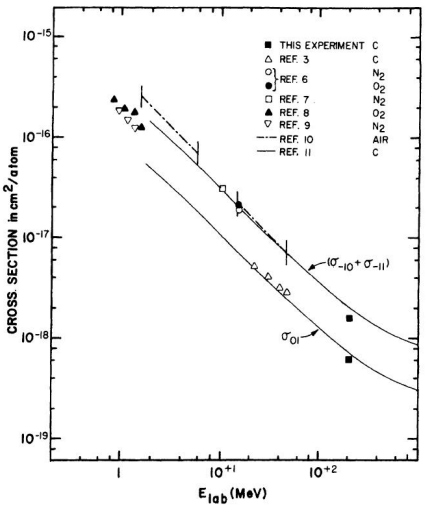

Figure 2.13: *Electron-loss cross section as a function of energy for hydrogen ions incident on different materials for experimental (symbols) an theoretical results (lines) [137].*

foil thickness of 20 μg/cm^2 ($\sim$ 0.09 μm for a standard carbon foil density of 2.25 g/cm^3) for an optimum beam stripping. This thickness is enough to transform all the negative hydrogen ions into protons with reliable accuracy: the fraction rate achieves is 99.9991%.

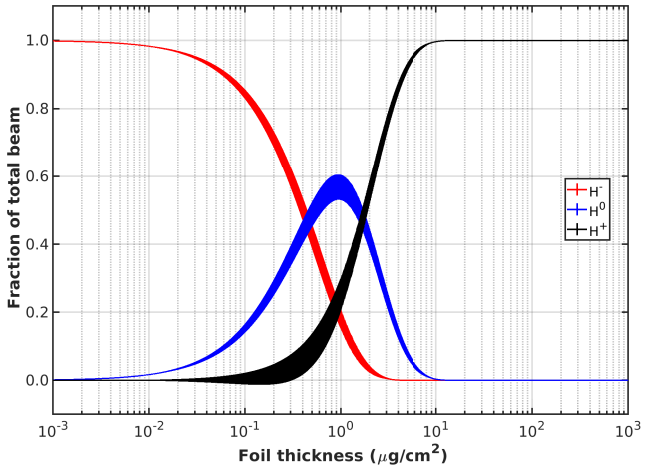

Figure 2.14: *Fraction of total beam for different charge states as a function of the stripping foil thickness for* AMIT *beam conditions. The width of the lines represents the error associated according to the extrapolated cross section data.*

Energy loss and scattering

In addition to the stripping phenomena, when the beam passes through the foil, two principal processes characterize the interactions of charged particles with matter: the particle energy loss and the deflection of the particles from their incident direction. These effects are primarily the cumulative result of inelastic collisions with the atomic electrons of the material and elastic scattering from nuclei. The extraction system by stripping process in a cyclotron has to balance the efficiency of the process with the particle matter interactions.

The inelastic collisions processes originate an energy transfer from the incident particles to the foil atoms. The macroscopic effect in a path length leads to an average energy loss according to Bethe-Bloch equation [115, 139]

$$-\left\langle \frac{dE}{dx} \right\rangle = Kz^2 \frac{Z}{A} \frac{1}{\beta^2} \left[\frac{1}{2} \ln \frac{2m_e c^2 \beta^2 \gamma^2 Tmax}{I^2} - \beta^2 \right] \tag{2.12}$$

where Z is the atomic number of absorbing material, A is the atomic mass of absorbing material, m_e is the electron mass, z is the charge number of the incident particle, $K = 4\pi N_A r_e^2 m_e c^2$, r_e is the classical electron radius, N_A is the Avogadro's number, I is the mean excitation energy and β and γ are kinematic variables. T_{max} is the maximum kinetic energy which can be imparted to a free electron in a single collision:

$$T_{max} = \frac{2m_e c^2 \beta^2 \gamma^2}{1 + 2\gamma m_e/M + (m_e/M)^2}, \tag{2.13}$$

A preliminary evaluation of these interactions has been realized to establish the optimal thickness of the carbon foils resulting in a maximum extraction of H^+ with the minimal losses. For

that purpose, the beam transmission and the energy losses for the final AMIT beam conditions have been studied. The stopping power and the projected range of a proton beam of 8.5 MeV in a carbon foil are obtained from PSTAR [140] program of NIST (see Table 2.5). These parameters measure the average rate of energy loss per unit path length, due to Coulomb collisions that result in the ionization and excitation of atoms as well as due to the transfer of energy to recoiling atoms in elastic collisions; whereas the projected range represents the average value of the depth to which a charged particle will penetrate along the initial direction.

Taking these magnitudes into account, the influence of the thickness of the foil in the energy loss has been calculated (Figure 2.15(a)). The effect of the input beam incidence angle respect to the stripper results in an enlargement of the effective foil thickness seen by the particles, slightly increasing the energy loss of the beam (Figure 2.15(b)). Therefore, establishing an admissible upper limit of energy loss in the stripping process of 100 keV, a maximum thickness of 2 mg/cm^2 ($\sim$ 9 μm for a standard carbon foil density of 2.25 g/cm^3) has be established as the optimum. This value is significantly higher than the minimum thickness obtained for an efficiency stripping process.

Table 2.5: *Stopping power of a* 8.5 *MeV proton beam in carbon*

Collision stopping power	46.17 MeV cm^2/g
Nuclear stopping power	$2.249 \cdot 10^{-2}$ MeV cm^2/g
Total stopping power	46.20 MeV cm^2/g
Projected range	103.9 mg/cm^2

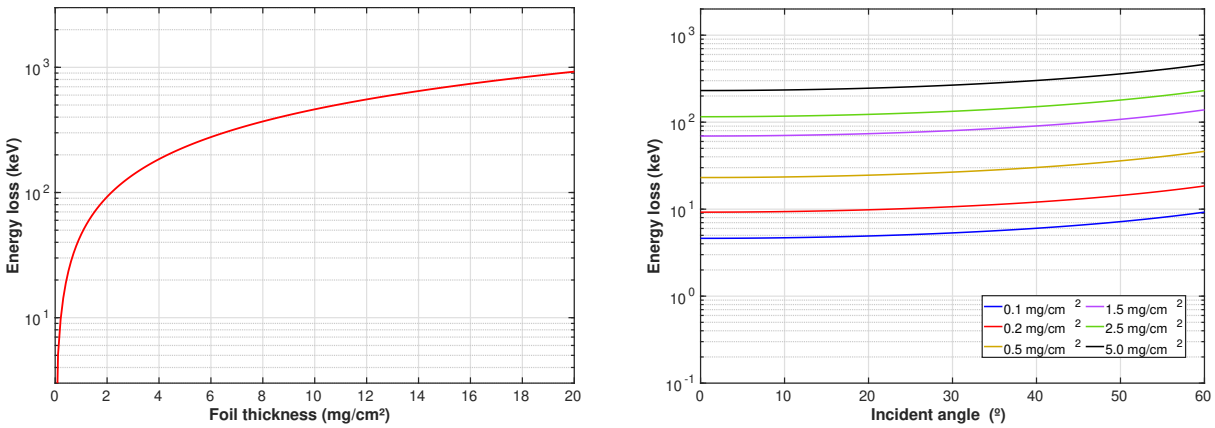

(a) (b)

Figure 2.15: *Energy loss by a proton beam of* 8.5 *MeV in carbon as a function of the foil thickness (a) and of the incident angle of the beam for several thickness.*

By the other hand, regarding the scattering processes, the particles can be deflected by single- and multiple-Coulomb scattering [139,141,142]. These processes could involve a significant source of beam losses and a gradual beam emittance growth [143, 144]. Particle scattering in stripping foils depends on the beam and the foil properties: the material, the thickness and the density. A

preliminary study performed with SRIM code [145] to simulate the particle matter interaction through the carbon foil showed a rms deviation of 0.35° of the beam from the an incident angle. This study considered a foil thickness between 5 and 50 μm, and incidence angle between 0° and 30°. Hence, the low angular deviation allows to conclude that the scattering process can be neglected in the AMIT beam extraction because the required thin foil does not affect substantially the particle trajectories, partly by the low energy of the beam.

Extraction mechanism

From the engineering point of view, AMIT cyclotron beam extractor consists of a set of three foils located in a movable mechanical structure (Figure 2.16) with longitudinal and rotational degrees of freedom. The foils present an intercepting area of ~ 110.5 mm^2 (8.5 mm length and 13 mm height). They are settled in a 57.28 mm diameter cylindrical structure deviated 28° with respect of the center of the cylinder to facilitate a perpendicular interception of the beam. In addition, the foils are separated 70° from each other. The cylindrical structure is capable to be rotated a maximum of 152.9°, and displaced 48 mm longitudinally with high accuracy (~ 0.1 mm). However, due to the angular separation between the carbon foils and the location of the structure in the vacuum chamber, the maximum angular rotation for a viable position to intercept the beam of each stripping foil is around 60°. This is in compliance with the minimum beam intercepting orbit. Hence, this combination of movements confers versatility to the extraction system of the cyclotron, allowing an in situ variation of the position during the operation to fix an optimum extraction point.

The multi-foils system allows replacing the stripping foil in case of exceeding the mean lifetime or by material damage. It can be produced by a combination of diverse factors as temperature rise, mechanical stress, fatigue due to thermal buckling, sublimation, radiation damage of the structure, etc.

Summarizing, the implemented mechanism endow the AMIT cyclotron with an adjustable beam extraction system allowing to choose the optimal beam conditions to optimize the radioisotope production.

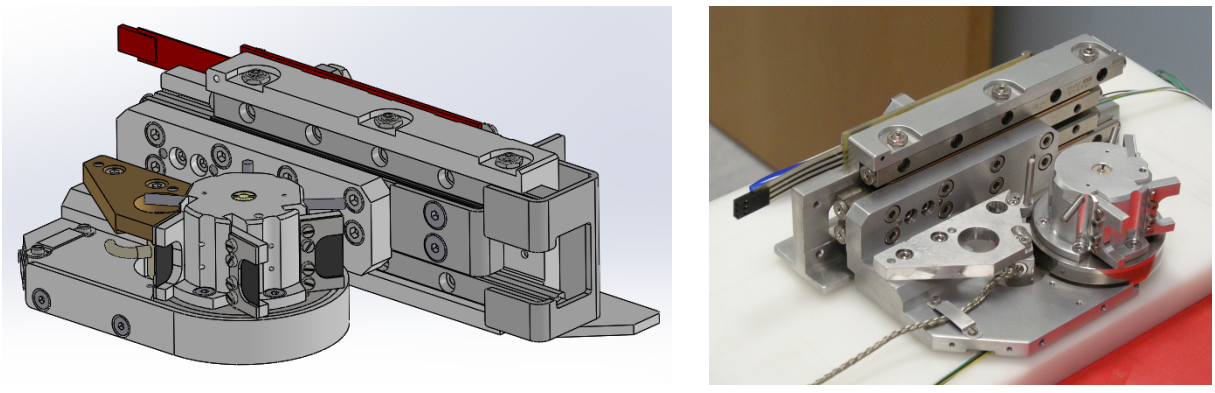

(a) (b)

Figure 2.16: *Design view of the* AMIT *extraction mechanism (a) and a picture of the final mechanical structure (b).*

2.2.6 Targetry

The radioisotope production in AMIT cyclotron is focused on a single-dose production under the principle of the dose on-demand for non-conventional facilities. In this way, the production is carried out through the nuclear reactions specified in the Table 2.1 by an external targetry system located at the end of the vacuum chamber, at the opposite side of the RF resonator. An available vacuum port is designed for the extraction path of the protons. Two different targets, devoted to each radioisotope of interest to AMIT cyclotron, have been designed.

The target system for ^{11}C [146] consists of a collimator, an energy degrader, an electrical insulator, a grid and the cylinder-shape target chamber which is filled with the nitrogen gas to be irradiated (Figure 2.17). The main function of the collimator is to limit the beam size entering the gas cavity, avoiding possible particle collisions with the walls. The target chamber is under high pressure conditions to reduce the length necessary to completely stop the proton beam, taking into account the gas expansion by the beam heating. An Al97/Mg3 30 μm window foil with a 1.5 mm hole diameter grid encloses the target material, nonetheless it allows the beam penetration. This window foil has relatively good resistance comparing traditional windows, but it provides low neutron production and low activation. The internal length of the target chamber is set to 175 mm to guarantee complete energy deposition in the radiated material. All the system is water-cooled to avoid excessive heating.

^{18}F radioisotopes are produced in a conventional target consisting of a Niobium cavity to hold ^{18}O-enriched water (Figure 2.18). The internal length of the cavity is 1 cm with a diameter of 1 cm diameter, and it includes an expansion room for thermal expansion. An Aluminium alloy (AL6082) structure case for low radiation and activation supports the target cavity as well as the collimator and a grid foil.

This is a 22.5 mm radius circular aperture at the end of the vacuum chamber located at $\sim$420 mm of radius from the cyclotron center ($x = 91$ mm $y = -410$ mm). After that, there is a short beam line of $\sim$ 25 cm until the collimator target window.

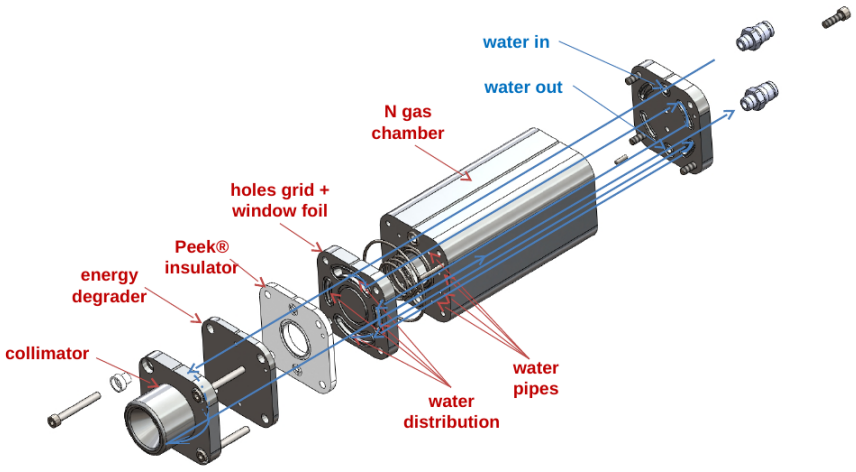

Figure 2.17: *Layout of the different components of the* ^{11}C AMIT *target system.*

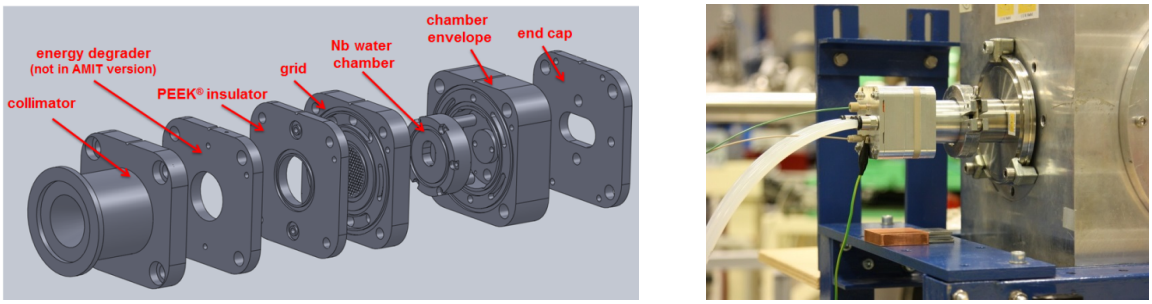

(a) (b)

Figure 2.18: *(a) Layout of the different components of* ^{18}F AMIT *target and (b) a picture of the attachment to the vacuum chamber.*

2.2.7 Beam diagnostics

A suitable control of the main beam characteristics is determinant to allow the tuning and optimization of the radioisotope production as well as to minimize possible beam losses, establishing the significance to develop adequate beam diagnostics. However, the compactness of the cyclotron makes their design very challenging due to the space limitation inside the vacuum chamber. Additionally, the diagnostics will work in hard conditions imposed by the high magnetic field and the high radiation environment produced by the target. Different beam diagnostics have been designed to characterize the beam at the different stages of the cyclotron: ion source characterization, commissioning stage and cyclotron operation [147, 148].

To properly monitor the transmitted beam current during acceleration, a movable beam probe mechanism has been designed. The beam probe, electrically insulated from the driven stage, is inserted in the radial direction by an in-vacuum actuator with enough motion range to intercept the beam in the central region. The beam probe is made of graphite to withstand continuous beam power in an area of a few square millimeters, enhance its the temperature acceptance, according to thermomechanical simulations, and keep its activation as low as possible for an easy maintenance.

Furthermore, other beam diagnostics have been devised as a beam current measurement integrated with the stripping foil to evaluate the beam current deposited in the foil, a beam profile monitor in different positions of the cycle, a Compact Diagnostic Line (CDL) with a Secondary Electron EMission grid (SEM-Grid) to measure the transverse beam profile, and an energy monitor at the target position. In addition, a segmented beam probe to evaluate the beam profile in different positions of the cycle has been proposed.

2.2.8 Vacuum system

The vacuum system plays an important role in the cyclotron because the compactness of the machine limits the available space for the vacuum pumps installation. In addition to the fact that the internal ion source releases a continuous gas flow in the central region of the cyclotron. The deterioration of the vacuum level has a strong impact on beam losses because the second

slightly bounded electron of the H^- ions can be easily stripped. A complete assessment of this effect is given in chapter 6.

Vacuum distribution has been simulated with Molflow code [149, 150] to evaluate different configurations of the vacuum pumps, taking into account the pumping system capacity, the impact on the whole accelerator size, the maintenance requirements, the high radiation environment as well the interactions with the other cyclotron systems. From those simulations, a configuration with two diffusion pumps connected to the cylindrical resonator was chosen as a preferred option. The pumps system has capability to achieve Ultra High Vacuum (10^{-7} mbar), but due to the gas injection from the ion source, the pressure level in the chamber during operation is much higher (around $10^{-4} - 10^{-5}$ mbar).

Molflow simulations are based on a volumetric flow rate of an ideal gas under the consideration of a steady-state molecular flow, that is to say, the mean free path is considerably greater than the dimensions of the vacuum vessel. With that in mind, some parameters are relevant from the point of view the vacuum technology theory [151]. The throughput is defined as the quantity of gas, at a specified temperature, flowing per unit time across a specified cross section aperture:

$$Q = C(P_2 - P_1) = C\Delta P \tag{2.14}$$

where ΔP is the difference of pressure and C is the conductance, a magnitude which quantifies how an specific gas flows through an aperture. It can be interpreted as the inverse of the flow resistance produced by external friction between gas molecules and the wall surface and internal friction between the gas molecules themselves. The conductance is related with the properties of the gas and some geometric considerations. According to the Kinetic Theory of gases, the arithmetic average velocity of the particles follows the Maxwell-Boltzmann distribution in a steady-state molecular flow:

$$v_{av} = \sqrt{\frac{8k_BT}{\pi m}} \tag{2.15}$$

Furthermore, the volumetric flow rate passing through an infinitely thin hole of surface area, A, between two volumes is given by:

$$Q = A\,\frac{v_{av}}{4}\,\Delta P \tag{2.16}$$

Therefore, the conductance is expressed by:

$$C = A\,\frac{v_{av}}{4} \tag{2.17}$$

Molflow code perform a vacuum calculation in an imported volume considering these magnitudes as input parameters. A summary of the parameters used for AMIT vacuum simulations is shown in Table 2.6. The results are easily scalable following the above equations. The vacuum pressure distribution is shown in Figure 2.19. It can be noted that the pressure level keeps almost constant lengthwise the cyclotron except in front of the ion source, where the gas flux increases significantly the pressure. Furthermore, the dee region has a larger pressure due to the gas evacuation limitations through the opening holes at the back of the structure. Figure 2.20 shows the pressure level along two different directions in the vacuum chamber: along the center

of the gap (at $y = 0$) and along the perpendicular direction passing through the center of the machine (at $x = 0$). Hence, it is clear how around the ion source there is peak of pressure that will affects to the beam transmission along the central region.

Table 2.6: *Parameters for* AMIT *vacuum simulations*

Gas	H_2
Ion source slit aperture	0.2×8 mm
Conductance	0.70 l/s
Throughput (Input gas flow)	0.043 mbar·l/s = 2.546 sccm
Injection pressure inside the chimney	0.06 mbar

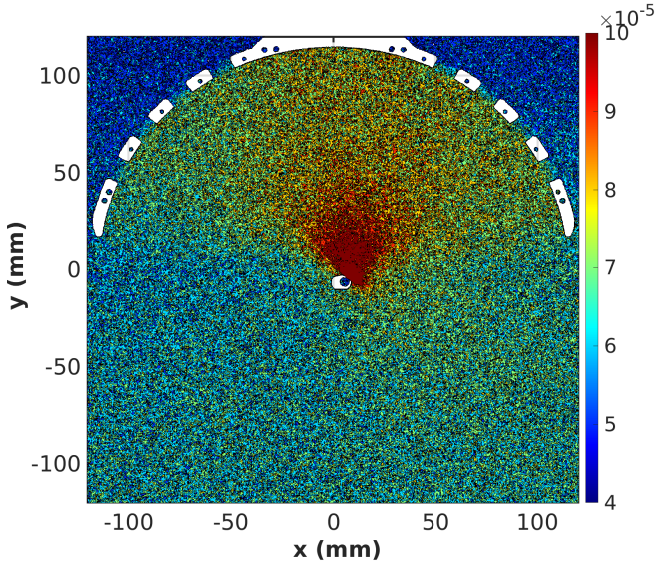

Figure 2.19: *Pressure distribution in the median plane of* AMIT *cyclotron with pressure level as color map.*

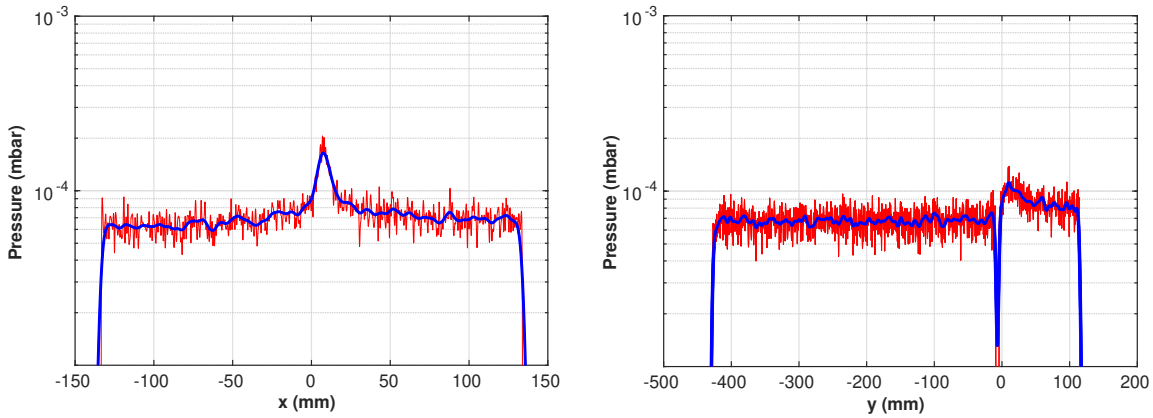

(a) (b)

Figure 2.20: *Pressure level along x-coordinate at gap center (a) and along y-coordinate at $x = 0$ (b). The red line represents the raw data from Molflow simulations and the blue line is a smoothing spline fit.*

Neither clock nor weather-glass is ever right;
but we believe in both, devoutly
— Charles Dickens

Chapter 3

Multi-particle beam dynamics code

Beam dynamics studies are primordial over the course of the entire life of an accelerator project. They determine the main component specifications in the early design stage, validate the final engineering design, contribute to a better understanding of accelerator behavior during the commissioning stage as well as they are essential to optimize the output beam properties according the ultimate project goals. These studies demand precise simulation tools describing the movement of the particles subjected to external electromagnetic fields and as well as to the self-fields caused by the Coulomb interactions between the particles. High accuracy beam dynamics models are required to reproduce the real behavior of the beam during the acceleration including all high-order effects. Several beam dynamics computational tools applied to cyclotrons are currently available [152], being OPAL one of the most complete and versatile codes. Moreover, OPAL have been benchmarked and successfully applied to simulate different particle accelerators [153–156]. This chapter starts with a brief introduction to OPAL code, describing its computational structure and its capabilities in beam dynamics studies for particle accelerators. A second section tackles the application of the code to AMIT cyclotron for a comprehensive assessment of beam dynamics.

3.1 The OPAL framework

OPAL (Object Oriented Parallel Accelerator Library) [157, 158] is a versatile open source Particle-In-Cell (PIC) code developed for large-scale charged-particle optics simulations in accelerators and beam lines. The OPAL framework provides parallel calculations through the increasingly sophisticated mathematical models and evolving computer power available on the desktop as well as on supercomputer centers. It may be considered one of the most effective tools for the study of space charge effects in particle accelerators by detailed 3D modeling capabilities. Moreover, it includes the feature to combine linear and non-linear beam tracking with Monte Carlo simulations of the particle-matter interaction [159, 160].

OPAL has been developed since 2008 from a scientific collaboration led by the Accelerator Modeling and Advanced Simulations (AMAS) group at Paul Scherrer Institut (PSI) with the

primary purpose to simulate the particle orbits in cyclotrons with and without space charge. Afterward, it was extended to the particle tracking in other types of accelerators and beam lines. Adopting the MAD language with extensions, OPAL is the successor of MAD9P (Methodical Accelerator Design version 9-Parallel). It is based on the CLASSIC [161] class library and IPPL (Independent Parallel Particle Layer) [162] as the framework which provides parallel particles and fields using data parallel approach.

High precision particle accelerator modeling with the OPAL code can be applied to linacs, cyclotrons, Fixed-Field Alternating-Gradient devices (FFAG) and next-generation light sources. The framework is organized in different flavors:

- OPAL-CYCL tracks particles with 3D space charge including neighboring turns in cyclotrons and FFAGs with time as the independent variable.
- OPAL-T can be used to model beam lines, linacs, RF-photo injectors and complete X-ray Free-Electron Laser.

The particle motion in OPAL is based on the time integration of the general equations of motion for relativistic charged particle in electromagnetic fields, expressed by:

$$\frac{d\mathbf{r}}{dt} = c\boldsymbol{\beta} \tag{3.1}$$

$$\frac{d\mathbf{p}}{dt} = q\left(\mathbf{E} + c\boldsymbol{\beta} \times \mathbf{B}\right) \tag{3.2}$$

where $\mathbf{p} = m_0 c\gamma\boldsymbol{\beta}$ denotes the relativistic momentum of a particle, m_0 is the rest mass, q is the charge of particles, c is the speed of light, γ is the relativistic factor, $\boldsymbol{\beta} = \mathbf{v}/c$ is the normalized velocity vector, E and B are the electric and magnetic fields. On the other hand, the phase space evolution, *i.e.*, the position-momentum space $(\mathbf{x}, \mathbf{p}) \in \mathbb{R}^{3\times3}$, is determined by the collisionless Vlasov-Poisson equation:

$$\frac{df(\mathbf{x}, \mathbf{p}, t)}{dt} = \gamma m_0 \, \partial_t f + \mathbf{p} \cdot \nabla_x f + q(\mathbf{E}(\mathbf{x}, t) + \frac{1}{\gamma m_0} \, \mathbf{p} \times \mathbf{B}(\mathbf{x}, t)) \cdot \nabla_{\mathbf{p}} f = 0 \tag{3.3}$$

where $f(\mathbf{x}, \mathbf{p}, t)$ is the density function in time t of the charged particle distribution in phase space.

The electric and magnetic fields are expressed as superposition of external fields and self-fields (space-charge fields) due to electromagnetic fields created by the beam itself:

$$\begin{aligned} \mathbf{E} &= \mathbf{E}_{ext} + \mathbf{E}_{self} \\ \mathbf{B} &= \mathbf{B}_{ext} + \mathbf{B}_{self} \end{aligned} \tag{3.4}$$

The external fields, that may explicitly depend on time, are treated independently of the particles whereas the self-fields depend on position and momentum of a collection of particles. The external fields, composed by the electric provided by RF cavities ($\mathbf{E}_{ext}$) and magnetic fields ($\mathbf{B}_{ext}$), are responsible for the acceleration and focusing of the beam. By using the coordinate system moving with the particles through an appropriate Lorentz transformation, a quasi-static approximation

of the system is achieved, in which the self-induced magnetic field becomes negligible ($\mathbf{B}_{self} \approx 0$) and the electric field is described by the electrostatic potential, ϕ:

$$\mathbf{E}_{self} = -\nabla\phi \tag{3.5}$$

that can be obtained from Poisson's equation:

$$\nabla^2\phi(\mathbf{x}) = -\frac{\rho(x,t)}{\varepsilon_0} \tag{3.6}$$

where ρ is spatial charge density and ε_0 the vacuum permittivity. By means of the inverse Lorentz transformation, the self-field is afterward computed in the laboratory frame, as required in the equation (3.4). Thus, the Poisson problem discretized by finite differences can be efficiently solved on a rectangular grid by a PIC approach [163].

In OPAL-CYCL flavor [153] the Vlasov-Poisson equation system is solved with conditions of external static 3D magnetic field and fixed-frequency RF field. There are two options to import external magnetic fields into OPAL. In the first method, devoted to magnetic field measurements in the median plane, the vertical magnetic field component B_z in the median plane is used. To compute particle trajectories outside the median plane, the magnetic field is expanded in the z-direction by interpolation from the third order field [164] using Lagrange's 5-point formula, according to:

$$\begin{aligned} B_r(r,\theta,z) &= z\frac{\partial B_z}{\partial r} - \frac{1}{6}z^3 C_r \\ B_\theta(r,\theta,z) &= \frac{z}{r}\frac{\partial B_z}{\partial \theta} - \frac{1}{6}\frac{z^3}{r}C_\theta \\ B_z(r,\theta,z) &= B_z - \frac{1}{2}z^2 C_z \end{aligned} \tag{3.7}$$

where $B_z \equiv B_z(r,\theta,0)$ and

$$\begin{aligned} C_r &= \frac{\partial^3 B_z}{\partial r^3} + \frac{1}{r}\frac{\partial^2 B_z}{\partial r^2} - \frac{1}{r^2}\frac{\partial B_z}{\partial r} + \frac{1}{r^2}\frac{\partial^3 B_z}{\partial r \partial \theta^2} - 2\frac{1}{r^3}\frac{\partial^2 B_z}{\partial \theta^2} \\ C_\theta &= \frac{1}{r}\frac{\partial^2 B_z}{\partial r \partial \theta} + \frac{\partial^3 B_z}{\partial r^2 \partial \theta} + \frac{1}{r^2}\frac{\partial^3 B_z}{\partial \theta^3} \\ C_z &= \frac{1}{r}\frac{\partial B_z}{\partial r} + \frac{\partial^2 B_z}{\partial r^2} + \frac{1}{r^2}\frac{\partial^2 B_z}{\partial \theta^2}. \end{aligned} \tag{3.8}$$

In the second option, a full 3D magnetic field map of the region of interest is numerically calculated by modeling and performing finite elements analysis making use of commercial software and loaded into OPAL. In the same way, RF fields are imported from numerical calculation modeling and OPAL-CYCL introduces a time dependence through a cosine function.

The external fields and space charge fields are used to perform the tracking of each particle from the integration of the equation (3.2) in a specific time step, Δt, by using the different implemented integrators: a fourth-order Runge-Kutta integrator, a second-order Leap-Frog integrator or a Multiple-Time-Stepping variant of the Boris-Buneman integrator (MTS). The time step is associated with an equivalent step Δs in space depending on the particle energy.

OPAL code includes neighboring multibunch effects in cyclotrons through different space charge models: Fast Fourier Transform (FFT) based Particle Mesh (PM) Poisson solver for periodic and open boundary problems and the Smoothed Aggregation Algebraic Multi Grid (SAAMG) solver that includes arbitrarily shaped beam pipe boundaries [165].

In addition, aside from the multi-particle simulation mode, OPAL-CYCL also provides a single-particle tracking mode, a useful tool for a preliminary study of a cyclotron allowing the determination of basic beam parameters and for a better understanding of fundamental effects, such as reference orbit, phase shift history, central region and focusing effects.

A remarkable feature of OPAL is the capability of incorporating the accelerator geometry by a triangle mesh modeling to include a CAD model of the accelerator or relevant part of it [166]. This is essential for precise beam dynamics simulations with complex geometries, emphasizing the high relevance in the optimization of the accelerator in the design stage as well as for the characterization and operation. The mesh is able to model arbitrary accelerator geometries and provides methods to test the collisions of particles with the inner surface of the geometry, check whether a given point is inside the accelerator geometry and computes the distance from a given point and the boundary in a certain direction vector to the boundary.

The phase-space of the input beam is defined through the `DISTRIBUTION` command, providing a generator of different distributions (`GAUSS, MATCHEDGAUSS, FLATTOP, BINOMIAL`) or by an external file adapted to user's requirements with the `FROMFILE` option. Regardless of the type, the initial distribution is specified in the local reference frame of the OPAL-CYCL Cartesian coordinate system. The phase space (x, y, z, p_x, p_y, p_z) is transformed to the global Cartesian coordinates (X, Y, Z, P_X, P_Y, P_Z) using the starting coordinates of the cyclotron (r_0, ϕ_0, z_0), the starting momenta, p_{total} determined by the beam initial energy and the momentum of the reference particle $(p_{r0}, p_{\phi 0}, p_{z0})$, according to:

$$\begin{aligned} X &= x\cos\phi_0 - y\sin\phi_0 + r_0\cos\phi_0 \\ Y &= x\sin\phi_0 + y\cos\phi_0 + r_0\sin\phi_0 \\ Z &= z + z_0 \end{aligned} \tag{3.9}$$

$$\begin{aligned} P_X &= (p_x + p_{r0})\cos\phi_0 - (p_y + p_{\phi 0})\sin\phi_0 \\ P_Y &= (p_x + p_{r0})\sin\phi_0 + (p_y + p_{\phi 0})\cos\phi_0 \\ P_Z &= p_z + p_{z0} \end{aligned} \tag{3.10}$$

3.2 AMIT beam dynamics model

A successful computational implementation of an accelerator depends to a large extent on the reliability of the employed beam dynamics code as well as on its capability to reproduce the diverse influential physical phenomena. OPAL arises as an appropriate and powerful tool to perform beam dynamics studies given its capability to perform multi-particle simulations including different accelerators elements, boundary geometry implementation as well as particle-matter interactions models based on Monte Carlo algorithms. Given these features, the code can be used to reproduce in good agreement the real behavior of the cyclotron.

From a computational point of view, OPAL-CYCL includes different implementations to read the field functions attending to the electric and magnetic field format. The function to be used is defined by the parameter `TYPE` of the command `CYCLOTRON`, being `TYPE=BANDRF` the best suited for AMIT simulations. This format supports 3D electric field maps from an external file (an important feature developed especially for compact cyclotrons). The RF fields have to be imported in a regular mesh in a *h5part* file, a H5hut [167] format, high performance parallel data container based on Hierarchical Data Format version 5 (HDF5). In respect of the magnetic field, it is required the vertical magnetic field component, B_z, in the median plane stored in a cylindrical sequence as it is shown in Figure 3.1. Then, the field will be extrapolated according to the equations (3.7).

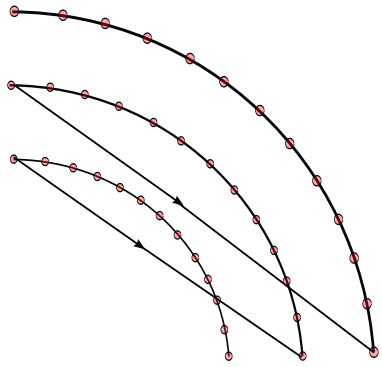

Figure 3.1: *2D magnetic field map on the median plane as required for `BANDRF` cyclotron type. The primary direction corresponds to the azimuthal direction whereas the secondary one to the radial direction. The number of points of the field map is arbitrary.*

Hence, OPAL-CYCL represents the base of the beam dynamics model to characterize and optimize the radioisotope production of AMIT cyclotron. Nevertheless, the development of the complete model of the cyclotron requires the use of several codes to obtain the different fields as well as for the post-processing stage. The electric and magnetic fields, the geometry and the initial particle distribution must be obtained externally and imported into the OPAL input file. Figure 3.2 shows the working scheme flowchart employed for the AMIT beam dynamics study, from the required external files to the OPAL simulation cycle. A description of each necessary step of the process is presented in the following sections.

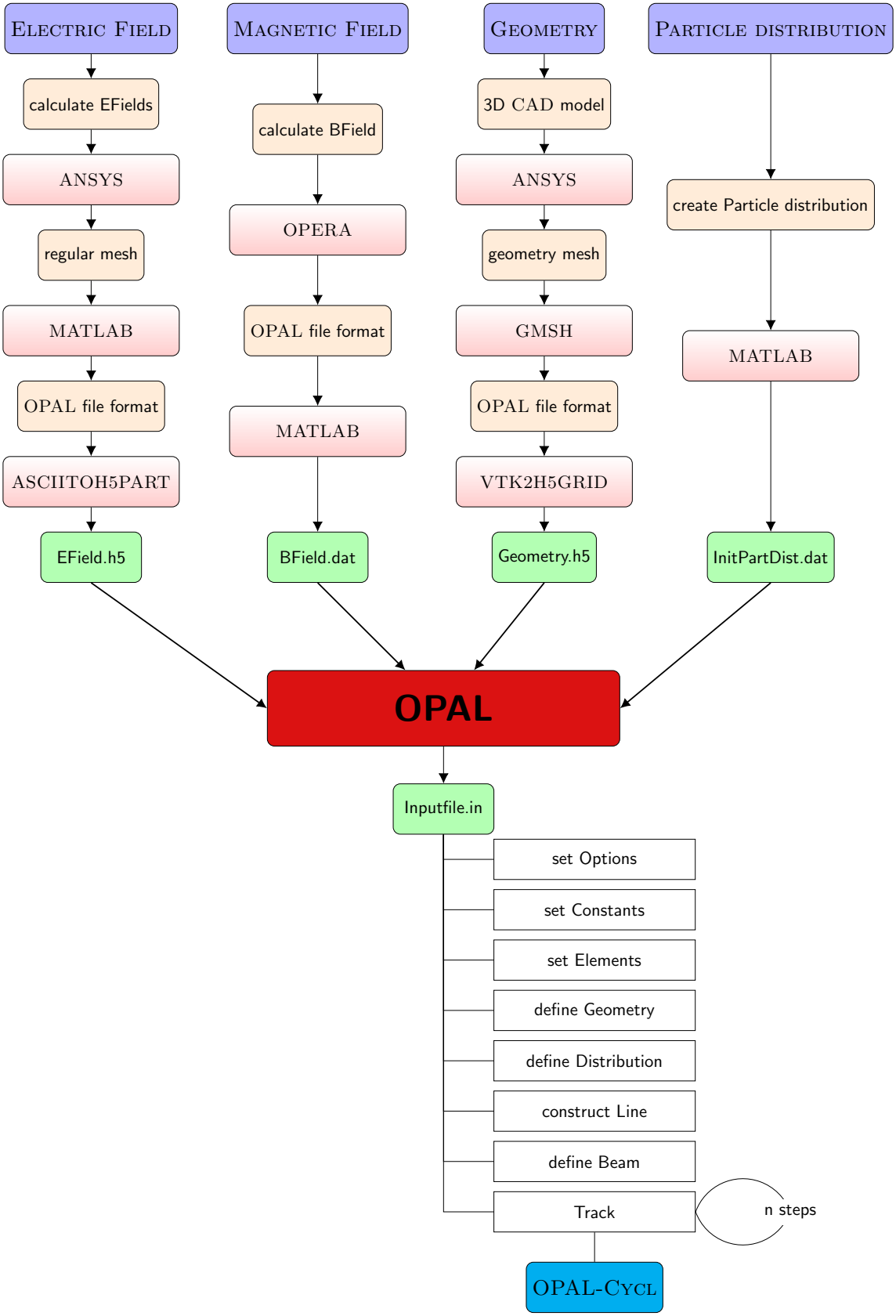

Figure 3.2: *Working scheme flowchart followed in the beam dynamics analysis.*

It has to be commented that electric and magnetic fields are treated separately from each other in OPAL simulations due to the absence of coupling between the magnetic field created by the magnet and the electric field produced by the dee electrode. Both fields have been studied separately, using the most appropriate code in each case. On the one hand, ANSYS has been used to study the electric field. On the other side, in the case of the magnet, OPERA was used for its optimization capabilities, although a benchmarking was done with ANSYS. Additionally, each field is required in a different file format, adapted to the best code implementation, as it was discussed above. Devoted C++ classes are used for the internal treatment of electric and magnetic fields in OPAL code source in a separate way. Although the computational details of this calculation are beyond the scope of this thesis, a brief description of the main results of these studies is presented for a better understanding of the beam dynamics simulations.

Magnetic field

The magnetic field at the median plane was calculated in a preliminary study, beforehand of this dissertation. The TOSCA (OPERA-3D) [168] code was used for the electromagnetic simulations of AMIT superconducting magnet, providing the vertical magnetic field in a circular area with radius of 650 mm, in a sized mesh of 1 mm radius and 1° azimuth. The field has been adapted to the field format of `BANDRF` cyclotron type in OPAL through a MATLAB script. Figure 3.3 shows the distribution of the magnetic field in the median plane, with particular detail in the region corresponding to the beam acceleration. Moreover, the magnetic field profile along the horizontal and vertical directions is illustrated in Figure 3.4. It is clearly appreciable the slightly decreasing intensity of the magnetic field with radius in the acceleration region ($\rho < 115$ mm), responsible for the weak focusing in AMIT cyclotron. The magnetic field outside the median plane is extrapolated by OPAL during the simulations according to the equation (3.7).

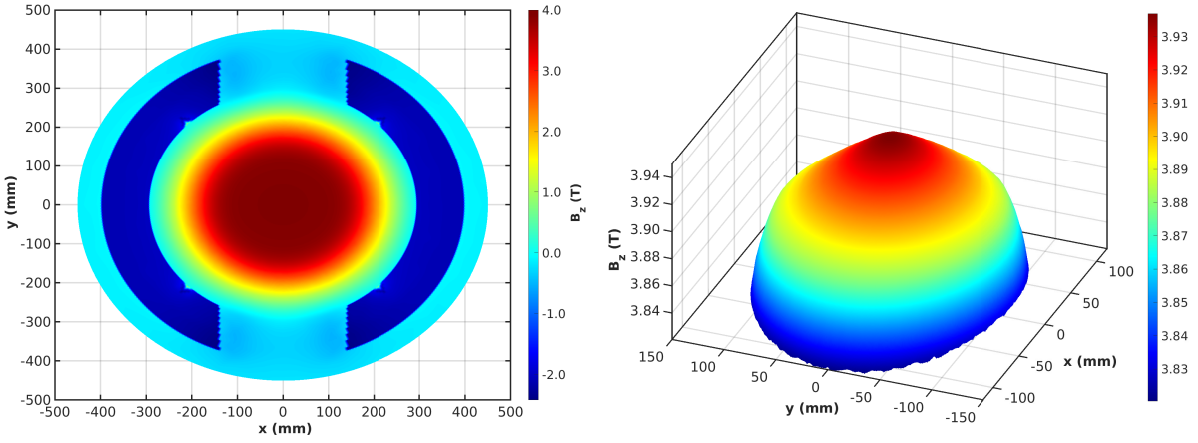

(a) (b)

Figure 3.3: *Vertical magnetic field B_z distribution in the median plane (a), showing in more detail the field map in the acceleration region (b). The field discontinuity in the return yoke is produced by the aperture performed to insert the independent vacuum chamber.*

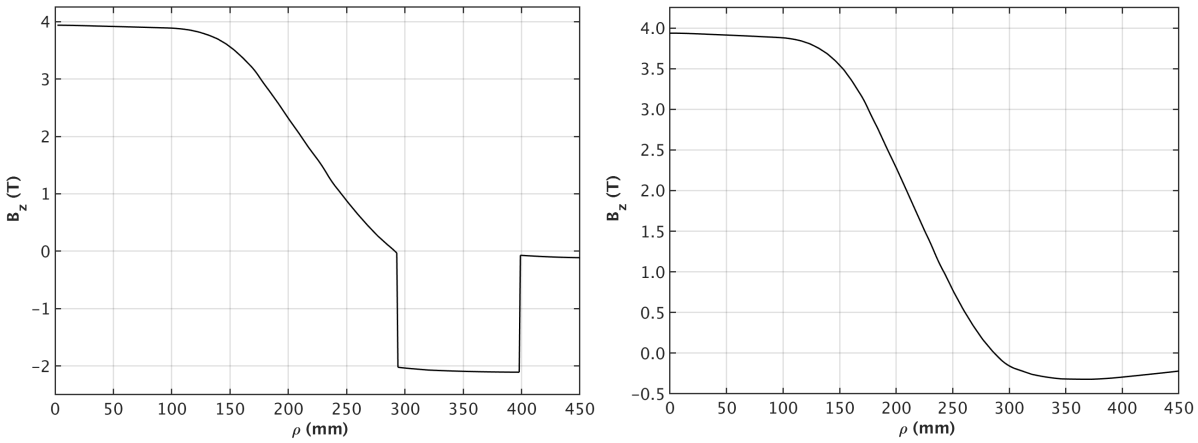

(a) (b)

Figure 3.4: *Vertical magnetic field B_z of* AMIT *magnet in radial direction along (a) x-axis ($\theta = 0°$) and (b) y-axis ($\theta = 90°$).*

Electric field

The RF electric field has been calculated with ANSYS code [169], employing first the DesignModeler tool to import the 3D model of the RF cavity and perform geometrical adaptations. Later on, the Thermal Analysis tool calculates the electric field map in the region of interest [170]. This approximation is valid given the 60 kV of the dee and the crossing gap time compared with the RF frequency. From the Fourier's law, the electric field distribution can be obtained through analogous stationary thermal simulations:

$$\mathbf{q}(\mathbf{r}) = -k\vec{\nabla}T(\mathbf{r}) \quad \longleftrightarrow \quad \mathbf{E}(\mathbf{r}) = -\vec{\nabla}V(\mathbf{r}) \tag{3.11}$$

where $\mathbf{q}$ is the heat flux, k is the thermal conductivity, T is the temperature, $\mathbf{E}$ is the electric field and V is the voltage. With that in mind, ANSYS can be employed to solve the mathematical equation, referred to temperatures by default, that governs the case under study. The problem is completely defined with initial conditions, taking into account that no temporal condition is needed since the case is stationary, which correspond to voltage values: the dee and puller will be at 60 kV, whilst the rest is at 0 kV.

The region of interest to compute the electric field calculation corresponds to the acceleration region in the cyclotron, that is to say, the area including the dee and dummy-dee. A non-regular mesh is performed in three different parts to obtain a fine mesh as required by beam dynamics studies (Figure 3.5). The first one, is the ion source slit region with a mesh size of 0.025 mm due to the tiny width of the aperture. Secondly, is the acceleration gap with a mesh size of 0.8 mm. The third considered region is the remaining area of the acceleration region, where the electric field is almost negligible and therefore the default mesh is selected because a very precise meshing is unnecessary. The meshing procedure and the selection of the regions have been carefully optimized within the context of this thesis. The accuracy of the results have been

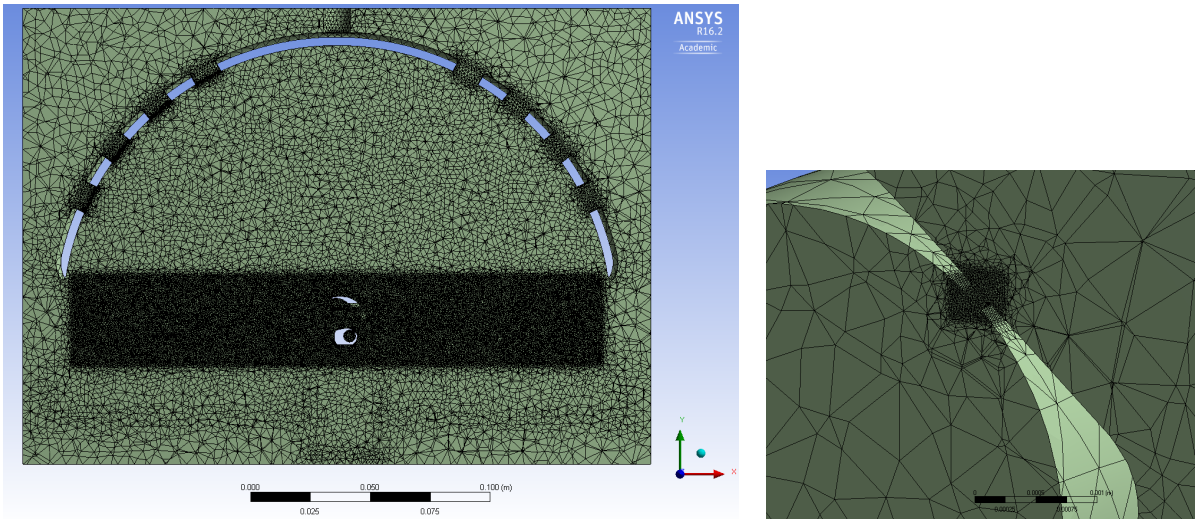

(a) (b)

Figure 3.5: ANSYS *optimized mesh for* AMIT *electric field calculation (a) with a detailed view of the fine mesh in the ion source slit (b).*

evaluated taking into account both the ANSYS and OPAL computational times and the size reduction of the files.

The electric field components and the voltage provided by ANSYS (Figure 3.6) are exported to *ASCII* files. Thereupon, an interpolation performed with MATLAB transforms the data for each region to a regular data mesh. Finally, the data are adapted according to the requirements of external electric field maps in OPAL to a *h5part* file, making use of *ascii2h5block.cpp* program, a dedicated C++ feature elaborated by the OPAL developer group.

Geometry

An imported geometry file provides boundaries for the accelerator components, acting as a terminator for particles that cross the geometry surface. At present, the `GEOMETRY` command is an experimental feature in OPAL, but it has been successfully used along this dissertation.

Adding arbitrary geometries to OPAL-CYCL requires a careful preparation [166, 171]. Initial CAD model of the accelerator has to be modified to obtain an inverted solid created by the subtraction of all elements from the geometry. This 'vacuum space' is exported to *stp* format and a 2D or 3D mesh is generated using GMSH [172]. The meshed geometry is saved into a *vtk* file and converted it into *h5* format through a *vtk2h5grid* program, specifically created by the OPAL developer team. During the initial stages of a simulation, OPAL creates a voxel mesh to speed up the tests that have to be performed every time-step.

Following these procedure, a proper geometry file for the AMIT cyclotron has been obtained. The meshed volume as displayed in GMSH is shown in Figure 3.7.

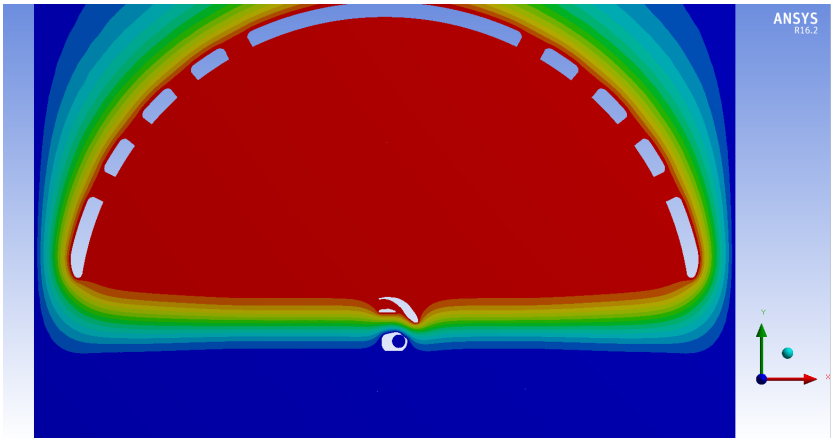

(a)

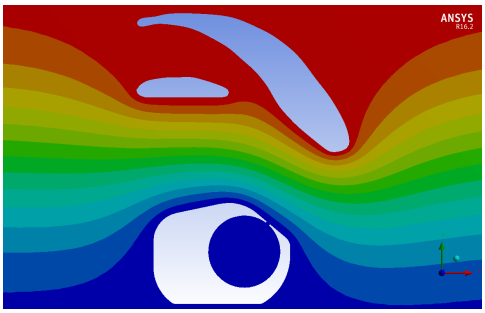

(b)

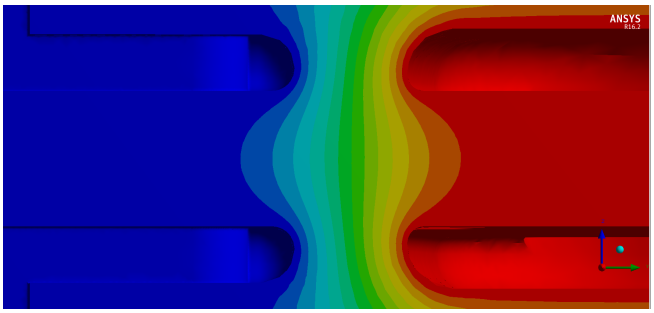

(c)

Figure 3.6: *(a) Voltage distribution in the median plane from* ANSYS *calculation with a detailed view of the central region (b), showing the compression of the equipotential lines in the first gap, and the voltage distribution in the axial plane (c). The color scale of the voltage is uniformly calibrated from blue to red for voltages between 0 and 60 kV.*

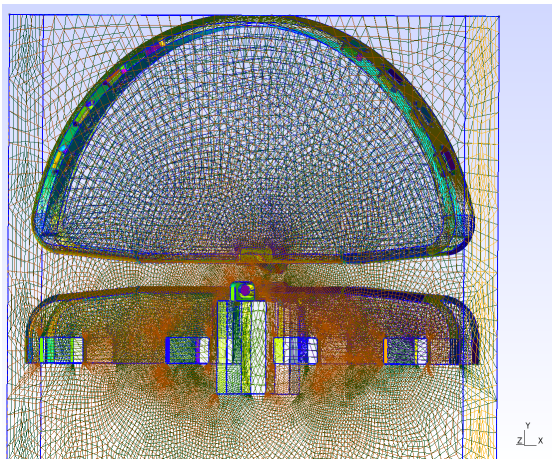

(a)

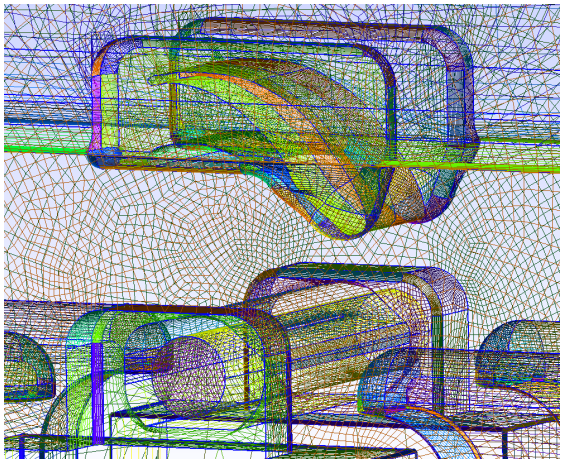

(b)

Figure 3.7: *Meshed volume as displayed by GMSH of* AMIT *acceleration region (a) with a detailed view of the central region (b).*

Particle distribution

The initial particle distribution can be adapted to each specific beam dynamics study employing the type `FROMFILE` in the `DISTRIBUTION` command. However, the actual initial distribution of AMIT cyclotron is to a large extent unknown. The particles are injected into the cyclotron from the slit of the ion source chimney when the electric field applied to the puller penetrates into the aperture and extracts the particles from the plasma. As it has been described in subsection 2.2.3, the slit size is 6x0.2 mm^2 with a 0.1 mm thickness to improve the penetration of the electrical field for the extraction of the particles. In addition, there is a plasma expansion gap of 0.2 mm between the arc column and the extraction slit to facilitate the production of the H^-. In the absence of dedicated studies about plasma extraction for the AMIT internal ion source, randomize distributions are considered. Future research can take into account the implementation of any simulation code to reproduce the ion beam distribution inside the plasma, but this is out of the scope of this dissertation. Therefore, to overcome the uncertainty associated with the unavailability of plasma simulations and the lack of knowledge of the initial conditions, Gaussian particle distributions have been considered over the entire volume since the plasma column to the boundary of the slit, covering the whole possible range of the injection zone.

The distribution is described in the local reference frame, that is to say, is defined by the six phase space variables of the bunch. At the beginning of the simulation OPAL transforms the distribution to the global Cartesian coordinates of the cyclotron by the equations (3.9) and (3.10). Therefore, the initial distribution is referenced to the local Cartesian coordinate system along the width, $\tilde{x}$, depth, $\tilde{y}$, and height, $\tilde{z}$, of the slit, as it is exposed in Figure 3.8. The distribution is generated in MATLAB from randomize normal distribution. It is uniform along the $\tilde{x}\tilde{z}$ plane of the slit, whereas the distribution of particles is centered in the plasma arc column and it is interrupted for deeps inside the plasma, that is to say, is emitted from the surface of the plasma column. For instance, Figure 3.9 shows a particle distribution along the different directions of the slit. In addition, Figure 3.10 illustrates the location of such distribution in the ion source geometry for a further clarification.

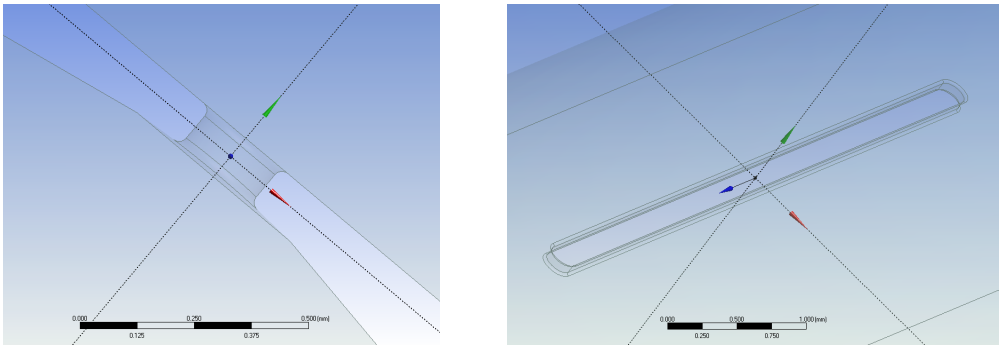

(a) (b)

Figure 3.8: *Local Cartesian coordinate frame for the initial particle distribution in the slit of the ion source along the width, $\tilde{x}$ (red axis), depth, $\tilde{y}$ (green axis), and height, $\tilde{z}$ (blue axis).*

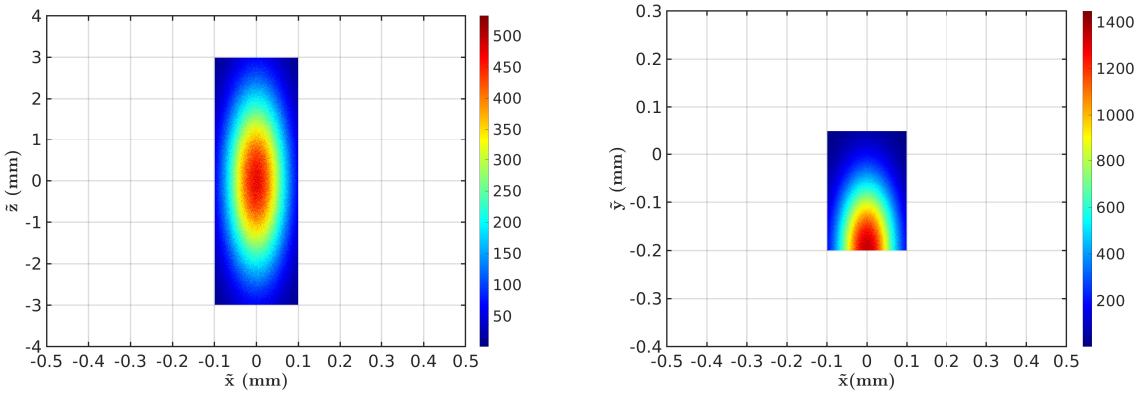

(a) (b)

Figure 3.9: *Particle distribution in the slit in the $\tilde{x}\tilde{z}$ and $\tilde{x}\tilde{y}$ cross section. $\tilde{x}\tilde{z}$ represent the plane of the slit opening, and $\tilde{x}\tilde{y}$ is the plane in depth.*

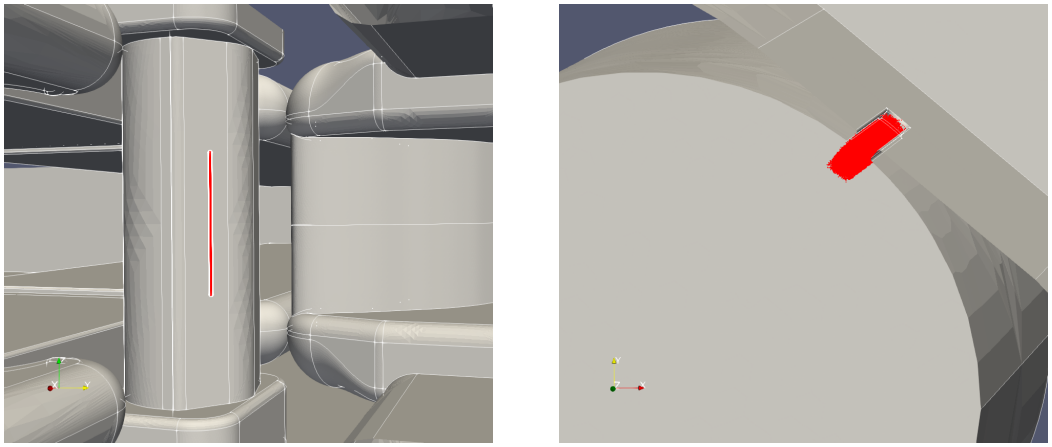

(a) (b)

Figure 3.10: *Particle distribution in the slit represented superposed with the geometry.*

In addition to the spatial distribution, the initial particle distribution includes a momentum distribution. This is calculated from a Gaussian distribution for a corresponding energy of 5 eV [173], the expected energy of the H^- ions at the edge of the plasma column. The momentum distribution is included for completeness, but it is not relevant in the final results because the uncertainty regarding the initial energy is very low in comparison with the gain in the first steps of acceleration.

Particle tracking

OPAL input file contains all the parameters to describe the framework of the simulation. It has to include the control statements, the beam line including all the physical elements considered, the initial beam definition and the field solver commands among others. All the external files have to be appropriated called in the input file with the pertinent command. In addition, different type of variables can be created to be used in different parameters. A template of the

OPAL input file for AMIT cyclotron is shown at the end of this section. The simulation to fully describe the AMIT cyclotron is performed with two main elements: `CYCLOTRON` and `STRIPPER`, in addition to the inclusion of the `GEOMETRY` command. The input file is executed through a *bash* script, that also includes a first post-processing of the output files. AMIT OPAL simulations have been mainly run in parallel environment, exploiting most of High Performance Computing (HPC) resources provided by CETA-CIEMAT[1] for the development of the thesis.

The parameters for the particle-in-cell (PIC) simulations were chosen in order to perform reliable accelerator simulations balancing the run time needed. The time step in OPAL-CYCL is set by the steps per revolution period (`STEPSPERTURN`) and the beam frequency parameter (`BFREQ`). Subsequently, it fixes the spatial step according to the energy of the beam through the relativistic factor: $ds = dt \cdot \beta \cdot c$. Thus, the AMIT simulations have been performed with $10^5 - 10^6$ number of particles with 100 steps per turn, establishing a time step of ~ 0.17 ns. The `FIELDSOLVER` was not considered in the main beam dynamics study due to some code issues related to the solver with negative beams. However, it will be included in future studies to evaluated the space charge effects in the performance of the cyclotron.

OPAL writes out several output files according to the tracking mode. The phase space data and some interesting parameters, like RMS envelope size, external fields or energy are stored in the H5hut file-format. The phase space data of the central particle (considered as reference particle) and an off-centering particle are stored in an *ASCII* file. A third type of output file is used to log the statistical properties of the beam in the *ASCII* variant of the SDDS format [174]. In addition, some elements give an extra output file in the HDF5 or *ASCII* format to record the particles removed when some conditions are satisfied. For instance, `CYCLOTRON` element saves particles out of the considered limits, `STRIPPER` element records the particle hitting on it and particles are recorded when they cross the boundary defined by `GEOMETRY`. The frequency of the data output can be set using the different options of `OPTION` statement in the input file. The output files are post-processed and analyzed in devoted MATLAB scripts developed in the scope of this thesis.

[1]This work was partially supported by the computing facilities of Extremadura Research Centre for Advanced Technologies (CETA-CIEMAT), funded by the European Regional Development Fund (ERDF). CETA-CIEMAT belongs to CIEMAT and the Government of Spain.

```
Title,string="AMIT_cyclotron";

Option, VERSION         = 20400;
Option, PSDUMPFREQ      = 1;
Option, STATDUMPFREQ    = 1;
Option, SPTDUMPFREQ     = 1;
Option, BOUNDPDESTROYFQ = 1;
Option, ENABLEHDF5      = TRUE;
Option, ASCIIDUMP       = TRUE;
Option, TELL            = TRUE;

REAL nstep  = 100;
REAL turns  = 100;
REAL Edes   = 5*1E-9;
REAL R0     = 8.323315536567458;
REAL phi0   = -34.025870750692341;
REAL freq   = 60.134;
REAL ph     = 300*DEGRAD;

REAL an_st      = 255*DEGRAD;
REAL rstart_st  = 108;
REAL rend_st    = 108+8.5;

REAL gamma = (Edes+HMMASS)/HMMASS;
REAL beta  = sqrt(1-(1/gamma^2));
REAL P0    = gamma*beta*HMMASS;

INF_GEOM: GEOMETRY, FGEOM="Geometry.h5", XYZSCALE=0.001;

AMIT: CYCLOTROM,
      TYPE="BANDRF", CYHARMON=1, GEOMETRY=INF_GEOM,
      RINIT=R0, PHIINIT=phi0, ZINIT=0.0,
      MAXZ=+6, MINZ=-6, MINR=0, MAXR=650,
      FMAPFN="MagneticFieldInputFile.dat", BSCALE=1.0, SYMMETRY=1,
      RFPHI=TABLE(2,ph), RFFREQ=TABLE(2,freq),
      ESCALE=TABLE(2,1E-6), SUPERPOSE=FALSE,
      RFMAPFN={"ElectricField1.h5part","ElectricField2.h5part"};

SF: STRIPPER,
    XSTART=rstart_st*cos(an_st), XEND=rend_st*cos(an_st),
    YSTART=rstart_st*sin(an_st), YEND=rend_st*sin(an_st),
    OPCHARE=+1, OPMASS=PMASS, STOP=TRUE;

C1: Line = (AMIT,SF);

Dist1: DISTRIBUTION,
       TYPE=FROMFILE, SCALABLE=TRUE, SBIN=10,
       FNAME="InitialParticleDistribution.dat";

FS: FIELDSOLVER,
    FSTYPE=NONE,
    MX=16, MY=16, MT=16,
    PARFFTX=TRUE, PARFFTY=TRUE, PARFFTT=TRUE,
    BCFFTX=OPEN, BCFFTY=OPEN, BCFFTT=OPEN,
    BBOXINCR=2.0,;

beam1: BEAM,
       PARTICLE=HMINUS, MASS=HMMASS, CHARGE=-1,
       BFREQ=freq, PC=P0, NPART=1E6, BCURRENT=10e-6;

SELECT, LINE=C1;

TRACK, LINE=C1,
       BEAM=beam1, TIMEINTEGRATOR="RK-4",
       MAXSTEPS=nstep*turns, STEPSPERTURN=nstep;

RUN, METHOD="CYCLOTRON-T", BEAM=beam1, FIELDSOLVER=FS,
     DISTRIBUTION=Dist1, BOUNDARYGEOMETRY=INF_GEOM;

ENDTRACK;
Stop;
```

The world is full of obvious things which
nobody by any chance ever observes
— Arthur Conan Doyle

Chapter 4

Ion source characterization

In the previous chapters an introduction of the radioisotope production for nuclear imaging techniques based on the use of accelerators has been presented. A detailed description of the general concepts about the performance of cyclotron accelerators is included. In addition, an overview of the AMIT project describing all the subsystems and the presentation of the beam dynamics code OPAL have encompassed the framework in which this dissertation is developed.

In this chapter the experimental characterization of the ion source of the AMIT cyclotron is discussed. It constitutes a relevant issue within the project because an in-depth knowledge of the beam production process allows to ascertain a relevant part of the final performance of the accelerator. The use of an internal source introduces some uncertainties related to the beam initial conditions in the cyclotron injection. Furthermore, the ion source allows a thorough control of the plasma conditions and, consequently, the optimum radioisotope production. Therefore, the ion production that must be carefully studied.

The high magnetic field in the cyclotron result in a space limitations within the central region, restricting the use of beam diagnostics for an in-depth ion source characterization. For this reason, a parallel commissioning of the ion source has been performed in a facility specifically designed for this purpose. The main objectives are the validation of the ion source design, the characterization of its starting behavior and the analysis of the associated phenomena with the plasma particle extraction as well as the optimum operational conditions to be employed in the cyclotron. Hence, it becomes one of the main objectives of this thesis. It has to be commented that the experimental measurement campaign has been carried out with the collaboration of several people from the Particle Accelerator Unit at CIEMAT.

4.1 Experimental setup

In order to characterize and optimize the ion source of the AMIT cyclotron, a dedicated test facility has been designed, constructed and commissioned at CIEMAT [128]. The objectives of the IST facility are to validate the design of the ion source and verify its operation, performing experimental measurements to determine the optimal operating conditions of the ion source, as well as the characterization of the resultant beam. The measurements are taken with beam diagnostics focused on electrical measurements of the extracted beam, depending on the operational parameters of the source, the geometry of the system and the extraction conditions. During the operation, the arc current, the arc voltage, the gas flow, the vacuum pressure, the magnetic field and the extraction voltage are monitored and recorded. All these parameters influence on the internal performance of the ion source as well as on the extracted beam.

The Ion Source Test bench (IST) consists of a mechanical structure that holds a vacuum chamber where the ion source is introduced (Figure 4.1). The chamber is designed to be introduced between the magnet poles. The ion source has been previously described in subsection 2.2.3. The particles are produced by an electric discharge applied by the Ion Source Power Supply (ISPS) to the cathodes of the source, generating a plasma by electron emission and ion production from the hydrogen gas. The plasma is confined by the external orthogonal magnetic field. An electrical shielded box is installed inside the vacuum chamber with a devoted puller mechanism. A positive DC high voltage is applied to the box through the high-voltage system to extract the negative particles from the ion source, which is grounded. This high-voltage system allows the validation of the ion source with a technically simple facility. The electrical box shields the electric field like a Faraday cage and therefore the trajectories of negative ions inside are unaffected by any accelerating field. The gas handling system controls the flow rate of hydrogen into the source in a

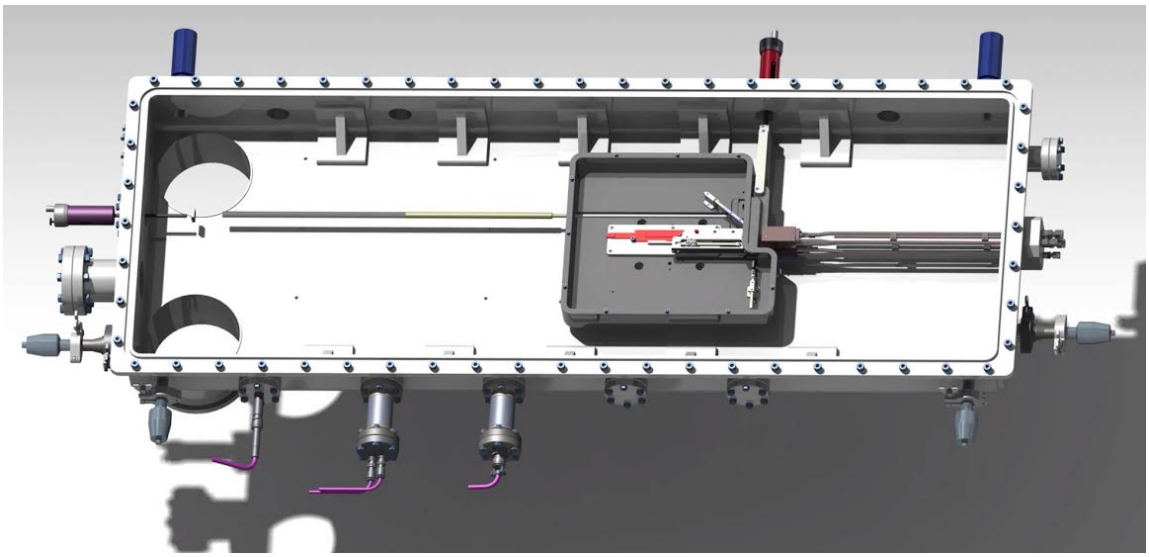

Figure 4.1: *Vacuum chamber of the Ion Source Test bench including the main components: the ion source that is longitudinally introduced, the electric shield box with the puller as well as beam diagnostics.*

range of 0 to 10 sccm. To achieve a low level of stripping losses as well as a rapid pumping speed, the vacuum system uses two diffusion pumps and one rotary vane vacuum pump. A schematic overview of the ion production in the facility is shown in Figure 4.2.

A warm dipole magnet produces the magnetic field necessary to generate the operating conditions of the source as well as to bend the beam out the ion source. The IST magnet (Figure 4.3) is a dipole with a cylindrical pole and copper coils built by ANTEC MAGNETS [175]. The electromagnetic design and calculation of the magnetic field was performed with OPERA [168]

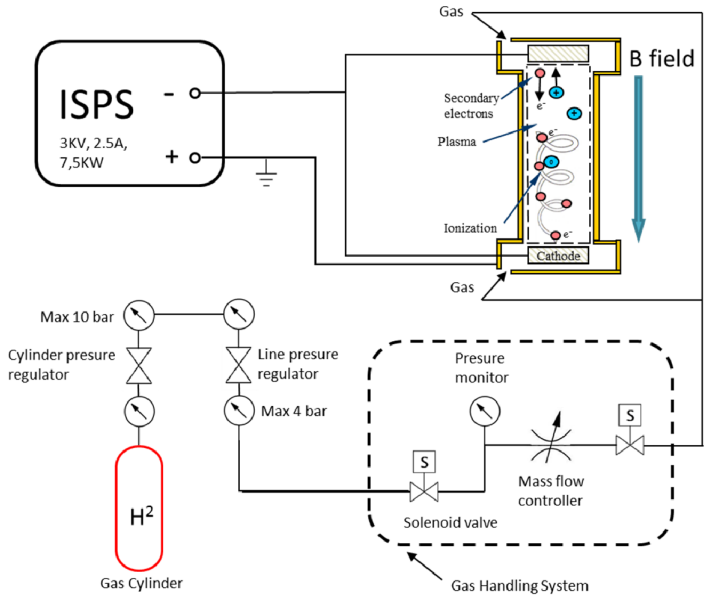

Figure 4.2: *Diagram of ion source operation at the IST.*

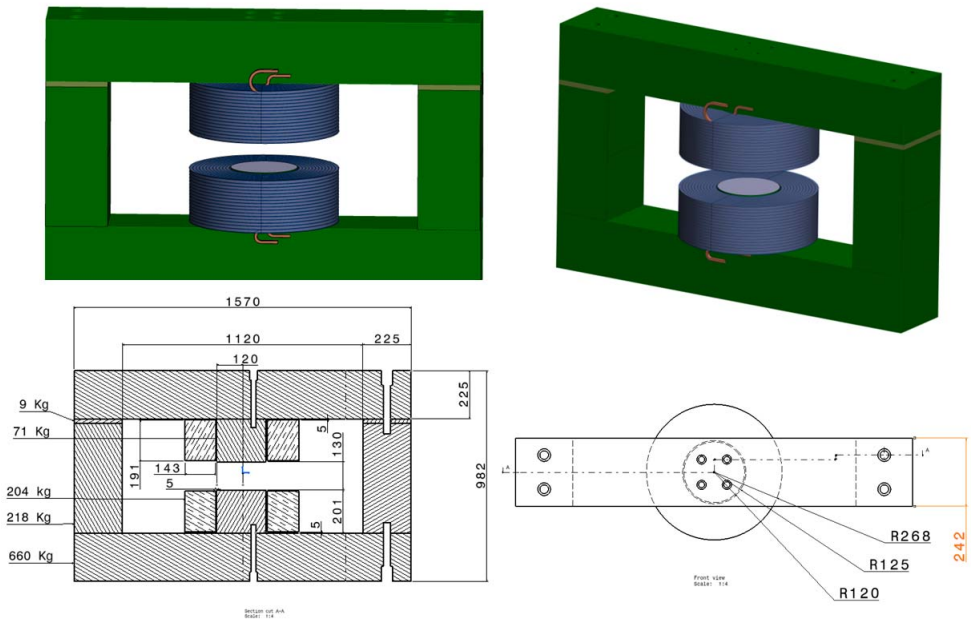

Figure 4.3: *IST magnet layout and main dimensions.*

(Figure 4.4). The magnet provides a maximum field of 0.86 T in a good field region of 150 mm of radius and 40 mm of vertical aperture. The magnetic field can be tuned by the applied current to the magnet coils, providing an adjustable feature (Figure 4.5). Hence, the trajectory of the beam can be modified during the operation for a proper characterization. The final assembly of the IST is displayed in Figure 4.6, showing the magnet and the mechanical structure supporting the vacuum chamber.

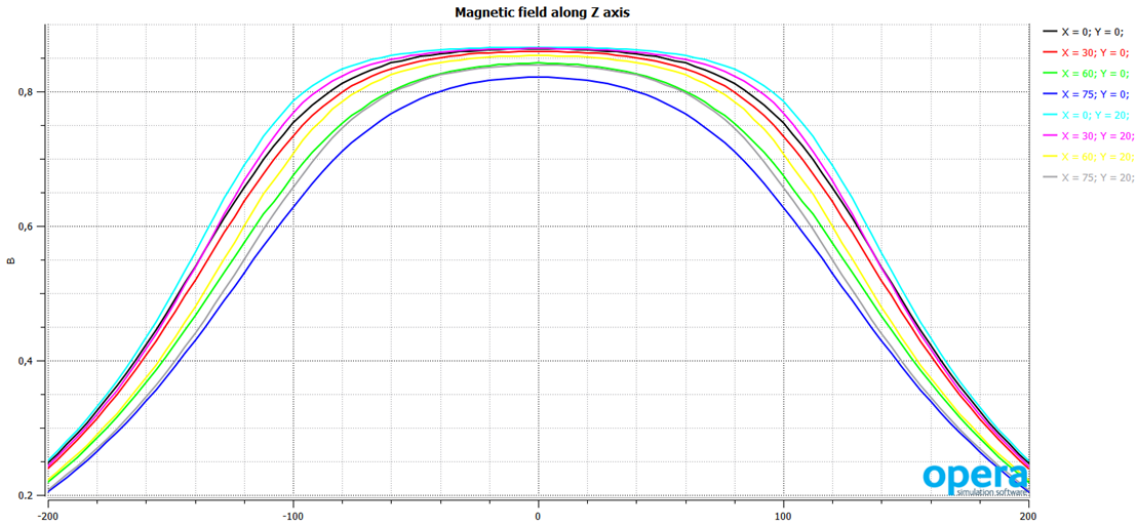

Figure 4.4: *IST dipole magnetic field profile, calculated with* OPERA*, along z direction in different positions of the middle plane.*

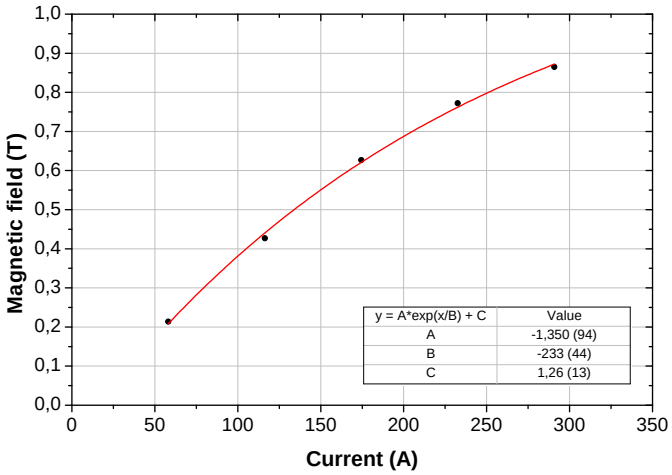

Figure 4.5: *Vertical magnetic field at the magnet center as a function of the coil current. Dots have been calculated from* OPERA *simulations and fitted through a growth exponential function.*

The IST facility includes several interceptive beam diagnostics for an optimum characterization. On the one hand, the total beam current generated is measured with some beam probes which can be located at three different positions, two of them with a fixed structure and the third with a movable system by a piezoelectric motor to provide variable measurements. On the other

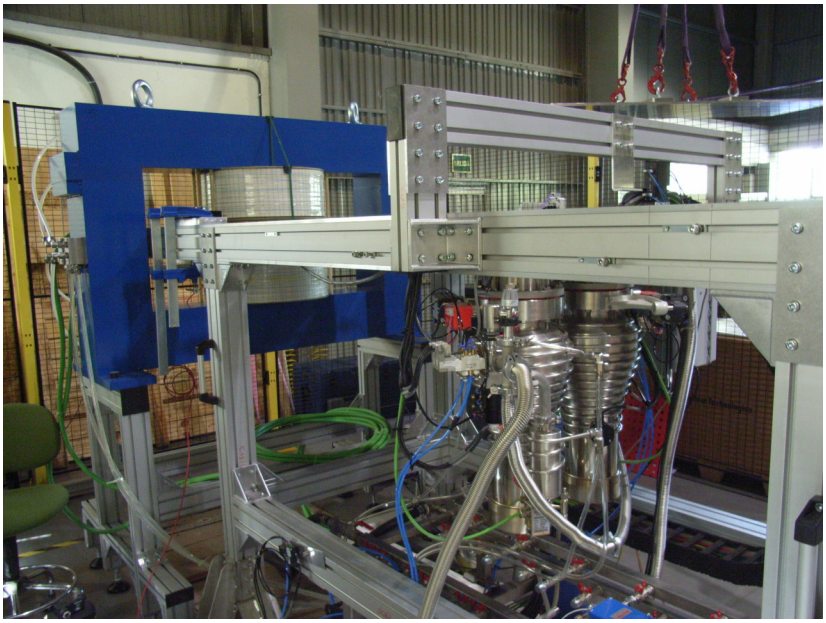

Figure 4.6: *Picture of the IST showing the magnet and the mechanical structure supporting the vacuum chamber and other subsystem as vacuum pumps and the water cooling system.*

hand, the transverse beam profile can be measured through a Al_2O_3 fluorescent screen [148]. A schematic top view of these intercepting beam diagnostic inside the shielding box is illustrated in Figure 4.7, where the ion source is also shown, placed in front of the puller.

The versatility of the IST facility has additionally allowed to test and verify some other subsystem of the AMIT cyclotron beyond the ion source. The vacuum system, the beam diagnostics, the water cooling system and the operational control system among other minor elements have been tried and tested. Additionally, the facility design and assembly has provided remarkable experience which will be very useful for the cyclotron commissioning and operation.

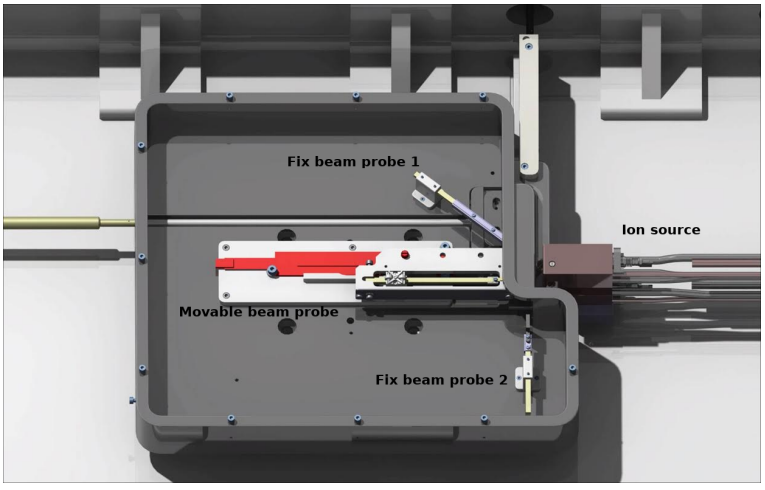

Figure 4.7: *Detailed top view of the electric shield box with the beam diagnostics.*

4.2 Ion source experimental operation

The characterization of the ion source in the IST was performed along some experimental campaigns. Numerous measurements was taken, considering all possible variations of the control parameters. This section collects those results that are relevant for illustrating the physical behavior of the ion source related to the ion source performance and the extracted beam.

4.2.1 Ion source performance

The operation of a cold cathode PIG ion source requires the alignment of the hollow anode of the ion source in a magnetic field between two cathodes, where the neutral gas is supplied. When the cathodes, which are connected at the same negative potential with respect to the anode, receive an increase of the voltage, the ion production begins by the thermionic electron emission. Electrons from the cathode are accelerated by the potential difference between the cathode and the anode. Their movement is along expanding helical orbit crossing the hollow anode and proceed toward the opposite cathode due to the axial magnetic force. The gas injected is ionized, generating a plasma which is confined by the magnetic field. Then, the internal resistance of the plasma decreases and the arc voltage drops. The cathodes are self-heated by high energetic ionic bombardment, that it is supplied by the thermionic emission. The standard behavior of the source in this stage is described by the decrease of the arc voltage while the arc current is increased (Figure 4.8(a)).

The experimental characteristic curves of the ion source during the operation are determined by the plasma properties. The plasma resistivity [176] is defined as:

$$\eta = \frac{m_e \nu_e}{e^2\, n_e} \tag{4.1}$$

where m_e is the electron mass, n_e is the electron density and ν_e is the Maxwellian-averaged electron-ion collision frequency of binary collisions that depends on ion density and temperature. The plasma inside of the ion source can be considered as an equivalent electric circuit. Thus, as a first approximation, the arc voltage and current are related with the resistance according to Ohm's law, and therefore with the resistivity and the internal geometry of the chimney. For a constant arc current, the voltage changes as the gas load changes (Figure 4.8(b)). As the initial flow rate increases, more atoms or molecules are available for plasma production and the resistance decreases, causing a slight decline of the arc voltage. As the gas flow raise further, the drift velocity of the charged particles is reduced, the electron collision frequency increases and the plasma resistance increases. Furthermore, modifications in the plasma density produce variations in the ionization probability as well as in the probability of recombination for charged particles due to the adjustment of electron mean free path. Thus, these two effect affecting to the plasma resistivity compete with each other while the gas flow rate changes.

The magnetic field is other magnitude to consider because it modifies the movement of the charged particles in the plasma and consequently, it affects to the averaged electron-ion collision frequency. However, the volume of the plasma is small and the internal pressure is high, so

the influence of the magnetic field is of less relevance and the plasma conditions remain almost unchanged against variations of the magnetic field as long as it reaches certain value that evince the stability of the plasma (Figure 4.8(c)).

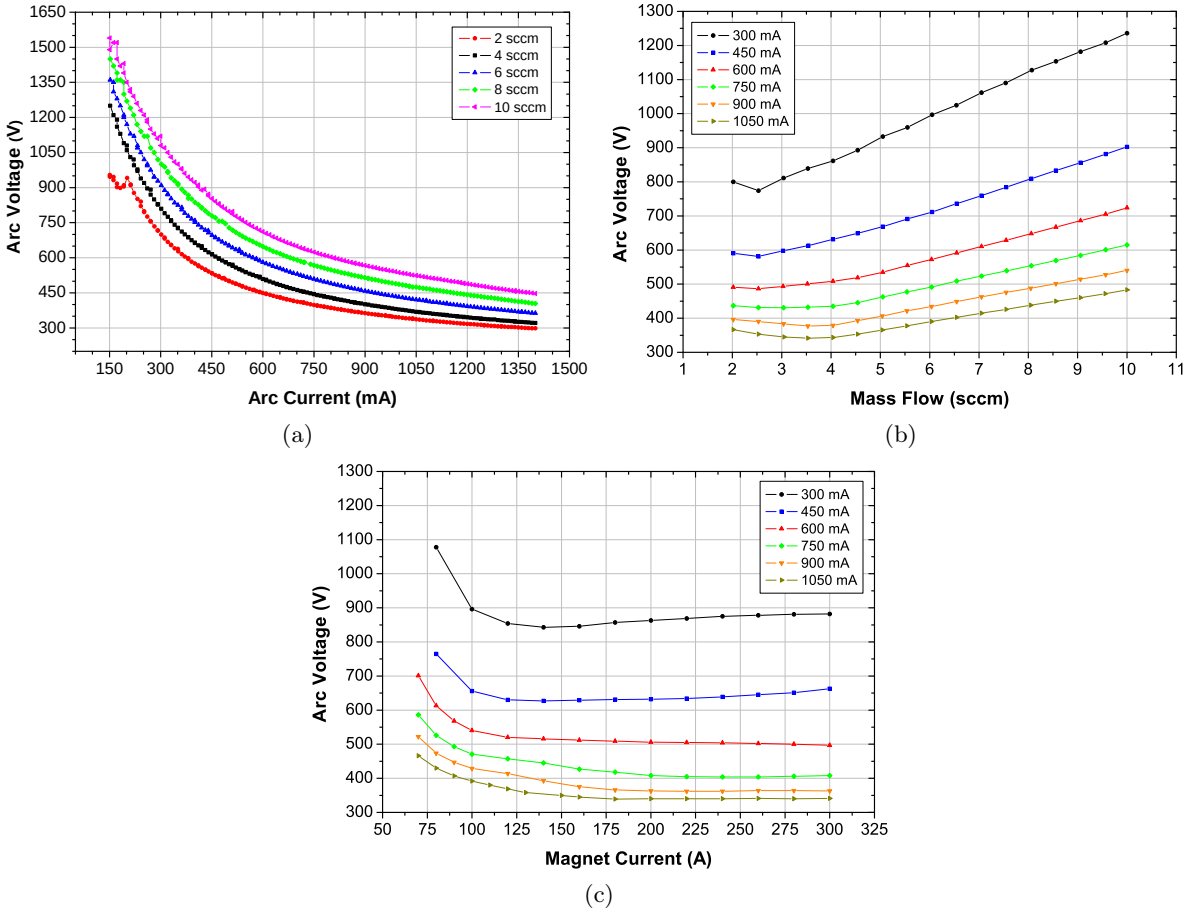

Figure 4.8: *Characterization of the ion source performance. (a) Arc voltage in front of the arc current for different gas flow. (b) Arc power as a function of the gas flow at different arc currents. This measurement is taken with a magnetic field of* $\sim 0.5\ T$ *(*$I_{coil} = 135\ A$*). Arc power as a function of magnet coil current at different arc current (c) (4 sccm of gas flow rate).*

4.2.2 Beam extraction measurements

Once described how the plasma is obtained in thermionic mode, the extraction of the particles from the plasma is going to be analyzed. The produced beam is directly related to plasma status and the extraction conditions, specifically the electric field that depends on the applied voltage and the puller-ion source distance. The plasma expands through the drift region, free of external fields, before the ions are extracted. This is to allow the plasma density to fall to a value at which ions can be extracted. The plasma is formed at the positive source potential and the ions are accelerated by a negative extraction electrode, which is polarized positive with respect to the plasma electrode. The electric potential penetrates through the chimney aperture, extracting

negative charged particles from the plasma. The electrons are bent by the magnetic field with small radii, due to their tiny mass (see equation (1.2)), and they collide outside of the source. H^- ions are transported by the electric field from the source into the electric shield box.

Beam perveance

The extracted current from a charged particle source has two different regimes as a function of the extraction voltage. The first is the so-called space-charge (SC) limited emission regime. In the SC-regime the electron beam emission is limited by the beam itself. This leads to reduced emission of the cathode because the space charge of the particles already emitted compensates the extraction field, making it impossible to extract a higher current density. The maximum current density, J, can be calculated by the Child-Langmuir law [132, 133]:

$$J = \frac{4\sqrt{2}}{9}\,\varepsilon_0 \sqrt{\frac{q}{m}}\,\frac{V^{3/2}}{d^2} \tag{4.2}$$

applied to parallel plates surfaces, where V is the applied extraction potential and d is the separation between the extractor and the emission surface.

However, the emitted current for a certain applied extraction potential depends on the puller geometry, which governs the electric field strength and distribution. The penetrating electric field through the slit is repelled by the plasma sheath potential, so an equipotential curved boundary, called plasma meniscus, is formed. The plasma meniscus is highly influential on the extraction conditions. Particles that cross the meniscus see the extraction field and constitute a beam. Meniscus shape introduces a first order correction to equation (4.2) for curved surfaces in terms of the total curvature of the emitting layer, ρ_0 [177]:

$$J = \frac{4\sqrt{2}}{9}\,\varepsilon_0 \sqrt{\frac{q}{m}}\,\frac{V^{3/2}}{d^2}\left(1 + \frac{4}{5}\,d\,\rho_0\right) \tag{4.3}$$

In case of emission from a concave surface with radius of curvature R, the density current is [177, 178]:

$$J = \frac{4\sqrt{2}}{9}\,\varepsilon_0 \sqrt{\frac{q}{m}}\,\frac{V^{3/2}}{d^2}\left(1 - \frac{8}{5}\,\frac{d}{R}\right) \tag{4.4}$$

The total beam current extracted, I, is found by multiplying the current density by the area of the emission aperture:

$$I = \frac{4\sqrt{2}}{9}\,\varepsilon_0 \sqrt{\frac{e}{m_u}} \cdot S \sqrt{\frac{Z}{A}}\,\frac{V^{3/2}}{d^2}\left(1 - \frac{8}{5}\,\frac{d}{R}\right) \tag{4.5}$$

where S is the emission area, Z is the ion charge and A is the atomic weight in amu.

The ratio between current and extraction voltage is called the beam perveance:

$$P = \frac{I}{V^{3/2}} \tag{4.6}$$

It is the proportionality constant that describes the system. For a specific charged particle, the perveance only depends on the geometry. As long as the emission is space-charge-limited, the perveance is roughly constant. When the voltage is further increased and the beam emission is

no longer space-charge-limited, the beam perveance decreases. Perveance refers to the strength or ability of the plasma to deliver ions.

As extraction voltage is increased, the extracted current density saturates due to the emission limit of the plasma. Then, the ion source starts to emit in the production-limited emission according to the thermionic regime, which is the heat-induced flow of charge carriers from a surface or over a potential-energy barrier.

Beam current measurements

The H^- beam current produced by AMIT ion source has been measured at IST as a function of different DC extraction voltages. The high voltage of the puller is restricted to reduce HV breakdown phenomena due to the excessive spark occurring in the space between the extractor and the ion source. To diminish this effect, a resistor was placed between the high voltage power supply and the extractor. Therefore, all measurements are referenced with respect to the effective voltage in the electric shield box. The current is measured at the entrance of the electric shield box with the fixed beam probe 1 (see Figure 4.7) to minimize possible beam losses. The results (Figure 4.9) manifest the transition in the operating regime of ion production: Firstly the space-charge limited emission is dominant and above a certain extraction voltage the current extracted from the plasma is limited by the production emission and it increases slowly for higher voltages with an approximate slope of $10-45$ μA/kV according to plasma properties.

It has to be pointed out that these measurements have been taken through a voltage ramp increase of 100 V/s monitored by the control system. In addition, the beam current data has a fluctuation of around 10 μA. This is caused by instabilities in the beam and by the accuracy of the measurement itself. The plotted results do not show the error bars with the uncertainty to clarify the presentation, but this value must be taken into consideration.

These results allow to verify the performance of the ion source and the extraction of the particles, however, they are not valid to determine the current that can be injected in the cyclotron, because the voltage conditions are totally different.

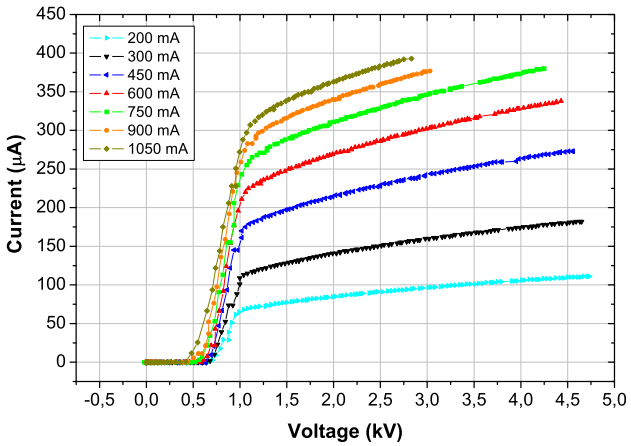

Figure 4.9: *Beam current measurement in front of extraction voltage for different arc current with a fixed gas of* 4 *sccm an magnetic field of* ~ 0.5 *T* ($I_{coil} = 135$ *A*).

The beam current extracted from the ion source can be increased by modifying on the plasma density conditions through the arc discharge current and the gas flow rate (Figure 4.10). These measurements shown how the high interrelation between the different magnitudes plays a fundamental role in the optimization of the ion source, allowing the tuning of the beam extracted current through different control parameters of the ion source.

The dependence between the extracted beam current of H^- with respect to the gas flow rate and the arc current comes from the particle interaction reactions in the plasma. As the gas load increases, a greater number of ionization occurs for a given arc current, but electrons with adequate energy for production are limited and the high pressure inside the chimney decreases the survival of H^- ions. In addition, other processes such as insufficient supply of gas molecules, the increase percentage of neutral particle that is positively ionized, the excess supply of electrons with destructive energy and the neutralization rate must be taken into account. Therefore, the ion source operational parameters to obtain a specific beam current under different extraction conditions have great interdependence and must be carefully analyzed. Although the same behavioral trend always occurs, the values of the control parameters do not produce exactly the same results.

The final objective of the characterization is focused on providing enough current to be injected into the cyclotron to fulfill the beam requirements at the target for an optimum radioisotope production. Therefore, the ion source parameters influence must be perfectly characterized to satisfy an adequate beam current injection during the cyclotron operation. The results presented in Figure 4.10 show how the modification of the arc current provides almost the same beam current for different gas flows until the arc current increases to a certain value, from which the obtained beam current has a particular evolution according to the considered gas flow. On the other hand, the variation of the gas flow rate at fixed arc current (Figure 4.11) provides a quickly increase of the beam current until a value around 4 sccm, which saturate the balance between ion production-destruction reactions. Thus, this gas load value seems to be optimum

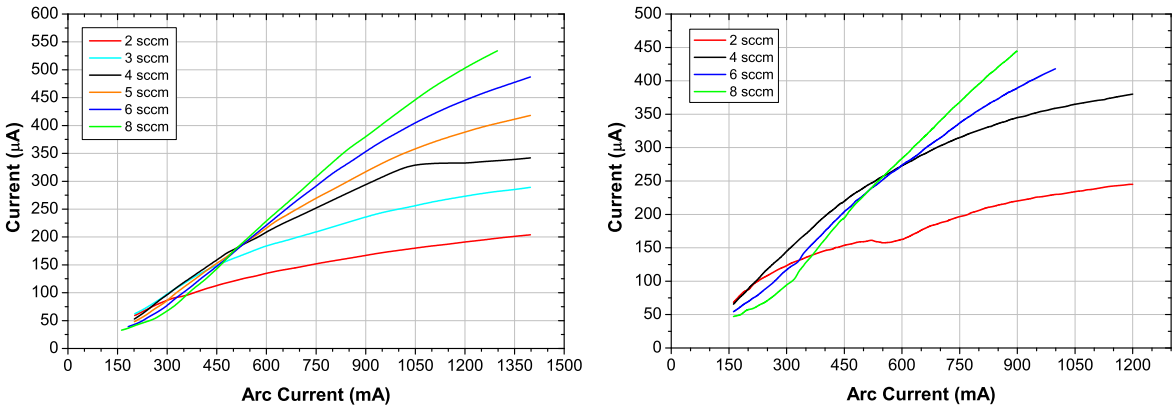

(a) (b)

Figure 4.10: *Beam current measurement as a function of arc discharge current for different gas flow rate with a effective extraction voltage of* 1.5 *kV (a) and* 2.5 *kV (b).*

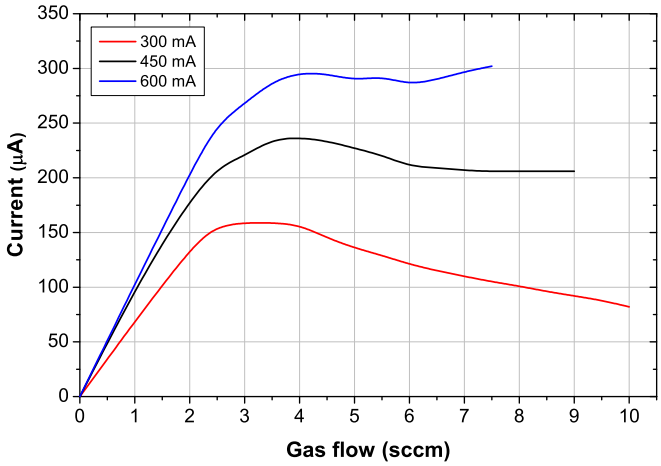

Figure 4.11: *Beam current measurement as a function of the gas flow rate for different arc current at* 2.5 *kV effective extraction voltage.*

for the ion source operation.

It is also important to consider that there are other factors that influence the production of H^- beam, although with less relevance, such as the magnetic field, the vacuum chamber pressure, the extraction gap distance, the chimney-puller alignment, the internal geometry of the chimney, the cathode lifetime... Those factors can provoke the non-repeatability of the factor values during the measurements, that is to say, the ion source parameters and the beam current do not present exactly the same values, even though the trend of these magnitudes remains unaltered. However, their influence on the final outcomes is limited by the carefully systematic method of measurements employed during the experiments. Thus, all results are affected in the same way by these secondary phenomena.

The measurements performed at the IST provide sufficient knowledge to establish a procedure for ion source operation. First, the designed ion source have been validated for its deployment in the cyclotron. Secondly, the most important ion source control parameters have been established as optimum considering the achievable beam current, minimizing the arc current and the gas flow rate. Hence, the arc current and the gas load must be controlled to improve the lifetime of the internal components as well as to enhance the vacuum level. Furthermore, the experimental operation has given information to optimize the ion source design at a mechanical level, as well as to correct certain defects identified in the facility. In addition, the experimental measurements have provided a high relevant experience to the group for the commissioning of the cyclotron as well as to its final operation. Last by not the least, the experimental results are in agreement with other experimental measurements for Penning ion source in similar test facilities [173, 179–182], despite the difference in the dimensions of the source or in the particular facility design between each one.

Cathode lifetime influence

The cathode lifetime is one of the main factors determining the total operating life of the ion source. Their deterioration is of great relevance in the operation of the cyclotron, since it affects the availability of the machine for radioisotope production and increases the cost associated with the replaceable material. The experimental test at the IST has provided meaningful information about this issue. After many hours of ion source operation, the time needed by the ion source to reach the thermionic mode was increased, denoting a wear of the cathodes. When the material wear was extremely high, the ion source could not be turned on. The removal and replacement of the cathodes revealed an important erosion of the surface, with a misalignment of one of them (Figure 4.12). The sputtering of the cathodes by ions from the discharge produces a crater-shaped erosion profile. The lifetime at the moment of the replacement was 23.57 A·h, value that takes into account not only the operational time but also the current support during this time, because the arc discharge current determines the hit of the electrons and the material erosion. The high wear during the tests was produced because the ion source was operated close to the limits of the arc voltage and current supported.

Figure 4.12: AMIT *ion source cathodes after several hours of operation at the IST facility. The erosion of the surface is clearly appreciated.*

The effect of cathode wear has been studied comparing the behavior of the source and the ion production for new cathodes and eroded cathodes (Figure 4.13). The extracted current is affected by the wear of the cathodes, with $\sim 30\%$ more current measured at the beam probe with new cathodes. Therefore, the reduction of the arc current arises as an important factor to decrease the damage of the cathodes, extending the operation time of the source.

Plasma expansion gap study

Another parameter evaluated during the ion source experiments was the relationship between the inner anode wall and the plasma arc column, where the ion production takes place. This geometric parameter influences on the negative hydrogen ions survival, modifying consequently the plasma conditions. In addition, it determines how much the electric field penetrates into

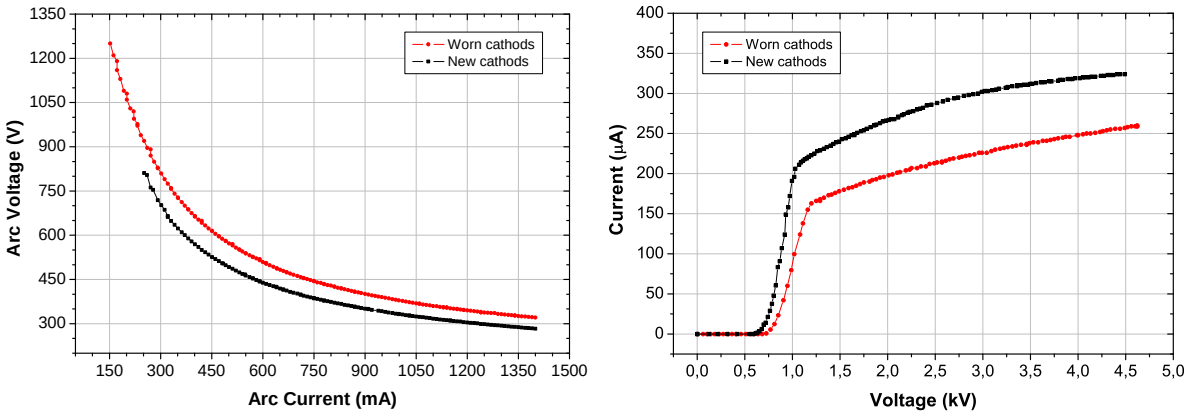

(a) (b)

Figure 4.13: *Ion source characterization (a) and beam current produced (b) with new and worn cathodes for* 4 *sccm of gas flow rate. Beam current has been measured at* 450 *mA of arc current.*

the chimney to extract the ions. Hence, after some theoretical analysis and by similarity with previous studies [179,180], it was decided to manufacture three cylindrical chimneys with different plasma expansion gap distances of 0.2, 0.3 and 0.4 mm between the plasma column and the internal wall of the anode. The chimneys have equal dimension of the anode hole and the same slit size.

Figure 4.14 shows the characterization of the ion source and the produced beam under different chimneys. Although for steady plasma conditions there is an obvious difference in the extracted current (Figure 4.14(b)), the variation of the plasma parameters has a more direct influence on the beam production, observable with measurements at fixed extraction voltage (subfigures 4.14(c)-4.14(d)). In other words, the extracted current varies under changes in the source parameters such as the arc current and the gas flow rate in a non-reproducible way and without a clear trend observed. Therefore, it is difficult to conclude in an optimum plasma expansion gap for the chimney, although a 0.2 mm distance has provided a higher beam current during the measurements. Moreover, with this expansion gap distance, the beam current is slight higher for the established gas flow rate as optimum (4 sccm). A relevant factor in the inconclusive results is the high uncertainty associated with the accuracy of the chimney processing. This is a delicate part of small dimensions, and therefore the fine adjustment between the hole in the anode and the wall of the anode is highly complex from a technical point of view. Furthermore, it was not possible to verify after manufacturing the different distances of the plasma column, increasing the uncertainty about the real difference between the chimneys. Summarizing, the measures with different expansion gap have not been conclusive. Consequently, the comprehension of a real improvement base on that geometry modification depends on future measurements and analysis of the results, having remained outside the scope of this thesis.

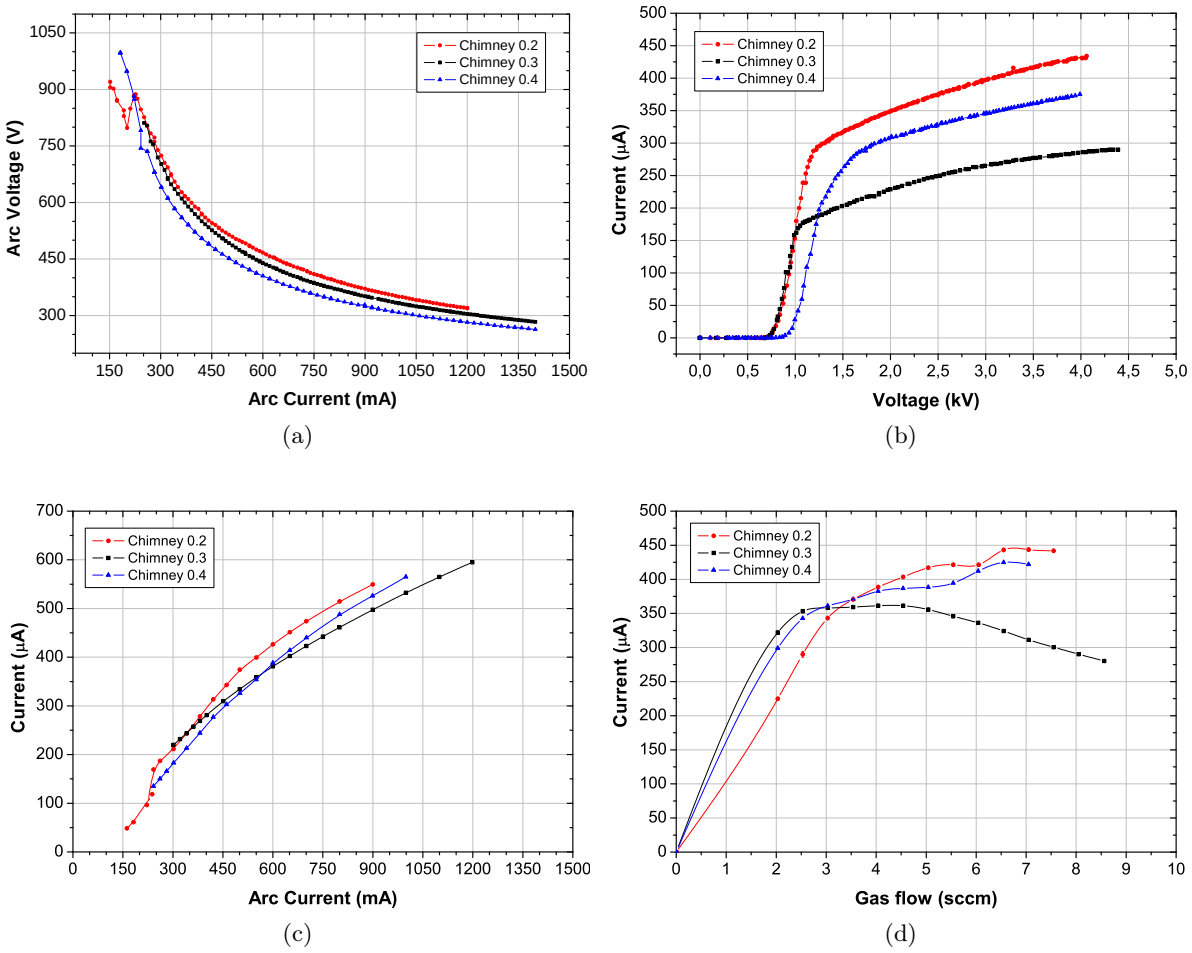

Figure 4.14: *(a) Arc discharge characteristic curve for different expansion gaps (gas flow rate - 4 sccm). (b) Beam current extracted varying extraction voltage (gas flow rate - 6 sccm, arc current - 450 mA). (c) Beam current extracted varying arc voltage (gas flow rate - 6 sccm, extraction voltage - 2.5 kV). (d) Beam current extracted varying gas flow (arc current - 450 mA, extraction voltage - 2.5 kV).*

4.3 Beam profile characterization

In order to characterize the beam profile, the ion source test bench has been simulated with the OPAL code to reproduce the particle extraction from the ion source. Although OPAL is not focused on high voltage DC facilities, it is possible to adapt OPAL-CYCL flavor to DC extraction system removing the electric field variation, by setting the beam frequency negligible for the static fields. The main goal of these simulations is to provide the beam profile to compare with the experimental measurements provided by interceptive beam diagnostics.

OPAL simulations make use of the fields and the geometry from external files. The magnetic field in the median plane is obtained from OPERA calculation and arranged from exponential fit of the nominal data (see Figure 4.5). The electric field in the gap between the ion source and the puller has been calculated with ANSYS [169] (Figure 4.15). Inside the Faraday cage the electric field is canceled. The field calculation has been performed with high accuracy employing

a mesh of 0.4 mm for gap region an a fine mesh region in the slit with 0.025 mm. Initial particle distribution is considered in the slit volume with a momentum associated to 5 eV as an average ion energy. Optionally, the simulation can include the geometry of the system to detect the possible collision with the puller or in some part of the Faraday cage.

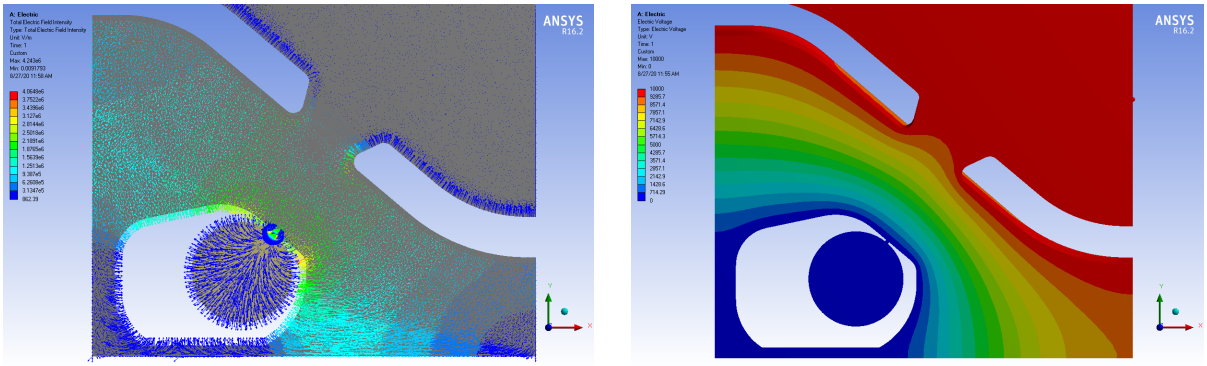

(a) Total electric field intensity (b) Voltage

Figure 4.15: *Electric field (a) and voltage (b) distributions for the IST DC extractor. The intensity of the electric field is represented by colored arrows according to the field magnitude and the voltage color scale is uniformly calibrated from blue to red for voltages between 0 and 10 kV.*

The beam path is determined by the value of the magnetic field and the applied extraction voltage. The magnetic field determines the curvature of the particle trajectories. For non-relativistic beam under uniform magnetic field, without electric field, the trajectory is circular and the radius is given by the field intensity, particles properties (mass, charge) and their velocity, in accordance with equation (1.2):

$$\rho = \frac{mv}{qB} \tag{4.7}$$

The extraction voltage determines the acceleration of particles in a fixed gap. Therefore it fixes the initial velocity of particles at the entrance of the Faraday cage. As a first approximation, for a non-relativistic particle moving in a uniform electric field, the velocity of particles is:

$$qV = \frac{1}{2}mv^2 \longrightarrow v = \sqrt{\frac{2qV}{m}} \Longrightarrow \rho = \frac{1}{B}\sqrt{\frac{2mV}{q}} \tag{4.8}$$

Hence, the radius of the beam can be approximately estimated under a given conditions of voltage and magnetic field. Additionally, multi-particle simulations have been performed to accurately determine the beam path under diverse operating conditions (Figure 4.16) and to fix the beam diagnostics positions for experimental measurements (Figure 4.17).

The beam path is influenced by many variable factors. Apart from magnetic field and extraction voltage, which can be controlled during the operation, other parameters can result in unexpected beam deviations. On the one hand, the position of the vacuum chamber with respect to the magnet defines the origin of coordinates of the magnetic field. As the field distribution decreases with respect to the center of the pole and the region of good uniformity of the magnetic field is limited, a good alignment between the vacuum chamber and the magnet is required. On

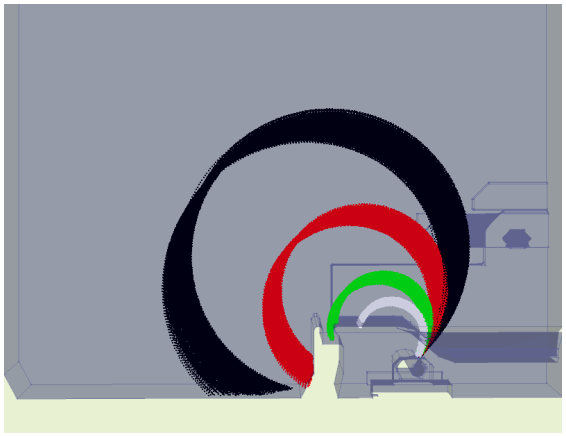

Figure 4.16: *Beam trajectories for different magnetic fields applied at 5 kV of extraction voltage.*

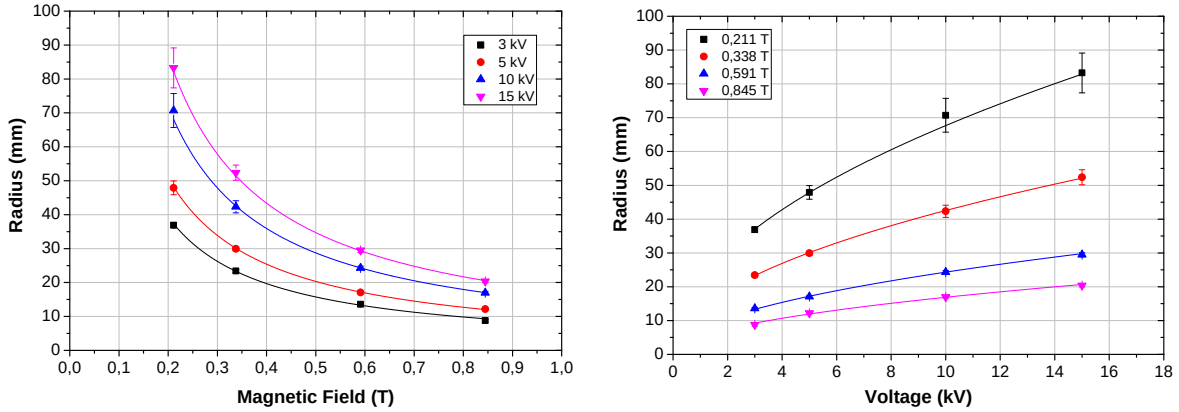

(a) (b)

Figure 4.17: *Beam radius as a function of magnetic field (a) and extraction voltage (b).*

the other hand, the alignment between chimney and puller apertures affects to the beam transmission since the gap between ion source and puller fixes the electric field that accelerates the particles. At the IST facility, the puller position is controlled by a movable structure with two movement directions that can adjust the alignment with precision previously to the operation.

These effects have been evaluated to determine their level of influence on beam dynamics. Small deviations in the beam path have been observed with respect to an ideal orbit under the magnetic field and voltage considered. Moreover, beam axial divergences are observed, causing collisions with geometry at some points outside the puller and the base of the box. The simulations have led to conclude the setting operating criteria that minimize unwanted effects, fixing optimum positions for puller respect of ion source, and the reference positioning of vacuum chamber respect of the magnet.

In addition, a comparison of the beam profile at a given position has been performed using the transverse interceptive beam diagnostic and OPAL simulations. First, from previous simulations of the trajectories, an optimum position has been determined to situate the beam profile monitor diagnostic. The simulations are carried out from a Gaussian distribution of many particles (10^7)

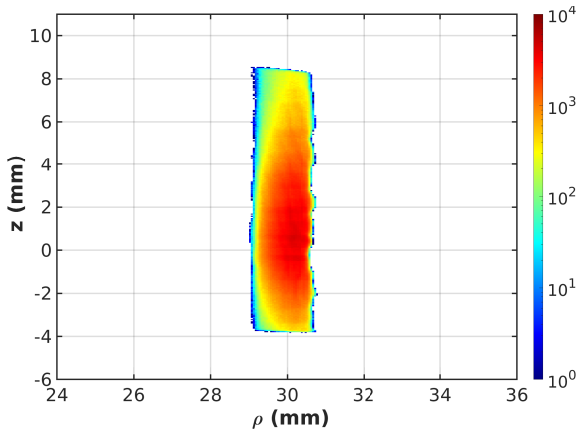

Figure 4.18: *Simulated beam distribution at the profile monitor. The color scale represents the particle density.*

from the aperture of the ion source until an interceptor element that stops the beam. The results provide the beam profile (Figure 4.18). Moreover, the beam size is characterized in ~ 1.7 mm wide (92% confidence level) and 10 mm high (80%). It is clear how the beam is not axially centered because the misalignment of the puller respect of the electric shield box.

Experimental measurements have validated the results of the simulations through a transverse interceptive fluorescent screen of Al_2O_3 recorded in-situ by a live camera during the operation of the source. Furthermore, the device allows to measure the beam size with a 2-millimeter grid printed on it. The experimental measurements were performed at a fixed position of the screen, modifying the magnetic field, and consequently the radius of the orbits, to monitor the transition of the beam on the screen. The results were recorded in video by the camera. Figure 4.19(a) shows a screen capture of the beam profile where the delay shine of the beam produced by fluorescence is appreciated. Nevertheless, the high beam deposition, concentrated in a very small region of space, damage the device during the experiment and an area of the screen was

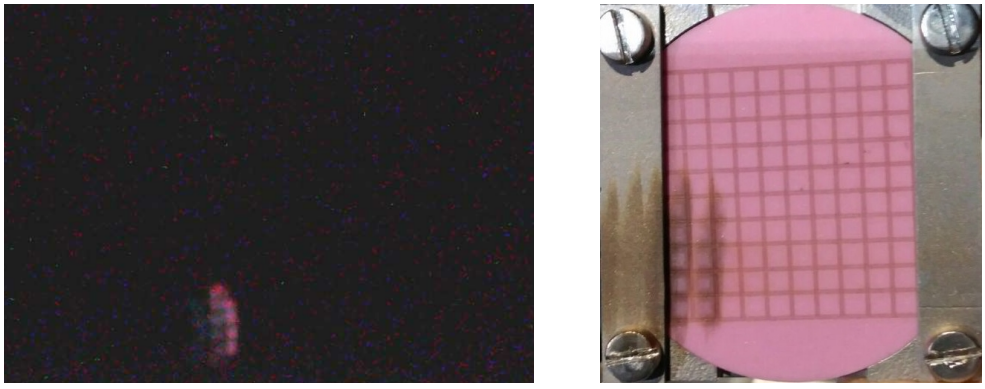

(a) (b)

Figure 4.19: *Experimental measurements of the beam profile. (a) Beam profile live image from the camera. The screen emit visible light of the intercepted beam. (b) The beam interception caused the screen to burn in some areas.*

found to be burned (Figure 4.19(b)). As a conclusion, the experimental results were in good agreement with the simulation outcomes obtained with OPAL within the margins of error.

Everything unknown is taken to be magnificent

— Cornelius Tacitus

Chapter 5

AMIT beam dynamics study

The main goal of AMIT cyclotron is to achieve an optimized radioisotope production devoted to on-site production in non-dedicated facilities. This ambitious purpose requires an exhaustive beam dynamics analysis to correlate all the accelerator subsystems as well as to evaluate their influence in the final beam requirements and optimize the operation of the machine. The beam dynamics of AMIT cyclotron, as it has been exposed in chapter 2, are determined by two main features: the classical weak focusing nature of the cyclotron and the compactness of the accelerator, which are imposed by the ultimate goal of the cyclotron. The primary goal of beam dynamics studies of the AMIT cyclotron is to analyze the motion of the particles through the magnetic and electric fields, with special attention to the central region. Furthermore, the optimum conditions of the accelerator have to be set given the design of the different subsystems and the different physical interactions that can take place. Therefore, the beam dynamics aim to enhance the radioisotope production with a suitable beam quality as well as to minimize the particle losses and consequently the damage and activation of the different components, among other issues.

The beam dynamics studies for AMIT cyclotron are based on simulations performed with OPAL code. The analysis assesses the main effects that directly or indirectly affect the final radioisotope production. For that purpose, two principal figures of merit have been considered, without prejudice to other parameters:

- Final energy. A lower limit of 8.5 MeV is imposed by the production of a single-dose of ^{11}C in a reasonable irradiation time.

- Beam current. The current is directly connected to the radioisotope production, and therefore, it must be optimized along the cyclotron. However, given the uncertainty associated with the current produced by the ion source in the final operational conditions, only the beam transmission factor or relative current can be evaluated during this stage of the project. This factor provides the percentage of particles surviving after completing the whole acceleration process. It is determined by several factors: the central region acceptance, the axial and radial deviations, the total phase excursion, the beam residual interactions, the extraction process and the transmission to the target. With that in mind,

the beam survival rate is chosen as a relevant beam dynamics outcome.

In relation to this last point, the minimization of losses in AMIT cyclotron is directly associated with the number of turns performed by the beam during the acceleration. The particles can be removed from the beam by several causes, decreasing the final beam current as well as raising the damages and the activation of the components. The electron detachment of the negative hydrogen ions can be easily originated by stripping interactions with the residual gas. The interaction probabilities are increased with the traveled distance by the particles through the acceleration. For that reason, the number of turns becomes a significant parameter to evaluate. A dedicated analysis of the beam stripping interactions will be presented in the chapter 6 of this dissertation.

Taking these key points into consideration, the principal results of the AMIT beam dynamics studies performed with the OPAL code are presented in this chapter. Two separated sections describe all the aspects of the beam dynamics:

- Firstly, a global beam dynamics study of the accelerator evaluates the different features of interest. It is based on the design parameters and the outcomes of numerical calculations for the electric and magnetic fields. This overall study characterizes the cyclotron performance with special analysis of different aspects such as radiofrequency, initial beam conditions, beam focusing and extraction system, with the main aim of obtaining a comprehensive understanding of their impact in the final AMIT configuration.

- In a subsequent section the final assembly of the subsystems and their influence on the beam dynamics is evaluated. After presenting the global aspects of the dynamics, it is important to evaluate the impact of the final tolerances of the different subsystems once they have been manufactured and assembled. In particular, the requirements for the output energy and current have been carefully analyzed employing the cyclotron settings obtained from the final assembly. Taking into account the overall previous studies, this section will provide a more realistic estimation of the final operation of the cyclotron regarding the main beam dynamic effects to achieve the ultimate goals of the project.

5.1 AMIT beam dynamics overview

As it has been presented in the chapter 2 of this thesis, the particle acceleration process in AMIT cyclotron starts with the beam injection from the internal ion source. Thereafter, the beam is accelerated by a time varying electric field generated by a radiofrequency cavity on a one 180° dee configuration. The magnetic field originated by the superconducting magnet bends the particle trajectories according to their energy. Once the beam achieves the required energy, it is extracted employing a stripping mechanism. From then on, the resultant proton beam is transported to the target, accomplishing successfully the acceleration process. Given the special relevance of diverse phenomena throughout the acceleration process, the beam dynamics analysis has been structured in three regions to realize an overview of the acceleration process:

- Central region. It includes the beam injection and the first turns.
- Intermediate region. It covers the main path after the first turns until the extraction point, evaluating mainly the synchronism evolution and the beam focusing.
- Beam extraction. The final beam conditions in diverse extraction situations are assessed.

5.1.1 Central region assessment

The central region involves the beam injection and the trajectory during the first turns. It is of decisive relevance on the beam dynamics because it determines the suitable performance of the cyclotron acceleration. For AMIT cyclotron, the central region has been designed and developed to optimize the acceleration during the first gaps, maximizing the phase acceptance with a special geometry of the ion source and the puller, as it has been detailed in section 2.2.4.

Central region phase acceptance

The injection of the particles into the cyclotron occurs through the electric field which originates a force to remove the ions out from the plasma. The geometry of the puller has been optimized to concentrate the field lines and improve the particle injection. The electric force pulls the particles out the ion source, starting the acceleration of the beam. A schematic view of the central region with the electric field lines with the background geometry of the puller and the source is presented in the Figure 5.1.

The particles will be injected when the voltage produces an attractive force, according to the phase of the electric field, and the particles achieve to cross satisfactorily the first gap. The RF provides different acceleration or even deceleration in some cases that limits the particle injection in the cyclotron and its transmission in the central region. Hence, the central region phase acceptance is defined as the range of the RF cycle producing a proper beam injection through the puller structure and suitable first turns. Therefore, a phase acceptance of the central region is produced according to the RF frequency, the magnetic field and the geometry.

The electric field has to present the adequate polarity to extract the particles from the source and accelerate them enough to cross the first gap without colliding with the puller. In the ideal

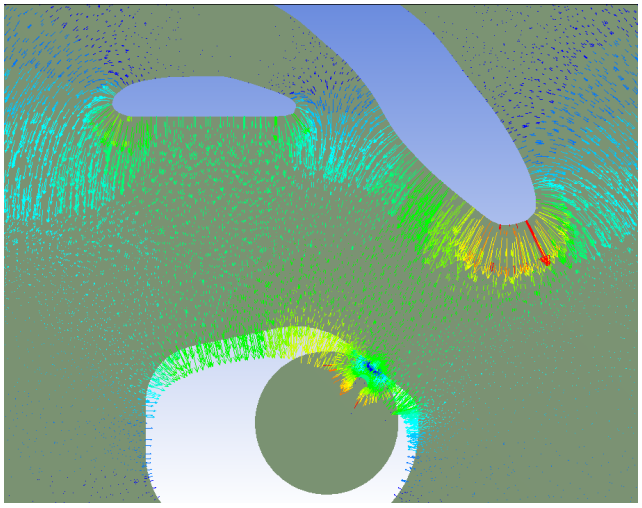

Figure 5.1: *Schematic view of the central region with the electric field lines in the median plane with the background geometry of the puller and the source. The intensity of the electric field is represented by colored arrows according to the field magnitude: high intensity, long arrow - red color; low intensity, short arrows - blue color.*

case, the particles gain enough energy to be extracted from the plasma and to reach the puller, crossing between the two parts and saving the back of the source. In other phase of the RF cycle, that is to say, at a different time, the particles will perceive a different acceleration, even some particles could not gain enough energy to reach the puller before the polarity of the electric field change, and being also decelerated once the electric field reverse its sign. In addition, some particles are lost by collisions with the puller because the energy gain is not enough to cross the central region. Other particle tracks are embedded within the ion source for those phases in which the field produces a force in the opposite direction. To illustrate this, Figure 5.2 shows different orbits in the median plane of particles injected at different phases of the RF cycle. This trajectories have been obtained from single-particle simulations of the reference particle, arising from the center of the ion source slit, thus only the effect of the initial phase at the injection is evaluated.

With that in mind, different phase intervals can be distinguished according to the acceleration that occurs. From these simulations, the phase acceptance range for the reference particle has been estimated as $\phi_{RF} \in [248-340]^{\circ}$. It is important to note that some particles within that range are extracted from the source when the voltage does not have the correct polarity yet (corresponding to $\phi_{RF} \sim [248-270]^{\circ}$). However, these particles immediately perceive an accelerating voltage due to the quick change on the polarity, even though they present a radial dispersion with respect to the main phase range. The remaining RF cycle with opposite direction ($\phi_{RF} \sim [90-248]^{\circ}$) produces a force in the ions directed inwards the source. In addition, particles injected in the phase range $\phi_{RF} \sim [0-90] \cup (340-360]^{\circ}$, despite seeing the voltage with the proper polarity, would not contribute to final acceptance because the energy gain is not enough to raise and cross the puller.

When a total beam arising from a distribution over the entire volume of the slit of the

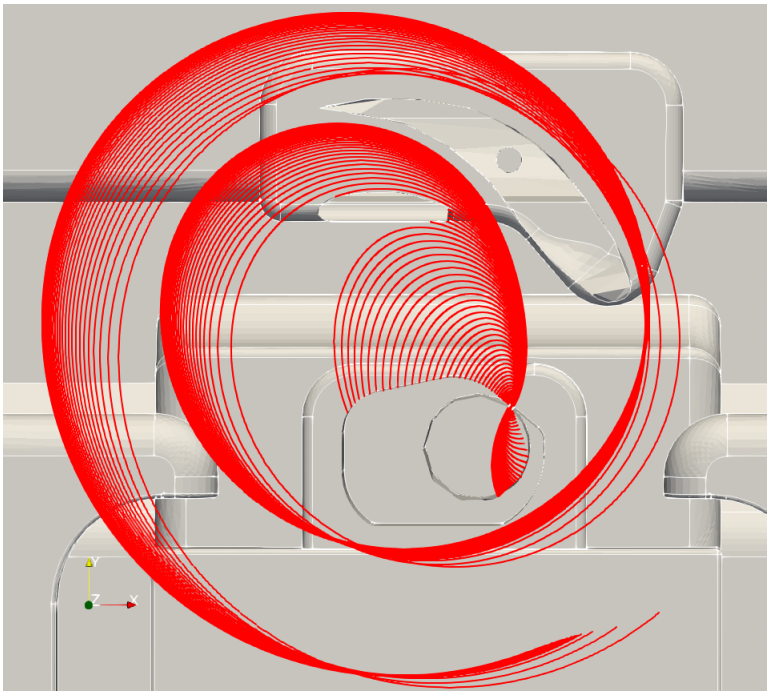

Figure 5.2: *H^- trajectories of the reference particle at different initial phases of the electric field. Particles are extracted from the center of the ion source slit.*

ion source (see section 3.2) is considered, the phase acceptance range is slightly modified in comparison with the reference particle results. This is due to the fact that each particle will perceive a slightly different electric field and phase evolution according to its initial position and consequently some particles of the beam can be injected adequately. Hence, from OPAL multi-particle simulations a central region phase acceptance of ∼100° is obtained, being $\phi_{RF} \in [243\text{–}342]^\circ$ the phase interval resulting in adequate injection into the cyclotron. The phase acceptance is shown in Figure 5.3, highlighting the phases that define the central region phase acceptance in a RF cycle. This range refers to the initial phase of the electric field, when the particles are still at the ion source.

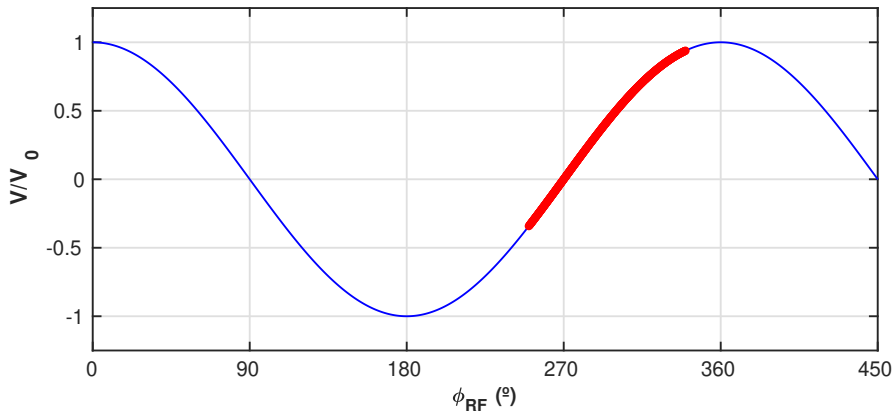

Figure 5.3: *RF cycle according to a cosine function, remarking the central region phase acceptance.*

It is important to comment that the different initial conditions of the particles at the ion source hardly modify the orbits in the central region and that therefore the effect on the phase acceptance is limited. However, only few particles of the initial beam injected at the limits of the phase acceptance range can be transmitted, consequently the contribution to beam current of these phases will represent is restricted.

In addition to that, once the beam is injected, its acceleration will depend on the phase evolution in each gap which will be fully conditioned by the initial RF phase. The phase excursion will determine the proper acceleration though the entire trajectory. In the central region, after the first gap, a phase bunching occurs, that is to say, the phase acceptance interval length in the subsequent gaps is reduced to $\sim 25 - 30°$, as it exposed in Figure 5.4.

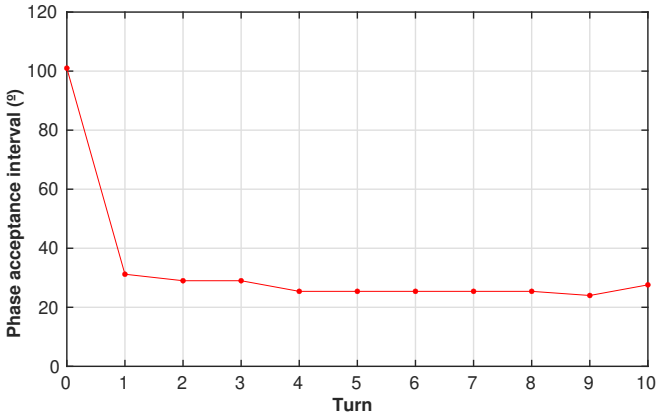

Figure 5.4: *Phase acceptance range evolution in the central region. The phase range is calculated once per turn in the accelerating from the dee to the dummy-dee. The fist value (Turn = 0) represents the phase range in the injection.*

Axial excursion

In the first turns, the axial motion of the particles are affected mainly by the electric field forces, as the magnetic field component is negligible. Thus, the axial forces depend on the intensity of the electric field in each gap, which is variable according to the oscillating radiofrequency behavior, as it has been exposed in section 1.2.1.

The axial effect in the central region is displayed in Figure 5.5, where the axial momentum, p_z, the electric field, E_z, and the axial coordinate, z are plotted for a particle starting at the axial extreme of the slit. It is clearly illustrated how in each gap an axial electric force arise altering the coordinate of the particle. This force is highly pronounced in the first stage of each gap because the beam traverses the second half of the gap in less time than the first half due to the energy gain. The electric field will be the main axial focusing strength in the accelerator until the weak focusing forces provided by the radial decreasing magnetic field will be significant in the intermediate acceleration region of the cyclotron. Therefore, the axial focusing effects description will continue with more detail further on this dissertation.

In addition, there is an influence on the axial movement according to the RF initial phase, that is to say, distinctive focusing effects are appreciated for diverse injection phases due to the

electric field perceive in the subsequent gaps will be slightly different. Figure 5.6 shows the diverse axial excursion in the central region for different RF initial injection. The tracks correspond to single-particles arising from an axial extreme of the slit because the focusing effects are more appreciable the further from the median plane.

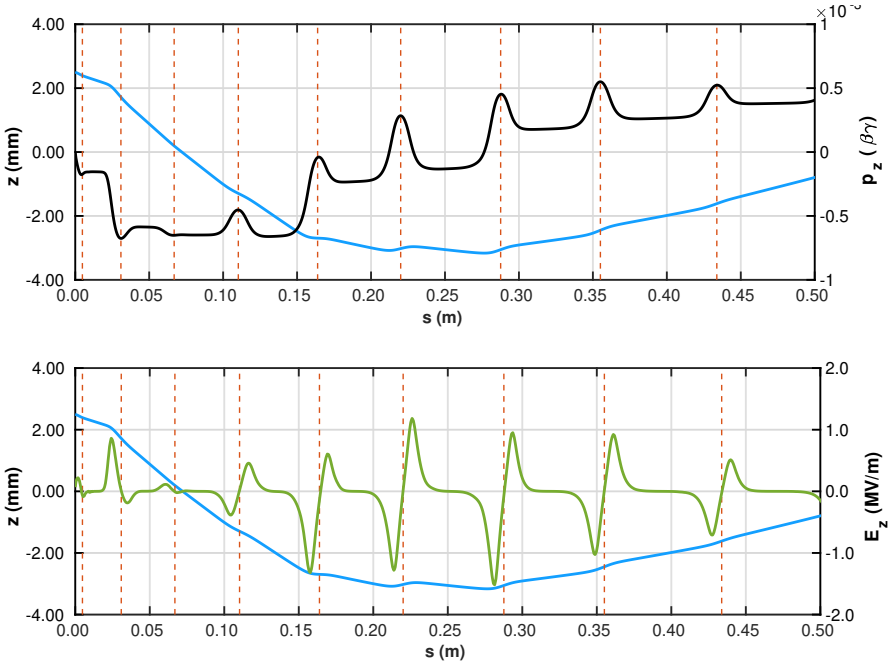

Figure 5.5: *Detail of a single particle axial motion in the central region. The black solid line represents the momentum p_z (right axis - top), the blue solid lines are the axial component z (left axis) and the green line is the axial electric component E_z (right axis - bottom). Accelerating gaps are plotted as vertical red dashed lines. Each narrow peak in pz is produced by the electric forces during a gap cross. The consequent change in axial coordinate is then appreciated.*

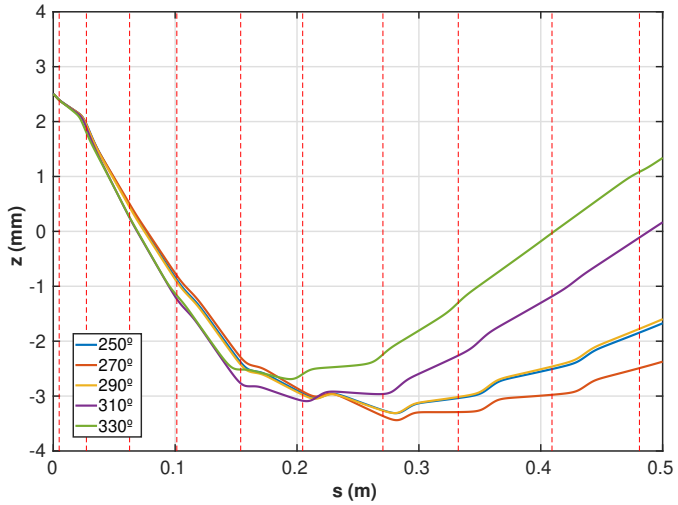

Figure 5.6: *Beam axial size in the central region for different RF initial phases in front of the traveled distance, s. Accelerating gaps are plotted as vertical red dashed lines*

Energy spread

The initial energy distribution has been also analyzed through the comparison between a mono-energetic beam and a beam with an initial energy spread energy. However, the results have not shown any significant difference, since H^- ions have a very low energy compared with the energy gain per gap. Therefore, the effect on the output beam is negligible and the particles in the initial distribution are considered with the same mean energy of 5 eV, according with the expected energy of the H^- ions at the edge of the plasma column [173].

Additionally, an interesting effect in the central region is the increase of the energy spread in the first gaps. The different acceleration of the particles according to the initial distribution gives rise to a slightly different electric field that causes a deviation in the energy gain, and consequently in the particle energies after crossing the gaps. This common effect in cyclotron dynamics is more significant in the first turn. The energy spread in the subsequent gaps is diminished because the most energetic particles will arrive ahead of the peak of the electric field and therefore the spread is stabilized in few turns. Figure 5.7 illustrates this effect along the central region.

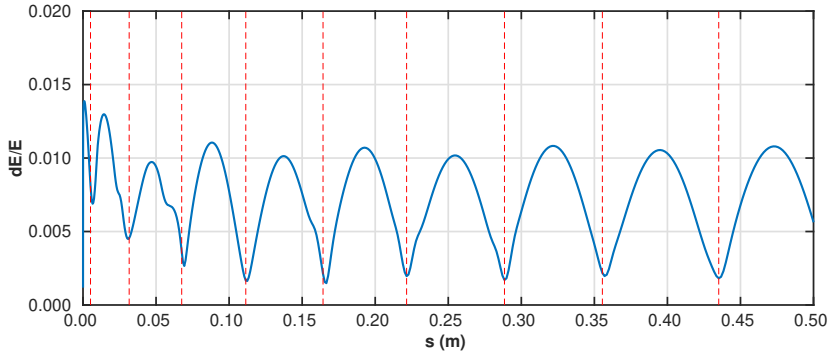

Figure 5.7: *Energy spread in the central region for the whole beam. The vertical dashed red lines represent the accelerating gaps.*

Beam transmission and losses in the central region

It has to be pointed out that not all the particles injected within the central region phase acceptance will be adequately accelerated when the entire beam is considered. Depending on their initial position in the slit of the ion source, some particles will collide in different areas of the central region, specially such particles injected at the limit of the phase acceptance interval. This is because not all the particles in a complete beam achieve to cross the puller and the whole central region, in particular, those particles coming from the limits of the phase acceptance interval.

The evaluation of the beam losses in the central region has been obtained from multi-particle simulations with the geometry of the central region included in OPAL. Only the particles from the phase acceptance range pointed out before are taken into account in this evaluation since all particles beyond that interval will be lost or even not injected. In this way, the beam transmission reduction can be determined more intuitively. Three critical areas have been obtained from

particle losses point of view: the surroundings of the slit, because some particles arising from the extremes slit size hit against the edges of the slit; the puller and the back part of the ion source, by particles from the limits of the phase range. A summary of the rate of losses produced in the central region and the mean energy associated are shown in Table 5.1. The percentage of losses showed in this table refers to the ratio of particles within the acceptance range that do not cross the central region. The results indicate a relevant rate of losses in the central region, but the low energy of the losses minimizes their significance.

With that in mind, and considering the central region phase acceptance range obtained, the beam transmission in the central region is $\sim$26%, referred to the total RF cycle. Thus, it is easy to estimate the beam current transmitted given the current injected according to the ion source performance and the injection conditions.

Table 5.1: *Beam losses at the central region for particles starting within the phase acceptance range. The losses percentages for the three difference areas of collision are referred to the total central region losses.*

Total central region losses	5 %	
	Rate (%)	Mean energy (keV)
Slit of the ion source	77.5	0.2 (1)
Puller	14.6	32.5 (4)
Back rear ion source	7.9	95.6 (1)

Injection of other particle types

It is important to remark that inside the ion source other particles, like protons or electrons, perceive the electric forces and they can be injected into the cyclotron. By the one hand, the electrons have the same electric charge than H^-, and therefore they will be accelerated by the same RF cycle polarity. However, their mass are $\sim$1800 times lower. Consequently, and according to the equation (1.2), the high magnetic field will produce a tiny bend radius ($\sim$0.2 mm) and the electrons will not be able to cross the first gap, colliding in the area around the ion source.

On the other hand, positive-charged ions, mainly protons, are generated in the plasma inside the ion source. These particles are extracted from the slit when the electric field has the opposite polarity to accelerated H^-. Nevertheless, the magnetic field bends the protons trajectories until they collide in the back area of the source, as it is shown in Figure 5.8, and consequently, they are not injected into the cyclotron acceleration process.

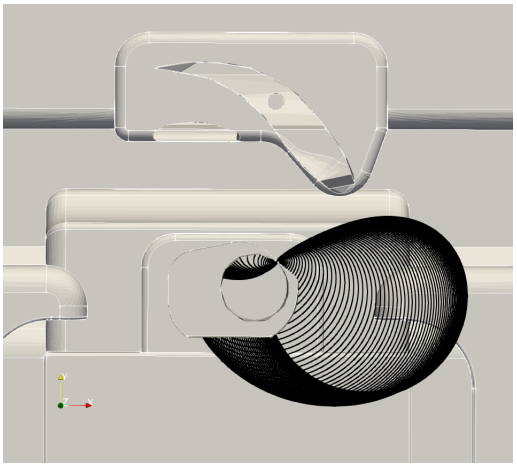

Figure 5.8: *Proton particle paths at different initial phases of the electric field.*

5.1.2 Intermediate acceleration region

The second area to consider in this preliminary beam dynamics study is the intermediate region of the cyclotron. It is defined as the subsequent acceleration region after the first turns and just before the extraction of the beam. While the central region is orientated to improve the beam current injected from the ion source, maximizing the phase acceptance, the main objective of the intermediate region is to optimize the synchronous point that allows enhancing the energy and beam current at the extraction point as well as the beam focusing along the path. Hence, in this subsection, the beam evolution along the path is presented for a better comprehension of the beam transportation, with a detailed analysis of relevant features as the synchronism of the beam with the radiofrequency system and the diverse focusing effects.

Beam evolution

Once the beam is injected into the cyclotron and crosses conveniently the central region, the beam continues the acceleration process along several turns until it reaches the extraction region. The energy evolution for a reference particle along the trajectory are plotted in Figure 5.9 in front of the traveled distance and the radius. The acceleration process is adequate whereas the particles achieve the gaps when the electric field presents the adequate polarity to accelerate them. For instance, the Figure 5.10 shows the phase evolution in the gap from the dee to the dummy-dee for a reference particle. In this gap, the electric field has to be at $\phi \in [90, 270]$ to accelerate suitably the particles. When the particles are enough accelerated, they will reach the extraction region, where the H^- will be stripped to be transported to the target.

In addition to that, the beam evolution depends on the initial radiofrequency conditions, that is to say, the RF phase during the injection. To illustrated that, Figure 5.11 shows the energy of a reference particle injected at different RF phases as a function of the number of turns performed. It is clear how the number of turns needed to reach the extraction point changes for different initial phases according to the synchronous phase and the maximum phase excursion

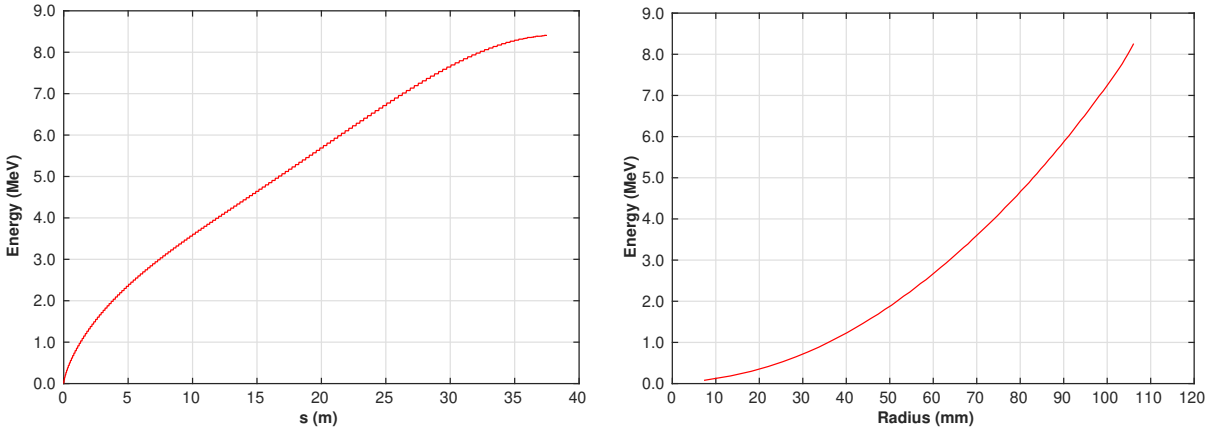

Figure 5.9: *Energy evolution of the beam along the trajectory as a function of the traveled distance and of the mean radius.*

each particle can make. As it will be further explained in the chapter 6, the total number of turns performed by the beam is an important factor that influences the total path of the beam and, therefore, in the likely beam losses produced by interactions with the residual gas. Hence, the phase acceptance becomes an important factor to characterize the beam dynamics of the cyclotron.

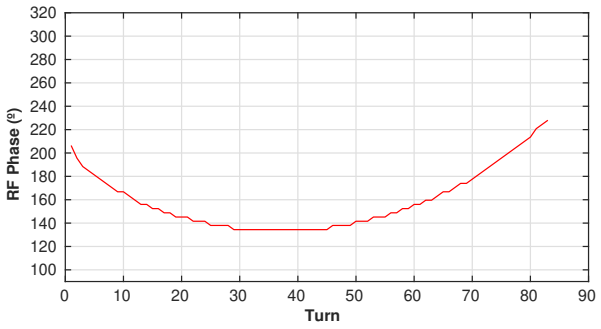

Figure 5.10: *Radiofrequency phase evolution perceived by a reference particle in the accelerating gap from the dee to the dummy-dee.*

Synchronism evaluation

As it has been exposed previously, the initial stages of the acceleration are determined by the central region configuration, defining the RF cycle range that produces a suitable acceleration and transmission through that region. However, the relativistic increase of velocity during the acceleration imposes a decrease in the revolution frequency of particles with the radius by the relativistic factor γ, according to the equation (1.6). Moreover, the weak focusing status of this cyclotron implies a decreasing magnetic field strength with the radius, which also affects to the revolution frequency of the particles.

In a classical cyclotron the particles are not synchronized with the RF fields. Therefore, the particles perceive different voltage each accelerating gap along their path. This feature impacts

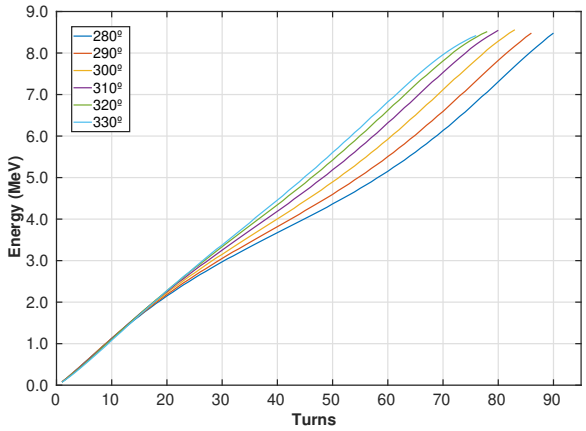

Figure 5.11: *Energy evolution of the reference particle in front of the number of turns for different initial RF phases.*

on the phase acceptance of the acceleration according to the oscillating frequency of the electric field because some particles that cross adequately the central region could be decelerated in an intermediate part of the path, disrupting the acceleration process before to reach the striping foil. The optimum acceleration results from the balance between the RF frequency and the magnetic field, in such a way that the accelerating field presents the proper polarity in each gap when the particles arrive. Therefore, as a consequence of the non-synchronization in a classical cyclotron, it is essential to choose the RF frequency value in accordance with the magnetic field that allows the particles to be accelerated the most prolonged possible time, with the objective of maximizing the energy as well to fulfill the current requirement at the target.

With that in mind, an extensive study of RF-beam synchronism has been carried out to maximize the acceleration in the cyclotron. The purpose of this evaluation is a careful comprehension of all the effects concerning the radiofrequency balance in AMIT classical cyclotron. It is based on the magnetic field provided by OPERA calculations, with a maximum value of 3.94 T, as it has been described in section 3.2. The RF frequency is adapted to this field to preserve the acceleration through the cyclotron until the extraction region. For other magnetic field value, the RF frequency must be adjusted, but the physical effects coming about are exactly the same. It should be noted that this magnetic field value (3.94 T) is slightly lower than the nominal field (4 T). However, the aim of this section is to present the physical effects associated with the non-synchronous acceleration of a classical cyclotron, which are independent of a specific value. In a subsequent section the analysis will be extended considering the nominal field.

The impact of different RF frequencies on the beam evolution is illustrated in Figure 5.12. The figure shows the evolution in RF phase, energy and radius of a single particle starting at the center of the slit (reference particle). For a better understanding, two RF frequency values are analysed considering different initial RF phases: the first one ($f_{RF} = 59.18$ MHz), optimized to preserve the phase acceptance during the acceleration; and the second value ($f_{RF} = 59.12$ MHz) for which there is a clear desynchronization. In the latter case, it is significant how some particles are decelerated at an intermediate point of the path depending on the initial phase of the electric

field. It is important to note that the figures of the phase excursion represent the phase of the electric field once per turn, when the particles cross the gap from the dee to the dummy-dee, and consequently the accelerating phase is within $\phi \in [90, 270]$.

Extensive multi-particle simulations have been performed with OPAL to determine the dependence of the total phase acceptance along the whole path with the RF frequency and the initial phase perceived by the particles during the injection. For that purpose, an array of RF frequencies are evaluated. The simulations are performed from a initial distribution arising from the entire slit volume (see section 3.2). The maximum extraction point, located in a estimated radius enough to achieve the required energy, is considered fixed in this calculations. Figure 5.13 shows an interval of RF frequencies values providing the acceleration of the beam until the extraction region. The particles must reach the gap when the electric field finds itself in an adequate polarity to kick and accelerate the beam. Hence, for some radiofrequency values, not all phases favorably accelerated through the central region provide a proper acceleration until the extraction radius, explaining the discontinuous range for some RF frequencies. For some frequencies, the particles reach the accelerating gaps quite distant from the synchronous point and therefore many particles can not be accelerated and slow down before achieving the extraction point. Thus, a delicate balance of the radiofrequency afford the acceleration in AMIT cyclotron.

The optimization of the RF frequency affects in a relevant way into the whole beam dynamics. For that reason, the final energy of the beam, the number of turns needed to reach the extraction point without deceleration and the survival rate of the beam at the end of the trajectory has been evaluated for a good comprehension of the AMIT cyclotron beam dynamics. Since the extraction position has been considered constant in this study, the average final beam energy (Figure 5.14) is almost the same for different RF frequencies evaluated, within the range of the rms energy spread. Some discrepancies are observed between particles injected at diverse moment of the RF cycle due to the variation on the energy gain per gap. In the same way, the number of turns (Figure 5.15) realized are different according to the RF initial phase. Furthermore, a slight decrease on the number of turns is observed for greater RF frequencies. This is produced because the synchronous point is belatedly achieved for low frequencies and the particles perform a large phase excursion, whereas the synchronous point is early reached for high frequencies values, reducing the total phase excursion.

Regarding the beam transmission, the RF frequencies appropriated for a suitable acceleration are those that preserve the phase acceptance during the whole path maximizing the extracted beam current. Figure 5.16 shows the survival rate of particles reaching the extraction region, fixed in this analysis, with respect to the total particles simulated for each RF initial phase. Moreover, the total beam transmission according to the RF cycle for each considered frequency is shown. By the one hand, it is observed how the beam transmission decreases in the limits of the phase acceptance interval. This is due to the particle losses in the central region, as it was exposed in the previous section. On the other hand the low beam transmission for some radiofrequencies values is produced by the deceleration of the beam in the intermediate region. At low frequencies the isochronous point is reached too late. However, the beam transmission diminishes smoothly

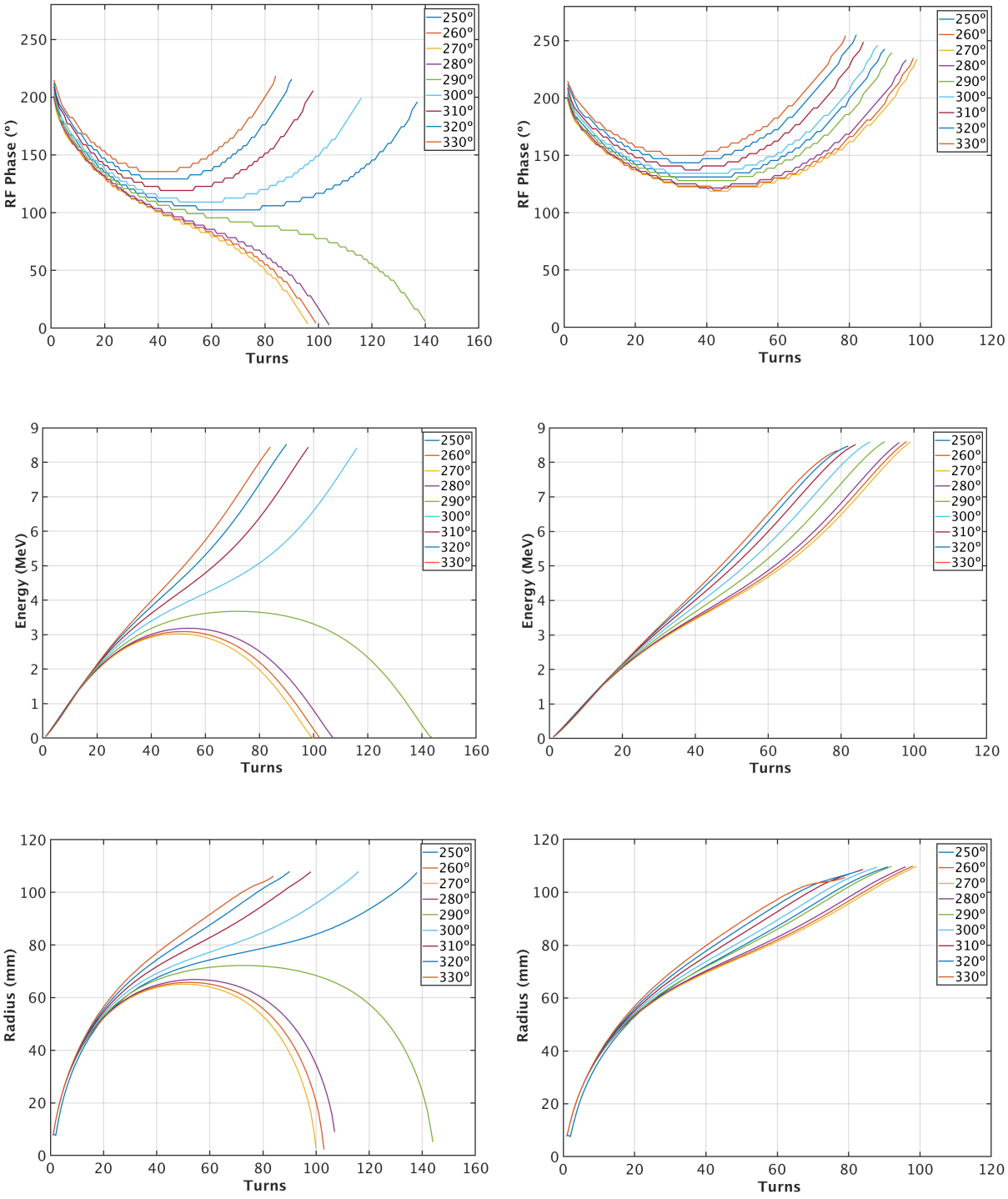

Figure 5.12: *Beam parameters evolution as a function of the number of turns for different RF initial phases for two RF frequency cases: $f_{RF} = 59.12$ MHz (left side) and $f_{RF} = 59.18$ MHz (right side). Electric field phase in each turn (top), energy (medium) and radius (bottom) of reference particle are plotted. The RF phase is represented once per turn, when the particles cross the gap from the dee to the dummy-dee. The parameters are displayed once per revolution cycle when the reference particle crosses the medium plane between dee and dummy-dee.*

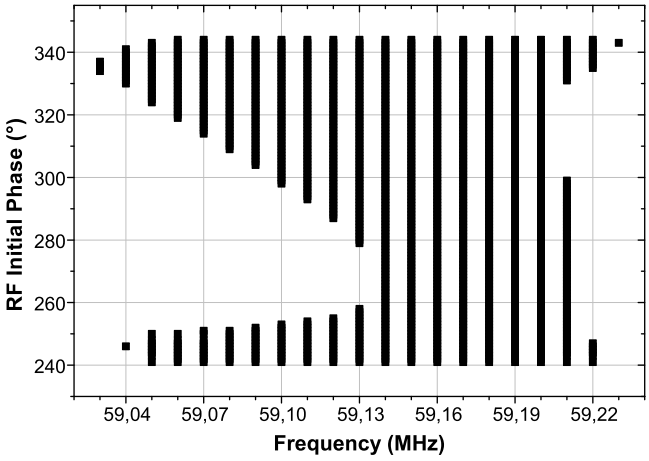

Figure 5.13: *RF frequency and initial electric field phase dependance for particles reaching the extraction point for a stripping foil located at* 110 *mm of radius. The discontinuous intervals of initial phases for a given frequency are due to particles deceleration at an intermediate point of the path.*

because there are still particles from initial phases that reach the synchronous point, achieving the extraction region without deceleration. At high frequencies, the particles reach the isochronous point earlier, so that the total acceleration time is limited and the particles do not gain enough energy to achieve the extraction point, and consequently the beam transmission declines abruptly.

The optimum RF frequencies under the considered conditions in this analysis provide a total beam transmission of 25% (see Figure 5.16(b)). This transmission value refers to the range of phases that are accelerated in the cyclotron, including all associated intrinsic losses during the beam transportation (in the central region and losses by axial deviations). In other words, it is a percentage value of transmission with respect to continuous extraction. It is referred to all the RF phase cycle to facilitate the calculation of the final beam current achievable. Since

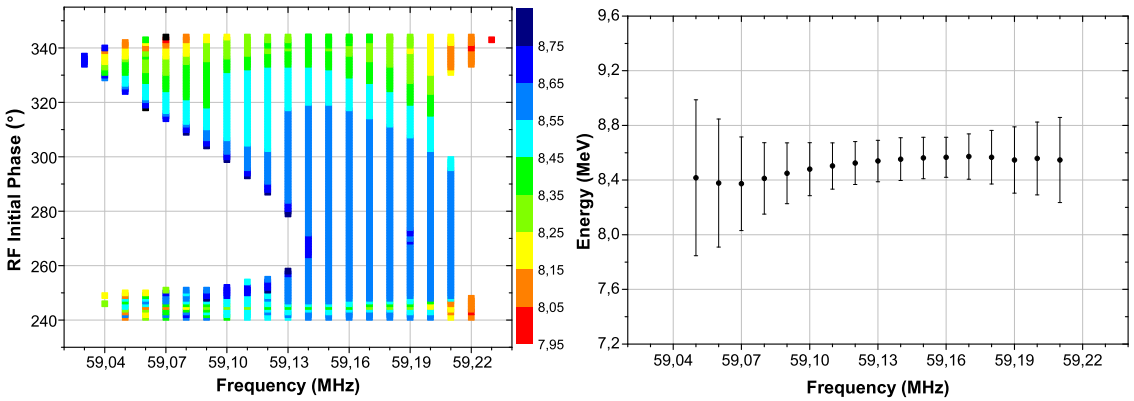

(a) Energy-phase dependence (b) Mean energy

Figure 5.14: *Beam energy at extraction point for different frequencies. (a) Initial RF phase dependence and (b) mean value. The error bars represent the rms energy spread at the end of the acceleration considering the entire phase acceptance range. The mean data of some radiofrequency with very low transmission and low statistics are removed to clarify the presentation of the results.*

the ion current provided by the ion source has been experimentally characterized at IST under DC extraction conditions (see Chapter 4), the beam transmission rate can be used to evaluate the final current accelerated by the cyclotron. Given the measured beam current at the IST ($> 200\,\mu$A) and the transmission rate about 25%, the final output current will fulfill the AMIT beam requirements ($> 10\,\mu$A). Therefore, this result represents a reasonably high transmission efficiency.

This evaluation of the synchronism in the AMIT cyclotron allows to ascertain the beam transmission of the cyclotron under a particular configuration or operation mode of acceleration, that is to say, the RF frequency and the applied magnetic field. The results show how the tuning of the RF over the evidenced frequency range modify substantially the conditions of accelera-

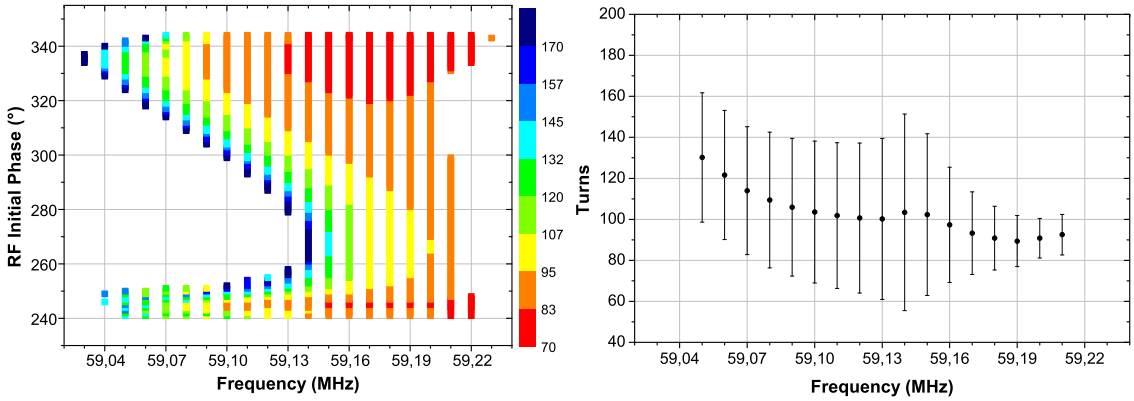

(a) Number of turns-phase dependence (b) Mean number of turns

Figure 5.15: *Number of turns needed to reach the extraction point for different frequencies. (a) Initial RF phase dependence and (b) mean value. The error bars for the averaged values represent the rms deviation at the end of the acceleration considering the entire phase acceptance range. The mean data of some radiofrequency with very low transmission and low statistics are removed to clarify the presentation of the results.*

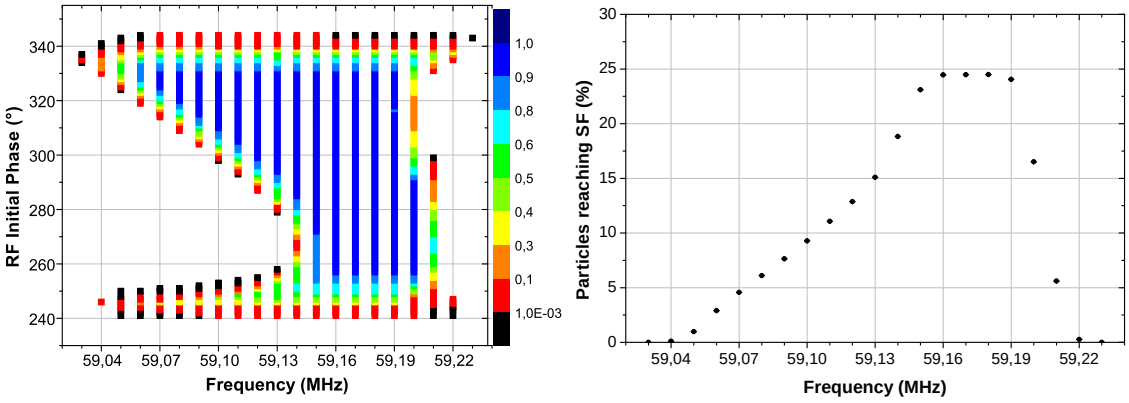

(a) Survival rate-phase dependence (b) Total rate

Figure 5.16: *Beam survival rate at extraction point for different frequencies. The survival rate in (a) denotes the percentage of particles reaching the extraction point respect of initial number of particles simulated at the same RF initial phase. The total rate (b) is referred respect to all the RF phase cycle.*

tion, allowing to maximize the extracted beam current. In addition, some beam characteristics under these acceleration conditions has been presented, as well the behavior of the beam under variation of the RF system. This examination method of the acceleration can be applied for any modification of the configuration parameters, and therefore, it would be employed further on this dissertation to the analysis of the beam dynamics under the nominal conditions.

Axial beam focusing

The beam focusing plays a fundamental role in the beam dynamics of a cyclotron. As it has been described in section 1.2.1, focusing forces in a classical cyclotron are provided by both the radially decreasing magnetic field and the electric field along the accelerating gap. With that in mind, the particle motion in the vertical plane is described according to a harmonic oscillator: the particles perform stable oscillations about the horizontal median plane. The electric forces are predominant in the first turns, where the variation of the magnetic field is practically negligible. On the other hand, the electric field is insufficient to support the beam focused during the entire transportation until the extraction point because depending on the RF phase during the crossing gap, the forces could be defocusing. This effect has been described in the central region section. As the beam is accelerated, the decreasing magnetic field starts contributing to the beam focusing forces. Hence, the focusing effects are appreciated as a result of the whole beam transportation. It has to be noted that the focusing strength is linear with the z coordinate of the particles, that is to say, it affects significantly for particles with an axial shift pronounced.

To better illustrate the beam vertical focusing, Figure 5.17 shows the axial coordinate and

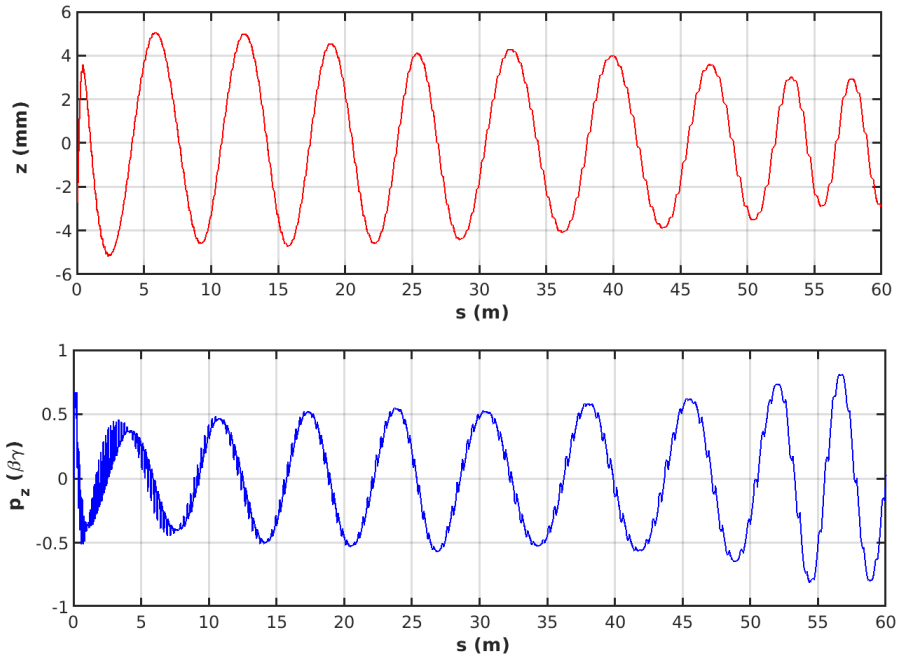

Figure 5.17: *Axial coordinate z (top-red) and axial momentum p_z (bottom-blue) for a single particle along the path.*

the momentum evolution along the path of a particle starting at the extreme of the slit height, due to the focusing effects are more distinguishable on particles far from the median plane. Although during the first turns a particle has axial divergence by central region effects, few steps later focusing effects are appreciated. Two differentiated tendencies of the axial behavior of particles are observed. On the one hand, attending to the whole path, z, after a slight initial increment, changes periodically in an attenuated oscillation as a damped wave, that is to say, in each oscillation the maximum amplitude of the coordinate is reduced by the effect of the radial decreasing magnetic field. The same impact is exhibited by the momentum, that it is increased along the path. On the other hand, small oscillations of the axial component appear, especially in the first stages of the path, due to the effect of the electric field. This effect is more evident by the fluctuations from the main sinusoidal wave of the momentum throughout the stage of the acceleration.

Figure 5.18 shows a detail of the axial fluctuations at the beginning of the intermediate region of the path. The electric focusing is clearly distinguishable: a focusing effect occurs at the entrance of each gap, z decrease after the cross, reaching a maximum of focusing right at the intermediate point of the gap. However, there is a slight defocalization impact in the last part of the gap by the change of the axial electric field component, E_z. It can be noted the total focusing on these gaps since the output z is lower than at the entrance.

As it has been exposed in the central region beam dynamics description, the electric focus-

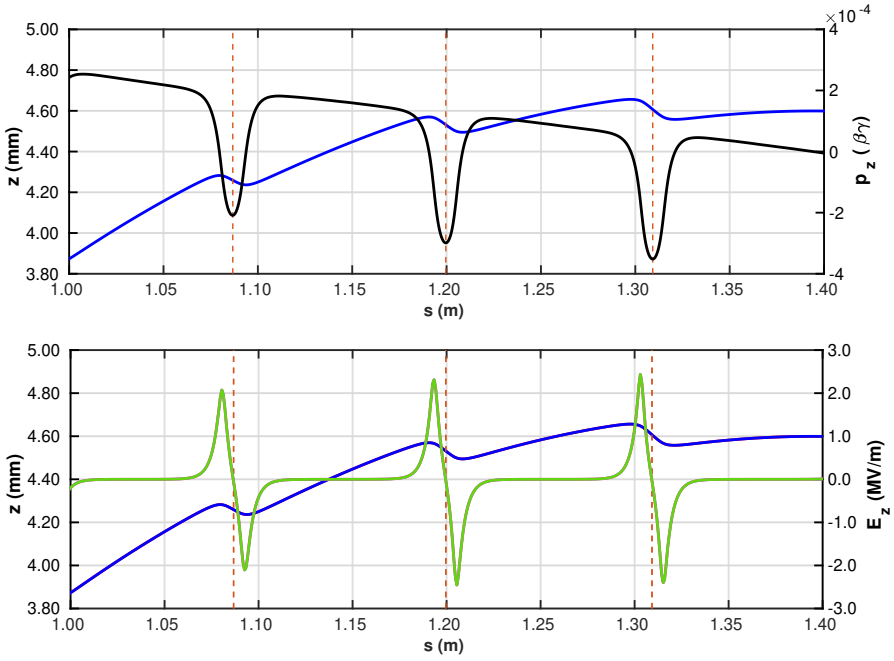

Figure 5.18: *Detail of a single-particle axial movement in a location in the intermediate region. The black solid line represents the momentum p_z (left axis - top), the blue solid lines are the axial component z (right axis) and the green line is the axial electric component E_z (left axis - bottom). Accelerating gaps are plotted as vertical red dashed lines. Each narrow peak in pz is produced by the electric focusing forces during a gap cross. The consequent change in the axial coordinate is then appreciated.*

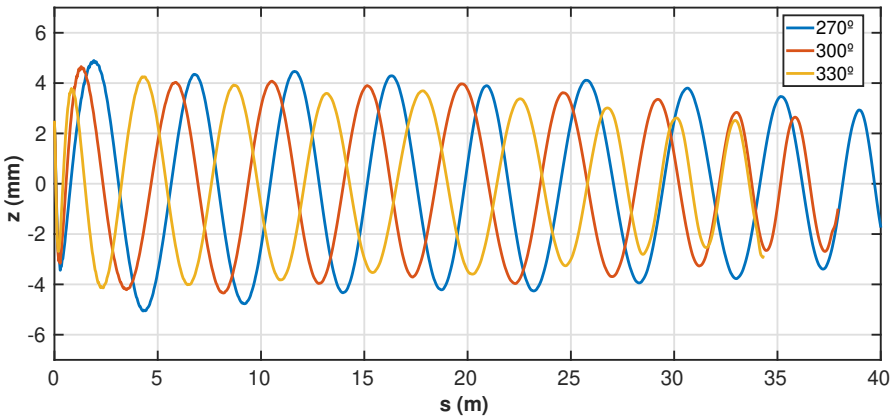

Figure 5.19: *Beam axial excursion along the path for different RF phase initial conditions.*

ing, and consequently the axial movement is influenced by phase of the RF field during each accelerating gap by means of two features: first, the RF phase acceptance in the injection and through the central region and secondly, by the non-isochronism of the cyclotron, resulting in different arrival times at each gap. Therefore, the influence of the RF phase in the beam focusing is prolonged along the whole acceleration, as it is displayed in Figure 5.19. It is observed how the different phase excursion of the particles influences in the axial evolution, since the electric focusing in the subsequent gaps will be different according to the initial RF phase during the injection of the particles.

The axial oscillations of each individual particle are affected by its initial axial position. A linear relationship between the initial axial position and the maximum amplitude. Consequently, the maximum axial excursion have been monitored through multi-particle simulations at different initial axial position covering the whole phase acceptance range, obtaining the maximum amplitude of the oscillation as a function of the initial position (Figure 5.20). The results include the variations produced by the different focusing effect according to the radiofrequency phase

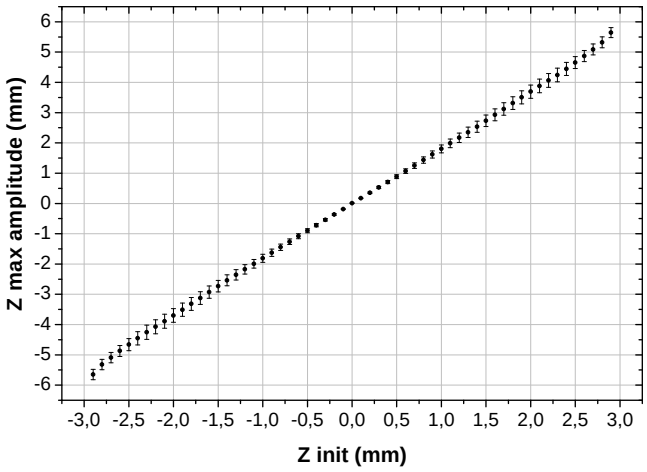

Figure 5.20: *Maximum axial amplitude as a function of initial axial position. The error bars represent the axial variations introduced by the initial RF phas conditions over the phase acceptance range.*

conditions. This maximum axial excursion relation with the initial position is relevant because it affords to determine potential beam losses. Particles with high maximum axial amplitude can collide with the upper or lower inner part of the dee. Therefore, this outcome allows to estimate the optimum height of the slit of the ion source to minimize the axial beam losses.

For an extensive comprehension of the beam focusing effects, multi-particle simulations have been performed considering a initial distribution from the entire volume of the slit, verifying the focusing effects described. Multi-particle simulations also include other effects affecting to the focusing such as non-null initial axial momentum or the radial-axial coupling in the injection, in other words, that particles not radially centered in the slit perceive a slightly different RF field. Figure 5.21 illustrates the trajectories of the particles along the axial direction, showing the net focusing effect in the entire beam.

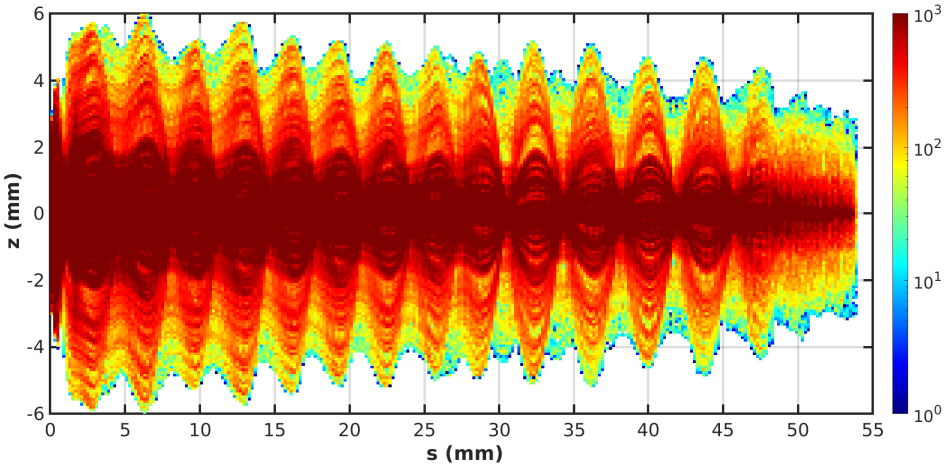

Figure 5.21: *Representation of the beam axial movement for the whole beam within the phase acceptance range. The color scale represents the distribution of the number of particles.*

Beam axial losses

The axial movement analysis has provided a detailed comprehension of the different focusing forces involved in the axial motion of the beam. The combined effect of the electric and magnetic fields provides sufficient focus to achieve a well-centered beam at the end of the path. However, the outcomes have shown a maximum axial excursion of the beam near to the limit of the inner edges of the dee (see Figure 5.20). Hence, some particles arising from the extremes of the slit will collide against the top and bottom area of the dee or other components (dummy-dee, rear part of the ion source...). The beam losses characterization by axial collisions is summarized in

Table 5.2: *Beam losses by axial collisions with the geometry in the intermediate region of the acceleration.*

Total axial losses	0.2 %
Mean energy	1.9 (3) MeV
Maximum energy	3.02 (5) MeV

Table 5.2. The losses rate is obtained from particles coming from the evaluated phase acceptance range. The axial losses are produced in different orbits of the trajectory, for radius between 35 and 70 mm. Beyond that, the magnetic field axial forces will focus the beam. In this intermediate region the energy of losses is not negligible and they can provoke some important damages in the impacted components despite the beam losses rate is fairly limited. Figure 5.22 shows the energy distribution of the particles lost by axial collisions, illustrating that the losses are produced in different areas of the path by the oscillatory motion of the particles. In addition, the physical locations of the total losses are showed in Figure 5.23, including both central region losses and axial deviations. The analysis of the ion source slit size presented in the chapter 6 will conclude an optimum height of the slit to remove this undesired axial losses.

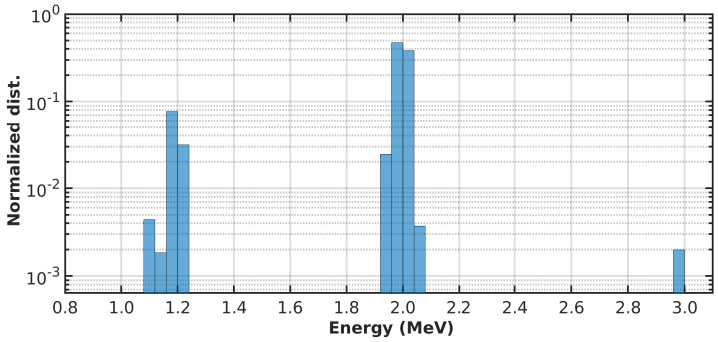

Figure 5.22: *Energy distribution of the beam axial losses. The distribution is normalized over the number of particles lost.*

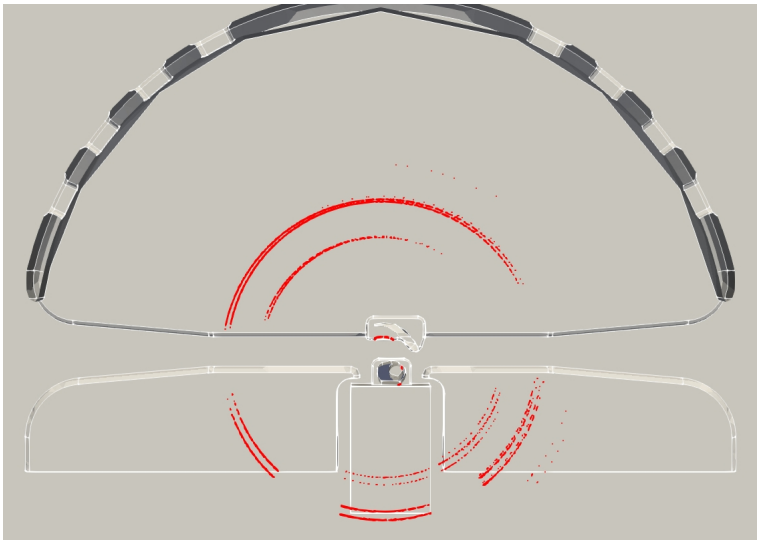

Figure 5.23: *Spatial distribution of the beam losses along the cyclotron. Losses are concentrated in the central region due to collisions with the puller and in the upper and lower parts of the accelerator due to axial deviations.*

Radial beam evolution

In the same way that the axial movement, the beam also performs an oscillatory motion in the radial plane. The radius of curvature of the particles is determined by their momentum and the magnetic field. Therefore, at each energy value, the radius of curvature is modified, and consequently the radius increases at each crossing of the gap by the energy gain supplied by the electric field. As it has been exposed previously in this section, the radius of each particle is not constant along each turn, it presents a sinusoidal oscillatory movement around the associated ideal radius. This effect is illustrated in Figure 5.24, where the radial position, ρ, and the radial component of the momentum, p_ρ, are plotted as a function of the trajectory. It is clear evidenced the oscillation of the radius along the path and how the radius grows in each accelerating gap. Once the central region is crossed, the radial oscillations begin to be observed, which decrease slightly along the particle path. Additionally, the radial oscillations are affected by the initial properties of the beam, both by the initial distribution and by the initial RF phase conditions. Under these considerations the radial oscillations are wider, despite of the radial width of the beam it is well constrained on the walls of the dee and the radial oscillations does not give rise to losses. Figure 5.25 shows the radial evolution of the total beam, illustrating how according the initial conditions, each particle performs a particular radial oscillatory movement.

A relevant property in the AMIT cyclotron related to the radial movement is the superposition of the beam once the central region has been crossed, that is to say, particles from different injection conditions and at different turns of acceleration may overlap. This effect is due to the non-synchronize acceleration in a classical cyclotron, producing orbits with a very different phase

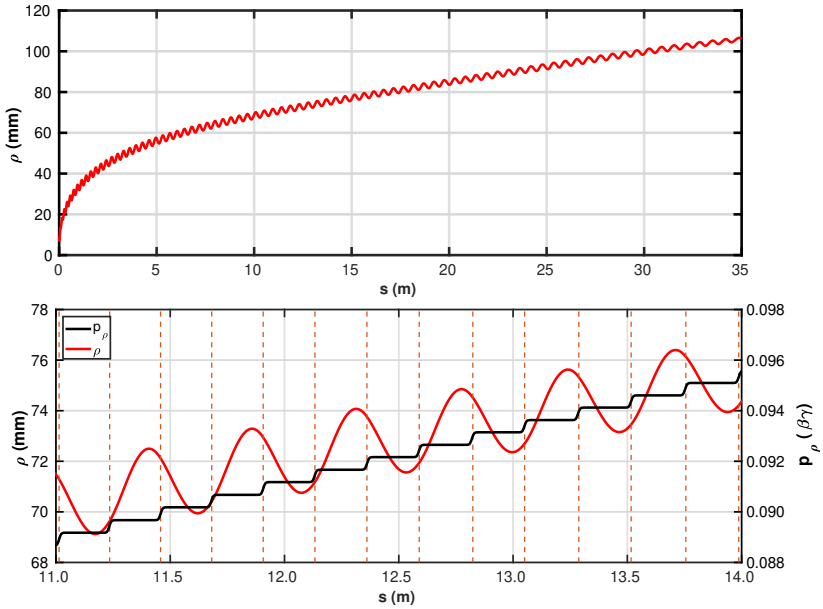

Figure 5.24: *Radial motion of a reference particle along the beam path (top) with a detail of the motion in a location in the intermediate region (bottom). The black solid line represents the momentum p_ρ (right axis) and the red solid line is the radial component ρ (left axis). Accelerating gaps are plotted as vertical red dashed lines.*

excursion. Therefore, the beam can not be separated according to the number of turns (Figure 5.26), effect also influenced by the increasing radial beam size. Hence, the turn separation is not possible from median to high energies of the beam and, consequently, the beam extraction at the end of the acceleration processes has to be based on an electron stripping mechanism.

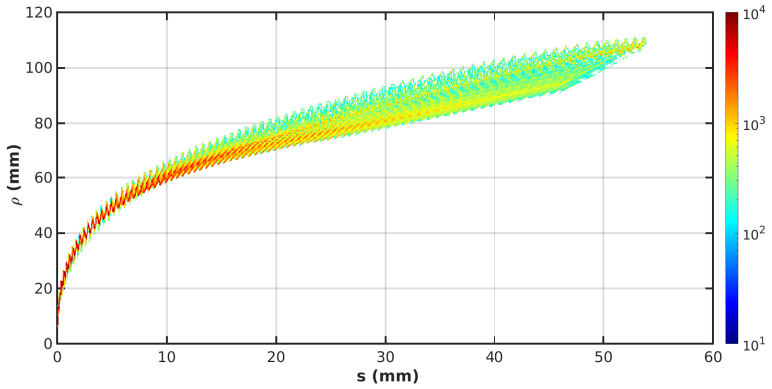

Figure 5.25: *Radial movement of the beam starting at different times within the phase acceptance range.*

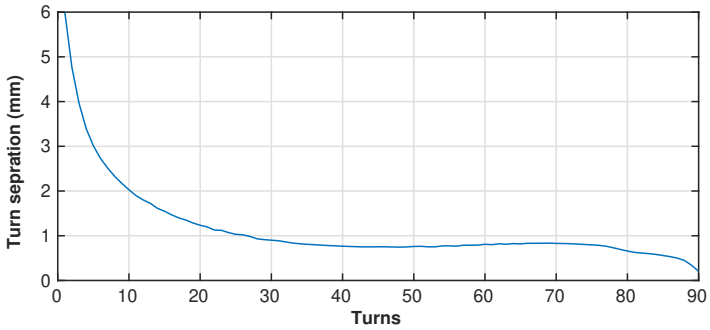

Figure 5.26: *Beam turn separation as a function of the number of turns performed.*

5.1.3 Beam extraction

The extraction system of the AMIT cyclotron, as it has been exposed in section 2.2.5, is based on stripping foils that remove easily the electrons from H^- ions. Then, the resultant proton beam travels through a drift space without electric fields until reach the position of the target port at the end of the vacuum chamber. This is a 22.5 mm radius circular aperture located at 420 mm of radius from the cyclotron center ($x = 91$ mm, $y = -410$ mm). The main objective of the extraction system is to achieve a good conversion of H^- ions to protons, allowing the adequate transport without losses to the target. This stripping extraction method enables to tune the output beam energy, as well as other characteristics, by modifying their radial position respect to the center of the cyclotron. The stripper angular position has to be accommodated, according to its radial position, to achieve an suitable beam propagation until the target.

The energy of the beam extracted from the cyclotron depends on the radial position of the extraction point. According to the beam requirements of the cyclotron (see figure 2.4), the

minimum energy to achieve a significant production of ^{11}C, the most selective radioisotope, is 6 MeV, although this energy is far away from the optimum radioisotope production objective. The upper energy limit is determined by the maximum viable acceleration of the beam in compliance with the non-synchronism particles-radiofrequency. This maximum acceleration is determined by cyclotron configuration considered, that is to say, magnetic field, voltage and RF frequency values, which they have set the geometrical boundaries of the dee during the design stage of the cyclotron. Therefore, the stripping foil must be placed in a radius lower than the maximum energy associated with a given cyclotron configuration, but in a position to fulfill the minimum energy requirement for radioisotope production.

The extraction position also influences other parameters of the beam. First, the final beam current is affected, due to beam losses increase as long the beam traveled distance rises by the interaction of the ions with the residual gas. Besides that, the stripper position modifies the final beam focusing due to the radial decreasing magnetic field: a higher radius implies a stronger beam axial focusing. This parameter influences on the propagation to the target, since once the beam leaves the acceleration region, there are no more focusing effects, and the beam dispersion can increase considerably. An adequate transmission in the drift space until reaching the target is a decisive feature to specify the optimum extraction positions. A wrong stripper location would result in a high energy beam impacting at some point of the vacuum chamber out of the target, increasing the radioactive activation and the damage of the materials.

With that in mind, from the point of view of the beam dynamics study, the stripping foil position has to be optimized according to the beam energy, the final relative current (number of particles reaching the stripper) and the beam transportation to the target.

In order to analyze the characteristics of the output beam on the stripper and to establish the optimum extraction position for a suitable propagation to the target, beam dynamics studies have been performed modifying the radial and the angular position of stripping foil. The actual movement of the extraction mechanism is a combination of linear displacement, different than the radial axis, and angular rotation over itself. Therefore, there is a relation between this movement and the stripping foil radial-angular position. In order to present clearly the effect of the stripper position with respect to the center of the accelerator, firstly, an analysis of the independent variation of the radial and the angular position is presented. In this way, the beam energy adjustment is explicitly shown as well as other relevant information for the extraction. Afterward, an analysis with the actual movement implementation will complement the beam extraction study in section 5.2.1.

Beam characterization at the stripping foil

First, the characteristics of the beam at the stripping foil for different positions are studied through multi-particle simulations for a given cyclotron configuration. The RF frequency considered is adopted according to a maximized phase acceptance range (see section 5.1.2). In this section, the extraction position is defined by the radial position, R_{SF} and the angular (azimuth), φ_{SF}, referred to the cyclotron center. The extraction position parameters are varied within the

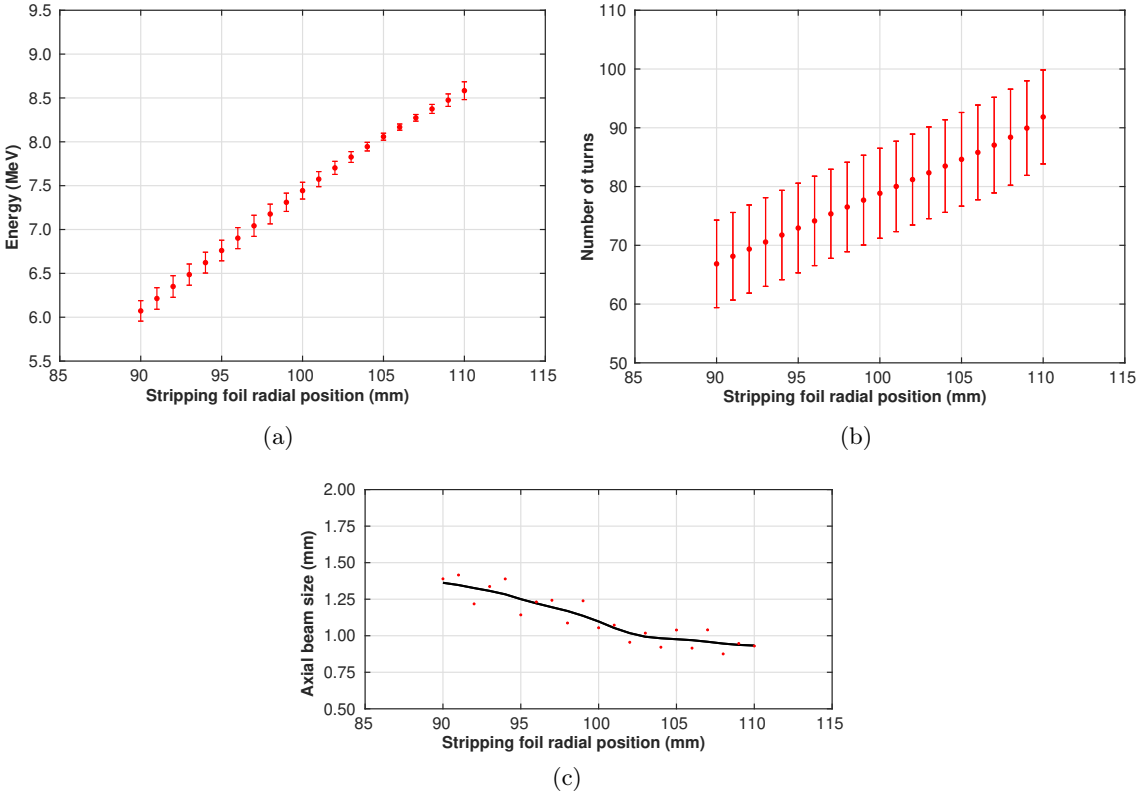

Figure 5.27: *Beam properties at the stripping foil located at a fixed angular position ($\varphi_{SF} = 251.5°$) and a variable radius: (a) Beam energy with rms spread, (b) number of turns performed to reach the stripping foil and (c) rms axial beam size with a smooth interpolation (black line) with the stripper radial position.*

ranges $R_{SF} \in [90, 112]$ mm and $\varphi_{SF} \in [240, 270]$. This analysis allows the evaluation of the effect of each parameters.

It has been observed that the beam survival rate remains unaltered for different extraction location of the stripper whereas it is placed at lower radius than the maximum achievable according to the cyclotron configuration. The RF frequency and the magnetic field have been established in the design stage of the project to fix the maximum beam acceleration regarding the energy requirements. Therefore, the beam can be only accelerated until a maximum radius close to the inner dee walls. For the RF frequency considered in this preliminary beam dynamics analysis ($f_{RF} = 59.18$ MHz) the maximum radius is ~ 110 mm. For slightly higher radii, the beam survival rate decreases dramatically. For instance, the beam survival rate for radius of 112 mm is reduced to 3% respect of 110 mm radius. With that in mind, only data until a stripping foil radial position of 110 mm are considered.

The beam properties at stripping foil as a function of the radial position for a fixed angular location ($\varphi_{SF} = 251.5°$) are shown in Figure 5.27. The mean energy and the number of turns scale linearly with the radial position, whereas the axial beam size is slightly reduced by the enhanced magnetic focusing.

It is appreciated how the rms energy spread of the beam at the stripping foil depends strongly on the radial position. This effect is produced by the different beam evolution regarding the initial

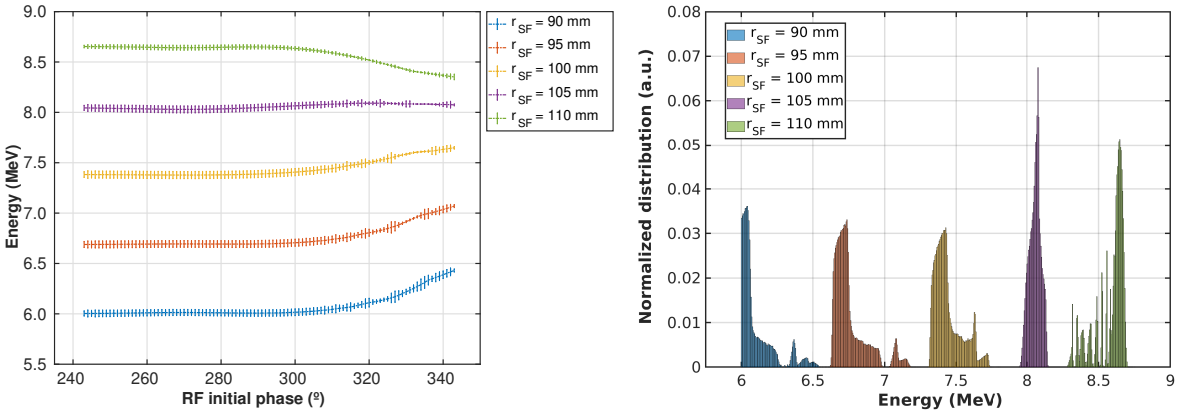

(a) (b)

Figure 5.28: *(a) Final energy as a function of the RF initial phase and (b) energy distribution at the stripping foil located at a different radius as a function of the RF initial phase.*

conditions of the RF cycle, that is to say, the energy gain is conditioned by the initial RF phase. Therefore, according to the extraction radius, particles injected in diverse points of the RF cycle will achieve different energies, as it is illustrated in Figure 5.28(a). Hence, the energy distribution resultant in the stripping foil depends on the extraction radius (Figure 5.28(b)). Furthermore, it is observed how at certain radius, all the particles arising from diverse initial conditions of the RF cycle have acquired the same acceleration. This is originated because the particles that are more advanced in the phase excursion have begun to obtain less energy per gap while those that are phase delayed increase the gain. Consequently, this position is an optimum point for the given RF frequency and in this case, the energy at the stripping foil has a minimum spread.

The beam profile at different stripping radial positions varies slightly in compliance with the focusing effects, as it is illustrated in Figure 5.29. As the beam moves forward in the cyclotron, the radial decreasing magnetic field enhances the axial focusing. It is clear how the axial size of the beam at the stripping is reduced from 8 mm at $r_{SF} = 90$ mm to 6 mm height at $r_{SF} = 110$ mm. The beam is well centered axially at the stripping foil, with low dispersion of momentum (Figure 5.30). In addition, the beam is perfectly intercepted in a reduced area in the radial direction (less than 1 mm radius) in comparison with the total length of the foil (8.5 mm).

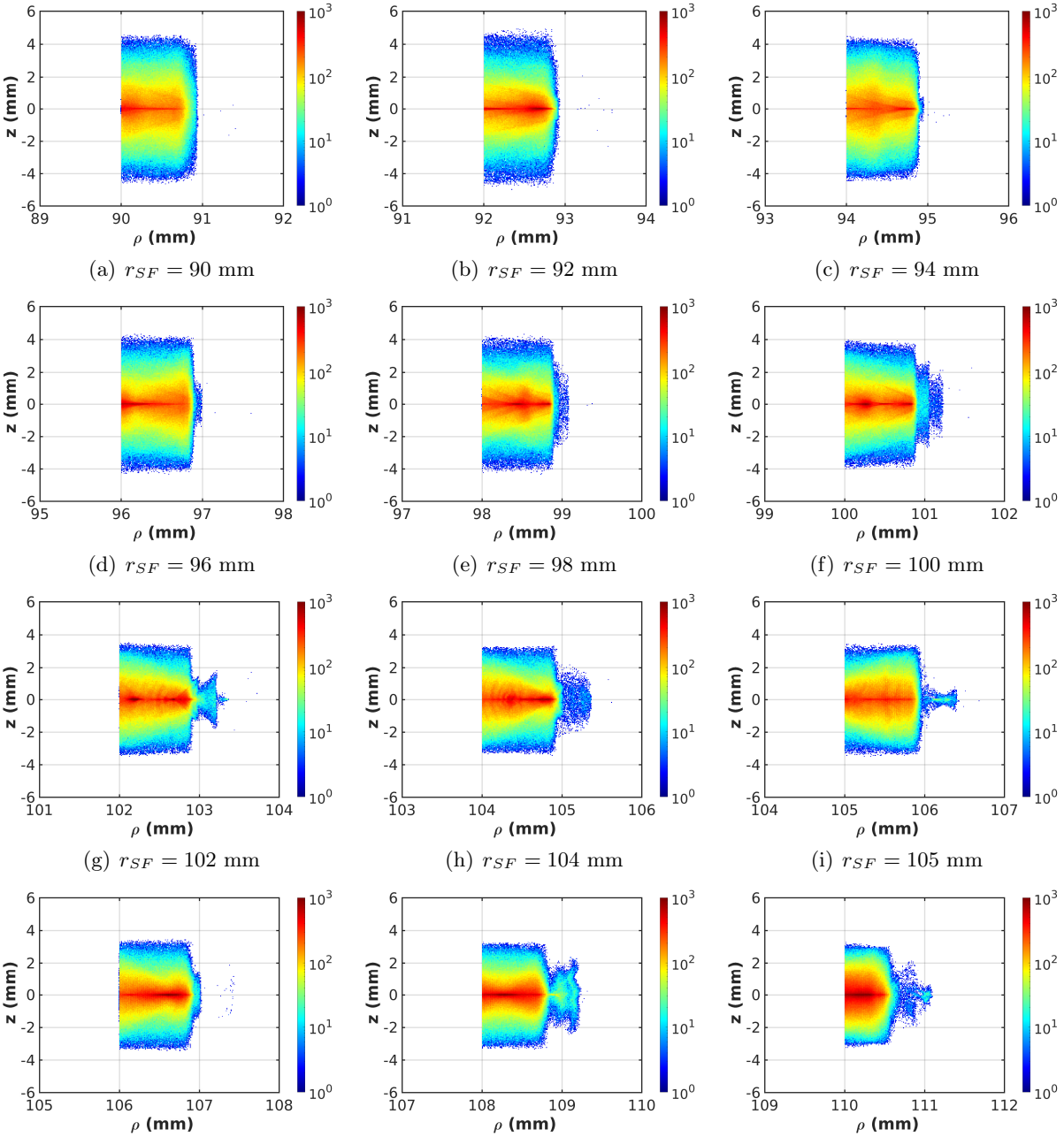

(a) $r_{SF} = 90$ mm (b) $r_{SF} = 92$ mm (c) $r_{SF} = 94$ mm

(d) $r_{SF} = 96$ mm (e) $r_{SF} = 98$ mm (f) $r_{SF} = 100$ mm

(g) $r_{SF} = 102$ mm (h) $r_{SF} = 104$ mm (i) $r_{SF} = 105$ mm

(j) $r_{SF} = 106$ mm (k) $r_{SF} = 108$ mm (l) $r_{SF} = 110$ mm

Figure 5.29: *Beam profile at stripping foil for different radial positions at a fixed angle (φ_{SF}=251.5°). The color scale illustrates the particle density in logarithmic scale.*

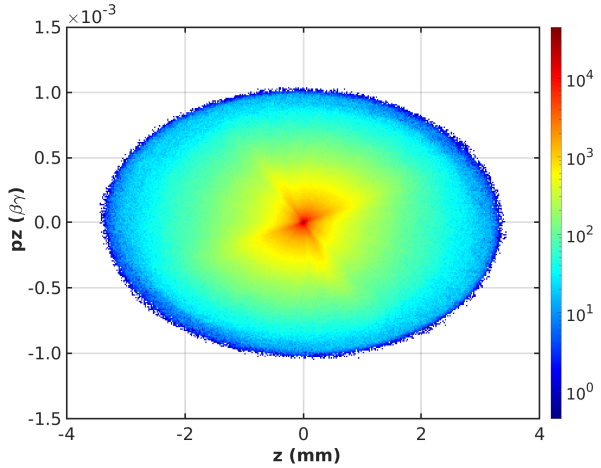

Figure 5.30: *Axial phase space at the stripping foil located at* $r_{SF} = 110$ *and* $\varphi_{SF} = 251.5°$. *The color scale illustrates the particle density in logarithmic scale.*

With regard to the extraction angular position adjustment, the interception of the beam in different azimuth result in some slight size variation because the beam along the cyclotron path is continuously oscillating. However, the impact of the angular position on the beam size in both radial and angular directions is totally negligible, only small fluctuations of the order of 0.1 mm in axial and less than 0.03 mm in radial are observed. Therefore, its impact in the beam properties at the extraction is limited. Nevertheless, the angular position has to be calibrated to perform an adequate beam transportation from the stripping foil until the target, as it is going to be presented below.

Beam transportation to the target

Once the beam has been characterized in the extraction point, the optimum position for the stripping foil resulting in a proper transportation to the target must be established. The remaining magnetic field and the direction of the beam momentum after the stripping process determine the motion of the beam. To illustrate the influence of the different radial and angular positions of the stripper, Figure 5.31 shows the trajectories for the reference particle, arising from the center of the slit of the ion source, at different stripper locations.

With that in mind, it is clear how the extraction emplacement plays a fundamental role in the final beam transportation. A wrong position of the stripper will incur in a high-energy proton beam colliding in the rear part of the vacuum chamber or even in a lateral, increasing the activation of the machine. Figure 5.32 illustrates the final beam position at the end of the chamber for different locations of the stripping foil. Hence, the position of the extraction system have to be optimized to supply a proper beam transportation to the target port.

Given the relevant role of the beam transmission in the requirement fulfillment, a detailed analysis with multi-particles simulations provides the adequate combination of the stripping foil locations resulting in a valid beam transportation (Figure 5.33). In addition, the beam transmission rate has to be maximized, that is to say, the beam must be well focused within the

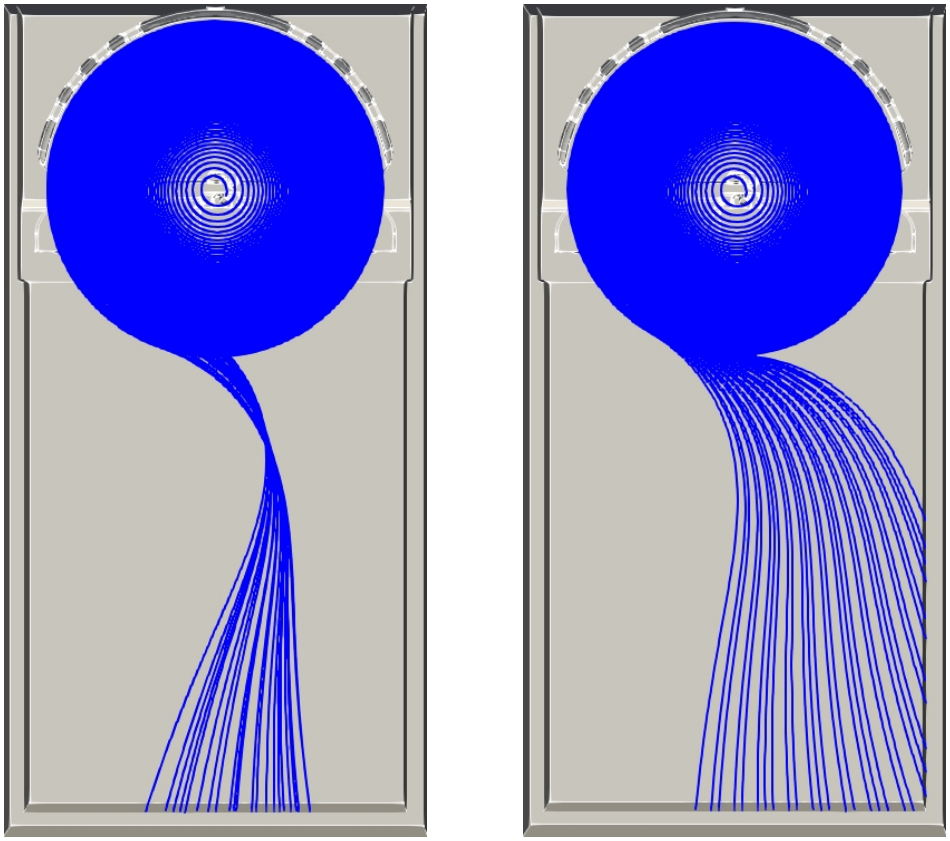

(a) (b)

Figure 5.31: *Beam trajectories for a reference particle at different stripping foil position: (a) radius variation with fixed angle ($\varphi_{SF} = 251.5°$) and (b) modifying the angular location for fixed radius ($r_{SF} = 110$ mm).*

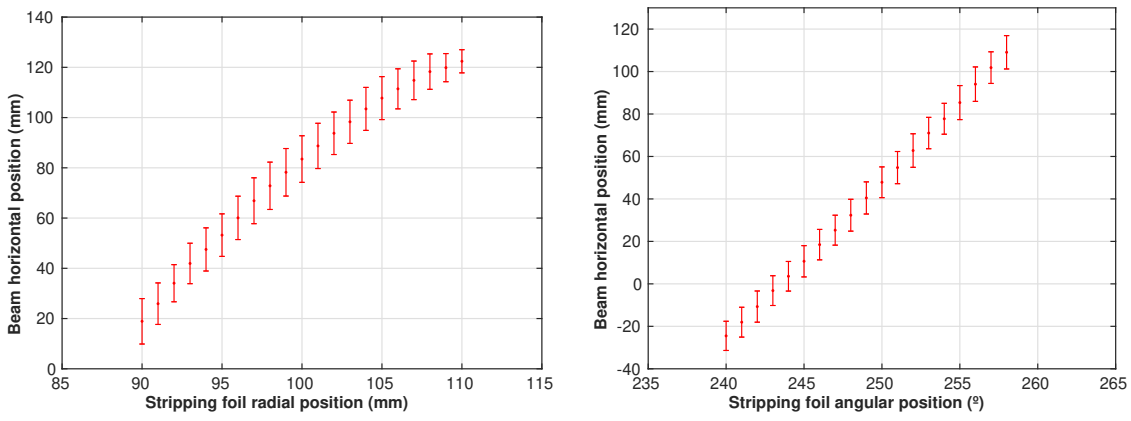

(a) (b)

Figure 5.32: *Beam position at the end of the vacuum chamber for (a) different radial location of the stripping foil at a fixed angle ($\varphi_{SF} = 255.5°$) and (b) diverse angular position at a fixed radius ($r_{SF} = 110$ mm). The error bars represents the rms beam size in such horizontal direction.*

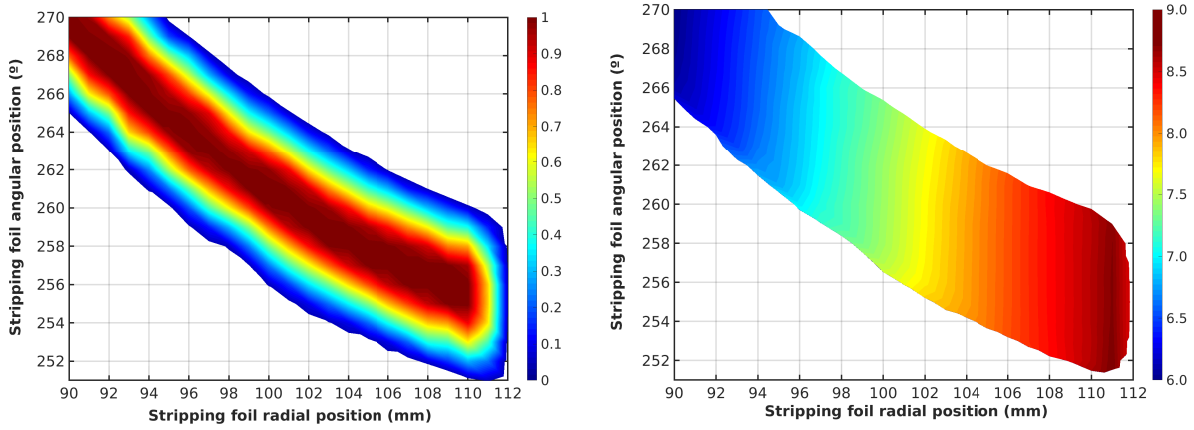

(a) (b)

Figure 5.33: *Stripping foil positions for an adequate beam transportation to the target aperture showing (a) the beam survival rate from the stripper until the target and (b) the final mean energy of the beam.*

target port, without losses outside that aperture or in the another point of the vacuum chamber. If only the stripper locations providing beam transportation with minimum losses are considered (beam survival rate higher than 98%), a tight range of $\sim 3°$ for each radial position can be set as optimum. Thus, the optimum position for the stripping foil resulting in a proper transportation to the target is set by a tiny interval of angular positions for each radius location of the stripping foil. To complement the analysis, Figure 5.33(b) also illustrates the energy of the beam in the extraction position. Therefore, the radial extraction position determines the final energy of the beam, while the angular location has to be adapted to transport the entire beam into the target aperture. The combination of the beam transmission factor and the final energy allows the estimation of radioisotope production using the saturation yield values in the energy range of

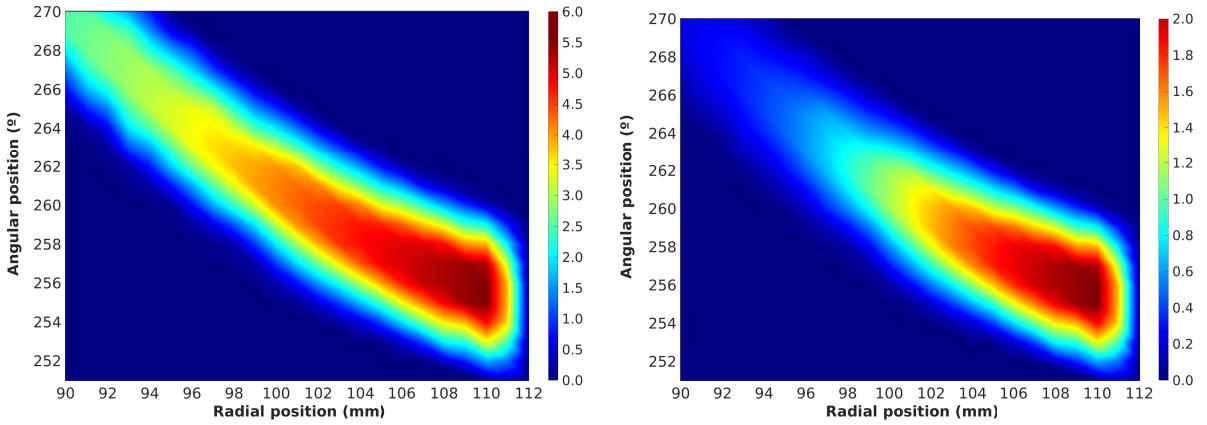

(a) ^{18}F (b) ^{11}C

Figure 5.34: *Relative radioisotope production of (a)* ^{18}F *and (b)* ^{11}C *according to the nuclear reactions* $^{18}O(p,n)^{18}F$ *and* $^{14}N(p,\alpha)^{11}C$ *respectively at different position of the extraction. The relative radioisotope production is expressed in GBq/*μA *(color scale).*

interest (see section 2.1.1, Figure 2.3(b)). The activity produced is calculated from a polynomial fit of the saturation yield data in the energy range of interest taking into account the beam survival rate. Therefore, the results, illustrated in Figure 5.34, shows the relative radioisotope production for ^{18}F and ^{11}C in function of the initial beam current injected.

Beam characterization at the target aperture

When the position of the stripping foil is appropriately established, the proton beam is transported to the target aperture without losses, coming through it entirely. However, the beam profile is modified during the transportation. Once the beam is suitably extracted by the stripping foil, a relevant dispersion in the transverse horizontal direction is produced, while the axial distribution is slightly increased even though the remaining magnetic field provides a reduced focusing force. This last effect is appreciated in Figure 5.35, illustrating the axial phase space in the target, in comparison with the equivalent in the stripping foil (Figure 5.30).

Figure 5.36 shows the beam profile at the target aperture for a stripping foil position providing a suitable transportation. It is clearly evident how the transverse horizontal size –in this case x direction– is considerably expanded. Despite this, the beam can come through the target aperture without colliding in the outline edges. Nevertheless, this larger transverse beam size is the cause of the reduced interval of extractions positions that provide proper beam transportation, because in other locations the beam particles can collide in the target aperture, losing part of it in the edges with the associated issues of radiation activation, material damages and reduction of the final beam current.

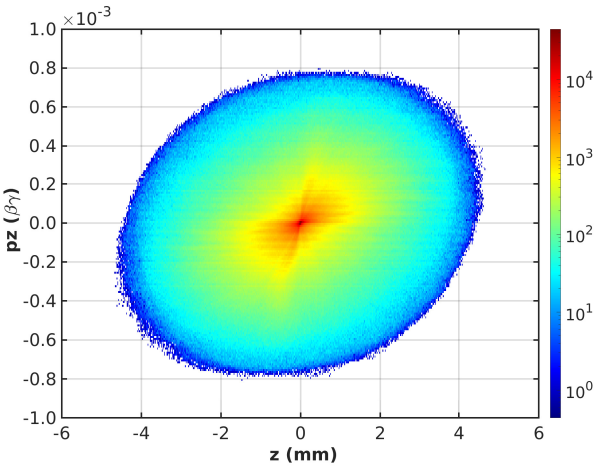

Figure 5.35: *Axial phase space at the target aperture for a proper stripper location ($r_{SF} = 108$ mm - $\varphi_{SF} = 255.5°$). The color scale illustrate the particle density in logarithmic scale.*

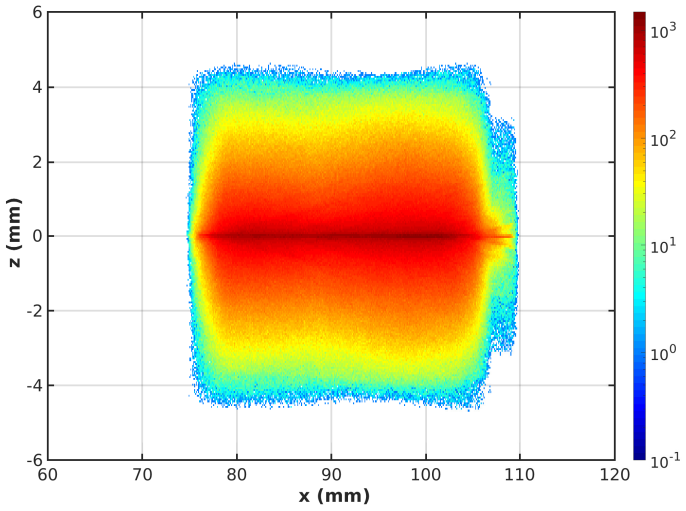

Figure 5.36: *Beam profile at the target aperture for a proper stripper location (r_{SF} = 108 mm - φ_{SF} = 255.5°).*

5.2 Beam dynamics analysis in the final assembly

In the previous section, a beam dynamics study focused on analyze the different relevant effects on the beam acceleration has been presented. The results obtained from electric and magnetic fields computed by finite element software and using the design parameters of the cyclotron. The purpose of that preliminary study is to provide significant information to understand the behavior of the AMIT cyclotron, the influence of different parameters on the final state of the beam and to determine the appropriate adjustment of each variable parameter to maximize the radioisotope production with a high quality beam and minimum losses. The analysis was presented in the different stages of the acceleration to clarify the exposition of the different phenomena. The subsequent section is centered to review the beam dynamics of the AMIT cyclotron incorporating the final settings of different subsystems as well to evaluate the sensitivity of several parameters slightly outside the design values. The objective is to perform a realistic implementation of the cyclotron, complementing the overview results of the previous section to optimize the final operation of the accelerator.

5.2.1 Extraction system movement

The subsection 5.1.3 has presented the characterization of the beam extraction at different radial and angular positions according to cylindrical coordinates (radius-angular) referred to the cyclotron center. The beam properties, such as final energy and the beam transport to the target, has been analyzed under the variation of the extraction point. However, based on the beam dynamics design requirements, the engineering design of the extraction system has been conditioned by the intrinsic space limitations of the accelerator, resulting in a mechanical structure with a particular movement. The radius and the angular extraction position (referred

to the cyclotron center) can be set indirectly by a longitudinal and rotational movement of the extraction structure. For this reason, a further beam extraction analysis is carried out to integrate the real movement of the stripper.

From the engineering point of view, the extraction mechanism (see subsection 2.2.5) consists of a set of carbon foils located in a movable mechanical arrangement with longitudinal and rotational degrees of freedom. The structure has been designed taking into account the limited space inside the vacuum chamber and considering the need to emplacement it from the back of the camera so as not to affect other components, which results in intricate movement. Figure 5.37 shows a schematic top view of the extraction mechanism with the directions of the movement of the structure. The longitudinal displacement, l_{SF}, fixes the extraction radius of the beam, whereas the rotation movement, φ_{SF}, establishes the angular position with a minor influence in the radius. The longitudinal displacement does not follow a radial direction, but it moves along y coordinate –according to the reference system presented in this dissertation–. Combining both independent motions, the stripper can be placed in an array of positions respect of the cyclotron center, with a movement adequately versatile to reproduce the optimum extraction position analyzed in previous section. The correlation between the actual extractor movement and the position referred to the cyclotron center (radial and angular variables) is illustrated in Figure 5.38, showing the equivalent position of the stripping foil at different longitudinal and rotational displacement.

Once the extraction system movement has been clearly described and it has been connected to the cyclotron frame, the positions of the structure to achieve an adequate final beam arrangement

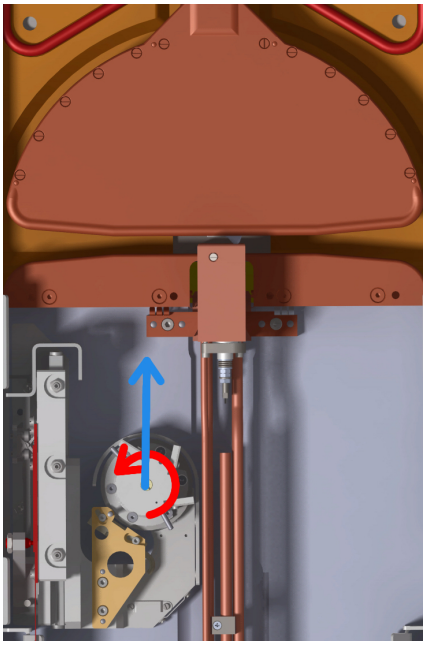

Figure 5.37: *Schematic top view of the extraction mechanism in the vacuum chamber with the directions of the movement of the structure. The blue arrow indicates the longitudinal displacement, l_{SF}, and the red arrow denotes the rotation movement, φ_{SF}.*

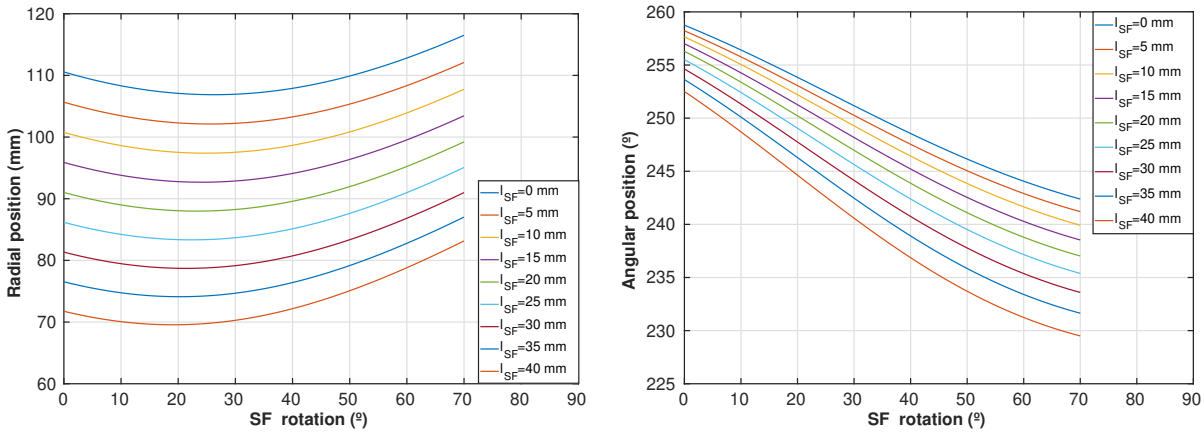

(a) (b)

Figure 5.38: *Relation between real stripping foil displacement (given by l_{SF} and φ_{SF}) and the equivalent position referred to the cyclotron center (radial (a) and angular (b) position). The positions are calculated from the inner part of the foil.*

has to be evaluated. A comparison between figures 5.33 and 5.38 provides a general notion of the actual position of the stripper that makes available the beam transmission to the target with suitable beam properties. Additionally, a superposition of the realistic movement with the optimum radial and angular extractions positions refereed to the cyclotron is illustrated in Figure 5.39 to clarify completely the extraction mechanism movement compatible with the beam transportation and energy analyzed in the previous section. These results show that the extraction mechanism can perform the beam extraction with total transmission to the target from

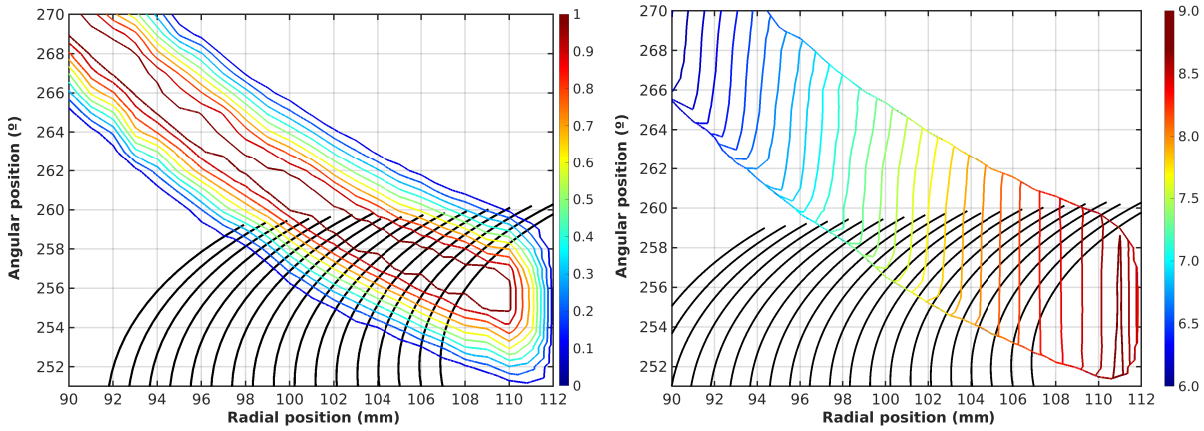

(a) (b)

Figure 5.39: *Extraction positions referred to the cyclotron center for an adequate beam transmission to the target with a contour plot (color lines) of the beam survival rate from the stripper (a) and the beam energy (b), with a superposition of the real movement of the extraction mechanism (solid black lines). Each black line represents a longitudinal position l_{SF} of the structure over all the rotational motion that intercepts the beam. From right to left, the longitudinal position plotted are $l_{SF} \in [0, 16]$ mm spaced at 1 mm interval.*

101 mm radius to 108.5 mm, with an associated energy tuning is limited to $[7,4-8,6]$ MeV. Beyond that radial position interval the beam will be partially transported to the target, reducing the beam current and increasing the activation of the machine.

Additionally, the extraction structure movement also modifies the incidence angle of the beam on the stripping foil (Figure 5.40). The expected positions of the final structure that would provide valid beam transmission, according to the results presented in Figure 5.39, entails a maximum angular deviation of the stripping foil of $\sim 20°$. The effect of this deviation on the extraction point and the beam transmission is negligible, as it has been corroborated through specific multi-particles simulations. The outcomes provided the preservation of the total beam transmission for some stripper positions, despite the non-perpendicular incident angle interception in the stripping foil.

In addition to that, the preliminary study about the extraction system (see section 2.2.5) performed with SRIM code [145] showed a rms deviation of $\sim 0.35°$ of the beam from the incident direction after crossing a carbon foil with a suitable thickness. Therefore, the momentum direction of the beam is almost unaltered in the extraction process. However, it should be noted that the stripping process involves an energy loss that is increased when the incidence is not perpendicular (see Figure 2.15(b)).

Summarizing, the actual extraction system mechanism is adapted to perform an adequate stripping of the H^- beam and adjusting properly the transportation to the target of the resultant proton beam in accordance with the beam requirements of the cyclotron. Figure 5.41 illustrates a representation of the reference particle track within the 3D model of the cyclotron, showing the entire trajectory, the extraction process and the subsequent deviation of the emerged proton. Furthermore, a tune of the final energy can be performed preserving the subsequent beam transportation. However, the adjustment of the extraction positions is limited in comparison with the design conditions of the mechanism. The results obtained from this study will allow carrying out small modifications in the extraction mechanism to cover a large range of variation of the stripper positions that will result in a total transmission of the beam.

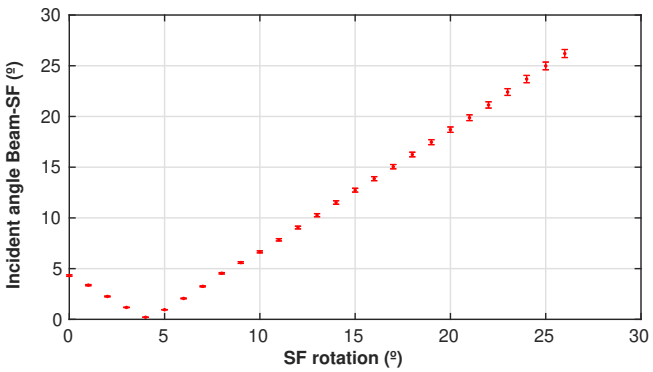

Figure 5.40: *Beam incident angle on the stripping foil for different rotation at fixed longitudinal displacement ($l_{SF}=0$ mm). The angle is calculated from the mean momentum of the beam on the stripper and the orthogonal direction of the foil, and consequently, 0° indicates perpendicular interception.*

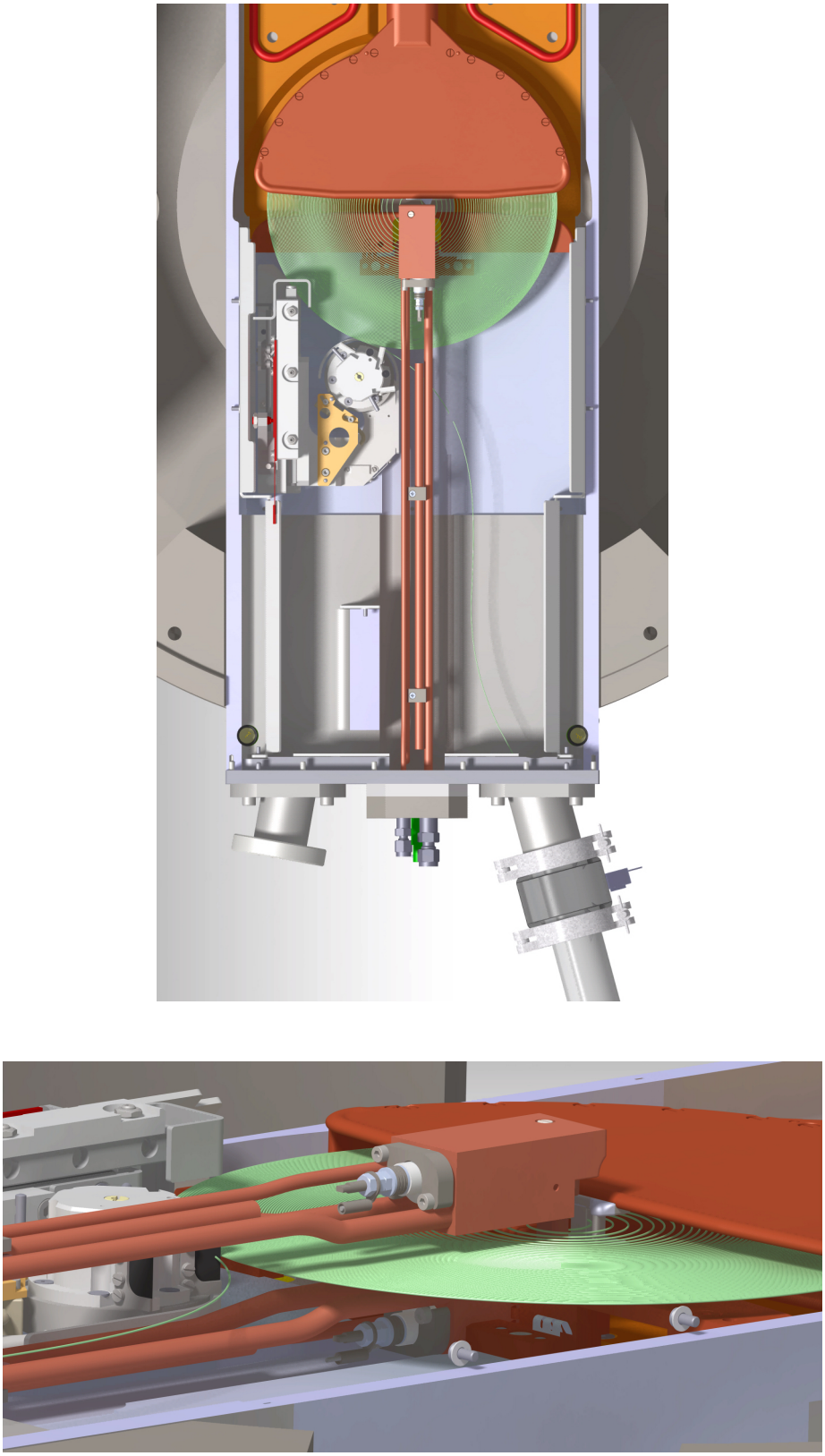

Figure 5.41: *Reference particle track (green line) within the 3D model of the cyclotron showing the extraction process and the beam transportation to the target.*

5.2.2 Cyclotron operation mode

The results of the preliminary beam dynamics study of the AMIT cyclotron has been presented in section 5.1. Making use of multi-particle simulations performed with OPAL, a deep knowledge about the beam acceleration has been acquired. The analysis have provided information about the radiofrequency system, the total phase acceptance, the beam characteristics along the acceleration process and the beam extraction, among other issues. Furthermore, they have established a working scheme to implement beam dynamics studies of a given cyclotron configuration.

Additionally, it is necessary to take into account some variations of the cyclotron parameters in the final assembly as well as the tuning capacity of the principal parameters in the cyclotron related to the electric and the magnetic fields. This analysis will provide meaningful information with regard to a fine tuning of the cyclotron operation conditions assessing the impact of the actual parameters achieved in some components to anticipate possible issues in subsystem not yet commissioned as the magnet as well as potential enhancements of the cyclotron. Therefore, the beam dynamics study is extended to analyze other cyclotron configuration able to provide the radioisotope production beam requirements according to the final assembly of the subsystems.

As it has been exposed along the beam dynamics studies of this thesis, an adequate beam acceleration in a classical cyclotron requires a particular combination of the magnetic field, the RF frequency, and the applied accelerator voltage. This conjunction of parameters is called the cyclotron configuration or operation mode for a clear exposition along this dissertation. A minimum alteration in any of these factors would modify the entire beam dynamics and can incur in serious variations in the final current and energy, the beam quality, the optimum extraction conditions, the level of radioactive activation, etc. Therefore, it is highly relevant to understand the relation between the diverse parameters as well as to specify their influences or limitations during the operation.

The dependence between the main parameters that describe the beam trajectories for different configurations can be greatly simplified by applying the similarity theorem [134,183]. In a specific operation mode, the energy gain and the transit time are determined by the scaling parameter:

$$\chi = \frac{d^2 B^2 q/m}{V_0} = cte \tag{5.1}$$

where V_0 is the dee voltage, B the magnetic field strength, q/m the specific charge of the particles, and d the accelerating gap width. The scaling factor χ defines in the non-relativist energy range the relationship of a constant orbit geometry for a fixed source-puller gap:

$$\frac{B^2}{V_0} = cte \tag{5.2}$$

The similarity relationship enables to estimate the equivalence between the different parameters of the operation mode for constant orbit geometry. In this way, if the magnetic field is adjusted by a factor a, the dee-voltage must be change by a^2 to remain the same orbit geometry. However, some beam deviations arising from the time that the particles take to cross the

different accelerating gaps disturb the similarity condition. This transit time is not negligible in comparison with the RF period. The peak energy gain and the electric field phase excursion along the acceleration process are also affected. Consequently, large modifications in the acceleration mode will require readjustments of the central region to account such effects. Nevertheless, disregarding these restrictions, the similarity relationship is able to be employed to lay down the different cyclotron operation modes resulting in a beam transmission and acceleration in the cyclotron.

Cyclotron fine tuning

A detailed study on the expected variations of the cyclotron configuration parameters under the real tolerances in the radiofrequency and magnet system is presented. The RF frequency value is determined by the design and fabrication of the cavity. As it is shown in Table 2.3, the frequency is 60.134 ± 0.250 MHz, although low power measurements provided a tighter range [123]. Moreover, the nominal voltage (60 kV) can be increased until ~ 67 kV, according to high power tests and conditioning measurements. The results of those tests entail a reliable starting point for a beam dynamics optimization inasmuch as the value of the RF frequency has been experimentally corroborated. Hence, the cyclotron configuration must be adapted to this RF frequency, rearranging the magnetic field to keep the beam acceleration until the extraction region. The magnetic field is easily adjustable during the cyclotron operation through the current of the coils, and therefore it is convenient to perform the analysis adapting it to the measured radiofrequency values. The aim of this study is to determine the values of the cyclotron configuration parameters compatible with the final beam requirements.

The RF frequency value was estimated at the design stage of the project as the optimum value for a 4 T magnetic field. In the previous section, the study of the beam dynamics features was based on a lower magnetic field (3.94 T), and consequently, a lower optimum frequency was considered. This magnetic field was obtained from the results of the calculations with finite element software. This discrepancy between nominal field and the field provided by the simulations may be due to discrepancies in the magnetic models produced by modifications of the staking factors, small variations in geometries as the design has been adapted and intrinsic finite element simulations uncertainties. However, the difference in field values is not a real issue because a slight increase of the current of the coils will provide a 4T field, as it will be verified in future magnetic tests. Therefore, the dynamics study must be adapted to the nominal values, without despising the previous results that have provided meaningful information about general behavior of the beam in the cyclotron.

It is important to remark that in this analysis the simulations have been performed without taking into consideration the extraction system with the objective of identifying the maximum conditions of energy and radius achievable in each configuration. Therefore, all the results provide the maximum value attainable by the beam acceleration, independently of the location of the stripping foil.

Radiofrequency - magnetic field relation

The beam dynamics is evaluated under nominal conditions of frequency (f_{RF} = 60.134 MHz) and voltage (V = 60 kV), with modifications of the magnetic field that will provide an adequate acceleration through the cyclotron. The tuning between magnetic field and RF frequency is considerably sensitive. The RF frequency sets the phase of the electric field perceived by the particles in each accelerating gap, influencing directly the energy gain. By the other hand, the magnetic field is in charge of bending the trajectories in the non-acceleration region, and therefore it determines to the revolution of the particles, according to the equation (1.3). In consequence, the results of multi-particle simulations (Figure 5.42) show a constrained admissible combination of RF frequency and magnetic field values that provides a proper beam acceleration to achieve the beam requirements of the cyclotron, that is to say, enough average radius to reach the extraction point satisfying the minimum energy for radioisotope production. The averaged energy values at the maximum acceleration point, that is to say, averaged of the maximum attainable energy, are obtained from data of the whole beam distribution in the phase acceptance range.

This critical balance between radiofrequency and magnetic field is explained by the phase excursion along the acceleration. The beam acceleration continues whereas the polarity of the electric field perceived by the particles in each gap will be adequate to impulse them forward. For that reason, the phase of the radiofrequency must be lie in the correct range of the RF cycle in each acceleration gap, that in case of the gap from the dee to the dummy-dee corresponds to $\phi_{RF} \in [90, 270]$. For that purpose, the RF frequency and the particle revolution frequency, in compliance with the magnetic field, has to be finely tuned. The opposite situation produces the deceleration of the beam. Figure 5.43 illustrates the beam excursion for different magnetic field at the nominal RF frequency. As the magnetic field increases, the phase excursion of the particles is also risen and the achievable energy is higher. However, if the magnetic field is increased beyond 4 T, the revolution frequency is modified, and the particles will reach some gap

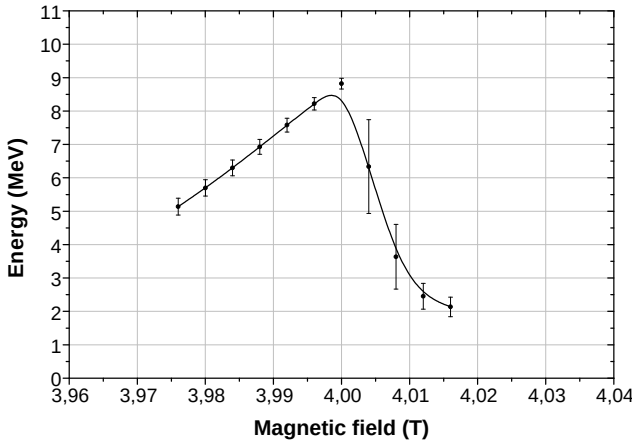

Figure 5.42: *Mean energy dependence on the magnetic field for the nominal RF frequency (f_{RF} = 60.134 MHz) at the maximum acceleration point. Solid line is a B-spline curve. The error bars represent the rms deviation considering the whole beam distribution in the phase acceptance range.*

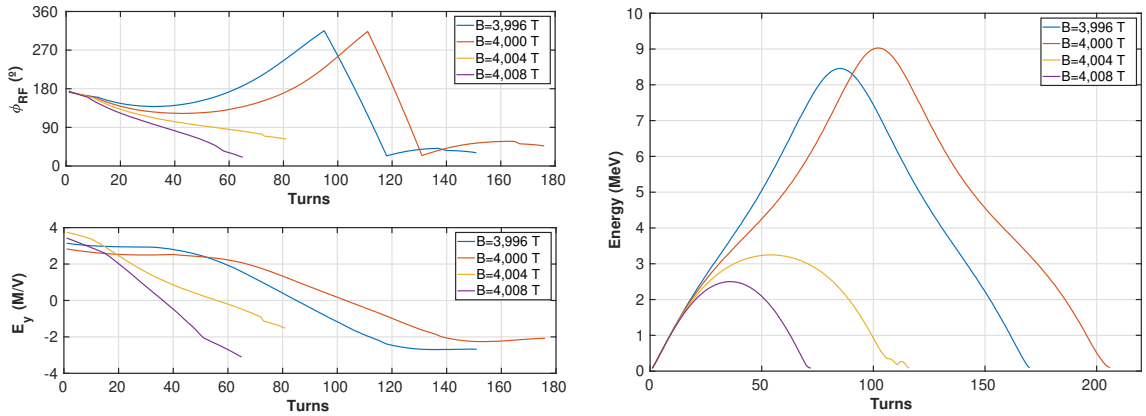

(a) (b)

Figure 5.43: *Beam excursion along the path for different magnetic fields at the nominal RF frequency ($f_{RF} = 60.134$ MHz). (a) Radiofrequency parameters at the center of the gap (top - RF phase, bottom - Electric field E_y) and (b) energy evolution. The particles are injected at $\phi_{RF} = 300°$ initial phase. It is shown how the combination of radiofrequency and magnetic field sets the maximum acceleration of the beam.*

out of the proper RF phase range, perceiving a non-accelerating field. This is clearly exposed in Figure 5.43(a), where it is appreciated how the electric field presents a decelerating strength when the particles achieve the gap out of the proper phase interval. Thereby, the maximum energy attainable depends on the relation between the RF frequency and the revolution frequency.

In addition, this fine tuning depends on the starting RF phase conditions. Particles will have a specific phase excursion along the acceleration path for each arrangement of magnetic field and radiofrequency according to the initial phase perceived in the injection. Therefore, small differences at the end of the process are appreciated, in particular in the maximum energy of the beam (Figure 5.44). This effect is especially remarkable for some cyclotron configurations in which not all the phase range presents the same acceleration pattern, that is to say, when some RF initial phases will provide a suitable acceleration but some particles injected in a slightly different RF phase will be out of the optimum accelerating in some intermediate point of the path. This particular case is illustrated clearly in Figure 5.44(c), where it is significant how initial RF phases do not reach high energies while other initial RF conditions provide correct acceleration. In this case, the variation of the magnetic field leads to a remarkable modification in the phase excursion and therefore in the final energy and total beam transmission. These results establish the magnetic field limit for a fixed RF frequency by the maximum energy achievable as well as by the effect on the phase acceptance range that affect to the energy spread for a fixed magnetic field (see Figure 5.42).

In the case of considering the different RF frequencies that the fine tuning of the system allows, the range of magnetic field is relocated to preserve the conditions for a suitable acceleration (Figure 5.45). The same tendency is observed for different RF frequencies if the magnetic field is suitably adapted. With that in mind, the beam requirements can be satisfied under different configurations.

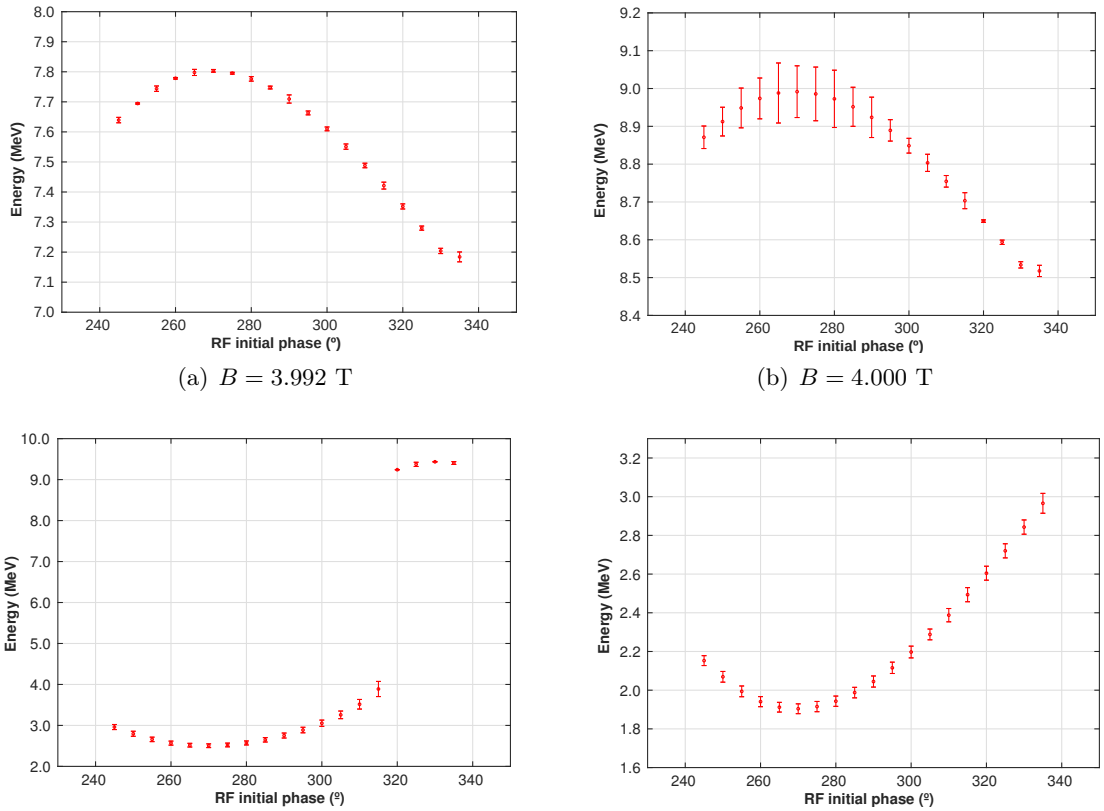

(a) $B = 3.992$ T (b) $B = 4.000$ T

(c) $B = 4.008$ T (d) $B = 4.016$ T

Figure 5.44: *Maximum energy averaged as a function of the initial electric field phase in the injection at the nominal RF frequency value (f_{RF}=60.134 MHz) for different magnetic fields. The particles from initial phases outside this range do not survive the central region. The error bars are the rms energy spread.*

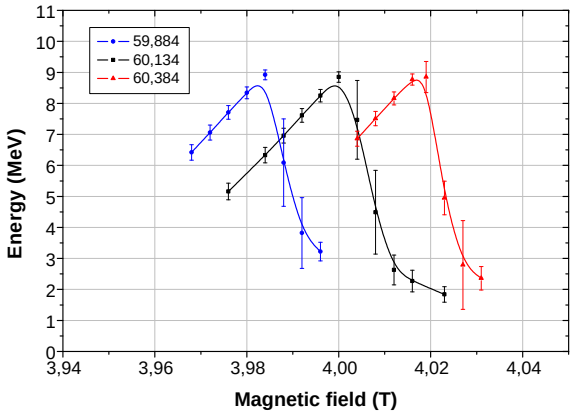

Figure 5.45: *Mean energy at the maximum acceleration point as a function of the magnetic field suitable for different RF frequency within the design tolerances. Solid lines are B-spline curves. The error bars are the rms deviation considering the whole beam distribution in the phase acceptance range.*

Voltage modifications

Once the fine tuning of the magnetic field and radiofrequency has been performed achieving final beam conditions within the accelerator requirements, it is pertinent to analyze the effect of voltage modifications in order to optimize the beam dynamics with a different voltage values.

The particles trajectories are partially determined by the applied voltage, due to the momentum modification and according to the equation (1.2), as it is shown in Figure 5.46. Hence, voltage modifications has a straightforward impact on the central region acceptance. A large variation of the voltage at fixed radiofrequency and magnetic field conditions will cause particle collisions somewhere in the puller. However, the designed puller provide reasonable transmission for a large range of voltages. Figure 5.47 illustrates the beam transmission rate –for all RF cycle– along the central region as a function of the voltage under the nominal conditions of RF frequency and magnetic field. It is clear how over an upper voltage limit the beam current will be drastically reduced by collisions in the central region.

In addition, the voltage determines the energy gain per accelerating gap. Therefore, increasing the voltage, the particles will achieve the extraction point faster, performing less number of turns and consequently minimizing the beam losses. Figure 5.48 illustrates this notable effect in the beam evolution, showing the beam energy as a function of the number of turns and these parameters for different voltage at an optimum stripping foil position ($r_{SF} \sim 108$) according with the results presented in section 5.2.1.

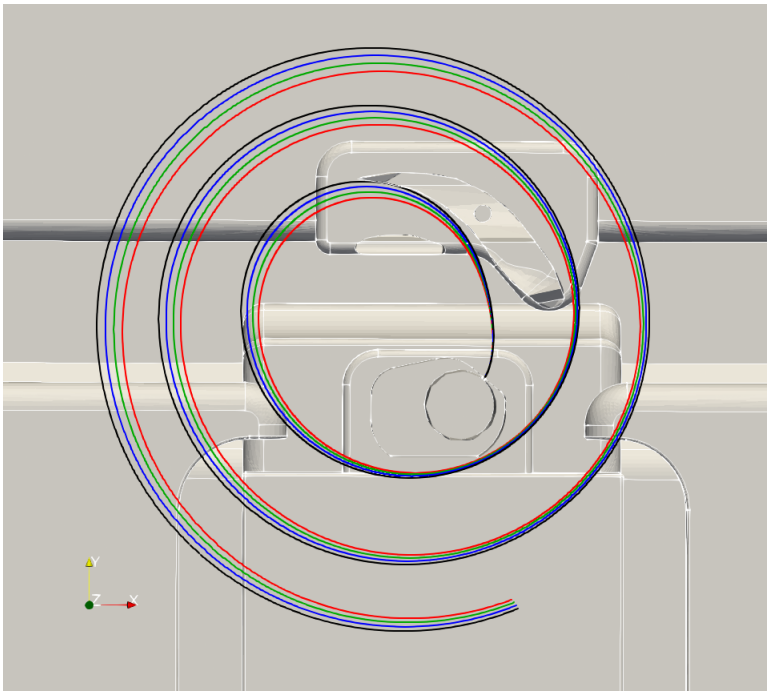

Figure 5.46: *Particle trajectories in the central region for different applied voltages (red* $\rightarrow V = 60.0$ *kV, green* $\rightarrow V = 62.4$ *kV, blue* $\rightarrow V = 64.8$ *kV, black* $\rightarrow V = 67.2$ *kV) at the same RF initial conditions. Particles are extracted from the center of the ion source slit. The RF frequency and the magnetic field are fixed at nominal values (*$f_{RF} = 60.134$ *MHz,* $B = 4$ *T).*

In this way, a remarkable conclusion is achieved. For each cyclotron configuration (magnetic field and radiofrequency), the applied voltage must be optimized according to the phase acceptance and the beam transmission, providing simultaneously a maximum energy gain per gap to minimize the time performed during the acceleration.

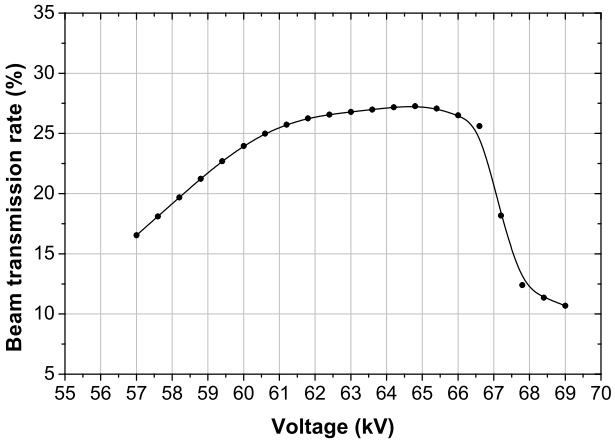

Figure 5.47: *Beam transmission rate for all RF cycle along the whole beam path as a function of the applied voltage under the nominal conditions of RF frequency (f_{RF} = 60.134 MHz) and magnetic field ($B = 4$ T). The solid represents a B-spline curve around the data.*

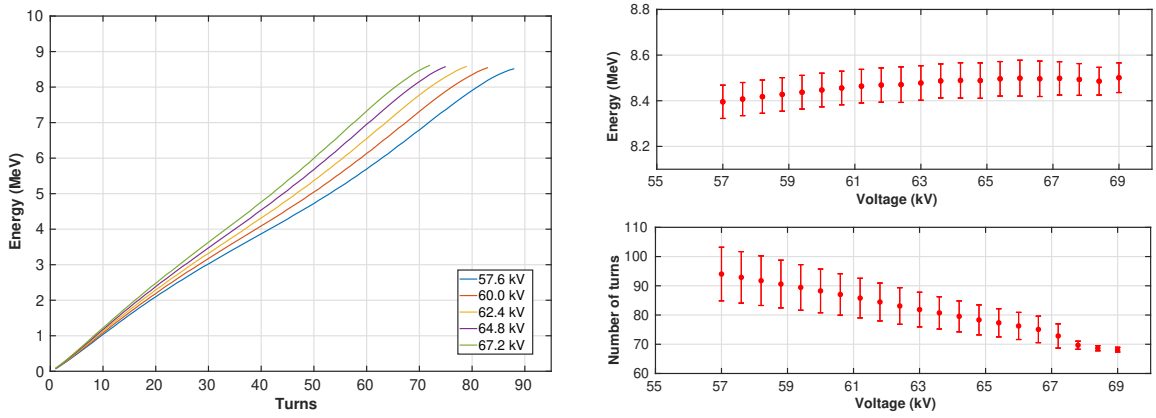

(a) (b)

Figure 5.48: *(a) Beam energy in front of the number of turns for different voltages for a reference particle and (b) the final energy at stripping foil (top) and number of turns performed to the extraction (bottom). The error bars represent the rms deviation for all phase acceptance range.*

Large-scale parameters variations

An interesting beam dynamics study aimed to optimize the AMIT cyclotron is a large-scale variation of the magnetic field. On the one hand, it is important to be aware of potential alterations on the beam dynamics and on the radioisotope production for future improvements of the cyclotron. On the other hand, some different mechanical problems have arisen during

the commissioning of some subsystems. A versatile beam dynamics analysis has to provide information concerning these modifications and a feasible solution of the associated issues.

The AMIT magnet is currently in the last commissioning stage. Some magnet and cryogenic tests have been already performed, although the magnetic measurements have not been realized yet at the nominal coil current and the final commissioning of the autonomous cooling system is ongoing. In addition, several supports of the cold magnet mass were broken during the high current measurements by problems related to the corresponding strain gauges [118]. They have been repaired and their test is still pending. Thus, some engineering issues could entail some variations on the maximum magnetic field that can be finally achieved in the cyclotron. Therefore, it is important to carry out a study given the special relevance of beam transport and acceleration

These magnetic field large-scale variations study has to determine the optimum cyclotron configuration parameters for an adequate acceleration. These large modifications take into account variations of the magnetic field in the range of 20% lower and 10% higher than the nominal field. As it has been exposed previously, any magnetic field modification imposes a RF frequency adjustment keep stable the synchronism condition, in compliance with equations (1.3), (1.5) and (1.6). Then, the ratio between the RF frequency and the magnetic field gives a proportionality parameter that must be kept under modifications of one of these two factors to maximizes the acceleration in terms of the final beam energy. This proportionality parameter can be estimated from the results obtained in section 5.1.2 and used to extrapolate the expected RF frequency value for a given magnetic field. The dependence between magnetic field and RF frequency has been verified through OPAL simulations, showing a linear coupling between them for the maximum attainable energy in AMIT cyclotron (Figure 5.49). The RF frequency acceptance for each magnetic field value is roughly $\sim$0.5 MHz around the expected value.

In addition to adjusting the magnetic field and radio frequency, suitable beam acceleration must consider modifying the voltage to maximize beam transmission from the injection to the extraction region. Hence, this large-scale variations study has been realized in two diverse situations: with constant voltage according to the design voltage of the cavity (60 kV), and with

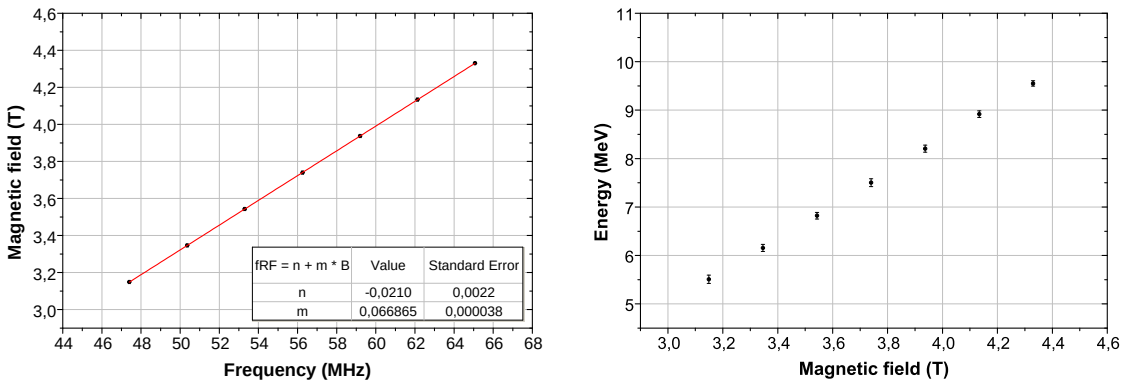

(a) (b)

Figure 5.49: *Magnetic field-RF frequency dependence (a) for a maximized energy (b).*

suitable modification of the dee voltage according to the constant orbit geometry relationship (see equation (5.2)).

First, the effect of large modifications of the magnetic field has been studied considering the fixed voltage at its nominal value. As it has been exposed, the frequency must be tuned to result in a higher energy, even though attending to the beam transmission a large variation of the magnetic field leads to a dramatic reduction of the transmission in the central region. The radius of the orbit is determined by the mean magnetic field, in accordance with equation (1.2): $R = p/qB$. When the accelerating voltage is not modified, the momentum of the particles is almost unaffected, leading to an important change on the particles trajectories. Hence, some particles remain out of the acceptance of the central region and hit the puller or the back part of the ion source, increasing the beam losses. To show the phase acceptance reduction, Figure 5.50 shows the RF cycle emphasizing the phase range that provides suitable acceleration along the entire path under different magnetic fields. In addition, single-particles tracks have been represented in Figure 5.51(a) to illustrate the modifications of the orbits in the central region and how the particles are lost by collisions in the puller.

The final beam resulting from these large-scale parameters variations (magnetic field and and the corresponding optimum RF frequency value) with a fixed accelerating voltage at nominal value is far from the fulfillment of the beam requirements for a suitable radioisotope production. The final relative current is highly reduced by the constraint on the central region phase

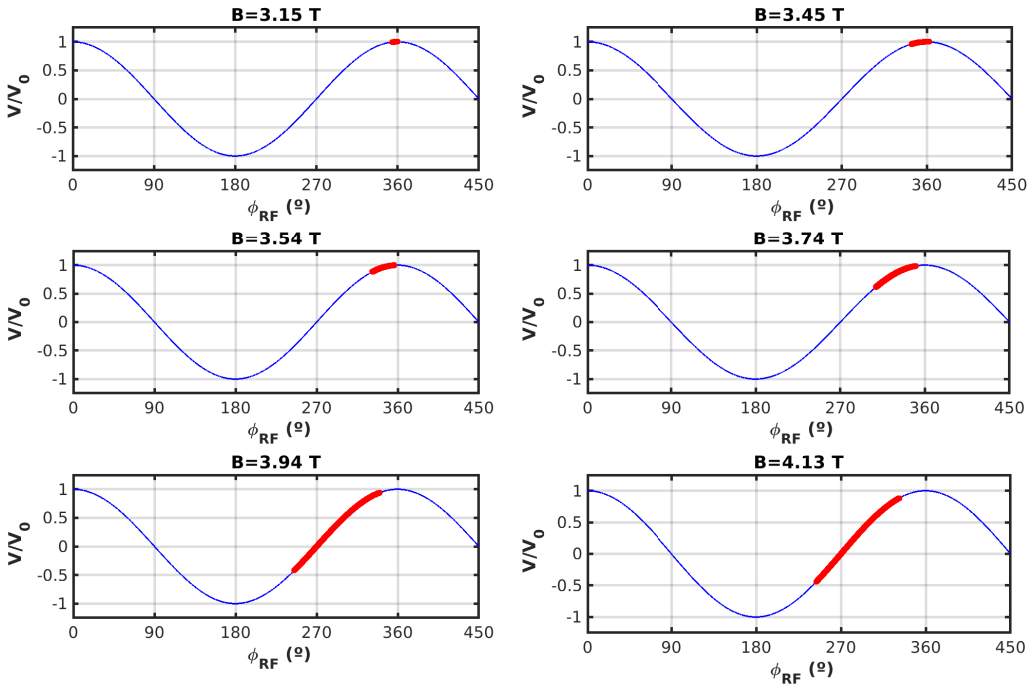

Figure 5.50: *RF cycle highlighting the initial RF phase range that provides a suitable acceleration under different magnetic fields applied at nominal accelerating voltage (60 kV). The reduction of the phase range is due to the central region acceptance.*

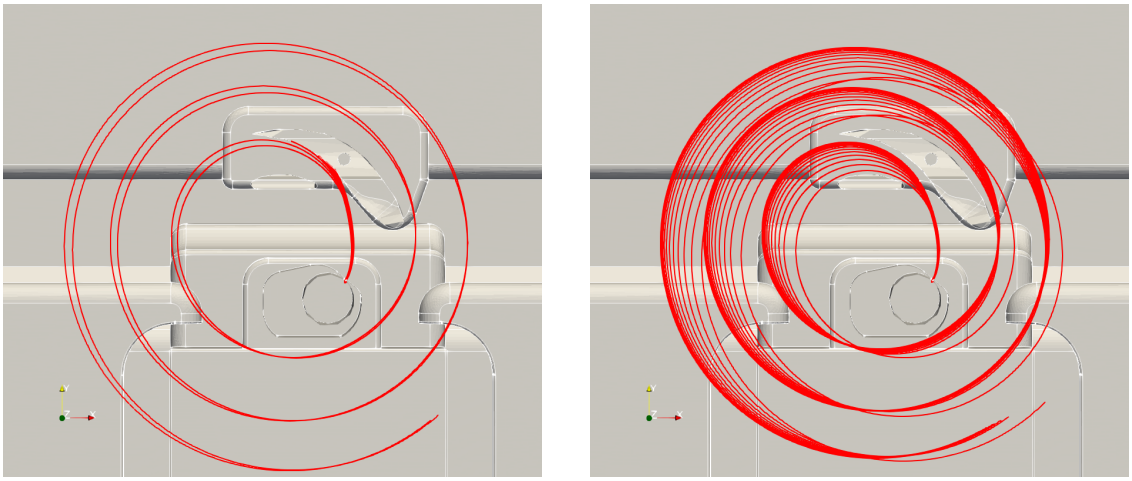

(a) (b)

Figure 5.51: *Particle tracks in the central region for a magnetic field of $B = 3.54$ T with (a) the nominal voltage ($V = 60$ kV) and (b) with adjusted voltage according to similarity theorems ($V = 48.60$ kV). Each track represents a different initial RF phase. The same initial phase interval is shown in both figures.*

acceptance (Figure 5.52(a)): variations of 0.2 T in the magnetic field reduce $\sim 50\%$ the beam transmission. Moreover, these modifications involve variations in the final energy achieved as well as the number of turns to reach the extraction point (Figure 5.53) because the dependence energy-radius is altered and since the maximum radius of extraction is limited by the dee, variations of the magnetic field will condition the energy enormously.

In the event of a large variation of the magnetic field and retuning the RF frequency, given the large transmission loss in the central region, the voltage adjustment according to the ratio can be used to obtain a constant orbit geometry relationship (equation (5.2), Figure 5.54) to achieve a suitable beam acceleration. The phase acceptance range is preserved through the central

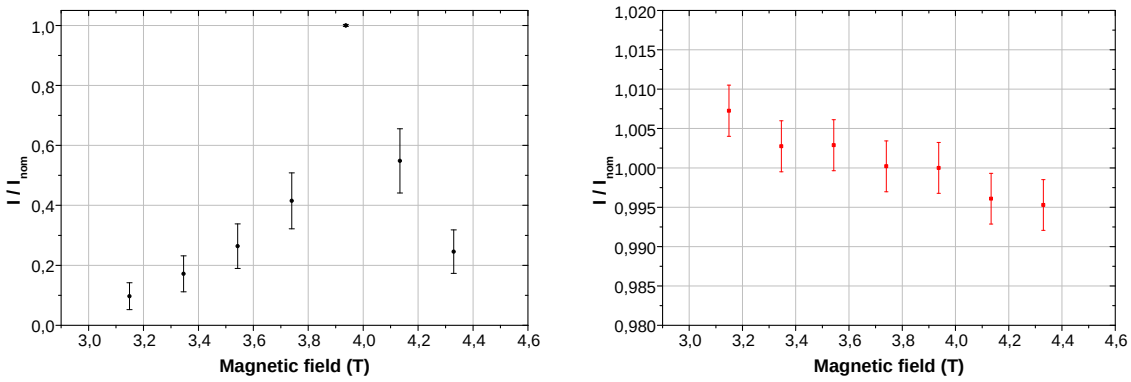

(a) (b)

Figure 5.52: *Relative beam transmission for different mean magnetic fields at optimum extraction point in case of nominal voltage (a) and modifying acceleration voltage (b). The results have been obtained for an injection current unaltered. The error bars are calculated from the statistical uncertainty associated with the number of particles reaching the stripping foil.*

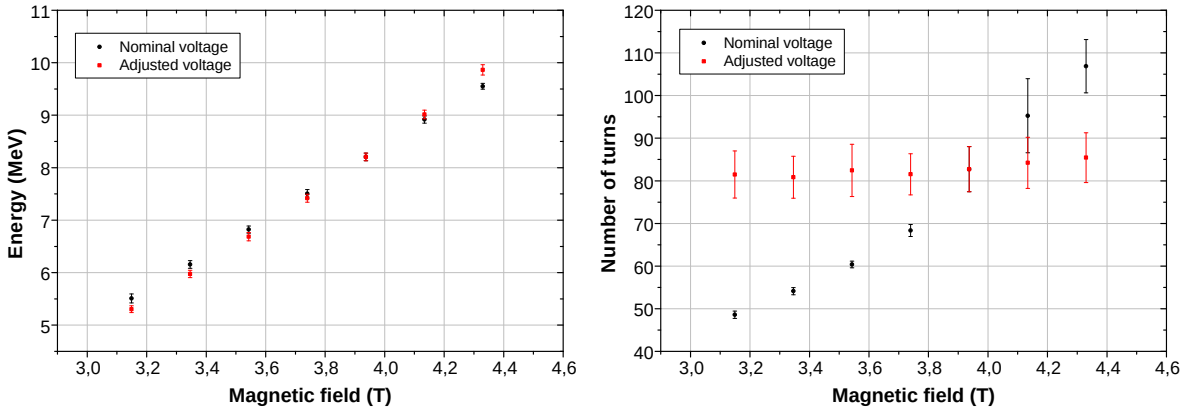

(a) (b)

Figure 5.53: *Final mean energy (a) and number of turns (b) needed to reach stripping foil at optimum position in case of nominal (black) and adjusted voltage (red) according to similarity theorems. The error bars are calculated as the rms deviation from the mean value at stripping foil for particles in all phase acceptance range.*

region and along the whole beam path adapting the accelerating voltage. This is illustrated in Figure 5.51(b), where the single-particle track-orbits in the central region are plotted for different voltage conditions with the same magnetic field. The diverse tracks represent different RF starting phases. For a lower magnetic field and nominal voltage, the orbits will impact in the inner part of the puller because the magnetic is not enough strong to bend the particle trajectories before to collide; whereas the adjustment of the voltage provides an adequate acceleration due to the reduction of the momentum gain in the acceleration gap let pass the beam. In consequence, the beam transmission is maintained by the voltage adjustment (Figure 5.52(b)). The final energy of the beam (Figure 5.53(a)) is not altered by the voltage, except for slight statistical fluctuations, because the energy is conditioned by the extraction radius imposed by the boundary geometry of the cyclotron independently of cyclotron configuration. Likewise, it establishes a minimum magnetic field for the radioisotope production objective, according to the beam requirements (see section 2.1.1), as well the chance of increase the radioisotope production with a slightly higher magnetic field. The number of turns realized to reach the extraction point (Figure 5.53(b)), related indirectly with the likely beam losses, is kept constant under these variations.

It has to be commented that the beam transmission results have been obtained for a constant injection current, unmodifying the beam current extracted from the ion source according to the applied voltage. Therefore, a relevant reduction in final beam current is expected in case of the adjustment of the voltage with a lower magnetic field.

The analysis of large-scale variation of the cyclotron configuration parameters provides worthwhile information about beam dynamics changes under those modifications. To summarize, a modification of the magnetic field alters largely the final beam energy. In case of a low magnetic field, the main issue arises from the energy reduction that disrupt the radioisotope production. This energy limitation is directly imposed by the geometry of the cyclotron because the beam can not be accelerated in orbits with radius greater than the internal boundaries of the dee.

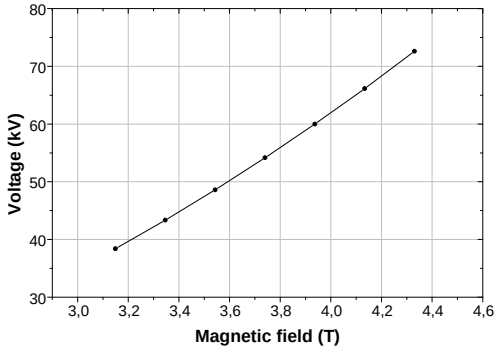

Figure 5.54: *Voltage in front of magnetic field according to the constant orbit geometry relationship.*

The current reduction by losses in the central region, can be solved easily adjusting the voltage according to the similarity theorems. For large variations on the cyclotron configuration a new central region design must be developed. The puller in the AMIT cyclotron is an independent piece from the dee-electrode, and therefore, it can be replaced by another one increasing the central region phase acceptance.

5.2.3 Acceleration gap distance modification

An important effect that influences the cyclotron configuration is the distance of the acceleration gap. In AMIT cyclotron, a nominal gap between dee and dummy-dee of 10 mm has been designed. However, the final assembly of the mechanical structure of the RF system provided a slightly larger gap distance ($\sim$11 mm). Although it could seem a negligible distance, this affects to the whole beam dynamics due to it modifies the electric field map in the cyclotron. Thus, the cyclotron configuration has been reviewed. Following the same working mode as previous sections, beam dynamics analysis of the AMIT cyclotron have been performed including this enlargement of the gap distance.

The nominal magnetic field, voltage and radio frequency values have been established for the nominal gap of 10 mm. Hence, the first consequence of a change in the gap distance is the total modification of the acceleration conditions in the central region. Locating the electrode slightly further away, the configuration parameters must be tuned, because otherwise the particles do not acquire enough energy to cross the puller without colliding (Figure 5.55). An eventual reduction of the magnetic field could increase the radius of the trajectories to enable the central region cross. However, the modification of the magnetic field would imply the re-tuning of the radiofrequency, whose design variation range is very tight, to keep the acceleration until the extraction point. Therefore, the modification of the acceleration voltage arises a suitable solution.

As in the last subsection, multi-particle simulations applying different voltages have been performed under fixed nominal magnetic field and radiofrequency values, but in this case the gap distance is enlarger to 11 mm. The main outcome is presented at Figure 5.56, showing the beam transmission for different applied voltages. The results specify a minimum voltage of 66 kV to achieve a meaningful beam transmission rate. The optimum value, that would provide

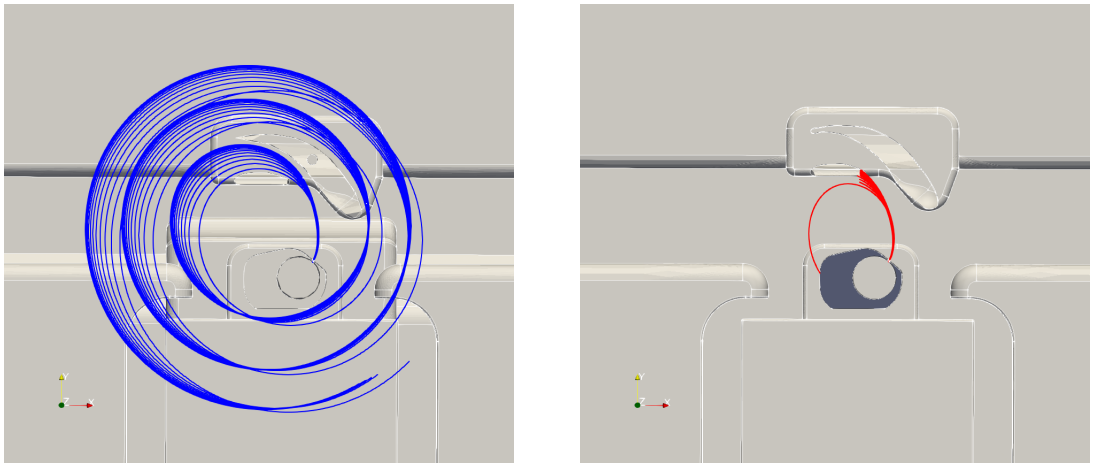

(a) $d = 10$ mm (b) $d = 11mm$

Figure 5.55: *Particle tracks in the central region for different distance of the acceleration gap in the same phase range.*

maximum transmission, is above the maximum voltage attainable. For comparison, Figure 5.47 shows the beam transmission at different voltages applied in case of nominal gap of 10 mm.

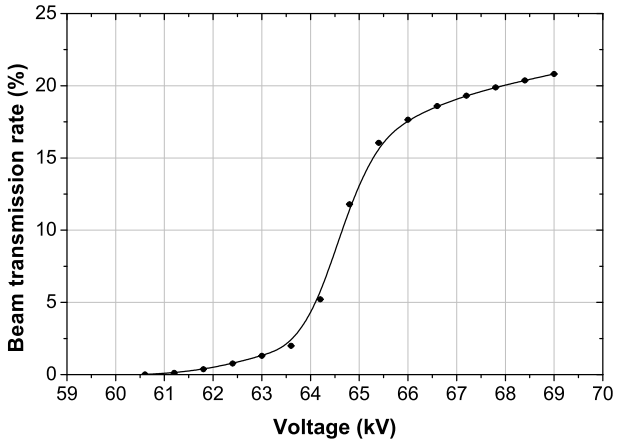

Figure 5.56: *Beam transmission rate for all RF cycle along the whole beam path as a function of the applied voltage for a gap distance of* 11 *mm. The solid represents a B-spline curve around the data.*

The beam evolution along the path, and the final characteristics of the beam are similar in comparison with the nominal gap. However, the axial beam focusing is slightly affected by the gap modification. A slightly stronger axial focusing is observed in comparison with the nominal gap, both along the beam path (Figure 5.57). With respect of the focusing in the radial direction, the beam size is more spread along the acceleration, especially from the enlargement of the gap distance from intermediate radii. These effects is produced by the alteration in the electric forces when the gap distance is modified. Nevertheless, the different focusing forces do not present high relevance in the final state of the beam and therefore, in the radioisotope production.

To conclude this analysis, the alteration of the gap distance implies a variation in the beam dynamics by the modification of the electric field, particularly relevant in the central region.

An increase of the applied voltage allows an adequate acceleration to the target, even though with a certain reduction in the achievable current. However, this solution would mean applying a voltage close to or higher than the reached in the radiofrequency system commisioning. Therefore, important risks would be assumed in the cyclotron operation. A simpler alternative to solve the alteration of the gap distance could be the modification of the central region by means of bringing the ion source closer to the dee in order to maintain the design distance of the first gap, avoiding the increase in voltage. This can be easily done by a mechanical insertion of a complementary piece to the back of the ion source. Additionally, a new dummy-dee could be manufactured to keep the nominal gap distance along the whole cyclotron. The beam dynamics implications of this possible modification have been left out of the scope of this thesis, but will be analyzed in a future study.

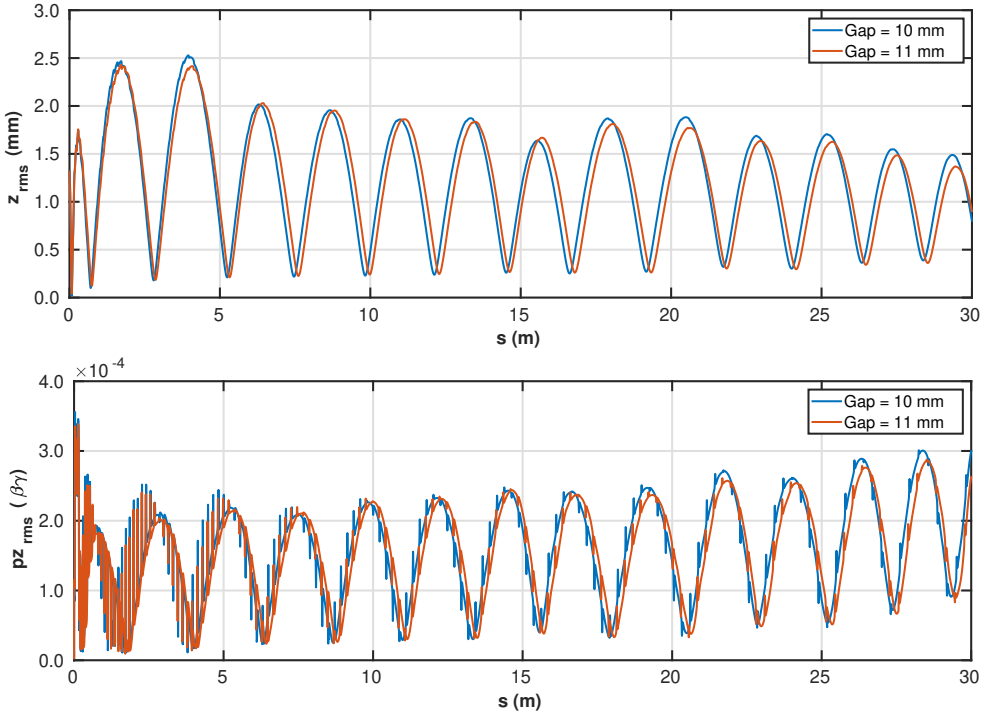

Figure 5.57: *Beam axial size z_{rms} (top) and rms axial momentum pz_{rms} (bottom) along the path for different distances of the acceleration gap.*

5.3 Conclusions

The beam dynamics analysis of the AMIT cyclotron have been presented in detail. On the one hand, the main characteristics of the beam along the acceleration process are presented with the aim of comprehending all the physical effects concerning a classical cyclotron, such as the evolution of synchronism and the beam focusing. The extraction of the beam is evaluated with special dedication, because it is a factor that allows tuning the final characteristics of the beam through the movement of the extraction system within a margin that provides total transmission

to the target. This study has established the optimal positions, allowing an optimization of the mechanical structure to extend the range of movement of the extraction system. On the other hand, the fine tuning of the cyclotron has assessed the configuration within the tolerances of the radiofrequency system and the magnetic field parameters. This study has been extended to consider large scale modifications for possible optimization in case any of the cyclotron subsystems is outside the design values. Finally, the impact of the gap distance alteration observed in the final assembly of the radiofrequency system with the vacuum chamber has been studied to fulfill the beam requirements.

It is important to point out that the final radioisotope production will depend on the injected current into the cyclotron and on the total beam transmission rate. On the one hand, the chapter 4 has provided the experimental measurement of the beam current supplied by the AMIT ion source with a DC extractor system. On the other hand, the beam dynamics study has illustrated a total beam transmission of $\sim 25\%$ respect of the total RF cycle, considering the phase acceptance range and including the intrinsic losses by central region collisions or axial deviations. With that in mind, and considering the relative radioisotope production results at the target, the cyclotron will fulfill the objectives. A significant decrease in the phase acceptance or a high rise of the losses due to space charge effects could result in a relevant reduction of the final current, limiting the compliance of the radioisotope production aims. However, the beam current outcomes provided by this beam dynamics study present enough safety margin to deal with any unforeseen event in this respect. Thus, the performance of the cyclotron and the final fulfillment of the objectives seems to be achieved.

We find it not strange, that man despises
What he conceives not
— Johann Wolfgang Von Goethe

Chapter 6

Beam stripping interactions

Compact cyclotrons of H^- ions with internal ion source as method of beam injection has as a main drawback the deterioration of the vacuum conditions in the acceleration region, specially in the central region. It is produced by the continuously gas insertion from the chimney of the ion source: most of the gas is not ionized and it flows out of the source by the pressure difference force. This feature, coupled with the low binding energy of the negative hydrogen ions, results in acceleration conditions where some residual beam interactions acquire high relevance in the beam transportation through the cyclotron, specially the interactions with the remaining molecules of the gas. These processes cause the stripping of the electrons of the H^- ions. Thus, they become in an important source of beam losses in this type of cyclotrons. For this reason, in the framework of this thesis, a detailed analysis of those physical interactions from the theoretical point of view is presented. Moreover, those physical interactions have been implemented as a new feature in OPAL beam dynamics code in combination with their practical application in the AMIT cyclotron beam dynamics.

6.1 Theoretical introduction

6.1.1 Interaction probability

The physical phenomena involving beam losses by stripping are considered stochastic processes, which each individual particle could experiment the interaction according to a certain probability. Assuming that particles are normally incident on a homogeneous medium, where the interaction will take place, and that they are subjected to a process with a mean free path λ between interactions. Hence, the probability density function for the interaction of a particle after traveling a distance x is [115, 184]:

$$F(x) = \frac{1}{\lambda} \cdot e^{-x/\lambda} \tag{6.1}$$

where $F(x)dx$ represents the probability of the particle suffering an interaction between x and $x + dx$. From this, the probability of suffering an interaction before reaching a path length x is

derived as:

$$P(x) = \int_0^x F(\mathfrak{x})d\mathfrak{x} = 1 - e^{-x/\lambda} \tag{6.2}$$

where $P(x)$ is the statistic cumulative interaction probability of the process. In the case of a non-intense interaction process, that means that the mean free path is higher than path length, the interaction probability can be approximated as:

$$\lambda >> x \implies \begin{cases} F(x) \simeq \dfrac{1}{\lambda} \\ P(x) \simeq \dfrac{x}{\lambda} \end{cases} \tag{6.3}$$

In the particular situation of a beam colliding with particles of a material, the interaction is overall described in terms of the cross section, σ. This quantity essentially gives a measure of the probability for a reaction to occur and may be calculated if the fundamental interaction phenomena between the particles is known. Assuming a thin slab of matter where the particles are uniformly distributed and the slice is not too thick so that the likelihood of one center sitting in front of another is low, the number of centers per unit perpendicular area which will be seen by the beam is then $N\delta x$, where N is the density of centers and δx is the thickness of the material along the direction of the beam. Then, the probability density to undergo an interaction of a certain type for the scattering of a single particle in an infinitesimal slice δx is given by:

$$dF(x) = N\,\sigma\,\delta x \longrightarrow F(x) = N\,\sigma \cdot e^{-x\,N\,\sigma} \tag{6.4}$$

Thus, the mean free path, λ, is related to the density of interaction particles and the cross section:

$$\lambda = \int_0^\infty x\,F(x)\,dx = \frac{1}{N\,\sigma} \tag{6.5}$$

The quantity $N\sigma$ is called frequently macroscopic cross section, Σ, or attenuation coefficient, μ. Likewise, the mean free path could be connected with the mean time of interaction or lifetime:

$$\tau = \frac{\lambda}{\beta c} = \frac{1}{N\sigma\beta c} \tag{6.6}$$

6.1.2 Residual gas interaction

Beam residual interactions with the molecules of the remaining gas in the acceleration region entail the most important source of losses in a H^- compact cyclotron. As a result, a degradation of the beam quality and a reduction of the final beam current can lead to a failure to comply of the accelerator requirements. Additionally, particle losses may induce an additional out gassing of the components as the stripped beam hits some components, resulting in an increase of the pressure level. From the point of view of the design of a cyclotron, one important objective is to improve the vacuum level to reduce the contribution from those beam-residual gas interactions. However, the compactness of the accelerator and the continuous gas injection restrict the quality of the vacuum in the machine. Therefore, a meticulously analysis of beam stripping processes is needed to optimize the gas injection, balancing the final extracted current and the beam losses.

Assuming a beam particles flux incident in a gas with density N (number of the gas molecules per unit volume under the vacuum condition), according to the equations (6.1) and (6.4), the number of particles interacting with the gas and removed from the beam along a distance traveled L is given by:

$$n = n_0\, e^{-\sigma N L} \tag{6.7}$$

where n_0 is initial number of particles. The inverse mean free paths (or lifetimes) should be added when several types of molecules in the residual gas or when diverse physical processes of comparable significance are taken into account, in order to find the total mean free path from all processes.

$$\frac{1}{\lambda_{total}} = \sum_j \frac{1}{\lambda_j} = N_{total} \cdot \sigma_{total} = \sum_j N_j\, \sigma_{total}^{,j} = \sum_j \left(\sum_i N_j\, \sigma_i^{,j} \right) \tag{6.8}$$

where the first summation is over all gas components and the second summation is over all processes for each component. The number of gas molecules per unit volume can be determined by Loschmidt number from the ideal gas law:

$$P = N k_B T \;\longrightarrow\; N = \frac{P}{k_B T} = \frac{P N_A}{R T} \tag{6.9}$$

where P is the gas pressure, T the temperature, k_B the Boltzmann constant, N_A the Avogrado's number and R the ideal gas constant. The fraction loss for the unit of traveled length will be, according to the equation (6.2):

$$f_g = 1 - e^{-\sigma N x} \tag{6.10}$$

Hydrogen ion beams reactions

The interaction processes to be considered depend on the incident particle species. Hydrogen ions are the most employed particles in accelerators. They have been studied with high accuracy, the internal structure and the physical principles that sustain them are a well-known acquaintance from atomic physics. Particularly, negative hydrogen ions is composed of two electrons, one tightly bound with a binding energy of 13.598434600291(12) eV [185] and another one slightly bound at 0.754195(19) eV [127] of binding energy. It is one of the most ions accelerated in cyclotrons for radioisotope production (see Table 1.3). During their acceleration and transport in a particle accelerator, the second electron becomes probable to be detached from the ion through interaction with the residual gas. On the other hand, proton beams could interact with the residual gas by means of electron-capture reactions. High energy neutral hydrogen atoms, arising from a previous stripping reactions, are also available to experiment a charge-exchange reaction. Overall, these processes can be classified according to the electric charge state of the hydrogen, $\sigma_{qq'}$, where the subscripts q and q' make reference respectively to the initial and final charge state of the particle. Thus, the charge-transfer processes for hydrogen ions to be considered, independently of the nature of residual gas, can be classified in the atomic reactions summarized in Table 6.1.

The experimental cross sections for hydrogen charge exchange reactions have been measured since 50s for interactions with different gases. The data have been published and compiled in different reports [186–191]. Moreover, theoretical studies for high energies cross section have been developed based on an extension of the Bethe theory for the total inelastic cross section in the Born approximation [136, 192, 193]. As example, the charge exchange cross section data of H^- colliding with molecular hydrogen gas (H_2) are plotted in Figure 6.1. As it can be expected from the electron binding energy in atomic hydrogen, the processes entailing two electrons in the reaction has a lesser order of magnitude cross section and, accordingly, those processes have lower reaction probability. For that reason, there are fewer experimental data available for these less probable reactions. Furthermore, it is important to remark that these charge transfer processes are more likely for energy of the incident particles around 10 keV. Hence, for cyclotrons beams, the interactions with the residual gas will be more probable in the central region, despite the beam will go through the rest of the accelerator sufficient time to experiment likewise those reactions though with less likelihood.

Table 6.1: *Charge transfer processes of hydrogen ions*

Single-electron detachment of H^-	(σ_{-10})	$H^- + X \longrightarrow H + X$
Double-electron detachment of H^-	(σ_{-11})	$H^- + X \longrightarrow H^+ + X$
Single-electron capture of H^+	(σ_{10})	$H^+ + X \longrightarrow H + X$
Double-electron capture of H^+	(σ_{1-1})	$H^+ + X \longrightarrow H^- + X$
Single-electron capture of H	(σ_{01})	$H + X \longrightarrow H^+ + X$
Single-electron detachment of H	(σ_{0-1})	$H + X \longrightarrow H^- + X$

Analytic cross section

Cross section data of the collision processes between ions, atoms and molecules of Hydrogen with gases are important for some research fields related to plasma physics as well as in the study of different technology devices involving the use of high energy hydrogen. Comprehensive reviews of these processes have evaluated the cross section as a function of the incident energy of the particles to develop an analytic expression to fit the experimental data for ease of numerical data retrieval.

A first analytic fit makes use of high-order polynomial function [194]:

$$\ln \sigma = \sum_{n=1}^{8} a_i \cdot (\ln E)^n \tag{6.11}$$

where a_n are adjustable coefficients by a least-squares weighting fit of the data. However, the application of this method has limitations near the energy threshold energy due to the sharp

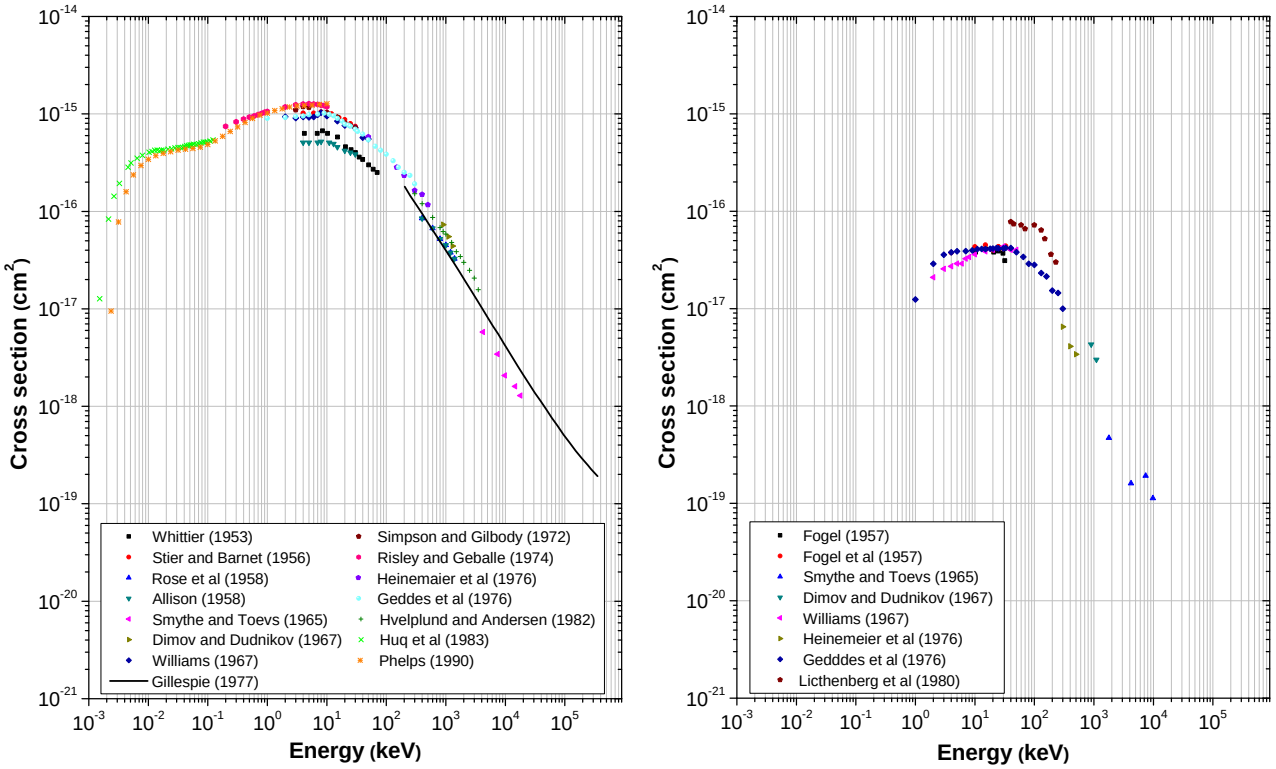

(a) σ_{-10} (b) σ_{-11}

Figure 6.1: *Electron detachment cross sections of H^- on hydrogen gas (H_2). Solid markers represent experimental data and solid line is the theoretical calculation.*

growth of the cross section. For some reactions the cross sections are well fit by an empirical modification of the Bethe-Born formula:

$$\sigma = a\left(\frac{E_{th}}{E}\right)^n \ln\left(\frac{E}{E_{th}}\right) \tag{6.12}$$

where a and n are parameters, and E_{th} is the energy threshold. The threshold behavior in the latter case is more accurately reproduced, although each of these methods fit better for different reactions.

A further method is based on the least-squares Chebyshev polynomial fits to the recommended cross sections as a function of the projectile energy [190]:

$$\ln\left[\sigma(E)\right] = \frac{1}{2}a_0 + \sum_{i=1}^{k} a_i \cdot T_i(X) \tag{6.13}$$

$$X = \frac{(\ln E - \ln E_{min}) - (\ln E_{max} - \ln E)}{\ln E_{max} - \ln E_{min}} \tag{6.14}$$

where T_i are the Chebyshev orthogonal polynomials, a_i $(i = 0, 1, ..., k)$ denote adjustable parameters relative to each reaction, k is the smallest number of coefficients providing an accurate fit (usually 6 or 8), E_{min} and E_{max} are parameters that limit the region of analytic representation

of the cross section. This procedure facilitates the cross section data interpolation in a restricted energy interval; however, it cannot be used for extrapolation, because it often show unreasonable physically behavior just outside the considered energy range.

The restrictions of these analytic functions can be removed by using analytic expressions that approximate low-energy and high-energy asymptotic trends. A semi-empirical expression for inelastic collision cross sections of hydrogen atoms and ions with gaseous atoms and molecules [195] has been used to develop functional forms to fit a compiled set of experimental data using the two-step least-squared method [188]. For the considered reactions, the analytical function formula used to obtain the cross sections is given by the general expression:

$$\sigma_{qq'} = \sigma_0 \left[f(E_1) + a_7 \cdot f(E_1/a_8) \right] \tag{6.15}$$

where qq' represents any combination of initial and final charge states of the particle, σ_0 is a convenient cross section unit ($\sigma_0 = 1 \cdot 10^{-16}$ cm^2) and $f(E)$ and E_1 are given by:

$$f(E) = \frac{a_1 \cdot \left(\dfrac{E}{E_R}\right)^{a_2}}{1 + \left(\dfrac{E}{a_3}\right)^{a_2+a_4} + \left(\dfrac{E}{a_5}\right)^{a_2+a_6}} \tag{6.16}$$

$$E_R = hcR_\infty \cdot \frac{m_H}{m_e} = \frac{m_H e^4}{8\varepsilon_0^2 h^2} \tag{6.17}$$

$$E_1 = E_0 - E_{th} \tag{6.18}$$

where E_0 is the energy of the incident particle in keV, E_{th} is the threshold energy of the reaction in keV, and the symbols a_i ($i = 1, 2, ..., 8$) denote adjustable parameters.

The analytic expression for cross sections (equation (6.15)) has been modified for reactions of hydrogen atoms and ions with hydrogen gas [196]. Additional experimental data have been taken into account and they have fitted with more accuracy through a linear combination of the function $f(E)$ (equation (6.16)) considering more setting parameters, thus making it possible not only to interpolate but also to extrapolate the cross section data to some extent. Hence, total cross sections for charge exchange reactions for hydrogen ions in different gasses according to this method are shown in Figure 6.2.

6.1.3 Electromagnetic stripping

The use of superconducting technology in accelerators have enabled to increase considerably the magnetic field providing a sharp size reduction. Specially relevant for compact cyclotrons applied to radioisotope production, the compactness of the accelerators has expanded their deployment in non-conventional facilities, allowing for the society benefit of this high level technology and its great diversity of applications.

Nevertheless, the use of high magnetic fields introduces a limitation in cyclotrons based on H^- beams. The detachment of the second slightly bound electron of the ions due to the opposite

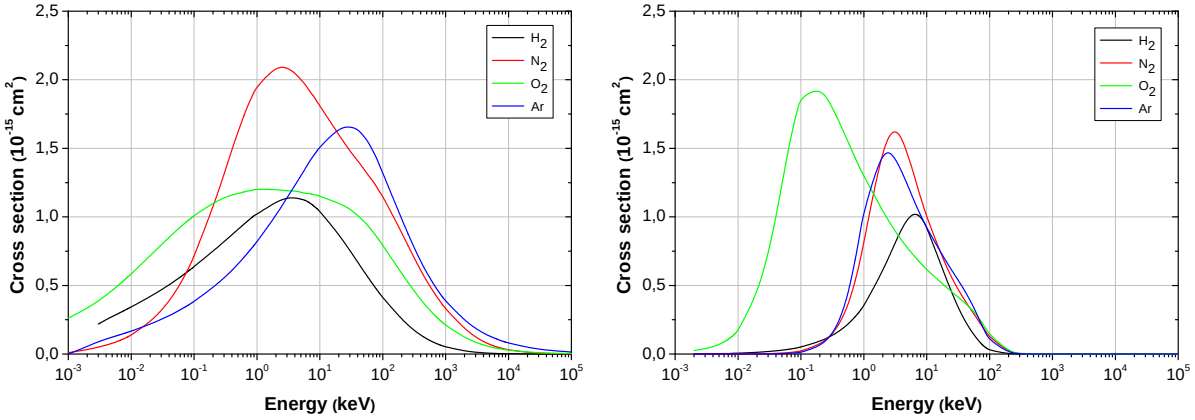

(a) H^- (b) H^+

Figure 6.2: *Charge exchange total cross sections in different gases for H^- and H^+ from analytic function fit (equations* (6.15)- (6.16)*).*

force in the subatomic particles arising from the motion through a transverse magnetic field can intensify excessively the beam losses. Thus, the lifetime of the ions in an electromagnetic field becomes of crucial interest in compact cyclotrons. This effect, called electromagnetic or Lorentz stripping, is relevant just for H^- beams due to the low binding energy of the second electron and it is extremely difficult to achieve double-electron detachment of a hydrogen atom in its ground state [197].

The electromagnetic stripping can be analyzed from the decay of an atomic system in a weak and static electric field. When ions travel in a magnetic field, the electrons and nucleus are bent in opposite directions according to their electric charge. The field component orthogonal to the velocity of particles produces an electric field in the ions rest frame according to the Lorentz transformation:

$$E = \gamma\beta c\, B \tag{6.19}$$

where γ and β are the relativist parameters and c the speed of light. This electric field gives rise a finite ion lifetime because the field induces the disassociation of the particles. The strength of this effect is a function of the energy of the ions and the magnetic field intensity B.

The fraction of particles dissociated by the electromagnetic field after a traveled distance L can be evaluated through the interaction probability (see equation (6.2)):

$$f = 1 - e^{-L/\beta c\gamma\tau} = 1 - e^{-t/\gamma\tau} \tag{6.20}$$

where τ is the particle lifetime in the rest frame of the ions. The mean free path, λ, is given by the relation:

$$\lambda = \beta c\gamma\tau \tag{6.21}$$

Thereby, the mean free path or the lifetime can be used to parametrize the beam losses by electromagnetic stripping. Theoretic studies have determined the electric dissociation rate of

H^- ions based on the formal theory of decay, obtaining an expression for the ion lifetimes [198]:

$$\tau = \frac{4mz_T}{S_0\mathcal{N}^2\hbar\,(1+p)^2\left(1-\dfrac{1}{2k_0z_t}\right)}\cdot\exp\left(\frac{4k_0z_T}{3}\right) \tag{6.22}$$

where $z_T = \varepsilon/eE$ is the outer classical turning radius, ε is the electron binding energy, N is a normalization factor, p is a factor which accounts for the polarization of the ionic wave function and has the value 0.0126 [198] based on perturbation theory, k_0 arises from the ionic wave function and is determined from the relation $k_0^2 = 2m(-\varepsilon_0)/\hbar^2$ and S_0 is the spectroscopy coefficient for finding the daughter atom in the ground state ($S_0 = 0.783\,(5)$). The normalization constant $\mathcal{N}$ is given by:

$$\mathcal{N} = \frac{[2k_0(k_0+\alpha)(2k_0+\alpha)]^{1/2}}{\alpha} \tag{6.23}$$

where α is a parameter for the ionic potential function [199] ($\alpha = 3.806{\cdot}10^{10}$ m^{-1}). The lifetime expression can be rewritten in terms of ε, α, S_0 and the electric field E [200]:

$$\tau(\varepsilon,S_0,\alpha) = \frac{4m\left(\dfrac{\varepsilon}{e}\right)}{S_0\,\hbar\,[\mathcal{N}(\alpha,\varepsilon)]^2(1+p)^2\left(1-\dfrac{E}{\varepsilon^{3/2}\left(\dfrac{8m}{e^2\,\hbar^2}\right)^{1/2}}\right)}\frac{1}{E}\cdot\exp\left[\frac{2}{3}\left(\frac{8m}{e^2\,\hbar^2}\right)^{1/2}\frac{\varepsilon^{3/2}}{E}\right] \tag{6.24}$$

$$= \frac{\sqrt{2\varepsilon m}\,\alpha^2}{S_0(1+p)^2\,e\left(\dfrac{\sqrt{2\varepsilon m}}{\hbar}+\alpha\right)\left(\dfrac{\sqrt{8\varepsilon m}}{\hbar}+\alpha\right)\left(1-\dfrac{\sqrt{2}\,\hbar\,e\,E}{4\sqrt{m}\,\varepsilon^{3/2}}\right)}\frac{1}{E}\cdot\exp\left[\frac{2}{3}\left(\frac{8m}{e^2\,\hbar^2}\right)^{1/2}\frac{\varepsilon^{3/2}}{E}\right] \tag{6.25}$$

Thus, it can be parametrized in a simpler way as:

$$\tau = \frac{a_F}{(1-\eta E)\,E}\cdot\exp\left(\frac{b_F}{E}\right) \tag{6.26}$$

$$a_F = \frac{4\varepsilon m}{S_0\,e\,\hbar\mathcal{N}^2(1+p)^2} = \frac{\sqrt{2\varepsilon m}\,\alpha^2}{S_0(1+p)^2\,e\left(\dfrac{\sqrt{2\varepsilon m}}{\hbar}+\alpha\right)\left(\dfrac{\sqrt{8\varepsilon m}}{\hbar}+\alpha\right)} \tag{6.27}$$

$$b_F = \frac{2}{3}\left(\frac{8m}{e^2\,\hbar^2}\right)^{1/2}\varepsilon^{3/2} = \frac{4}{3}\frac{\sqrt{2m\varepsilon^3}}{e\,\hbar} = \frac{4}{3}\frac{\varepsilon^{3/2}}{\sqrt{e\,\hbar\,\mu_B}} \tag{6.28}$$

$$\eta = \frac{\sqrt{2}\,e\,\hbar}{4\sqrt{m}\,\varepsilon^{3/2}} = \sqrt{\frac{m}{2}}\,\frac{\mu_B}{\varepsilon^{3/2}} \tag{6.29}$$

where the parameters, depending on fundamental constants and ion properties, take values of $a_F = 2.65\,(2)\cdot10^{-6}$ s V/m, $b_F = 4.4741\,(2)\cdot10^{9}$ V/m and $\eta = 1.49007\,(5)\cdot10^{-10}$ m/V.

Apart from that, an electromagnetic stripping mean lifetime of negative ions in magnetic fields has been obtained experimentally [201], determining a simple relationship depending on the induced electric field and some setting parameters:

$$\tau = \frac{A_1}{E} \cdot \exp\left(\frac{A_2}{E}\right) \tag{6.30}$$

where A_1 and A_2 parameters have been determined experimentally (Table 6.2). This expression has been widely used in previous studies as a first approximation to determine the influence of the magnetic field in a H^- beam. However, it could be derived from theoretical lifetime (equations (6.22) or (6.26)) taking into account some approximations: disregarding the polarization factor, p, and considering $\eta E << 1$. Thus, a relationship for the experimental constants A_1 and A_2 as a function of the binding energy can be laid down:

$$A_1(\varepsilon) = C_1 \frac{\varepsilon}{S_0 N^2} \tag{6.31}$$

$$A_2(\varepsilon) = C_2 \, \varepsilon^{3/2} \tag{6.32}$$

where C_1 and C_2 are constants independent of atomic structure that can be referred to fundamental constants [202, 203] by means of the theoretical expression under the considered approximation:

$$C_1 = \frac{4\,m}{e\,\hbar} = \frac{2}{\mu_B} = 2.157 \cdot 10^{23} \ \mathrm{A^{-1}\,m^{-2}} \tag{6.33}$$

$$C_2 = \frac{4}{3}\frac{1}{\sqrt{e\,\hbar\,\mu_B}} = 1.065 \cdot 10^{38} \ \ \mathrm{T^{1/2} A^{-1/2}\,J^{-1}\,s^{-1}} \tag{6.34}$$

In this way, a theoretical calculation of the setting parameters of the experimental mean lifetime expression has been attained in the scope of this dissertation with high accuracy and in good agreement with the experimental measurements (see Table 6.2).

Table 6.2: *Lifetime parameters for electromagnetic stripping of H^- ions*

Parameter	Jason *et al.* [204]	Keating *et al.* [200]	Theoretical
A_1 (10^{-6} s V/m)	2.47 (10)	3.073 (10)	2.714 (17)
A_2 (10^9 V/m)	4.49 (10)	4.414 (10)	4.47407 (17)

These results can be applied to calculate the lifetime of H^- ions at different energies immerse in magnetic fields with different intensity field (Figure 6.3). From that, the fraction of H^- beam lost over a drift distance of 1 m for different beam energies and magnetic field conditions has been obtained (Figure 6.4). With these results in mind, a limitation of the high magnetic field arises for high-energy H^- accelerators. For low beam energy and low magnetic field, those stripping effects are negligible; but a slight increase of one of those parameters enforces to considerate the beam losses associated. Some of the commercial or researcher cyclotrons for radioisotope production (see Table 1.3) have conditions resulting in non-negligible electromagnetic stripping

effects. Therefore, these results are the great relevance in the design stage of a cyclotron, and they have to be taken into account for a suitable operation of the machine due to the potentially dangerous losses that can be produced.

It has to be remarked that those beam stripping processes have entailed a challenge in the development of compact cyclotrons by the significant compromise between the main features of a cyclotron, such as the beam energy and the magnetic field. An increase of the compactness of the accelerator requires a high magnetic field, restricting the maximum beam energy to keep electromagnetic stripping losses under control; whereas a high beam energy limits the suitable mean magnetic field. With that in mind, a detailed analysis based on the theoretical model of the internal structure of the H^- ions and its interaction with electromagnetic fields provide relevant comprehension of the particle accelerators technology development.

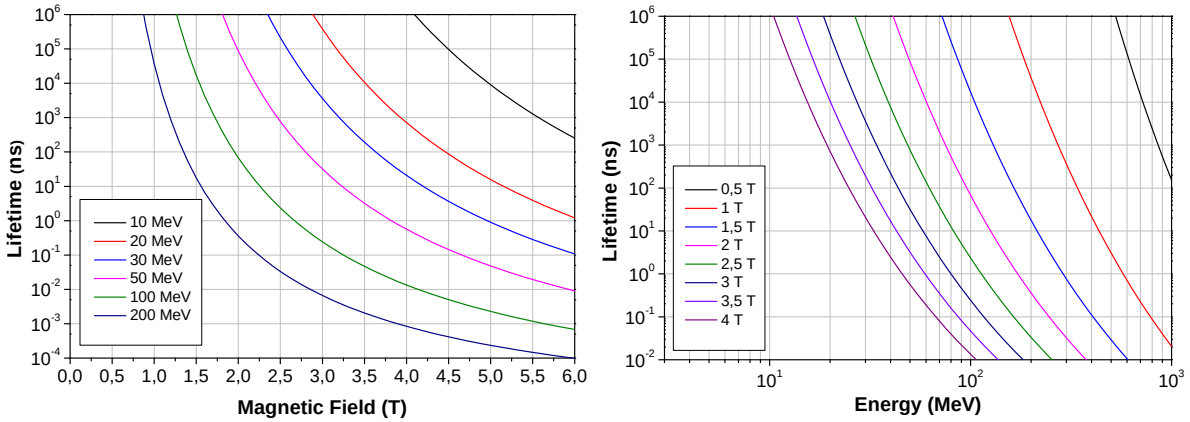

(a) (b)

Figure 6.3: *Mean lifetime of H^- ions according to theoretical results in front of the applied magnetic field for different energies (a) and in front of energy beam for different magnetic fields (b).*

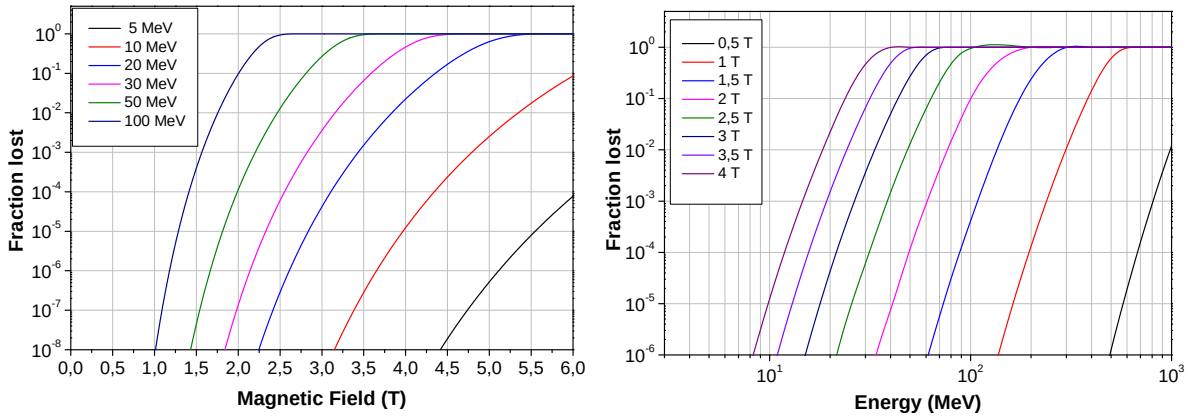

(a) (b)

Figure 6.4: *Fraction lost of H^- beam over a 1 m drift path for various energies as a function of B (a) and in front of energy of the beam for different magnetic fields (b) calculated from the theoretical lifetime expression.*

6.2 OPAL beam stripping interaction model

Beam stripping interactions could be considerably relevant in AMIT cyclotron whose internal ion source are continuously injecting part of the non-ionized gas through the ion source chimney slit. This contributes to deteriorate the vacuum, specially in the central region and increases the probability of interaction of H^- ions with the residual gas. Moreover, the high magnetic field applied can raise the beam losses by electromagnetic stripping; although a low stripping probability is expected given the relative low energy.

For this reason, a particle-matter interaction model would help to better understand the performance of an accelerator under these conditions from beam dynamics point of view. Beam stripping interactions models have been implemented into the OPAL code [205] in the framework of this thesis. The implementation has taken advantage of the physics models performed with Monte Carlo methods included in OPAL simulation code (see section 3.1). Hence, OPAL-CYCL is currently enabled to track particles considering these residual interactions in accelerators as AMIT cyclotron. This new feature increases the potential and versatility of OPAL, providing the capability to extend beam dynamics studies to cyclotrons considering these physical phenomena.

6.2.1 Code description

The beam stripping interaction algorithm starts considering the accelerator volume full of a residual gas according to temperature and pressure as input parameters. At this point, the gas density of the residual gas is calculated (equation (6.9)). Two different options of gas species have been currently implemented: molecular hydrogen, H_2, or dry air [206]. One of the main factors in the interaction is the pressure along the vacuum chamber. For precise simulations, a 2D pressure field map from an external file can be imported into the OPAL input file, providing more realistic conditions for the cyclotron vacuum and, therefore, more reliable results. In addition, a constant pressure for the whole volume can be also considered for a preliminary study.

The particle matter interaction algorithm evaluates the probability of each particle individually in each step through a Monte Carlo method, estimating the cross sections of the processes according to its energy by means of analytical functions (see section 6.1.2). The analytical function employed for each reaction has been assessed conforming to the best fit with the experimental data in the energy range of interest. The incident particles considered to interact with residual gas are H^-, H^+ and H, regarding processes showed in the Table 6.1, as well as H_2^+, due to its interest in some cyclotrons, through some of the most probably interactions with molecular gases. The electromagnetic stripping is only evaluated if the incident particle is a negative hydrogen ion.

When the stochastic evaluation method provides a probability higher than the physical interaction probability, the algorithm leads the incident particle to a reaction. This evaluation is performed independently for interactions with the residual gas and for electromagnetic stripping of H^-. The particle can be removed from the beam or transformed to a secondary heavy particle, attending to the physical phenomena produced, that will continue its movement in agreement

with the charge-to-mass ratio. In any case, the phase-space data (position and momentum) of the interacting particles are recorded in an output file for post-processing and analysis of the losses. Figure 6.5 summarizes the iterative steps evaluated by the algorithm until the end of the accelerating process or until the particle is removed from the beam.

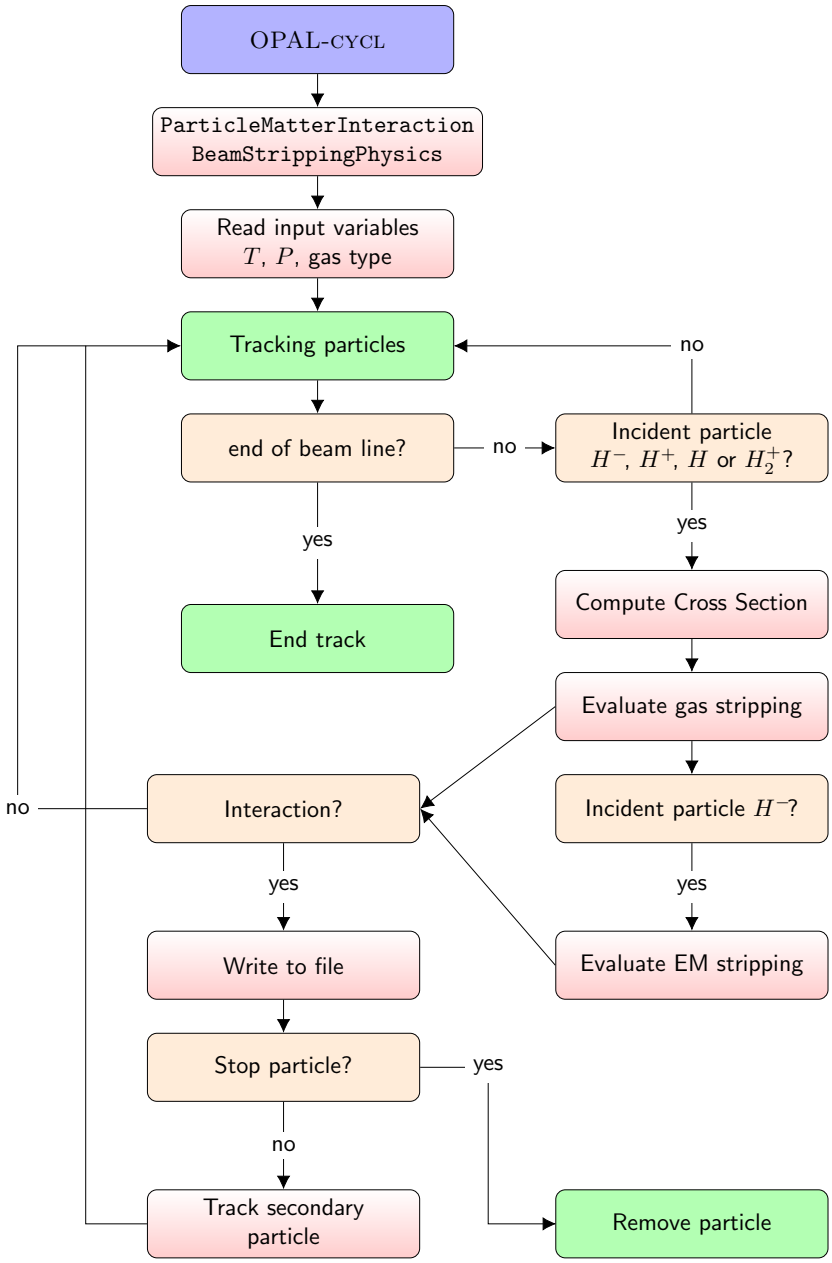

Figure 6.5: OPAL *beam stripping physics algorithm flowchart.*

It has to be pointed out that the implementation of the beam interaction with the residual gas is only considering the ion losses assessment by direct interactions, although the beam interaction could produce more losses by emittance blowup during acceleration or transport and it also modifies the beam quality. These features will be considered in future enhancements of the code.

6.2.2 Benchmarking study

The beam stripping physics algorithm has been tested through beam simulations of a large drift transmission at different energies and fixed pressure value. These simulations make possible the evaluation of the beam interactions with residual gas without overlapping other effects. Through iterative simulations performed for a high number of particles, the fraction lost per unit of traveled length has been verified in accordance with the analytic cross section evaluation (Figure 6.6). In the same way, the electromagnetic stripping of a 100 MeV H^- beam fixed has been assessed under an external magnetic field of $B = 2.3$ T. These values have been chosen to obtain a relevant electromagnetic stripping according to theoretical results expected (see Figure 6.4). The benchmark of the electromagnetic fraction lost are presented in Table 6.3.

The good agreement between the test and the expected results verifies the satisfactory beam stripping physics implementation into the OPAL code. Likewise, it has to be mentioned that a gas stripping test has been incorporated to the regression tests of actual OPAL versions for quality assurance and to keep the benchmarking of the beam stripping physics implementation with regard to any modification of the code.

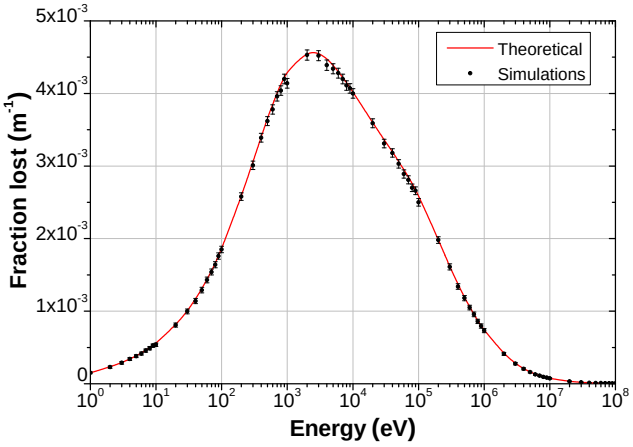

Figure 6.6: *Beam fraction lost per unit of length of H^- beam as a function of energy due to interactions with residual gas (air) in a large drift at $P = 1 \cdot 10^{-6}$ mbar.*

Table 6.3: *Electromagnetic stripping fraction lost test of H^- beam at fixed energy (100 MeV) and magnetic field of $B = 2.3$ T*

$f_L^{Theory}\ (m^{-1})$	0.5712 (2)
$f_L^{Simulation}\ (m^{-1})$	0.5703 (74)

6.3 AMIT beam stripping analysis

The relevance of the stripping interactions in compact cyclotrons of H^- ions with an internal ion source has led to analyze extensively those processes from the theoretical point of view. In addition, the computational implementation of a new particle mater interaction class in OPAL code has been performed. Therefore, it is essential to characterize the consequence of the continuous gas injection into the vacuum chamber as well as the interaction with high magnetic field. The study of these phenomena for the AMIT cyclotron complement the objectives of this dissertation to improve the final beam conditions for an optimum radioisotope production. The simulated stripping processes take into consideration simultaneously both interactions with residual gas and electromagnetic stripping. Henceforth, the following sections are going to present the analysis of those effects.

It has to be mentioned that all these beam stripping studies are based on H_2 as residual gas because vacuum studies conclude that other molecular or atomic gases contributions are negligible in comparison with the continuous hydrogen leak from the ion source.

6.3.1 Electromagnetic stripping evaluation

The previous electromagnetic stripping analysis based on a theoretical approach provide significant information about its impact on AMIT cyclotron. The maximum energy achieved at the end of the acceleration process, $\sim$8.5 MeV, in combination with a maximum $\sim$4 T magnetic field gives an ion lifetime of $\sim 10^{-2}$ s. This time is considerably higher than the whole transmission time of the particles in the cyclotron, $\sim 10^{-6}$ s. Hence, the electromagnetic stripping can be tentatively considered as a second-class of a source of losses in comparison with gas stripping in AMIT cyclotron.

Despite these initial estimates, this effect has been additionally verified by means of OPAL simulations to determine specifically its contribution to the beam losses. Iterative multi-particles simulations with a high number of particles to increase the statistical data (10^6 particles per run) have been performed to estimate possible losses by electromagnetic stripping. The outcomes provide a 0.005 % of losses during the entire beam trajectory until reaching the target. This result is in good agreement with the theoretical prediction. Hence, the electromagnetic stripping is totally negligible in AMIT cyclotron and consequently it can be concluded that the most of the beam losses produced by the electron detachment of H^- in the AMIT cyclotron will be originated by interactions with the residual gas, as it going to be presented in the subsequent sections.

6.3.2 Analysis of the beam stripping with the residual gas

Preliminary pressure level analysis

A preliminary evaluation of the losses induced by beam stripping interactions with a constant pressure along the accelerator chamber is realized to obtain a initial estimation of its impact, making use of the new implementation performed in OPAL code in the scope of this thesis For that purpose, iterative multi-particle simulations with stripping interactions have been performed. The simulations track an adequate statistical sample of particles along the whole beam path (from the injection to the target aperture). Given the stochastic nature of the stripping interaction, numerous simulations have been performed to achieve the most statistically accurate results as much as possible.

From this analysis, the impact of vacuum conditions with an average pressure level on beam losses can be obtained (Figure 6.7). It is clear how the beam losses increase exponentially with the pressure. These results performed with a constant pressure level constant can be considered as an upper limit to the expected losses in the real vacuum distribution. As it has been discussed in subsection 2.2.8, the average pressure in AMIT cyclotron is around $7 \cdot 10^{-5}$ mbar. This initial calculation provides a higher estimate of the vacuum losses close to 15%.

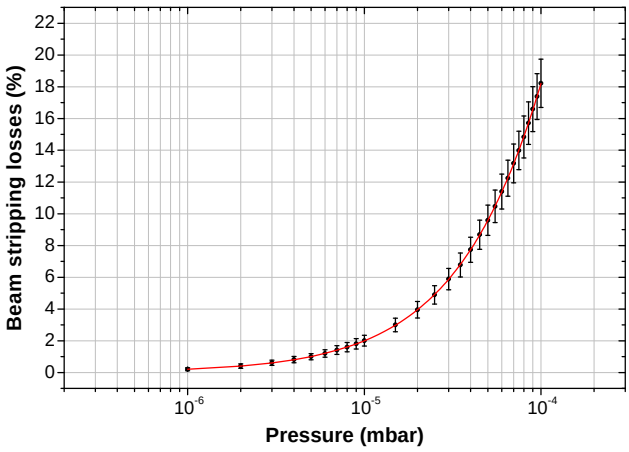

Figure 6.7: *Beam stripping losses as a function of a constant pressure level in* AMIT *cyclotron along the accelerator. The error bars represent the statistical uncertainty associated with the value. They have been calculated from statistical analysis of iterative simulations. The red line represents a exponential fit of the results.*

Pressure field map study

Once the impact that the vacuum level has on the possible losses has been studied, a more detailed analysis with the real pressure distribution on the cyclotron are going to be presented. Vacuum simulations performed with Molflow code have provided the pressure data on the acceleration chamber under the final arrangement of the accelerator (see subsection 2.2.8). The vacuum conditions assumed in those simulations were summarized in Table 2.6. For the implementation

in OPAL, the pressure data have been interpolated and adapted to the required format by a dedicated MATLAB script. In the same way as previous analysis, iterative multi-particle simulations considering the whole beam in the phase acceptance range have been performed including the pressure fieldmap.

The average rate of stripping losses induced reaches (14.6 ± 1.5) % when the pressure fieldmap is included, in accordance with the preliminary value obtained from average vacuum pressure level. Additionally to obtain the total rate of losses by stripping interactions, these simulations can provide relevant information about the characterization of the losses. It is clearly relevant since it provides information regarding the location where the losses occur as well as the energy of the particles. These factors are important to estimate the potential damages and the radioactive activation of the accelerator. Figure 6.8 illustrates the spatial distribution of those beam stripping losses. They are produced predominantly in the few millimeters after the ion source, during the

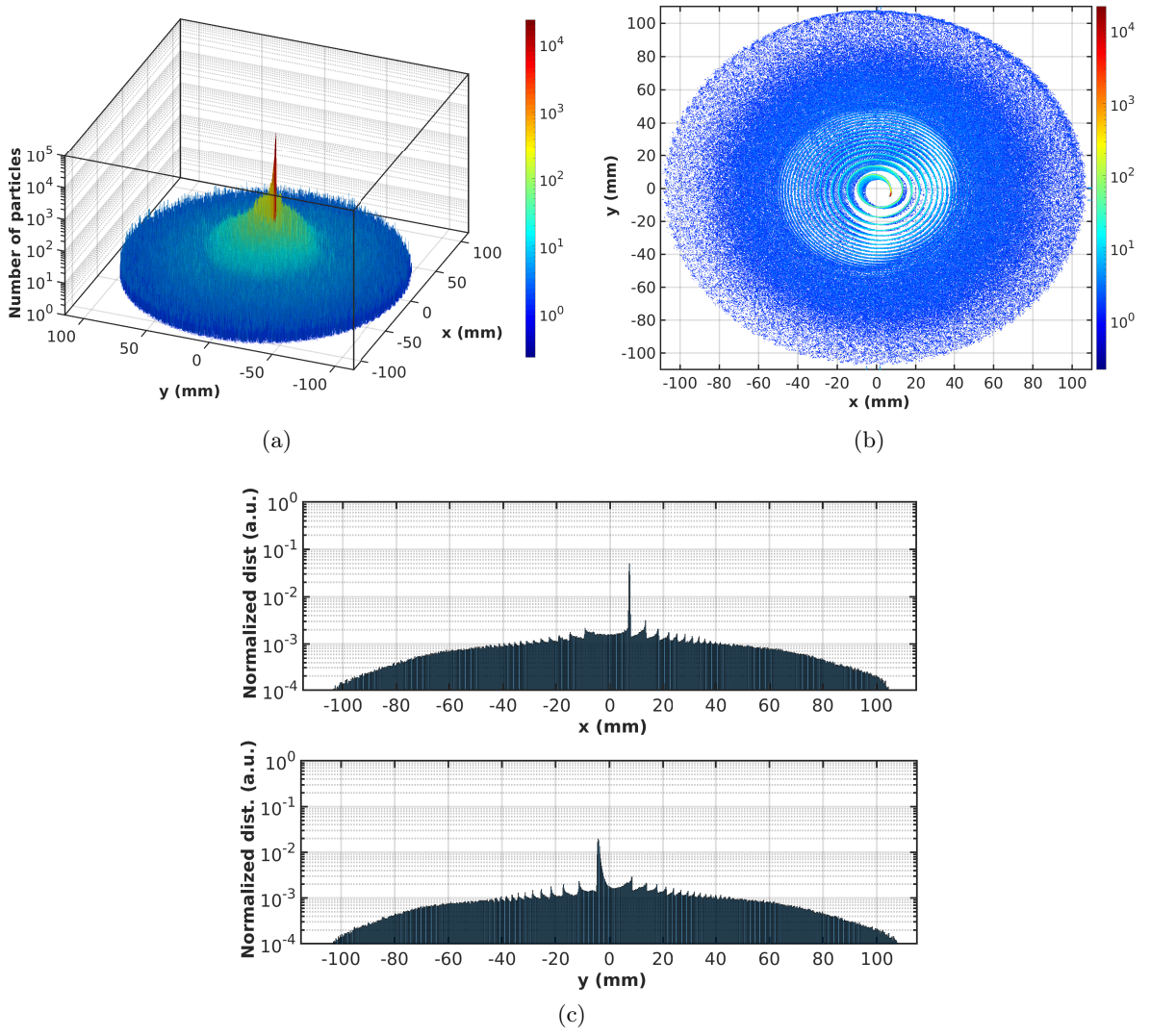

Figure 6.8: *Spatial distributions of the beam stripping losses produced by stripping interactions ((a) and (b)) and the normalized distribution over the total amount of losses along different directions.*

first acceleration gap. This beam losses distribution is well explained by the continuous neutral gas injection from the internal ion source into the vacuum chamber. Consequently, the pressure in the central region is one magnitude order increased in comparison with the rest of the chamber (see Figures 2.19 and 2.20). Furthermore, the beam losses during the first turns were expected higher since the cross sections of H^- interactions with gases are maximum for energies in the range of $(0.1 - 300)$ keV (see Figures 6.1 and 6.2). Nevertheless, although the vacuum level is enhanced out of the central region, the larger traveled distances will contribute, at a lower level, to some stripping losses through the whole accelerator. Consequently, the interaction probability never becomes negligible.

Figure 6.9 completes the beam losses characterization, showing the energy distribution of the stripping losses and the particle density distribution as a function of the radius. This last plot has been obtained from the particle losses distribution with the radius divided by the corresponding annulus area, that is to say, it represents the particles per unit area distribution. Thus, the increasing of the traveled length with the growth of the radius does not conceal the beam losses radial distribution trend. Moreover, each figure respectively includes the radius and energy of the particles corresponding with each histogram bin associated. The information gathered from these outcomes is very meaningful. It is important to remark that the prolongation of the stripping interactions along the entire path induces high energy losses, even though with lower rate than losses at low-energies, but highly relevant in the deterioration of the accelerator. Consequently, the beam losses entail an uninterrupted damage and degradation of several parts of the injection components and increased induced activation by interaction with the secondary particles for losses of energy above 2.5 MeV.

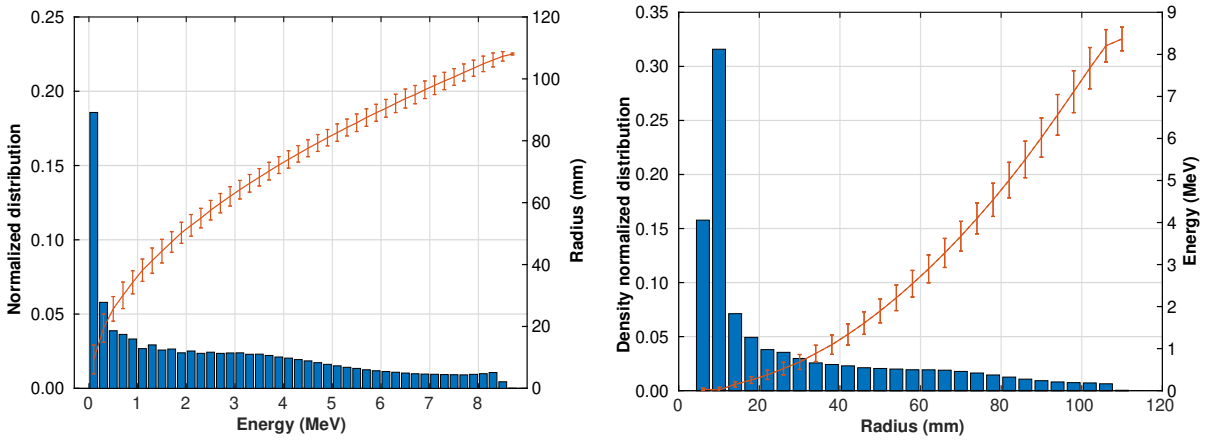

(a) (b)

Figure 6.9: *Histogram of normalized energy distribution of the losses (a) and particle density distribution as a function of the radius (b). The normalization is over the total amount of stripping losses. The particle density represent the rate of particles losses in a annulus. Solid orange line with error bars represents the radius (a) and energy (b) of particles corresponding with each histogram bin associated.*

An important parameter that is useful to estimate the traveled length by the particles and the probability of interaction with the vacuum is the number of turns, since higher the num-

ber o turns, the larger the distance traveled by the particles. Correspondingly, the interaction probability of electron detachment of the H^- ions with the residual gas or with the magnetic field is increased, according to the equation (6.2). For this reason the number of turns have been presented throughout this dissertation as a relevant outcome of the beam dynamics study.

This correlation is evaluated making use of the large variation in the total number of turns performed to the extraction for different initial RF phases. Beam dynamics studies performed have pointed out how the starting RF conditions determines the acceleration of the particles by the different phase excursion carries through. Thus, diverse initial RF phase conditions result in fluctuations in the number of turns performed to reach the extraction point and the stripping losses produced. Figure 6.10 illustrates the losses rate related to the number of turns to achieve the extraction point for different RF initial phase. A linear relation between these factors has been established. It is observed an analogous behavior between number of turns and the stripping losses, therefore, a linear relation between these factors has been established. Hence, the minimization of the number of turns needed to perform a suitable beam acceleration allows to reduce the beam losses by interactions with the residual gas.

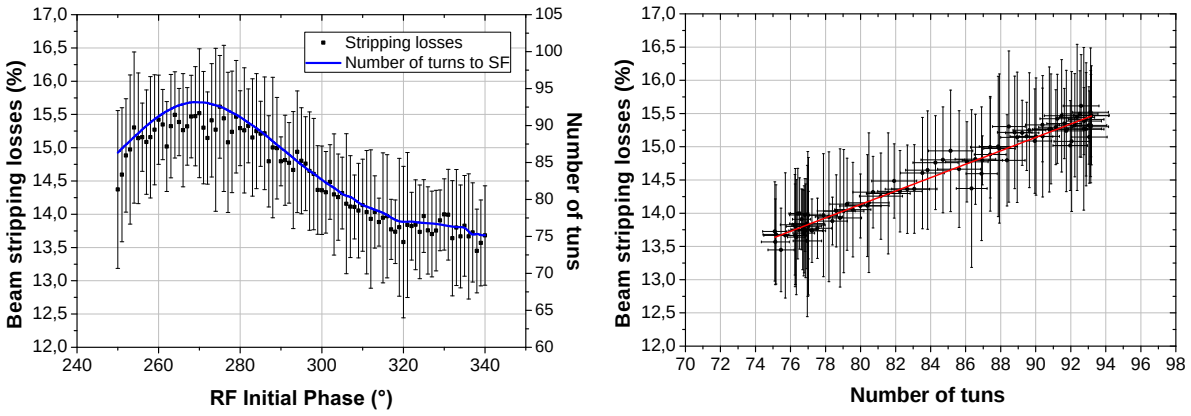

(a) (b)

Figure 6.10: *(a) Stripping losses rate (black dot with error bars -left axis) and number of turns (blue solid line -right axis) performed to reach the extraction point as a function of the initial RF conditions. (B) Stripping losses rate as a function of the number of turns with a linear fit (solid red line).*

Beam stripping optimization

Given the relevance of the beam stripping losses originated by interactions with the residual gas in a compact cyclotron with internal ion source, it is essential to analysis some improvements to minimize them and how they can be controlled. The vacuum level in the chamber is determined by the amount of neutral gas injected, depending on the input gas flow in the ion source and the size of the slit of the chimney. The pressure conditions inside the vacuum chamber can be controlled through two independent adjustments. Firstly, the gas load on the ion source varies the throughput. This parameter has the advantage of being controlled during the cyclotron operation. Secondly, the size of the slit of the ion source modifies the conductance

of the vacuum system. The mechanical design of the ion source allows a simple exchange of the chimney. Therefore, different size of the slit can be considered. The modifications of these parameters entail a linear variation of the pressure of the vacuum vessel, in the agreement of the equation (2.14). This adjustment is underpinned by the approximation that the pressure distribution keeps unaltered with those parameter modifications, that is to say, only the pressure level is affected. Furthermore, those factors also influences to the beam available to be accelerated: the gas flow determines the initial beam current (as it has been exposed in chapter 4) and the slit size affects the beam injection. With that in mind, an optimization of both factors has to be performed in order to reach a balance between the available beam for acceleration and the stripping losses that allows to maximize the total transmission.

Gas load optimization

Multi-particle simulations with a scaled pressure fieldmap have been performed according to different gas load. The average rate of stripping losses as a function of the gas load in the chimney is plotted in Figure 6.11. The interval of the gas load considered in this analysis is in agreement with the actual flow range provided by the gas supply system of the ion source. It is important to mention that the rate of losses is relative to the initial ion current, which depends on the gas injected among other parameters like slit aperture, magnetic field, cathodes... The energy and spatial distribution of the stripping losses are similar to the outcomes presented in the previous section.

This result is the great relevance because it influences directly in the final beam current, and therefore in the fulfillment of the beam requirements. Two opposite effects are related. On the one hand, the increase of the beam losses can reduce the beam current below the minimum needed for the radioisotope production. Wherefore, a significant gas load is recommended. On the other hand, the gas load also affects the current injected, as experimental measurements presented in the section 2.2.8 have shown (see Figure 4.11). However, the relation between gas load and

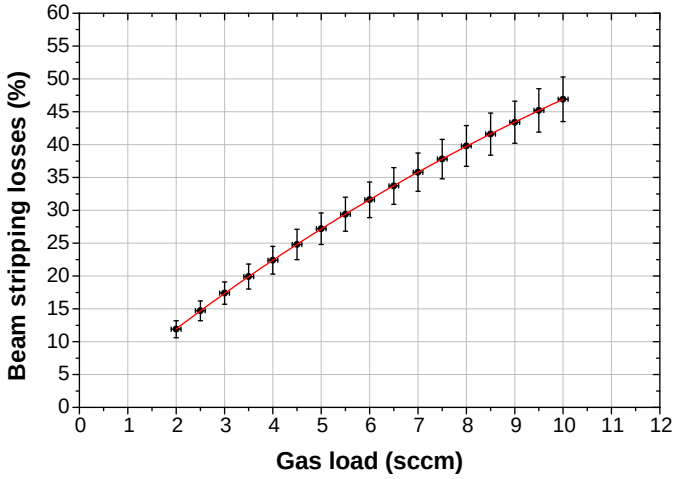

Figure 6.11: *Stripping losses rate as a function of the gas load of the chimney. The solid red line represents a negative exponential growth fit.*

current is influenced by other parameters implicated in the ion source operation. Therefore, the relation is nontrivial. The IST experimental measurements concluded an adequate gas load around 4 sccm. However, the combination with the associated stripping losses allow to establish a gas load slightly lower ($\sim$3.5 sccm) to achieve a maximized final beam current. Summarizing, the final status will represent a balance between both effects.

Ion source slit improvement

Another improvement that can be used to optimize the radioisotope production is the adjustment of the chimney slit size, modifying the stripping beam losses through a regulation of the pressure in the vacuum chamber. In a nominal case, the size of the slit is set to constraint the axial divergence. A 6×0.2 mm^2 slit has been considered as a reference aperture of the ion source chimney. Beam dynamics studies have established a linear relation between the initial position along the height of the slit and the maximum axial amplitude (see Figure 5.20). For the slit design size, a slight part of the beam is lost in axial collisions with the geometry (see Table 5.2). Therefore, a reduction of the height of the slit would lead to some advantages from the point of view of the beam losses. First, suppressing the axial losses, and secondly, improving the vacuum conditions due to the smaller the area of the slit opening, the lower the conductance from the source (see equation (2.16)).

Different slit sizes have been considered for this study, modifying both the height (between 6, 5, 4 and 3 mm), and the width (between 0.2, 0.3 and 0.4 mm). With that in mind, beam stripping losses have been evaluated varying the vacuum level in accordance with the size of the slit and the consequent conductance modification. The pressure scale has been set to achieve a value inside the ion source of $\sim$0.1 mbar, according to the adequate gas load provided by the experimental results (see section 2.2.8). The results of iterative multi-particle simulations show how the rate of losses increases linearly with the size of the slit (Figure 6.12) whether for changes in height or width.

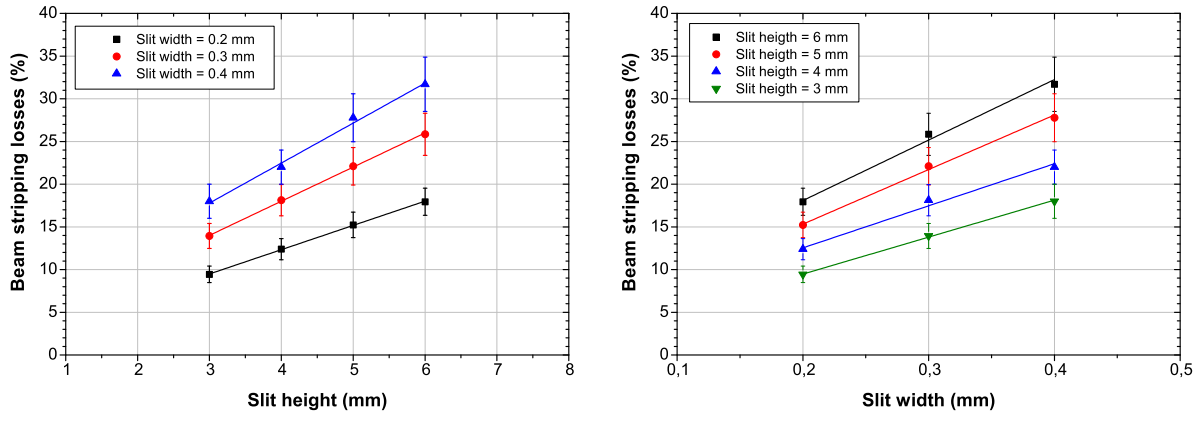

(a) (b)

Figure 6.12: *Beam stripping losses rate in front of slit size variations for changes in height or width. The modification of the slit entails a variation on the conductance of the gas.*

In addition to determining the rate of stripping losses with the residual gas, the size of the slit also affects to the beam size and the losses associated by axial deviations and the central region acceptance. On the one hand, a slight reduction in the height of the slit implies the total beam axial transmission, that is to say, the beam axial losses by collisions with the upper and lower part of the dee are removed. This optimization was estimated from the results presented in section 5.1.2 (see Figure 5.20), but it has been clearly verified with this study, as it is presented in Figure 6.13 showing the rms size and the maximum axial size for different slits considered. A slit of $\leq$5.5 mm height will provide the total axial transmission of the beam. On the other hand, the increase of the width slit from 0.2 mm to 0.4 mm involves a rise of 15% of the central region losses due to a variation in the acceptance, that is to say, particles arising from the extreme of the slit will not cross the puller. Therefore, the puller geometry should be modified to allow the total beam pass in case of increase the width of the slit. The effect of the increase in width on the final current can be estimated at first approximation if it is considered that the current extracted from the ion source is linear with the width of the slit. With that in mind, a net increase of the final current is obtained as the width is increased in the considered range, in spite of the lower transmission of the beam both by losses in the central region and by the increase of the stripping with the residual gas. Thus, the relative final current could be increased $\sim$60% in case of use a slit of 0.4 mm width. However, this conclusion must be carefully analyzed in future studies.

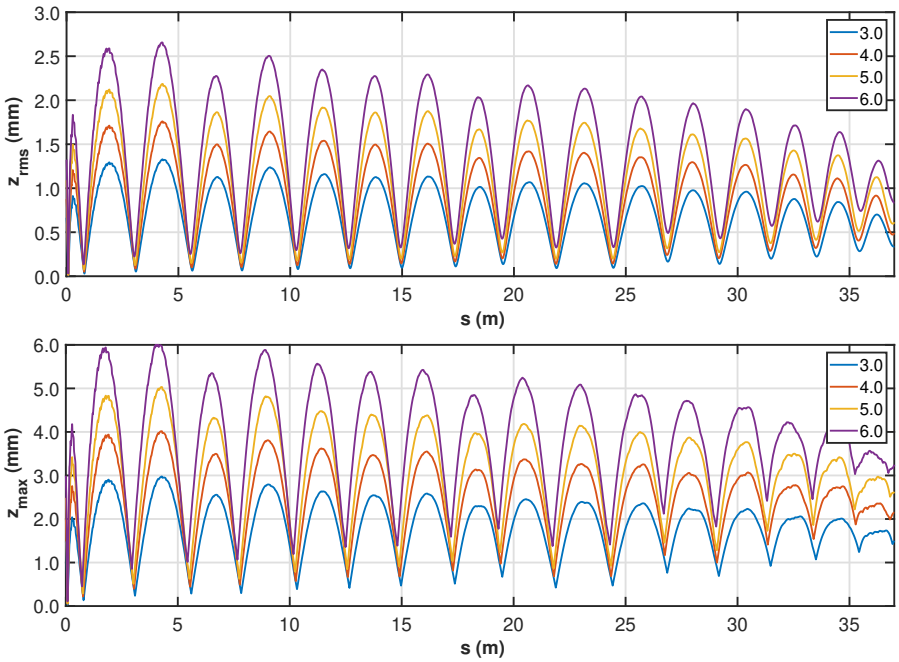

Figure 6.13: *Beam axial rms size (a) and maximum axial excursion (b) for different slit heights.*

The choice of the chimney slit has to consider all the aspects evaluated to provide sufficient beam current to fulfill the final requirements with minimal losses. Determining the influence of the slit area on the beam current extracted from the ion source is quite complicated, because many other parameters such as the plasma meniscus shape and the modification of the extracting electric field have an influence. A future study can perform experimental measurements of the

extracted beam current at the Ion Source Test facility for different slit sizes. The studies carried out for this thesis show that for the design slit a current extracted above the requirements is obtained, and therefore, a reduction of the slit is suitable to reduce the losses by stripping. Therefore, the appropriate slit size should be established based on slight variations from the chimney tested through experimental measurements and also taking into account a criterion of a stripping loss rate of less than 20% for the considered throughput conditions and balancing the width of the slit for simple manufacture but without excessively increasing the radial size of the beam. With that in mind, the slit of 5x0.3 mm would provide an improvement of the beam axial excursion, allowing to obtain a slightly higher injection current in the cyclotron but without increasing excessively the stripping losses. Therefore, balancing the data presented in this thesis, this slit can be considered an optimal slit for the AMIT cyclotron, although it should be verified experimentally in the commissioning.

6.4 Conclusions

The beam stripping interactions with the residual gas and the electromagnetic field have been carefully studied and applied to the AMIT cyclotron. The theoretical review of these processes has provided the basis for implementing these interactions in the OPAL code. Making use of semi-empirically analytic expressions with Monte Carlo methods, OPAL-CYCL has been extended in the actual release version to perform beam dynamics simulations in combination with these relevant interactions in cyclotrons. Once the benchmarking study has been carried out, this new OPAL feature has been applied to evaluate the beam stripping losses in AMIT. The results obtained have allowed to underestimate the relevance of the electromagnetic stripping, given the low energy of the beam, as well as to characterize the beam losses by interaction with the residual gas. This study shows a higher percentage of losses in the first acceleration gap, but without the extinction of these interactions to higher energies, which leads to a continuous damage of the internal components of the cyclotron and the activation of the machine. In order to minimize these effects, two factors have been presented to optimize the final beam current and total losses. On the one hand, the control of the gas load, balancing the higher production of particles at the ion source and the increase of losses. A slightly lower gas flow rate than the one that provides higher current experimentally is concluded to maximize the current. And on the other hand, the effect of the slit size of the ion source, to evaluate the modification of the injected current,the stripping losses and the axial and central region beam collisions.

It is very easy to criticize people for coming to erroneous conclusion after one knows the correct answer

— Gueorgui Gámov

Conclusions

Cyclotrons are becoming the most relevant alternative for radioisotope production beyond nuclear reactors. In particular, they allow to overcome the increasing radioisotopes demand for diverse medical procedures by means of a well known technology, relatively low cost compared with traditional production infrastructures, and adapted for an on-site production to extend the application of nuclear medicine techniques as well as the implicit benefit for the society.

AMIT cyclotron has been developed as an accelerator aimed at fulfilling these requirements for the current radionuclide supply system. Its cutting-edge design is based on a compact superconducting weak focused classical cyclotron configuration. It has been a technological challenge bringing together high technical specifications with specific beam requirements to achieve a reliable on-site radioisotope production in a compact facility. Therefore, the study of the beam dynamics has great relevance for the understanding of all associated physical effects and the possible optimization of the radioisotope production.

The beam dynamics of the AMIT cyclotron have been presented in this thesis using detailed simulations performed with OPAL code. The main acceleration characteristics have been carefully evaluated. A broad study has accounted for the aspects related to the central region, which have a great impact on the performance of the accelerator, analyzing the injection acceptance, the axial excursion, the energy spread and other relevant factors. In addition, the acceleration process along the whole path has been studied, with special attention to the synchronism evaluation, given the classical nature of the AMIT cyclotron, and the focusing effects. One of the main outcomes has been a beam transmission of 25% respect of the RF cycle, a good result according to the beam current requirement and the expected injection current. The extraction process and the beam transportation to the target has been assessed with a deep characterization of the beam and the extraction conditions to optimize the radioisotope production, establishing the extraction positions that provide total transmission efficiency from extraction to the target. Furthermore, a study of the fine tuning of the magnetic field and the radiofrequency as well as a large scale modifications of the accelerations conditions have been performed. Along with this, the cyclotron beam dynamics have included all the final settings of different subsystems after their manufacturing and assembly.

Apart from that, two fundamental aspects related to the optimum performance of the cyclotron have been evaluated. On the one hand, the experimental characterization of the ion source focused to become aware of the ion source performance under operation conditions and the beam characterization by means of measurements of the beam current and the beam profile.

A H^- beam current $>200\,\mu$A has been measured with a DC extraction system under different performance conditions of the ion source. On the other hand, the analysis of the beam residual interactions has been discussed through groundbreaking simulations performed with OPAL applied to the AMIT cyclotron. This analysis allows to optimize the final radioisotope production minimizing the beam losses. For that purpose, the injection conditions can be monitored by means of the gas load and the aperture of the ion source to control the vacuum pressure inside the accelerator. Thus, a reduction in stripping losses can be achieved from 40% to 20% by adjusting the gas load and an improvement of $10-15\%$ under modifications of the ion source chimney.

With that in mind, this dissertation has deeply analyzed the wide variety of effects affecting the beam acceleration from the injection to the target combining theoretical analyses, computational studies and experimental measurements. The main contributions of the thesis are summarized as follows:

- Collaboration in the commissioning of Ion Source Test bench, the final assembly of the components and the safety measures before the operation.
- Participation in the experimental characterization measurement campaigns of the cyclotron ion source with a DC high voltage extraction system. The operational conditions of the source, the ion current and the beam profile have been evaluated.
- Analysis of the experimental data of the ion source, verifying the results during the measurement campaigns and establishing the optimal operational ranges of the source according to the arc voltage and current, gas flow rate and the achievable beam current in different conditions.
- Verification of the beam profile after the ion source extraction by comparison with the experimental measurements and the outcomes provided by OPAL simulations.
- An extensive comprehension of OPAL code to perform the simulations, appraising most of its capabilities for a proper application to compact cyclotrons.
- Comprehensive beam dynamics studies of AMIT cyclotron with OPAL code. The principal effects of the beam transportation have been evaluated, with special attention to the central region of the cyclotron, the synchronism assessment, the focusing effects and the beam extraction to optimize the radioisotope production.
- Discussion of a fine tune of the different settings beyond the actual tolerances for a potential optimization of the cyclotron.
- Determination of the cyclotron configuration parameters to maximize the beam acceleration under different conditions of magnetic field, radiofrequency and accelerating voltage.
- Delimitation of the optimum position of the extraction system in a valid range of locations at different extraction energy for an adequate beam transportation to the target, minimizing the losses and the beam deviations in the drift transmission.

- Evaluation of the stripping mechanism efficiency and physical phenomena related to determine the optimum carbon foil thickness under the final beam requirements. The assessment has consisted in a theoretical study of the processes and the examination through simple particle-matter interaction codes.

- Study of the beam residual interactions on a compact cyclotron with especial focus on the reactions with the residual gas and the electromagnetic stripping of negative hydrogen ions. A detailed theoretical review based on previous studies has been performed, contributing to enhance the description of these relevant phenomena in cyclotrons.

- Computational implementation of those beam residual interactions in OPAL-CYCL, increasing the particle-matter physics considerations of the code to perform more reliable simulations. This part of the thesis work was carried out during a research stay at Paul Scherrer Institute (PSI).

- A benchmarking study of the beam stripping implementation in OPAL has verified the beam fraction lost in accordance with the theory and analytic evaluation.

- Assessment of the beam residual stripping interactions in AMIT cyclotron. This study has allowed to optimize some operational conditions like the gas load into the ion source and the aperture of the beam injection slit. These enhancements are focused to improve the beam qualities and to minimize the high-energy beam losses and the subsequent radioactive activation of the machine.

- Additionally, the active participation as part of the OPAL developer group during this thesis has allowed to improve new features as well as to enhance the code performance, collaborating in release versions OPAL-2.2 and OPAL-2.4.

Taking that into account, the results obtained provide remarkable information to reach the fulfillment of the project objective, aimed to optimize radioisotope production. Therefore, the objectives of this thesis have been satisfied.

Additionally, this thesis is a starting point for future studies that have been left out of the scope of this thesis. The results presented will be taken into account for future optimizations of the cyclotron, like new experimental measures with implementations ion source, as well as beam dynamics studies to correct the misalignment of certain subsystems. Moreover, these results will be applied in the upcoming commissioning of the cyclotron.

Publications derived from this thesis

International conference proceedings

- P. Calvo, A. Adelmann, A. Gsell *et al.*, *Beam stripping interactions implemented in cyclotrons with OPAL simulation code*, Proceedings of the 22th International Conference on Cyclotrons and their Applications (CYC 2019), Cape Town, South Africa, pp. 110–113 (2019)

- D. Obradors, P. Calvo, C. Oliver *et al.*, *Characterization of the AMIT internal ion source with a devoted DC extraction test bench*, Proceedings of the 8th International Particle Accelerator Conference (IPAC 2017), Copenhagen, Denmark, pp. 1740–1742 (2017)

- R. Varela, P. Calvo, C. Oliver *et al.*, *Beam diagnostics design for a compact superconducting cyclotron for radioisotope production*, Proceedings of the 5th International Beam Instrumentation Conference (IBIC 2016), Barcelona, Spain, pp. 108–110 (2016)

Articles submitted for publication

- A. Adelmann, P. Calvo, M. Frey *et al.*, *OPAL a versatile tool for charged particle accelerator simulations*, arXiv:1905.06654 [physics.acc-ph], to be submitted to Physical Review Accelerators and Beams (2019)

- P. Calvo, D. Obradors, R. Varela *et al.*, *Experimental characterization of the internal ion source for the AMIT compact cyclotron*, submitted to Nuclear Instruments and Methods in Physics Research Section A: Accelerators, Spectrometers, Detectors and Associated Equipment

- P. Calvo, I. Podadera, D. Gavela *et al.*, *Beam stripping residual interactions in AMIT compact cyclotron*, to be submitted to Physical Review Accelerators and Beams

Technical reports and Manuals

- A. Adelmann, P. Calvo, C. Metzge-Kraus *et al.*, *The OPAL Framework*, version 2.4, Paul Scherrer Institut (PSI) (2020)

- A. Bethani, E. Manoni, P. Calvo *et al.*, *Report on the ECFA Early-Career Researchers Debate on the 2020 European Strategy Update for Particle Physics*, CERN-OPEN-2020-006 (2020)

Oral presentations

- P. Calvo, *The AMIT compact cyclotron*, ARIES WP3 kick-off, Krakow, Poland, `https://indico.cern.ch/event/659942/` (2017)
- P. Calvo, *Plans and activities at each WP3 partner - CIEMAT*, ARIES WP3 kick-off, Krakow, Poland, `https://indico.cern.ch/event/659942/` (2017)

Pósters

- P. Calvo, D. Obradors, M. Domínguez *et al.*, *Optimization and characterization of the ion source for the compact superconducting AMIT cyclotron considering different chimney configurations*, Póster presentado en: 40th European cyclotron Progress Meeting, Legnaro, Italy (2017)
- P. Calvo, D. Obradors, R. Varela *et al.*, *Optimization of the ion source for the compact superconducting AMIT cyclotron for radioisotope production*, Póster presentado en: CERN Accelerator School's Introduction to Accelerator Physics course, Budapest, Hungary (2016)

References

[1] W. Crookes, *On the illumination of lines of molecular pressure, and the trajectory of molecules*, Philosophical Transactions **70**, 135 (1878)

[2] J. D. Cockcroft and E. T. S. Walton, *Experiments with high velocity positive ions*, Proceedings of the Royal Society of London Series A **129**, 477 (1930)

[3] E. O. Lawrence and M. S. Livingston, *The production of high speed light ions without the use of high voltages*, Physical Review **40**, 19 (1932)

[4] T. S. Pettersson and P. Lefèvre (LHC Study Group), *The Large Hadron Collider: conceptual design*, CERN-AC-95-05-LHC (1995)

[5] W. C. Röntgen, *Über eine neue art von strahlen. vorläufige mitteilung*, Sitzungsberichten der Würzburger Physik.-medic. Gesellschaft Würzburg, S.137-147 (1895)

[6] A. H. Becquerel, *Sur les radiations emises par phosphorescence*, Comptes Rendus Hebdomadaires des Séances de l'Académie des Sciences de Paris **122**, 420 (1896)

[7] M. Danlos and P. Block, *Note sur le traitement du lupus érythèmateux par des applications de radium*, Annales de Dermatologie et de Syphiligraphie **2**, 986 (1901)

[8] H. Dominici and J. Barcat, *L'action thérapeutique du radium sur les néoplasies*, Archives d'électricité medicalé expérimatales et cliniques **16**, 655 (1908)

[9] F. Proescher, *The intravenous injection of radium salts in man*, Radium **1**, 9 (1913)

[10] G. Hevesy, *The absorption and translocation of lead by plants. A contribution to the application of the method of radioactive indicators in the investigation of the change of substance in plants*, Biochemistry **17**, 439 (1923)

[11] H. Levi, *George Hevesy and his concept of radioactive indicators—in retrospect*, European Journal of Nuclear Medicine **1**, 3 (1976)

[12] K. Parodi, *Imaging in radiotherapy*, Proceedings of the CAS-CERN Accelerator School: Accelerators for Medical Applications, Vösendorf, Austria, CERN-2017-004-SP, pp. 71–78 (2015)

[13] A. P. Dhawan, H. K. Huang and D.-S. Kim, *Principles and Advanced Methods in Medical Imaging and Image Analysis*, World Scientific Publishing Company, 1st ed. (2008)

[14] D. E. Kuhl and R. Edwards, *Image separation radioisotope scanning*, Radiology **80**, 653 (1963)

[15] S. R. Cherry, J. A. Sorenson and M. E. Phelps, *Physics in Nuclear Medicine*, Elsevier Saunders, 4th ed. (2012)

[16] K. Goffin and K. van Laere, *Single-photon emission tomography*, *Neuroimaging Part I*, vol. 135 of *Handbook of Clinical Neurology*, Elsevier, chap. 13, pp. 241–250 (2016)

[17] *The Supply of Medical Radioisotopes. 2019 Medical isotope demand and capacity projection for the 2019-2024 period*, Tech. Rep. NEA/SEN/HLGMR(2019)1, Nuclear Energy Agency (NEA), OECD Publishing (2019)

[18] National Nuclear Data Center, information extracted from the NSR database, `http://www.nndc.bnl.gov/nudat2/`

[19] W. N. Cottingham and D. A. Greenwood, *An Introduction in Nucleear Physics*, Cambridge University Press, 2nd ed. (2001)

[20] T. F. Budinger, *Nuclear Medicine and Molecular Imaging*, vol. 1 of *Comprehensive Biomedical Physics*, edited by A. Brahme, Elsevier (2014)

[21] K. Lameka, M. D. Farwell and M. Ichise, *Positron emission tomography*, *Neuroimaging Part I*, vol. 135 of *Handbook of Clinical Neurology*, Elsevier, chap. 11, pp. 209–227 (2016)

[22] S. I. Ziegler, *Positron emission tomography: principles, technology, and recent developments*, Nuclear Physics A **752**, 679c (2005)

[23] M. D. Guimaraes *et al.*, *Functional magnetic resonance imaging in oncology: state of the art*, Radiologia Brasileira **47**, 101 (2014)

[24] S. DeBenedetti, C. E. Cowan, W. R. Konneker and H. Primakoff, *On the angular distribution of two-photon annihilation radiation*, Physical Review **77**, 205 (1950)

[25] S. E. Derenzo, *Precision measurement of annihilation point spread distributions for medically important positron emitters*, Proceedings of the 5th International Conference on Positron Annihilation (ICPA-5), Lake Yamanaka, Japan (1979)

[26] K. Shibuya *et al.*, *Annihilation photon acollinearity in PET: volunteer and phantom FDG studies*, Physics in Medicine and Biology **52**, 5249 (2007)

[27] E. do Nascimento, V. R. Vanin, N. L. Maidana and O. Helene, *Coincidence doppler broadening of positron annihilation radiation in Fe*, Journal of Physics: Conference Series **443**, 012024, 16th International Conference on Positron Annihilation (ICPA-16) (2013)

[28] J. F. Vansteenkiste, C. Deroose and C. Dooms, *Positron emission tomography*, *Murray and Nadel's Textbook of Respiratory Medicine*, Elsevier, chap. 21, pp. 360–371, 6th ed. (2016)

[29] *Cyclotron Produced Radionuclides: Guidance on Facility Design and Production of Fluorodeoxyglucose (FDG)*, Tech. Rep. Radioisotopes and Radiopharmaceuticals Series 3, International Atomic Energy Agency (IAEA) (2012)

[30] D. Petroni, L. Menichetti and M. Poli, *Historical and radiopharmaceutical relevance of [^{18}F]FDG*, Journal of Radioanalytical and Nuclear Chemistry **323**, 1017 (2020)

[31] Y. Huang, *An overview of PET radiopharmaceuticals in clinical use: regulatory, quality and pharmacopeia monographs of the United States and Europe* (2018)

[32] *Cyclotron Produced Radionuclides: Emerging Positron Emitters for Medical Applications: ^{64}Cu and ^{124}I*, Tech. Rep. Radioisotopes and Radiopharmaceuticals Reports 1, International Atomic Energy Agency (IAEA) (2016)

[33] P. Zanzonico, *Positron emission tomography: A review of basic principles, scanner design and performance, and current systems*, Seminars in Nuclear Medicine **34**, 87 (2004)

[34] S. M. Qaim, F. Tárkányi and R. Capote (editors), *Nuclear data for the production of therapeutic radionuclides*, Tech. Rep. Series No. 473, International Atomic Energy Agency (IAEA) (2011)

[35] T. Nunan, *A review of the supply of Molybdenum-99, the impact of recent shortages and the implications for Nuclear Medicine Services in the UK*, Tech. rep., Health Protection Agency, Administration of Radioactive Substances Advisory Committee (2010)

[36] U. Zetterberg, *A change in usage of cyclotrons for medical isotope production?*, Compact Accelerators for Isotope Production, Cockcroft Institute, Daresbury, UK (2015)

[37] *Manual for reactor produced radioisotopes*, Tech. Rep. Series No. 1340, International Atomic Energy Agency (IAEA) (2003)

[38] *Beneficial Uses and Production of Isotopes*, Tech. Rep. NEA No. 5293, Nuclear Energy Agency (NEA), OECD Publishing (2005)

[39] *Feasibility of Producing Molybdenum-99 on a Small Scale Using Fission of Low Enriched Uranium or Neutron Activation of Natural Molybdenum*, Tech. Rep. Series No. 478, International Atomic Energy Agency (IAEA) (2015)

[40] *Charged particle cross-section database for medical radioisotope production: diagnostic radioisotopes and monitor reactions*, Tech. Rep. IAEA-TECDOC-1211, International Atomic Energy Agency (IAEA) (2001)

[41] *Cyclotron Produced Radionuclides: Physical Characteristics and Production Methods*, Tech. Rep. Series No. 468, International Atomic Energy Agency (IAEA) (2009)

[42] A. Boschi, P. Martini, M. Pasquali and L. Uccelli, *Recent achievements in Tc-99m radiopharmaceutical direct production by medical cyclotrons*, Drug Development and Industrial Pharmacy **43**, 1402 (2017)

[43] T. J. McCarthy and M. J. Welch, *The state of positron emitting radionuclide production in 1997*, Seminars in Nuclear Medicine **28**, 235 (1998)

[44] *Cyclotron Produced Radionuclides: Principles and Practice*, Tech. Rep. Series No. 465, International Atomic Energy Agency (IAEA) (2008)

[45] P. Schmor, *Review of cyclotrons for the production of radioactive isotopes for medical and industrial applications*, Reviews of Accelerator Science and Technology **4**, 103 (2011)

[46] M. Jensen, *Particle accelerators for PET radionuclides*, Nuclear Medicine Review **15**, C9 (2012)

[47] D. J. Schlyer and T. J. Ruth, *Accelerator Production of Radionuclides*, *Industrial Accelerators and their Applications*, edited by R. W. Hamm and M. E. Hamm, World Scientific Publishing, chap. 4, pp. 139–181 (2012)

[48] V. Smirnov, *Modern compact accelerators of cyclotron type for medical applications*, Physics of Particles and Nuclei **47**, 863 (2016)

[49] C. Oliver, *Compact and efficient accelerators for radioisotope production*, Proceedings of the 8th International Particle Accelerator Conference (IPAC 2017), Copenhagen, Denmark, pp. 4824–4829 (2017)

[50] *Directory of cyclotrons used for radionuclide production in member states*, Tech. Rep. IAEA-DCRP/2006, International Atomic Energy Agency (IAEA), Industrial Applications and Chemistry Section (2006)

[51] V. Drozdovitch *et al.*, *Use of radiopharmaceuticals in diagnostic nuclear medicine in the United States: 1960-2010*, Health Physics **108**, 520 (2015)

[52] F. B. Payolla, A. C. Massabni and C. Orvig, *Radiopharmaceuticals for diagnosis in nuclear medicine: a short review*, Eclética Química Journal **44**, 11 (2019)

[53] *Radioisotopes in medicine*, Information Library, World Nuclear Association (2020)

[54] *Biomarker Generator,* `http://www.bestabt.com/our-solutions/overview/`, BEST ABT Molecular Imaging

[55] *Best Cyclotron Systems,* `http://www.bestcyclotron.com/products.html`

[56] R. Pommet, *Compact accelerators for PET production: LOTUS project*, Academia-Industry Matching Event on Superconductivity for Accelerators for Medical Applications, CIEMAT, Madrid, Spain (2016)

[57] T. Zhang, Z. Li, S. An, Z. Yin and F. Y. Jianjun Yang, *The cyclotron development activities at CIAE*, Nuclear Instruments and Methods in Physics Research Section B **269**, 2863 (2011)

[58] C. Oliver *et al.*, *Optimizing the radioisotope production with a weak focusing compact cyclotron*, Proceedings of the 20th International Conference on Cyclotrons and their Applications (CYC 2013), Vancouver, BC, Canada, pp. 429–431 (2013)

[59] J. Vincent *et al.*, *The Ionetix ION-12SC compact superconducting cyclotron for production of medical isotopes*, Proceedings of the 21th International Conference on Cyclotrons and their Applications (CYC 2016), Zurich, Switzerland, pp. 290–293 (2016)

[60] J. R. Alonso, R. Barlow, J. M. Conrad and L. H. Waites, *Medical isotope production with the IsoDAR cyclotron*, Nature Reviews Physics **1**, 533 (2019)

[61] General Electric Company, *GENtrace™ cyclotron*, DOC1681410 (2018)

[62] General Electric Company, *MINItrace™ Qilin. ^{18}F-production system*, DOC0453400 (2018)

[63] General Electric Company, *PETtrace™ 800 cyclotron series*, DOC077641 (2018)

[64] M. Abs *et al.*, *The IBA PET-Dedicated Cyclotrons: Main features and improvements*, Proceedings of the 14th International Conference on Cyclotrons and their Applications (CYCLOTRONS 95), Cape Town, South Africa, pp. 120–124 (1996)

[65] V. Nuttens *et al.*, *Design of IBA Cyclone 11 cyclotron magnet*, Proceedings of the 19th International Conference on Cyclotrons and their Applications (CYCLOTRONS 2010), Lanzhou, China, pp. 192–194 (2010)

[66] Ion Beam Applications, *Cyclone® 30* https://www.iba-radiopharmasolutions.com/sites/default/files/resources/files/cbr_c30_v5_r00.pdf (2010)

[67] Ion Beam Applications, *Cyclone® 70* https://www.iba-radiopharmasolutions.com/sites/default/files/resources/files/cyclone_70_web.pdf (2019)

[68] Ion Beam Applications, *Cyclone® KIUBE* https://www.iba-radiopharmasolutions.com/sites/default/files/resources/files/cbr_cyclone_kiube_v2_r05.pdf (2017)

[69] V. N. Starovoitova, L. Tchelidze and D. P. Wells, *Production of medical radioisotopes with linear accelerators*, Applied Radiation and Isotopes **85**, 39 (2014)

[70] M. Inagaki *et al.*, *Production of ^{47}Sc, ^{67}Cu, ^{68}Ga, ^{105}Rh, ^{177}Lu, and ^{188}Re using electron linear accelerator*, Journal of Radioanalytical and Nuclear Chemistry **322**, 1703 (2019)

[71] J. E. Stovall, L. D. Hansborough, and H. A. O'Brien, *Radioisotope production linac*, Proceedings of the 1981 Linear Accelerator Conference, Santa Fe, New Mexico, USA, pp. 344–348 (1981)

[72] L. D. Hansborough, R. W. Hamm and J. E. Stovall, *A Linear Accelerator for Radioisotope Production*, Tech. Rep. LA-9144-MS, Los Alamos National Laboratory (1982)

[73] R. W. Hamm, *Status of the AccSYs PULSAR™ system*, Proceedings of the Sixth Workshop on Targetry and Target Chemistry, Vancouver, BC, Canada, pp. 26–27 (1995)

[74] *PULSAR® - PET Isotope Production Systems,* `https://www.accsys.com/pulsar.html`, AccSys Technology Inc.

[75] M. Vretenar *et al.*, *High-frequency compact RFQs for medical and industrial applications*, Proceedings of the 28th Linear Accelerator Conference (LINAC 2016), East Lansing, MI, USA, pp. 704–709 (2016)

[76] R. E. Shefer, R. E. Klinkowstein, B. J. Hughey and M. J. Welch, *Production of pet radionuclides with a high current electrostatic accelerator*, Proceedings of the Fourth International Workshop on Targetry and Target Chemistry, Villigen, Switzerland, pp. 4–10 (1991)

[77] G. G. Gaehle, C. Dence, K. R. Lechner and M. J. Welch, *Utilizing the tandem cascade accelerator for the routine production of O-15 radiopharmaceuticals for neurological PET studies*, Proceedings of the Sixth Workshop on Targetry and Target Chemistry, Vancouver, BC, Canada, pp. 26–27 (1995)

[78] R. E. Shefer and Y. Kilnkowstein, R. E. ad Yanch, *High current electrostatic accelerator for boron neutron capture therapy*, Proceedings of the Fifth International Conference on applications of Nuclear Techniques: Neutrons in Research and Industry, Crete, Greece, International Society for Optics and Photonics, SPIE vol. 2867, pp. 41–47 (1997)

[79] P. Beasley and O. Heid, *Construction of a novel compact high voltage electrostatic accelerator*, Proceedings of the 2nd International Particle Accelerator Conference (IPAC 2011), San Sebastián, Spain, pp. 1722–1724 (2011)

[80] D. B. annd R. Barlow, T. Edgecock, R. Seviour and C. Johnstone, *A compact and high current FFAG for the production of radioisotopes for medical application*, Proceedings of the 7th International Particle Accelerator Conference (IPAC 2016), Busan, Korea, pp. 1957–1959 (2016)

[81] K. W. D. Ledingham *et al.*, *High power laser production of short-lived isotopes for positron emission tomography*, Journal of Physics D: Applied Physics **37**, 2341 (2004)

[82] D. Habs and U. Köster, *Production of medical radioisotopes with high specific activity in photonuclear reactions with γ-beams of high intensity and large brilliance*, Applied Physics B **103**, 501 (2011)

[83] W. Luo *et al.*, *Estimates for production of radioisotopes of medical interest at extreme light infrastructure – nuclear physics facility*, Applied Physics B **122**, 8 (2016)

[84] M. Seimetz *et al.*, *Proton acceleration with a table-top TW laser*, Journal of Instrumentation **11**, C11012 (2016)

[85] A. Zaeem *et al.*, *Activities study of short-lived radioisotopes with a filippov-type plasma focus*, Journal of Fusion Energy **28**, 268 (2009)

[86] M. Roshan *et al.*, *Potential medical applications of the plasma focus in the radioisotope production for PET imaging*, Physics Letters A **378**, 2168 (2014)

[87] F. Tabbakh, S. Sadat Kiai and M. Pashaei, *Conceptual achievement of 1 GBq activity in a Plasma Focus driven system*, Applied Radiation and Isotopes **129**, 211 (2017)

[88] *The Supply of Medical Isotopes: an economic diagnosis and possible solutions*, Tech. rep., Nuclear Energy Agency (NEA), OECD Publishing (2019)

[89] *Production of Long Lived Parent Radionuclides for Generators:* ^{68}Ge, ^{82}Sr, ^{90}Sr *and* ^{188}W, Tech. Rep. Radioisotopes and Radiopharmaceuticals Series 2, International Atomic Energy Agency (IAEA) (2010)

[90] *Therapeutic Radionuclide Generators:* $^{90}Sr/^{90}Y$ *and* $^{188}W/^{188}Re$ *Generators*, Tech. Rep. Series No. 470, International Atomic Energy Agency (IAEA) (2009)

[91] M. Seidel, *Cyclotrons for high-intensity beams*, Proceedings of the CAS-CERN Accelerator School: Course on High Power Hadron Machines, Bilbao, Spain, CERN-2013-001, pp. 17–32, arXiv:1302.1001 [physics.acc-ph] (2013)

[92] F. Chautard, *Beam dynamics for cyclotrons*, Proceedings of the CAS-CERN Accelerator School and KVI: Specialised CAS Course on Small Accelerators, Zeegse, The Netherlands, CERN-2006-012, pp. 209–229 (2006)

[93] Albert Einstein in letter to Lincoln Barnett, 19 June 1948, as quoted in L. B. Okun, *The concept of mass*, **42**, 31 (1989)

[94] E. Taylor and J. Wheeler, *Spacetime Physics*, W.H. Freeman and Company, chap. 8, pp. 248–249, 2nd ed. (1992)

[95] J. Allday, *Space-time. An Introduction to Einstein's Theory of Gravity*, CRC Press, chap. 5, pp. 119–120 (2019)

[96] H. Wiedemann, *Particle Accelerator Physics*, Springer, 4th ed. (2015)

[97] M. Steenbeck, *Device for producing electron rays of high energy*, US Patent No 2,103,303 (1936)

[98] M. S. Livingston and J. P. Blewett, *Particle Accelerators*, McGraw-Hill (1962)

[99] M. E. Rose, *Focusing and maximum energy of ions in the cyclotron*, Physical Review **53**, 392 (1938)

[100] R. R. Wilson, *Magnetic and electrostatic focusing in the cyclotron*, Physical Review **53**, 408 (1938)

[101] B. L. Cohen, *The theory of the fixed frequency cyclotron*, Review of Scientific Instruments **24**, 589 (1953)

[102] M. Reiser, *First-order theory of electrical focusing in cyclotron-type two-dimensional lenses with static and time-varying potentials*, Journal of Applied Physics **42**, 4128 (1971)

[103] S. Humphries, *Principles of Charged Particle Acceleration*, John Wiley and Sons (1999)

[104] L. H. Thomas, *The paths of ions in the cyclotron I. Orbits in the magnetic field*, Physical Review **54**, 580 (1938)

[105] E. D. Courant, M. S. Livingston and H. S. Snyder, *The strong-focusing synchroton—A new high energy accelerator*, Physical Review **88**, 1190 (1952)

[106] D. W. Kerst, K. M. Terwilliger, L. W. Jones and K. R. Symon, *Fixed field alternating gradient accelerator with spirally ridged poles*, Physical Review **98**, 1153, (Abstr.) (1955)

[107] H. A. Willax, *Proposal for a 500 MeV isochronous cyclotron with ring magnet*, Proceedings of the International Conference on Sector-Focused Cyclotrons and Meson Factories (CYC 63), Geneva, Switzerland, pp. 386–397 (1963)

[108] V. I. Veksler, Doklady Akademii Nauk SSSR **44**, 393 (1944)

[109] V. I. Veksler, Journal of Physics (USSR) **9**, 153 (1945)

[110] E. M. McMillan, *The synchrotron—A proposed high energy particle accelerator*, Physical Review **68**, 143 (1945)

[111] K. W. Ehlers, *Design considerations for high-intensity negative ion sources*, Nuclear Instruments and Methods **32**, 309 (1965)

[112] P. Heikkinen, *Injection and extraction for cyclotrons*, Proceedings of the CAS-CERN Accelerator School : 5th General Accelerator Physics Course, Jyväskylä, Finland, pp. 819–839 (1994)

[113] G. I. Dimov, *Use of hydrogen negative ions in particle accelerators*, Review of Scientific Instruments **67**, 3393 (1996)

[114] W. Kleeven, *Injection and extraction for cyclotrons*, Proceedings of the CAS-CERN Accelerator School and KVI: Specialised CAS Course on Small Accelerators, Zeegse, The Netherlands, CERN-2006-012, pp. 271–296 (2006)

[115] W. R. Leo, *Techniques for Nuclear and Particle Physics Experiments*, Springer, 2nd ed. (1993)

[116] S. Takács, F. Tárkányi, A. Hermanne and R. P. de Corcuera, *Validation and upgrading of the recommended cross section data of charged particle reactions used for production of pet radioisotopes*, Nuclear Instruments and Methods in Physics Research B **211**, 169 (2003)

[117] L. García-Tabarés *et al.*, *Development of a superconducting magnet for a compact cyclotron for radioisotope production*, IEEE Transactions on Applied Superconductivity **26**, 1 (2016)

[118] J. Munilla, *Development of a novel concept of efficient superconducting magnet for radioisotope production cyclotron*, Ph.D. thesis, Universidad Pontificia Comillas (2020)

[119] J. Munilla *et al.*, *Validation test of the forced-flow cooling concept for the superconducting magnet of AMIT cyclotron*, IEEE Transactions on Applied Superconductivity **26**, 1 (2016)

[120] J. Munilla *et al.*, *Cold tests and magnetic characterization of a superconducting magnet for a compact cyclotron for radioisotope production*, IEEE Transactions on Applied Superconductivity **28**, 1 (2018)

[121] J. Campmany *et al.*, *A new bench concept for measuring magnetic fields of big closed structure*, Physics Procedia **75**, 1222, 20th International Conference on Magnetism (ICM 2015) (2015)

[122] D. Gavela *et al.*, *Calculation and design of a RF cavity for a novel compact superconducting cyclotron for radioisotope production*, Proceedings of the 6th International Particle Accelerator Conference (IPAC 2015), Richmond, Virginia, USA, pp. 3055–3057 (2015)

[123] D. Gavela *et al.*, *Fabrication and tests of a RF cavity for a novel compact superconducting cyclotron for radioisotope production*, Proceedings of the 8th International Particle Accelerator Conference (IPAC 2017), Copenhagen, Denmark, pp. 4585–4588 (2017)

[124] G. J. Schulz, *Formation of H^- ions by electron impact on H_2*, Physical Review **113**, 816 (1959)

[125] K. Prelec and T. Sluyters, *Formation of negative hydrogen ions in direct extraction sources*, Review of Scientific Instruments **44**, 1451 (1973)

[126] R. K. Janev, D. Reiter and U. Samm, *Collision processes in low-temperature hydrogen plasmas*, Tech. Rep. Jül-4105, Forschungszentrum Jülich, Germany (2003)

[127] C. L. Lykke, K. K. Murray and W. C. Lineberger, *Threshold photodetachment of H^-*, Physical Review A **43**, 6104 (1991)

[128] D. Obradors *et al.*, *Characterization of the AMIT internal ion source with a devoted DC extraction test bench*, Proceedings of the 8th International Particle Accelerator Conference (IPAC 2017), Copenhagen, Denmark, pp. 1740–1742 (2017)

[129] A. H. Morton and W. I. B. Smith, *Improved cyclotron performance from control of initial ion motion*, Nuclear Instruments and Methods **4**, 36 (1959)

[130] M. Reiser, *Central-region factors influencing the duty cycle of a cyclotron beam*, Proceedings of the International Conference on Sector-Focused Cyclotrons and Meson Factories (CYC 63), Geneva, Switzerland, pp. 203–208 (1963)

[131] R. J. Louis, *The properties of ion orbits in the central region of a cyclotron*, Ph.D. thesis, The University of Britsh Columbia (1971)

[132] C. D. Child, *Discharge from hot cao*, Physical Review (Series I) **32**, 492 (1911)

[133] I. Langmuir, *The effect of space charge and residual gases on thermionic currents in high vacuum*, Physical Review **2**, 450 (1913)

[134] M. Reiser, *Central orbit program for a variable energy multi-particle cyclotron*, Nuclear Instruments and Methods **18-19**, 370 (1962)

[135] H. Tawara and A. Russek, *Charge changing processes in hydrogen beams*, Review of Modern Physics **45**, 178 (1973)

[136] G. H. Gillespie, *High-energy cross sections for H^- ions incident on intermediate and high-Z atoms*, Physical Review A **16**, 943 (1977)

[137] R. C. Webber and C. Hojvat, *Measurement of the electron loss cross sections for negative hydrogen ions on carbon at 200 MeV*, IEEE Transactions on Nuclear Science **26**, 4012 (1979)

[138] W. Chou, M. Kostin and Z. Tang, *Stripping efficiency and lifetime of carbon foils*, Nuclear Instruments and Methods in Physics Research Section A **590**, 1 (2006)

[139] M. Tanabashi *et al.* (Particle Data Group), *Review of Particle Physics*, Phys. Rev. D **98**, 030001 (2018)

[140] M. Berger, J. Coursey, M. Zucker, and J. Chang, *ESTAR, PSTAR, and ASTAR: Computer Programs for calculating Stopping-Power and Range Tables for electrons, protons, and helium ions*, (version 2.0.1), `http://physics.nist.gov/Star` (2017)

[141] J. D. Jackson, *Classical Electrodynamics*, John Wiley, chap. 13, pp. 624–660, 3rd ed. (1999)

[142] M. Aiba, C. Carli, B. Goddard and W. Weterings, *Stripping foils for the PSB H^- injection system*, Tech. Rep. sLHC-Project-Note-0005, Conseil Européen pour la Recherche Nucléaire (CERN) (2009)

[143] I. Yamane, K. Kitagawa, H. Someya and Y. Yano, *Injection of 1 GeV H^- beam into the JHF I-A Ring*, Tech. Rep. KEK 88-8, National Laboratory for High Energy Physics (KEK), Japan (1988)

[144] I. Yamane, *Treatment of H^0 and H^- beams spilled at the stripper foil at full energy charge-exchange injection scheme*, Proceedings of the eleventh meeting of the International Collaboration on Advanced Neutron Sources (ICANS-XI), Tsukuba, Japan, pp. 224–234, KEK Report 90-25 (1990)

[145] J. F. Ziegler, J. P. Biersack and M. D. Ziegler, *SRIM – The stopping and range of ions in matter*, Nuclear Instruments and Methods in Physics Research B **268**, 1818 (2010)

[146] F. Sansaloni *et al.*, *Production of $[^{11}C]CO_2$ with gas target at low proton energies*, Applied Radiation and Isotopes **78**, 10 (2013)

[147] I. Podadera *et al.*, *Beam diagnostics for commissioning and operation of a novel compact cyclotron for radioisotope production*, Proceedings of the 2nd International Beam Instrumentation Conference (IBIC 2013), Oxford, UK, pp. 660–663 (2013)

[148] R. Varela *et al.*, *Beam diagnostics design for a compact superconducting cyclotron for radioisotope production*, Proceedings of the 5th International Beam Instrumentation Conference (IBIC 2016), Barcelona, Spain, pp. 108–110 (2016)

[149] R. Kersevan and J.-L. Pons, *Introduction to MOLFLOW+: New graphical processing unit-based Monte Carlo code for simulating molecular flows and for calculating angular coefficients in the compute unified device architecture environment*, Journal of Vacuum Science & Technology A **27**, 1017 (2009)

[150] R. Kersevan and M. Ady, *Recent developments of Monte-Carlo codes MolFlow+ and SynRad+*, Proceedings of the 10th International Particle Accelerator Conference (IPAC 2019), Melbourne, Australia, pp. 1327–1330 (2019)

[151] A. Roth, *Vacuum Technology*, Elsevier, 3rd ed. (1998)

[152] V. Smirnov, *Computer codes for beam dynamics analysis of cyclotronlike accelerators*, Physical Review Accelerators and Beams **20**, 124801 (2017)

[153] J. J. Yang, A. Adelmann, M. Humbel, M. Seidel and T. J. Zhang, *Beam dynamics in high intensity cyclotrons including neighboring bunch effects: Model, implementation, and application*, Physical Review Special Topics - Accelerators and Beams **13**, 064201 (2010)

[154] Y. J. Bi *et al.*, *Towards quantitative simulations of high power proton cyclotrons*, Physical Review Special Topics - Accelerators and Beams **14**, 054402 (2011)

[155] T. Zhang, H. Yao, J. Yang, J. Zhong and S. An, *The beam dynamics study for the CYCIAE-100 cyclotron*, Nuclear Instruments and Methods in Physics Research A **676**, 90 (2012)

[156] M. Abs *et al.*, *Multimegawatt DAEδALUS cyclotrons for neutrino physics*, arXiv:1207.4895 [physics.acc-ph] (2012)

[157] A. Adelmann *et al.*, *OPAL a versatile tool for charged particle accelerator simulations*, arXiv:1905.06654 [physics.acc-ph] (2019)

[158] A. Adelmann *et al.*, *The OPAL Framework*, Paul Scherrer Institut (PSI), version 2.4 (2020)

[159] V. Rizzoglio *et al.*, *Evolution of a beam dynamics model for the transport line in a proton therapy facility*, Physical Review Accelerators and Beams **20**, 124702 (2017)

[160] V. Rizzoglio, *Precise beam dynamics models for transport lines in a cyclotron-based proton therapy facility*, Ph.D. thesis, ETH Zürich (2018)

[161] F. C. Iselin, *The classic project*, Tech. Rep. CERN/SL/96-061, Conseil Européen pour la Recherche Nucléaire (CERN) (1996)

[162] A. Adelmann and Y. Ineichen, *The IPPL (Independent Parallel Particle Layer) Framework*, Tech. Rep. PSI-PR-09-05, Paul Scherrer Institut (2009)

[163] J. Qiang and R. D. Ryne, *Parallel 3D Poisson solver for a charged beam in a conducting pipe*, Computer Physics Communications **138**, 18 (2001)

[164] M. M. Gordon and V. Taivassalo, *Nonlinear effects of focusing bars used in the extraction systems of superconducting cyclotrons*, IEEE Transactions on Nuclear Science **32**, 2447 (1985)

[165] A. Adelmann, P. Arbenz and Y. Ineichen, *A fast parallel Poisson solver on irregular domainsapplied to beam dynamics simulations*, Journal of Computational Physics **229**, 4554 (2010)

[166] D. Winklehner, A. Adelmann, A. Gsell, T. Kaman and D. Campo, *Realistic simulations of a cyclotron spiral inflector within a particle-in-cell framework*, Physical Review Accelerators and Beams **20**, 124201 (2017)

[167] M. Howison *et al.*, *H5hut: A high-performance I/O library for particle-based simulations*, 2010 IEEE International Conference on Cluster Computing Workshops and Posters (Cluster Workshops), vol. 1, pp. 1–8 (2010)

[168] *OPERA FEA Simulation Software*

[169] *ANSYS® Academic Research Mechanical*, Release 16.2, ANSYS, Inc.

[170] D. Soriano Guillén, *Sensitivity studies for the RF cavity of the AMIT cyclotron*, Master's thesis, Universidad Politécnica de Madrid (2018)

[171] D. Winklehner, *Adding arbitrary geometries to OPAL-CYCL*, private communication (2016)

[172] C. Geuzaine and J.-F. Remacle, *Gmsh: A 3-D finite element mesh generator with built-in pre- and post-processing facilities*, International Journal for Numerical Methods in Engineering **79**, 1309 (2009)

[173] S. R. Lawrie, D. C. Faircloth, A. P. Letchford, M. O. Whitehead and T. Wood, *Detailed beam and plasma measurements on the vessel for extraction and source plasma analyses (VESPA) Penning H^- ion source*, Review of Scientific Instruments **87**, 02B122 (2016)

[174] M. Borland, *A self-describing file protocol for simulation integration and shared postprocessors*, Proceedings of the 16th Particle Accelerator Conference and International Conference on High-Energy Accelerators, Dallas, USA, pp. 2184–2186 (1995)

[175] *ANTEC MAGNETS*, `https://antec-group.com/magnets/`

[176] L. Spitzer, *Physics of Fully Ionized Gases*, Interscience Publisher, 2nd ed. (1957)

[177] I. Langmuir, *Currents limited by space charge between concentric spheres*, Physical Review **24**, 49 (1924)

[178] J. R. Coupland, T. S. Green, D. P. Hammond and A. C. Riviere, *A study of the ion beam intensity and divergence obtained from a single aperture three electrode extraction system*, Review of Scientific Instruments **44**, 1258 (1973)

[179] D. H. An *et al.*, *The negative hydrogen penning ion gauge ion source for KIRAMS-13 cyclotron*, Review of Scientific Instruments **79**, 02A520 (2008)

[180] T. Y. T. Kuo and G. O. Hendry, *Recent development of internal H^-/D^- source for compact cyclotrons*, Proceedings of the 20th International Conference on Cyclotrons and their Applications (CYC 2013), Vancouver, BC, Canada, pp. 352–356 (2013)

[181] Z. Y. n *et al.*, *The study of discharge characteristic of the cold-cathode negative hydrogen PIG-type ion source*, Nuclear Instruments and Methods in Physics Research A **685**, 29 (2012)

[182] S. Silakhuddin and S. Santosa, *Investigation on operating parameters of the homemade Penning-type ion source for cyclotron*, Atom Indonesia **41**, 139 (2015)

[183] M. Reiser, *The effects of central-region conditions on time structure and quality of cyclotron beams*, Proceedings of the Fifth International Cyclotron Conference (CYC 69), Oxford, UK, pp. 289–304 (1969)

[184] S. Tavernier, *Experimental Techniques in Nuclear and Particle Physics*, Springer (2010)

[185] P. J. Mohr, D. B. Newell and B. N. Taylor, *CODATA Recommended values of the fundamental physical constants: 2014*, Review of Modern Physics **88**, 035009 (2016)

[186] S. K. Allison, *Experimental results on charge-changing collisions of hydrogen and helium atoms and ions at kinetic energies above 0.2 KeV*, Review of Modern Physics **30**, 1137 (1958)

[187] C. F. Barnett *et al.*, *Atomic data for controlled fusion research*, Tech. Rep. ORNL-5206/V1, Oak Ridge National Laboratory (1977)

[188] Y. Nakai, T. Shirai, T. Tabata and R. Ito, *Cross sections for charge transfer of hydrogen atoms and ions colliding with gaseous atoms and molecules*, Atomic Data and Nuclear Data Tables **37**, 69 (1987)

[189] A. V. Phelps, *Cross section and swarm coefficients for H^+, H_2^+, H_3^+, H, H_2 and H^- in H_2 for energies from 0.1 eV to 10 keV*, Journal of Physical and Chemical Reference Data **19**, 653 (1990)

[190] C. F. Barnett, *Atomic data for fusion. Volume 1: Collisions of H, H_2, He and Li atoms and ions with atoms and molecules*, Tech. Rep. ORNL-6068/V1, Oak Ridge National Laboratory, edited by H. T. Hunter, M. I. Kirkpatrick, I. Alvarez, C. Cisneros, and R. A. Phaneuf (1990)

[191] A. V. Phelps, *Collisions of H^+, H_2^+, H_3^+, ArH^+, H^-, H and H_2 with Ar and Ar^+ and ArH^+ with H_2 for energies from 0.1 eV to 10 keV*, Journal of Physical and Chemical Reference Data **21**, 883 (1992)

[192] G. H. Gillespie, *Double closure calculation of the electron-loss cross section for H^- in high-energy collisions with H and He*, Physical Review A **15**, 563 (1977)

[193] G. H. Gillespie, *Excitation and ionization contributions to sum-rule Born cross sections for collisions of one-electron ions with atoms*, Physical Review A **18**, 1967 (1978)

[194] R. K. Janev, W. D. Langer, K. E. Jr. and D. E. P. Jr., *Elementary Processes in Hydrogen-Helium Plasmas, Cross Sections and Reaction Rate Coefficients*, vol. 4 of *Atoms + Plasmas*, edited by G. Ecker, Springer-Verlag (1987)

[195] A. E. S. Green and R. J. McNeal, *Analytic cross sections inelastic for collisions of protons and hydrogen atoms with atomic and molecular gases*, Journal of Geophysical Research **76**, 133 (1971)

[196] T. Tabata and T. Shirai, *Analytic cross sections for collisions of H^+, H_2^+, H_3^+, H, H_2 and H^- with hydrogen molecules*, Atomic Data and Nuclear Data Tables **76**, 1 (2000)

[197] M. A. Furman and D. E. Johnson, *A possible design of the Linac-to-LEB injection girder for 1133 MeV H^- ions*, SSC-N-564 (2002)

[198] L. R. Scherk, *A improved value for the electron affinity of the negative hydrogen ion*, Canadian Journal of Physics **57**, 558 (1979)

[199] T. Tietz, *Analytical formula for continuos absorption coefficient of the hydrogen negative ion*, Physical Review **124**, 493 (1961)

[200] P. B. Keating, *Electric-field-induced electron detachment of 800-MeV H^- ions*, Physical Review A **52**, 4547 (1995)

[201] G. M. Stinson *et al.*, *Electric dissociation of H^- ions by magnetic fields*, Nuclear Instruments and Methods **74**, 333 (1969)

[202] David B. Newell and Eite Tiesinga (editors), *The International System of Units (SI)*, Tech. Rep. NIST SP 330, National Institute of Standards and Technology (2019)

[203] E. Tiesinga, P. J. Mohr, D. B. Newellf and B. N. Taylor, *The 2018 CODATA Recommended Values of the Fundamental Physical Constants*, `http://physics.nist.gov/constants`

[204] A. J. Jason, D. W. Hudgings and O. B. van Dyck, *Neutralization of H^- beams by magnetic stripping*, IEEE Transactions on Nuclear Science **28**, 2703 (1981)

[205] P. Calvo *et al.*, *Beam stripping interactions implemented in cyclotrons with OPAL simulation code*, Proceedings of the 22th International Conference on Cyclotrons and their Applications (CYC 2019), Cape Town, South Africa, pp. 110–113 (2019)

[206] A. Picard, R. S. Davis, M. Glaser and K. Fujii, *Revised formula for the density of moist air (CIPM-2007)*, Metrologia **45**, 149 (2008)